Plasma Oscillations and Operational Modes in Hall Effect Thrusters

by

Michael J. Sekerak

A dissertation submitted in partial fulfillment
of the requirements for the degree of
Doctor of Philosophy
(Aerospace Engineering)
in the University of Michigan
2014

Doctoral Committee:

Professor Alec D. Gallimore, Co-Chair
Assistant Professor Benjamin W. Longmier, Co-Chair
Daniel L. Brown, Air Force Research Laboratory
Associate Professor John E. Foster
James E. Polk, National Aeronautics and Space Administration

The Giants of 20th Century Science

Many of Whom are Referenced Herein with Great Reverence
Without Your Foundation, This Work Would Not be Possible

SOLVAY CONFERENCE 1927

colourized by pastincolour.com

A. PICARD E. HENRIOT P. EHRENFEST Ed. HERSEN Th. DE DONDER E. SCHRÖDINGER E. VERSCHAFFELT W. PAULI W. HEISENBERG R.H FOWLER L. BRILLOUIN
P. DEBYE M. KNUDSEN W.L. BRAGG H.A. KRAMERS P.A.M. DIRAC A.H. COMPTON L. de BROGLIE M. BORN N. BOHR
I. LANGMUIR M. PLANCK Mme CURIE H.A. LORENTZ A. EINSTEIN P. LANGEVIN Ch.E. GUYE C.T.R. WILSON O.W. RICHARDSON
Absents : Sir W.H. BRAGG, H. DESLANDRES et E. VAN AUBEL

"If I have seen further it is by standing on the shoulders of Giants."

-Sir Isaac Newton to Robert Hooke, 1676

2014

For Ann, Aviana and Maxwell.
Thank you for your love, support and patience.

ACKNOWLEDGMENTS

The origins of this journey can be traced to the last millennium, when I showed up on the campus of Caltech in 1999 to study and do research at JPL in the field of electric propulsion. I am very thankful for the opportunity provided by Prof. Fred Culick and the advising of Jay Polk to get me started in this field. If only I could have imagined then the circuitous path that would eventually lead to the completion of my Ph.D. so many years later. That path wound through the streets of Baghdad, the Rocky Mountains, down the isle with a wonderful women, onto the launch pads in Kodiak and Kauai, and eventually back to my midwestern roots. It has been 15 years since I showed up in California as a know-it-all kid and now this humbled old man will finally don the hood. Of course things do not always go according to plan as I had no intention of doing Hall thruster research as I focused on ELF. But fortuitous events led me to do a dissertation on the H6 and become a Hall thruster guy, and I couldn't be more pleased with the results.

First and foremost I want to acknowledge my advisor and mentor, Alec Gallimore. Thank you for taking in a student with a lot of constraints. I appreciate the wisdom and experience you have so readily shared during our many chats on everything from football, to leadership, to strategic vision and even EP on occasion. I did a very thorough trade space analysis to select Michigan and its been one of the best decisions I have ever made. It has been a great experience to be part of the amazing institute you have built with PEPL and I am proud to be a card-carrying member of the "Michigan Mafia."

I also want to acknowledge the education and mentoring from other Michigan faculty members including Y.Y. Lau, Brian Gilchrist, John Foster, Tim Smith, Iain Boyd and Ben Longmier. Especially to Ben, best of luck as you push hard to make your mark and build on the legacy of PEPL. Many thanks go to Dave McLean, Cindy Enoch, Tom Griffin and all of the aero staff. A special thanks goes to Denise Phelps for keeping all of us in line, which is akin to herding cats. And I appreciate the efforts of Alec's assistants, Colleen Root and Chanda Doxie, for your help with coordination.

To Jay Polk, thank you for staying in touch over the years and taking me on again, but this time without the Army intervening. Your guidance and mentoring has been immensely helpful. To Rich Hofer, your advice and critical analysis has taught me a lot about Hall thrusters, to which I am forever indebted. The guidance and advice from Dan Brown and Robbie Lobbia at AFRL have been invaluable and I thank you for helping me on this path. I also want to thank Hani Kamhawi and Wensheng at GRC for the invitation to work on the 300M-Ms. And I appreciate the seasoned advice of Dave Kirtley from MSNW to move on from the ELF when the hardware was falling behind.

At this point I will acknowledge my funding sources and most importantly I would like to thank NASA for selecting me to be part of the inaugural Space Technology Research Fellowship class. The support from the NSTRF has allowed me to focus on my research and develop a close collaboration with NASA centers. I have worked tirelessly to achieve the program's goals, which I wholly believe in, to "provide the nation with a pipeline of highly skilled engineers and technologists to improve America's technological competitiveness" and "perform innovative space technology research while building the skills necessary to become future technological leaders." I also want to thank AFRL/RQRS for financial and technical assistance for my research.

It is the people that make PEPL such a special place and I am grateful for the mentoring and friendships formed here. Thanks to the "older" students who guided when I first arrived: Rohit Shastry, Wensheng Huang, Adam Shabshelowitz, Laura Spencer, Ricky Tang, Ray Liang, and Tom Liu. I want to extend a special thanks to the two people who spent so much time and energy teaching me about high-speed diagnostics and Hall thrusters, Robbie Lobbia and Mike McDonald. Your work is outstanding and I am proud to stand on your shoulders as I build on your achievements. Not only did I learn plasma physics and Hall thrusters, but I gained an appreciation for greek yogurt. Another special thanks to Roland Florenz and our chats over coffee (or lattes and hot chocolate). Your crazy thruster was a wild ride and congrats on pulling it off; I hope the Marine Corps is everything you hoped it would be. And to the current PEPL students Chris Durot, Kim Trent and Scott Hall, best of luck on finishing your degrees. To the next generation of PEPL, Tim Collard, Ingrid Reese, Ethan Dale, and Frans Ebersohn, you bring a new energy to the lab and there are high expectations upon your shoulders to keep the lab at a high level. Thanks to Marcel Georgin for your help in data crunching. Working alongside Ken Hara and Brandon Smith in classes helped immensely and the office chats with Matt Obenchain were a welcome relief from the workload.

To my many friends who I have essentially ignored over the past 4 years, thanks for your patience and I look forward to skiing, biking and beers again. Robert Moeller, thanks for your support and friendship for our combined almost 3 decades from when we met at Caltech to when we finished. The tireless support of John and Barb Falk has helped immensely and the kids love all the time spent with Grandma and Grandpa. And Martha and Jack Hicks have provided many enjoyable evenings. A special thank you to my parents, Jim and Val Sekerak, and my sisters, Lisa and Becky, for your support and keeping me grounded. Although you won't remember any of this, Aviana and Maxwell, you have provided so many laughs and fond memories that always made me smile during the long hours of work.

Most significantly, the biggest and most heartfelt thank you goes to my wonderful, beautiful and infinitely patient wife, Dr. Ann Sekerak. Your understanding of all the nights spent alone while I worked "second shift" can never be repaid...but I will try. Thank you and I love you.

Michael Sekerak
Saline, MI
2014

TABLE OF CONTENTS

LIST OF FIGURES

LIST OF TABLES

LIST OF APPENDICES

LIST OF ACRONYMS

AC Alternating Current

AEHF Advanced Extremely High Frequency

AFB Air Force Base

AFRL Air Force Research Laboratory

ARM Asteroid Retrieval Mission

BHT Busek Hall Thruster

BPT Busek Primex Thruster

CCW Counter Clockwise

CFD Computational Fluid Dynamics

CFF Cathode Flow Fraction

CW Clockwise

DAQ Data Acquisition

DC Direct Current

DFT Discrete Fourier Transform

DSMC Direct Simulation Monte Carlo

EEDF Electron Energy Distribution Function

EP Electric Propulsion

ESA European Space Agency

GEO Geostationary Earth Orbit

GRC Glenn Research Center

HARP High-speed Axial Reciprocating Probe

HDLP High-speed Dual Langmuir Probe

HDLP-ISR High-speed Dual Langmuir Probe with Ion Saturation Reference

HET Hall Effect Thruster

HIA High-speed Image Analysis

ISR Ion Saturation Reference

JPL Jet Propulsion Laboratory

LEO Low Earth Orbit

LIF Laser Induced Fluorescence

LVDT Linear Variable Differential Transformer

LVTF Large Vacuum Test Facility

NASA National Aeronautics and Space Administration

NHT Nested Hall Effect Thrusters

NRO National Reconnaissance Office

ODE Ordinary Differential Equation

OML Orbit Motion Limited

PEPL Plasmadynamics and Electric Propulsion Laboratory

PIC Particle-In-Cell

PID Proportional, Integral, Derivative

PPU Power Processing Unit

PSD Power Spectral Density

RMS root-mean-square

SCS Space Charge Saturation

SEP Solar Electric Propulsion

SMART Small Mission for Advanced Research in Technology

SOH State-of-Health

SPT Stationary Plasma Thruster

STEX Space Technology Experiment Satellite

USAFA United States Air Force Academy

USSR Union of Soviet Socialist Republics

TAL Thruster with Anode Layer

VF-5 Vacuum Facility 5

XIPS Xenon Ion Propulsion Systems

ABSTRACT

Plasma Oscillations and Operational Modes in Hall Effect Thrusters

by

Michael J. Sekerak

Co-Chairs: Alec D. Gallimore, Benjamin W. Longmier

Mode transitions have been commonly observed in Hall effect thruster (HET) operation where a small change in a thruster operating parameter such as discharge voltage, magnetic field or mass flow rate causes the thruster discharge current mean value and oscillation amplitude to increase significantly. In this study, mode transitions in HETs are induced by varying the magnetic field intensity while holding all other operating parameters constant and measurements are acquired with high-speed probes and ultra-fast imaging. Two primary oscillatory modes were identified and extensively characterized called global oscillation mode and local oscillation mode. In the global mode, the entire discharge channel oscillates in unison and azimuthal perturbations (spokes) are either absent or negligible. Downstream azimuthally spaced probes show no signal delay between each other and are very well correlated to the discharge current signal. In the local mode, signals from the azimuthally spaced probes exhibit a clear delay indicating the passage of spokes. These spokes are localized oscillations in discharge current density propagating in the $E \times B$ direction that are typically 10-20% of the mean value. In contrast, the oscillations in the global mode can be 100% of the mean discharge current density value. The spoke velocity is determined from high-speed image analysis using three methods yielding values between 1500 and 2200 m/s across a range of magnetic field settings. The transition between global and local modes occurs at higher relative magnetic field strengths for higher mass flow rates or higher discharge voltages. It is proposed that mode transitions represent de-stabilization of the ionization front similar to excitation of the well-studied Hall thruster breathing mode, which is supported by time-resolved simulations of the discharge channel plasma. The thrust is approximately constant in both modes, but the thrust-to-power and anode efficiency decrease in global mode due to increasing discharge current. New system characterization techniques are suggested that include discharge current, discharge voltage and magnetic field maps at different flow rates to identify modes of operation within a three variable parameter space.

CHAPTER 1

Introduction

"No amount of experimentation can ever prove me right; a single experiment can prove me wrong."

– Albert Einstein

1.1 Problem Statement

Hall Effect Thruster (HET)s have been under development since the 1960's, first flew in the 1970's, [1] and are increasingly used for and considered for a variety of space missions, ranging from satellite station-keeping to interplanetary exploration. Despite the extensive heritage of HETs, the physics of their operation is not fully understood as illustrated by inconsistencies in anomalous electron transport experiment and theory, whereby an unexplained excess of electrons cross magnetic fields lines above that predicted by classical diffusion [2] or Bohm diffusion [3]. Understanding the underlying physics of HET operation is important for many reasons including the ability to create first-principles predictive models. These models would enable rapid design iterations not possible currently and would reduce developmental costs because all existing simulations to calculate thruster performance are non-predictive, requiring empirical factors to match results from real thrusters. Additionally, labor and capital intensive life testing and flight qualification programs could be reduced in cost and augmented with accurate, predictive physics-based simulations. Fully understanding HET physics would ensure that ground testing adequately predicts thruster operation in space where the ambient pressures and local gas density are orders of magnitude lower than in vacuum chambers. Finally, improved models would facilitate the scaling of HETs to very high power and ensure that new designs for the recently developed magnetically shielded [4] or low/zero-erosion concepts are stable across a broad operating range.

Although electron transport is not well understood in HETs, it has been observed to change significantly between different operating modes with only a small change in thruster operating

conditions. Plasma oscillations have been proposed as a potential mechanism for anomalous electron transport and have been noted to change based on operating modes, so a detailed investigation of how oscillations change during mode transitions will provide insight into electron transport. Little work has been done to define and characterize these operating modes in modern HETs and to quantitatively determine their influence on plasma oscillations. This investigation induces mode transitions by varying magnetic field strength in a well characterized 6-kW class HET called the H6 and studies plasma oscillations with time-resolved probes and high-speed imaging.

1.2 Research Objectives and Contributions

The primary objective of the research presented here is to study mode transitions and plasma oscillation in HETs using time-resolved diagnostics in order to:

1. Develop new HET propulsion system characterization techniques to compare operation in ground-test facilities with on-orbit operation.

2. Improve our understanding of the underlying causes for the transition by investigating plasma oscillations in different modes of operation and the transition points.

The secondary objective is to improve time-resolved diagnostics and analysis techniques to facilitate the study of plasma oscillations. These diagnostics include the High-speed Dual Langmuir Probe (HDLP) developed by Lobbia [5] and the High-speed Image Analysis (HIA) developed by McDonald. [6]

This investigation has accomplished the listed objectives and made the following contributions to HET research and plasma physics measurement techniques by:

1. Developed new techniques to identify mode transition using discharge current monitoring, high-speed imaging of the discharge channel, and time-resolved probes in the plume. Two primary oscillatory modes were identified in thruster operation called global oscillation mode and local oscillation mode. Quantitative metrics were derived from the empirical results to identify thruster operational mode. These techniques have been successfully applied to the recently developed magnetically shielded thrusters to identify modes of operation.

2. Developed system characterization techniques that include discharge current, discharge voltage and magnetic field ($I_D - V_D - B$) maps at different flow rates, $\dot{m}$, to define operational mode within a three variable parameter space ($V_D, \dot{m}, B$). These results are used to calculate a transition surface for use by operators to maintain thruster operation in an optimal mode. These techniques are naturally extendable to comparing ground-test operation with on-orbit operation.

3. Extensively characterized plasma oscillations in the channel and plume in each mode with time-resolved diagnostics. For the azimuthal spokes observed in local mode, spoke velocities are calculated and an empirical dispersion relation is found. For the breathing mode oscillations in global mode, the frequency is characterized as a function of the operating parameters. A postulate is put forward and supported by simulations that mode transitions from local to global mode represent de-stabilization of the ionization front similar to excitation of the breathing mode.

4. Improved upon the ground breaking time-resolved techniques developed by Lobbia and McDonald. For the HDLP, an Ion Saturation Reference (ISR) probe was added for ion density measurements and to monitor plasma oscillations. Additionally, a new technique was developed to calculate ion density in a flowing plasma from a probe aligned with the flow. For the HIA, a new method was developed to calculate discharge current density using synchronized high-speed videos and discharge current measurements, and multiple methods were developed to reliably calculate spoke velocity.

1.3 Organization

The organization of this work is as follows. Chapter 2 provides a general overview of electric propulsion, the history of HET development, the fundamental physics behind HET operation, a discussion of mode transitions, and a discussion of relevant plasma oscillations in HETs. Chapter 3 describes the experimental setup including the facility, the H6 thruster, and diagnostics. The analysis methods are developed for the two measurement techniques at the cornerstone of this investigation: time-resolved probe measurements with the HDLP-ISR and optical measurements from HIA.

Chapter 4 presents the results from an investigation where mode transitions are intentionally initiated in an HET. Data are presented and discussed to quantify the impact of mode transitions on discharge current characteristics, plasma oscillations in the plume, plume shape, and thruster performance. Mode transitions are defined qualitatively and quantitative metrics are derived from the empirical results. The results of the mode transition investigation lead to recommendations for new methods to characterize thrusters.

Chapter 5 discusses azimuthal perturbations in the discharge channel commonly referred to as "spokes." An overview of possible mechanisms for spokes is provided and various techniques for calculating spoke velocity from HIA data are derived and compared across the test matrix. An empirical dispersion relation is derived for spokes and compared to existing theories.

Chapter 6 describes the observed axial ionization oscillations commonly referred to as "breath-

ing mode." Data are presented to support the postulate that mode transitions are de-stabilization of the ionization front axially in the discharge channel. Breathing mode frequency variations with operating parameters are empirically determined

Chapter 7 summarizes the data from the mode transitions investigations and discussed recommended future work to build on the results presented here. Appendix A describes a new technique for calculating ion density in flowing plasmas with flow aligned cylindrical Langmuir probes. Appendix B presents 2-D plume maps of an HET operating at nominal conditions including spatially and temporally resolved plasma properties and oscillation spectra. Appendix C presents results from a mode transition investigation using two different magnetically shielded HETs, the NASA-300MS and the H6MS.

CHAPTER 2

Background

"Mankind will not remain on Earth forever, but in its quest for light and space will at first timidly penetrate beyond the confines of the atmosphere, and later will conquer for itself all the space near the Sun."

– Konstantin E. Tsiolkovsky

2.1 Introduction

The idea of electric propulsion has existed for a century and HETs in particular have been in development for a half-century, but electric propulsion has only recently gained widespread acceptance in the space community. The next century of space missions are likely to see a growing reliance on electric propulsion systems. Section 2.2 discusses a brief history of electric propulsion and the benefits to space missions with a timeline of HET development. Section 2.3 describes the principles of HET operation including diagrams, magnetic field topology, and plasma properties in the discharge channel. Section 2.4 describes previous investigations into mode transitions. HETs are known to have a broad range of oscillations, but Section 2.5 surveys the low-frequency breathing mode and azimuthal spoke oscillations studied in literature.

2.2 Electric Propulsion

The opening quote from this chapter was penned by the visionary K. E. Tsiolkovsky in a letter to B.N. Vorob'yev in 1911 and epitomizes the human desire break the confines of Earth in pursuit of exploration. In order to accomplish this, he wrote in *A Rocket into Cosmic Space* in 1903: "I propose a reactive device for investigating the atmosphere, i.e., a type of rocket–however, a very grandiose rocket and one constructed in a special manner." [7] He started a derivation about rocket

flight from conservation of momentum

$$dV(M_d + M_p) = V_{ex} dM_p \tag{2.1}$$

where a rocket of dry mass M_d with onboard propellant M_p ejects a small amount of propellant dM_p with velocity V_{ex} to increase its velocity by dV. [7] Integrating Equation 2.1 yields the famous rocket equation

$$\frac{M_d}{M_d + M_{p0}} = \exp\left[-\frac{\Delta V}{V_{ex}}\right] \tag{2.2}$$

where M_{p0} is the mass of propellant at liftoff and ΔV is the total change in the velocity of the rocket. Equation 2.2 shows that in order to maximize the fraction of total liftoff mass, that is usable dry mass, the exhaust velocity should be maximized.

All propulsion systems in common use today are simply energy conversion devices. In the case of chemical propulsion, chemical potential energy is converted into thermodynamic energy in the combustion chamber through exothermic reactions, which is then converted into kinetic energy as the exhaust is expelled through a nozzle. In the case of Electric Propulsion (EP), external electrical energy is converted into kinetic energy by first ionizing a gas and then accelerating the exhaust through electrostatic or electromagnetic means. Ultimately, “rocket science” focuses on techniques to convert some other form of energy into high velocity matter ejected out of the device to impart momentum to the spacecraft through Newton’s third law. [8]

Equation 2.2 implies the highest achievable exhaust velocity is optimal to maximize the payload for a given mission. For this reason, many of the early pioneers focused exclusively on the fastest known particles at the time (early 1900’s), which were electrons in cathode tubes. [9] While Tsiolkovsky mentions using “electricity to produce a huge velocity for the particles ejected from the rocket device,” [7] Robert Goddard is the true pioneer of electric propulsion, having filed the first patent for an electrostatic accelerator. [9] Hermann Oberth, Ernst Stuhlinger and many others contributed to the early vision that became the active field of electric propulsion. An enlightening and entertaining summary of the first half-century of EP development was exquisitely written by Choueiri, [9] and the first authoritative textbook on electric propulsion was Jahn [10] with a recent textbook focusing on ion and Hall thrusters from Goebel and Katz [11]

EP systems can be broadly categorized into electrothermal, electrostatic and electromagnetic. In electrothermal thrusters, a resistor or electrical arc (resistojet and arcjet, respectively) are used to heat a gas which then exhausts from a nozzle similar to chemical propulsion systems. The critical difference between electrothermal systems and chemical systems is that the energy to heat the gas is supplied from an external power supply. Electrostatic or electromagnetic thrusters use

the Lorentz force where the force on a particle of charge q in an electric $\overrightarrow{E}$ and magnetic field $\overrightarrow{B}$ is

$$\overrightarrow{F} = \pm q\left(\overrightarrow{E} + \overrightarrow{v} \times \overrightarrow{B}\right) \tag{2.3}$$

Electrostatic systems, such as ion thrusters and HETs, ionize a gas to create charged particles which are accelerated by electric fields that are generated by the device according to Equation 2.3. Electromagnetic thrusters, such as pulsed-plasma thrusters and magnetoplasmadynamic thrusters, use both the electric and magnetic fields in Equation 2.3 to accelerate an ionized gas. Once other system factors are considered such as power supply mass, the optimum specific impulse for a mission is typically one that is of the same order as the ΔV for the mission. EP systems cannot operate at atmospheric pressures, but require the vacuum of space or rarified gas conditions where the ratio of molecular mean free path to a representative physical length scale, or Knudsen number, is large ($Kn > 10$ for the investigation presented here).

2.2.1 Benefits

The primary attraction of EP systems lies in their highly efficient utilization of propellant mass. The high exhaust velocities (i.e., large specific impulse) provided by these thrusters can enable a number of exploration missions outside of Earth's gravitational sphere of influence that would otherwise be impractical or impossible. The mission enabling capabilities of EP technology are currently being demonstrated in spectacular fashion with the Dawn mission. This ambitious mission to the asteroid Vesta and dwarf planet Ceres is the first mission ever to orbit two extraterrestrial bodies and requires a staggering 11 km/s in-space ΔV [12] from its ion propulsion system. The Dawn spacecraft has three ion thrusters each producing a maximum of 91 mN of thrust with a specific impulse of 3100 sec at an input power of $\sim$ 2.5 kW [13]. The Dawn mission would not be possible without EP; the ΔV is accomplished with only 358 kg of xenon propellant [12] whereas a traditional chemical propulsion system would require over 17,000 kg of propellant for the same payload mass. Consider a hypothetical mission such as a Neptune/Triton explorer that could require a change in velocity on the order of 25 km/s from Low Earth Orbit (LEO). A 10 metric-ton spacecraft could require 5,800 metric-tons of propellant using a traditional chemical propulsion system, but would require only 9 metric-tons of propellant with an ion thruster or HET [14]. Use of EP yields a 19 metric-ton spacecraft wet mass; this is within current space lift capabilities to LEO [15] and saves $58 billion with current $10,000/kg launch costs.

Unfortunately, the low thrust levels from ion thrusters and traditional single-channel HETs (a few hundred mN [16]) result in trip times that are impractical for human space flight; from the launch of Dawn to Vesta orbit insertion was nearly 4 years. The ion thrusters on the highly successful Deep Space 1 mission operated for over 16,000 hrs. [12] Propulsion systems such as

high-power EP with high specific impulse and high thrust are needed to enable ambitious planetary exploration missions.

2.2.2 Timeline of Hall Effect Thrusters

Below is a chronology of historical trends and important events in HET development. This shows that although HETs have a half-century of development and over four decades of flight operations, new advancements are still being made and their use is becoming more prevalent.

- Early 1960's: HET development efforts started in U.S. and Union of Soviet Socialist Republics (USSR). [1, 17, 18]
- 1971: First USSR Stationary Plasma Thruster (SPT)-60 thruster launched on the "Meteor" satellite (first operated in 1972). [1]
- 1970's: U.S. abandoned HET development due to lower efficiencies than ion thrusters and budgetary reasons. Soviets were unable to produce adequate grids for ion optics so ion thrusters were abandoned in the USSR. [18]
- 1970's-1980's: Significant Soviet HET development effort for station keeping with 2000-3000 engineers and scientists involved. [17] Primarily used for East-West station keeping and plasma contactors. [18]
- 1990's: Exchange program with western engineers visiting Russia to learn HET technology following collapse of the Soviet Union; resumption of HET research in U.S. and incorporation into U.S. systems.
- 1994: First use of a HET for North-South station keeping by Russia. [18]
- 1998: First U.S. flight of a HET; a D-55 Thruster with Anode Layer (TAL) made by TsNIIMASH in Russia was used on the National Reconnaissance Office (NRO) Space Technology Experiment Satellite Space Technology Experiment Satellite (STEX). [11]
- 2003: European Space Agency (ESA) Small Mission for Advanced Research in Technology (SMART)-1 mission launches with PPS-1350 G from SNECMA based on Russian SPT designs. [11]
- 2004: First commercial HET use in U.S., Space Systems/Loral on MBSAT with Fakel SPT-100 [19] with an example shown in Figure 2.1.

Figure 2.1: SPT-100 with key components and typical mounting on Space Systems/Loral spacecraft. Primary use on SS/L communication satellites is for north-south station keeping. Reproduced from Figure 1 of Ref. 19.

- 2006: First U.S. design HET, Busek Hall Thruster (BHT)-200, flew on the Air Force Research Laboratory (AFRL) TacSat-2 [11]; the BHT-200 also flew on the United States Air Force Academy (USAFA) FalconSat 5 launched in 2010 and is due to launch on FalconSat 6 in 2015.[1]

- 2008: Over 140 HETs have been operated in space, most of Russian design heritage. [11]

- 2010: Advanced Extremely High Frequency (AEHF) communication satellite launched with four Busek Primex Thruster (BPT)-4000 thrusters as shown in Figure 2.2; failure of liquid apogee engine forced orbit raising to Geostationary Earth Orbit (GEO) with HETs and saved the mission. [20]

- 2009: Magnetic shielding first observed on a BPT-4000 during ground testing. [21] From 2010-2013 National Aeronautics and Space Administration (NASA) Jet Propulsion Laboratory (JPL) scientists and Aerojet engineers learned the physics behind magnetic shielding and demonstrated it on a modified 6 kW lab thruster which reduced erosion below the threshold of detection. [4, 22]

- 2013: NASA selects magnetically shielded HETs as the baseline propulsion system for the proposed Asteroid Retrieval Mission (ARM) and begins development effort. [23]

[1]Busek Flight Programs: http://busek.com/flightprograms.htm, accessed March 27, 2014.

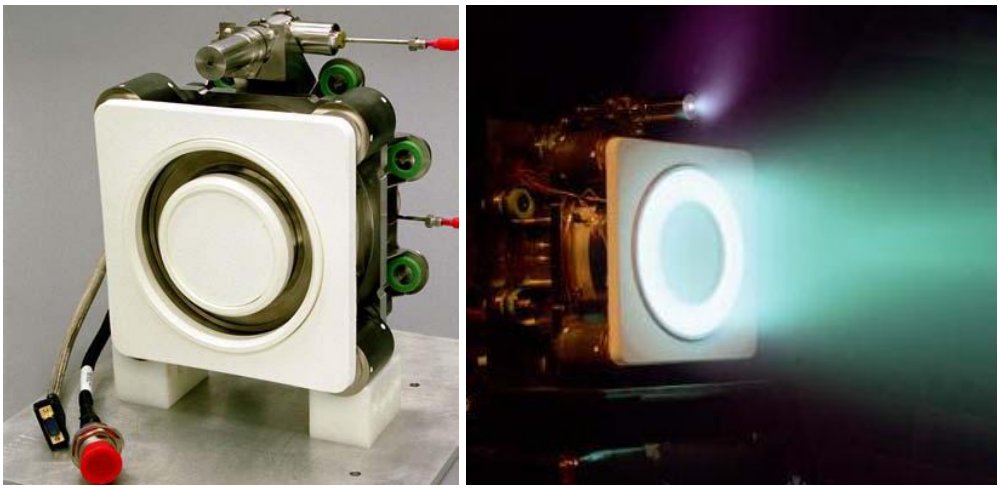

(a) Reproduced from Figure 3 of Ref. 24 (b) Reproduced from Figure 4 of Ref. 24

Figure 2.2: BPT-4000 Engineering Qualification Model.

2.2.3 Current State and Future Trends

Space Systems/Loral was the first commercial U.S. provider to use an HET in 2004 [11] for station keeping in GEO and has been using them routinely with a representative example shown in Figure 2.1. The AEHF satellites built by Lockheed Martin are a series of spacecraft to replace the Milstar military communication satellites that are critical to national security. The first AEHF launched in 2010 and had a failure of the liquid apogee engine that would take the spacecraft to GEO. Onboard were four BPT-4000 HETs shown in Figure 2.2 that were meant for station keeping only, but they were used in a 14-month orbit raising campaign to save the mission. [20] In March 2012 Boeing received its first contract for an all electric spacecraft, the 702SP, which will do orbit raising and station keeping with EP. [25] Although HETs were considered, ion thrusters were ultimately selected due to Boeing's heritage with Xenon Ion Propulsion Systems (XIPS). Finally, the ARM would use a 40 kW Solar Electric Propulsion (SEP) system with 10 tons of Xe to capture an asteroid up to 1000 tons and return it to long-term stable lunar orbit. For this mission, a 12.5 kW magnetically shielded HET operating at 800 V with a specific impulse of 3000 s and a capability of 3400 kg throughput would be developed. [23] Given the success of EP on the Dawn mission and AEHF coupled with the plans for Boeing's all EP spacecraft and new magnetically shielded HETs for ARM, there is a trend of spacecraft becoming more reliant on EP for main propulsion and not just station keeping.

Future missions with high-power capabilities (100+ kW) can achieve significant mass savings, increased thrust and throttle range with Nested Hall Effect Thrusters (NHT), where two or more annular channels are arranged concentrically. Two-channel (X2) and three-channel (X3) thrusters

have been built at the University of Michigan. The X2 is a 10-kW class thruster, but tests operating at a constant 6 kW showed the thrust could be varied from 275-450 mN and anode specific impulse from 1500-2700 s with an anode efficiency above 50%. [26] A typical single-channel HET will produce 100's of mN of thrust, but the X3 will produce 10's of N and offer a 52% decrease in thruster footprint compared to the equivalent single-channel thruster. [27]

2.3 Principles of Hall Effect Thruster Operation

2.3.1 Introduction

The fundamentals of HET physics and design have been thoroughly discussed in the literature [1, 17, 28–30] and specifically in a textbook about ion and Hall thrusters [11]. The primary components of a typical HET shown in Figure 2.3 are the annular discharge channel with the combined electrical anode and neutral gas distributor recessed into a dielectric, insulating channel. A cathode mounted either outside the discharge channel radius (external) or on channel and thruster centerline (internal) provides electrons to neutralize the plume and sustain the discharge. Modern systems typically use a hollow cathode for this purpose, but other cathode types can be used. The discharge voltage is applied from the anode (positive) to the cathode (negative) with a power supply, which is isolated from ground. A magnetic field is applied radially outward or inward across the discharge channel exit plane to impede the electron motion through the discharge channel to the anode. The magnetic field is crucial to HET operation and the field strength and topology are produced by a carefully designed magnetic circuit that consists of ferromagnetic pole pieces and permanent or electromagnets. The magnetic field causes a large resistivity in the plasma which creates an axial electric field to accelerate the ions downstream. These high exhaust velocity ions create the thrust to accelerate a spacecraft according to Newton's third law. The discharge channel walls in magnetic layer thrusters are dielectric materials with low sputter yield and relatively low secondary electron emission coefficients under Xe ion bombardment. Typical materials are boron nitride (BN) or Borosil (BN-SiO_2) for both flight and lab thrusters.

A heavy noble gas is typically used as a propellant with xenon the most common due to its large mass and low ionization energy. Most ions are singly charged because the high electric field typically removes the ion from the ionization zone before another electron collision can ionize it further, [17] but higher charge states are present nevertheless. The plasma throughout the discharge channel is quasi-neutral allowing higher charge densities and higher fluxes than ion thrusters, which are space charge limited. The electrons are magnetized meaning they respond to the magnetic field while the ions are non-magnetized due to their larger mass. The electrons ap-

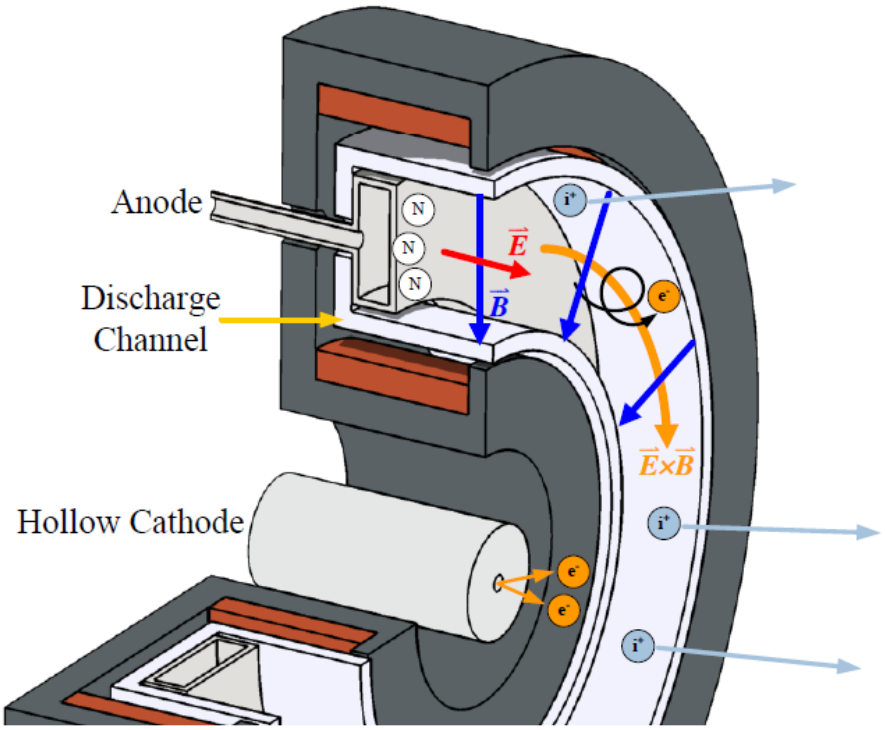

Figure 2.3: HET diagram showing the gas feed into the anode, the discharge channel, and an internal hollow cathode. Neutrals are injected from the rear of the discharge channel to be ionized and accelerated downstream by the electric field. Electrons emitted from the cathode neutralize the plume and propagate in the $E \times B$ direction, which is clockwise for a radially inward magnetic field. Reproduced from Figure 2.3 of Ref. 31

proximately execute $E \times B$ drift around the discharge channel in the azimuthal Hall current, which is where HETs derive their name.

HETs can be broadly categorized into three different types: magnetic layer, anode layer, and magnetically shielded. The device described in the preceding paragraphs and shown in Figure 2.3 is typically called a Hall thruster, Hall Current Thruster (HCT), Hall Effect Thruster (HET), Stationary Plasma Thruster (SPT), or magnetic layer thruster. This device will be described in more detail throughout this chapter. The Thruster with Anode Layer (TAL) has a significantly shorter discharge channel with the conducting walls. Although the physics discussed here applies to TALs, these devices will not be described in this work and detailed descriptions can be found in literature. [11, 17] Magnetically shielded thrusters are a recent development and are derived from magnetic layer thrusters with a special magnetic field topology to reduce discharge channel wall erosion. [4, 22] The walls of the first magnetically shielded thrusters were made of an insulating dielectric, but the use of conducting carbon walls has also been demonstrated. [32]

2.3.2 Scaling and Discharge Channel Plasma Properties

This section describes some of the critical scaling parameters for HETs and typical plasma properties inside the discharge channel. An important parameter quantifying the magnetization of a species (e: electrons, i: ions) is the Hall parameter, Ω, which is the cyclotron frequency, ω_c, divided by the collision frequency, ν

$$\Omega_{e,i} = \frac{\omega_{c\ e,i}}{\nu} \ . \tag{2.4}$$

The Hall parameter describes the number of times a particle orbits around a magnetic field line of force before undergoing a collision. The cyclotron frequency is

$$\omega_{ce} = \frac{qB}{m_e} \qquad \omega_{ci} = \frac{qB}{m_i} \ . \tag{2.5}$$

For electrons, the collision frequency in Equation 2.4 is the effective collision frequency, ν_{ef}, which is the sum of electron collisions with heavy species is [3]

$$\nu_{ef} = \nu_{en} + \nu_{ei} + \nu_w + \nu_a \tag{2.6}$$

where ν_{en} is the electron-neutral collision frequency, ν_{ei} is the electron-ion collision frequency, and ν_w is the wall collision frequency. The electron-neutral and electron-ion collision frequencies can further be divided into momentum transfer, electronic excitation and ionization collision frequencies. The anomalous collision frequency or the collision frequency from turbulent plasma fluctuations, ν_a, can be described by [3, 33, 34]

$$\nu_a = \frac{1}{16}\alpha\omega_{ce} \tag{2.7}$$

where α is an adjustable, empirical factor for simulations to match experimental results. For classic Bohm diffusion, $\alpha = 1$, but typically $0.1 \lesssim \alpha \lesssim 10$. The so called "anomalous electron transport" observed in HETs is captured in the ν_w and ν_a terms, where an experimentally validated, first principles-based theory to predict these collision frequencies would allow for predictive HET models.

In order for the electrons to be magnetized, meaning they complete many cyclotron orbits before a collision, the square of the Hall parameter must be large, $\Omega_e^2 = \omega_{ce}^2/\nu_{ef}^2 \gg 1$. The electron Larmor radius must be less than the characteristic length scale, L [11]

$$r_{L_e} = \frac{\mathrm{v}_{th_e}}{\omega_{ce}} = \frac{m_e}{qB}\sqrt{\frac{8qT_e}{\pi m_e}} = \frac{1}{B}\sqrt{\frac{8}{\pi}\frac{m_e}{q}T_e} \ll L \tag{2.8}$$

where v_{th_e} is the electron thermal velocity and T_e is in eV. The characteristic length scale, L, can

be the ionization zone length, L_i, the width of the channel, W, or the length of the channel, L_{chnl}. For ions to be non-magnetized, their Larmor radius must be greater than L [11]

$$r_{L_i} = \frac{\mathrm{v}_i}{\omega_{ci}} = \frac{m_i}{qB}\sqrt{\frac{2qV_b}{m_i}} = \frac{1}{B}\sqrt{\frac{2m_i}{q}V_b} \gg L \tag{2.9}$$

where the ion velocity, v_i, and beam voltage, V_b, will be described in Section 2.3.3. For 25 eV electrons in a 150 G field, r_{L_e} = 1.3 mm from Equation 2.8, which is smaller than the plasma or thruster length scales. For Xe propellant with a beam voltage of 270 V in the same 150 G field, r_{L_i} = 1.8 m from Equation 2.9, which is larger than the thruster length scales, but not the plume length scales. Ideally the ions in an HET are non-magnetized, but in reality they may have a small angular velocity component in the $E \times B$ direction that causes the ions to follow a slightly helical or spiral trajectory through the plume. This velocity will be very small compared to the axial velocity, but still may impart a small "swirl torque" on the spacecraft. The PPS-1350-G HET developed by SNECMA used on the ESA SMART-1 mission produced 70 mN of thrust at 1.4 kW. [35] A torque about the thruster centerline of 54-62 μN-m was calculated by disturbances in the spacecraft angular momentum. The direction of the torque was noted to be dependent on the direction of the magnetic field, i.e. the $E \times B$ direction, indicating it results from slightly magnetized ions.

An example of the plasma properties in the discharge channel from simulations using the Hall2De code [36] is shown in Figure 2.4 and experimental results will be shown later in Figure 5.13 of Section 5.6.1. The plasma potential is nearly constant for most of the discharge channel until a steep decline near the channel exit where the magnetic field peaks followed by a gradual slope out into the near-field plume. The electron temperature gradually increases from the anode with $T_e < 10$ eV until a sharp peak near the channel exit where $T_e \sim 30$ eV. The sharp decrease in plasma potential and increase in T_e near the channel exit constitutes the acceleration region. The electron density maximum value is upstream from the acceleration region in the ionization region where the peak is approximately $n_e \sim 2.6 \times 10^{18}$ #/m^3. The ion velocity vectors shown in Figure 2.4 show how the ions are focused onto discharge channel centerline by the magnetic lens topology.

The simulation results in Figure 2.4(c) shows that plasma density peaks on discharge channel centerline, so plotting discharge channel centerline plasma property profiles yields important information about the physical processes occurring in the discharge channel. Experimental results for channel centerline plasma potential, axial electric field, and electron temperature are shown in Figure 2.5. These data have been reproduced from the V_P and T_e values presented in Ref. [37] where the peak electron temperature is 33 eV and the peak plasma potential is $\sim$ 300 V. The axial electric field is calculated from $E_z = -dV_p/dz$ and peaks at $\sim$ 60 V/mm.

The important features to note in Figure 2.5 are the profile shapes. The plasma potential shape resembles an error function nearly centered on the exit plane with a smaller inner characteristic

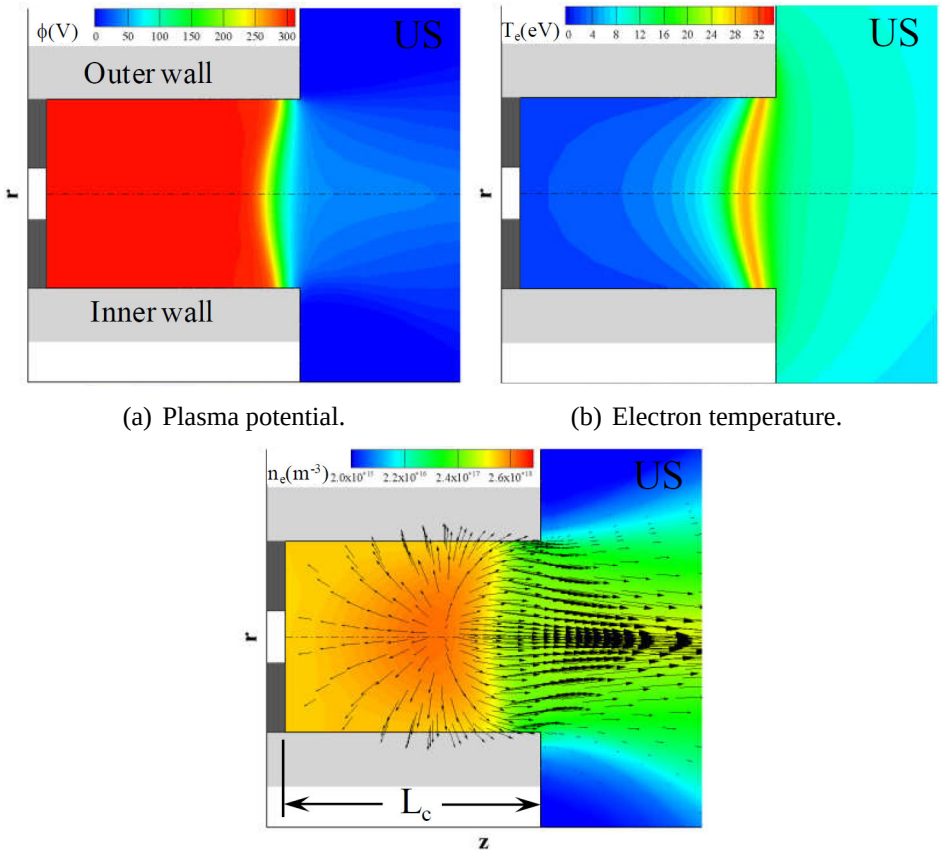

(a) Plasma potential.

(b) Electron temperature.

(c) Electron density.

Figure 2.4: Plasma properties within the discharge channel of the H6 from simulation: (a) plasma potential, (b) electron temperature, and (c) electron density with +1 ion current density vectors. The "US" stands for "Unshielded" or non-magnetically shielded. Reproduced from Figure 4 of Ref. 36.

length, L_{ch}, than the outer characteristic length $L_{ch_{in}} < L_{ch_{out}}$

$$V_p(z) \propto \text{erf}\left[\frac{1 - z/L_{chnl}}{L_{ch}}\right]. \tag{2.10}$$

From conservation of energy, the ion velocity is related to plasma potential by

$$v_i(z) = \sqrt{\frac{2q}{m_i}\left(V_D - V_p(z)\right)} \tag{2.11}$$

with the assumption that most ions are created $z/L_{chnl} < 0.9$ where the plasma potential is nearly the discharge voltage $V_p \sim V_D$. The primary acceleration region is $0.90 < z/L_{chnl} < 1.05$ with the ions asymptoting to their final velocity by $z/L_{chnl} \sim 1.5$. The axial electric field and electron temperatures both resemble sharply peaked Gaussian functions. The electron temperature is approximately

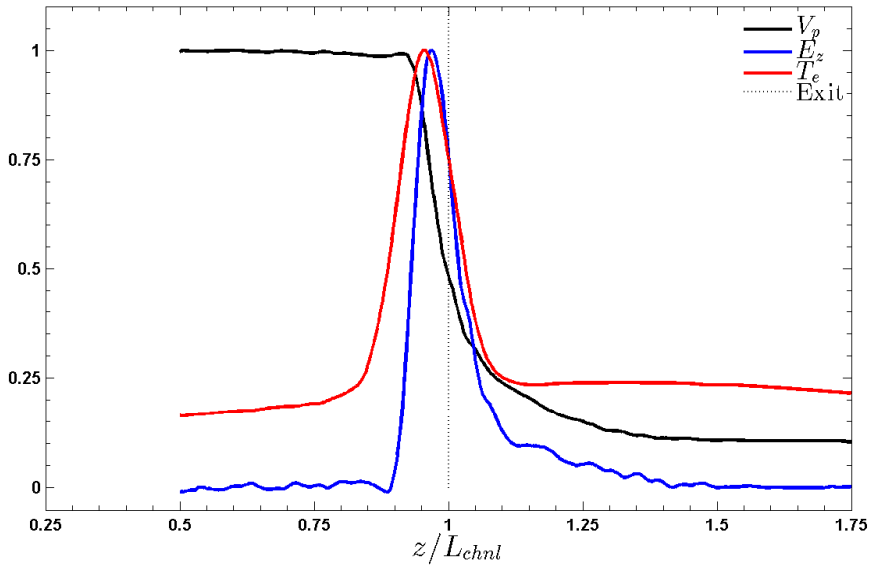

Figure 2.5: Plasma properties of the H6 at nominal conditions on discharge channel centerline including plasma potential relative to cathode, axial electric field and electron temperature. All profiles have been normalized to their maximum values. Reproduced from V_P and T_e data presented in Figure 15 of Ref. 37. Axial electric field is calculated from $E_z = -dV_p/dz$ and smoothed with a moving average filter.

symmetric about its peak and the electric field has a larger characteristic outer length than inner characteristic length similar to the plasma potential.

2.3.3 Currents, Voltages and Power

This section discusses some of the ion, electron and total currents that are typically discussed or measured in the discharge channel, the plume and through power supplies of HETs. The different electrical potentials that arise are also discussed and shown schematically. Some thruster efficiencies will be discussed, but a full phenomenological performance model will not be developed. Detailed phenomenological Hall thruster performance models are developed in [11, 30, 38] and only relevant efficiencies will be discussed here.

The discharge potential is applied between the anode (positive) and cathode (negative). For a typical laboratory setup, the power supply operates in voltage regulated mode where the output current is varied to maintain a constant output voltage. Therefore, by mode of operation the discharge current is allowed to vary to maintain the discharge voltage from anode to cathode. Consider a potential profile along discharge channel centerline starting at the anode as shown in Figure 2.6. The cathode will be taken as reference potential or zero so the anode will be at the discharge potential, V_D. A sheath will form near the anode with potential V_{a-s}, so the plasma will be slightly above

the discharge potential. Using a 49-mm radius, 2-kW laboratory HET, the plasma potential within 10 mm of the anode on channel centerline was measured to be 7-10 V above anode potential for 200-400 V discharges. [39, 40] The potential will be gradually decreasing (i.e. low axial electric field) along channel centerline towards the exit. Once in the primary ionization and acceleration zone, the potential will rapidly decrease and the electric field will be maximized, which is the mechanism for accelerating ions.

The cathode coupling voltage, V_{c-c} is the voltage necessary to draw current from the cathode [11], which is typically ~ 20 V. The axial profile of the plasma potential with respect to cathode is $V_{p-c}(z)$ or just $V_p(z)$, and the boundary conditions are $V_p(z = 0) = V_D$ at the anode and $V_p(z = \infty) = V_{p\infty} = V_{c-c}$ in the far field plume. The cathode to ground voltage, V_{c-g}, represents how the thruster is floating with respect to facility ground since the cathode, power supply and anode are isolated from ground. The cathode to ground voltage is typically ~ -10 V. The plasma potential measurements with downstream probes are initially calculated with respect to ground, V_{p-g}, so the plasma potential with respect to cathode is $V_p = |V_{p-g}| + |V_{c-g}|$. The plume maps in Appendix B will show that V_p is ~ 30 V for these tests, which is 10% of V_D. The potential profile is also shown for the cathode which reaches the same potential downstream from the exit plane; Figure B.4(b) will show the potentials do not converge until approximately three mean channel radii or eight channel widths downstream.

Figure 2.6 shows that ions are not accelerated through the entire discharge voltage, but on average are accelerated through the beam voltage, $V_b = V_D - V_p$. The voltage utilization efficiency or acceleration efficiency is

$$\eta_V = \frac{V_b}{V_D} \, . \tag{2.12}$$

A typical voltage utilization efficiency is $\eta_V \sim 0.9$. Using conservation of energy, the average ion velocity will be

$$\langle \mathrm{v}_i \rangle = \sqrt{\frac{2qV_b}{m_i}} = \sqrt{\frac{2q\eta_V V_D}{m_i}} \tag{2.13}$$

The discharge current, I_D, referenced throughout this work is the current through the power supply, as shown in Figure 2.6. However, this current is a complicated combination of different currents. The variables for the currents are labeled with subscripts according to: species-origin-destination. Species are ions(i) or electrons (e), origin is cathode (ca) or ionization zone (iz) and destination are anode (an), beam (bm) or emitted (em). Secondary electrons and charge-exchange ions are neglected for this simple discussion.

The discharge current is the sum of currents arriving at the anode, which is a combination of electron current from the cathode, $I_{e-ca-an}$, electron current from the ionization zone, $I_{e-iz-an}$, and ion current from the ionization zone, $I_{i-iz-an}$. The discharge current is also the sum of currents at the cathode, which is the emitted electron current, $I_{e-ca-em}$, and collected ion current. Neglecting

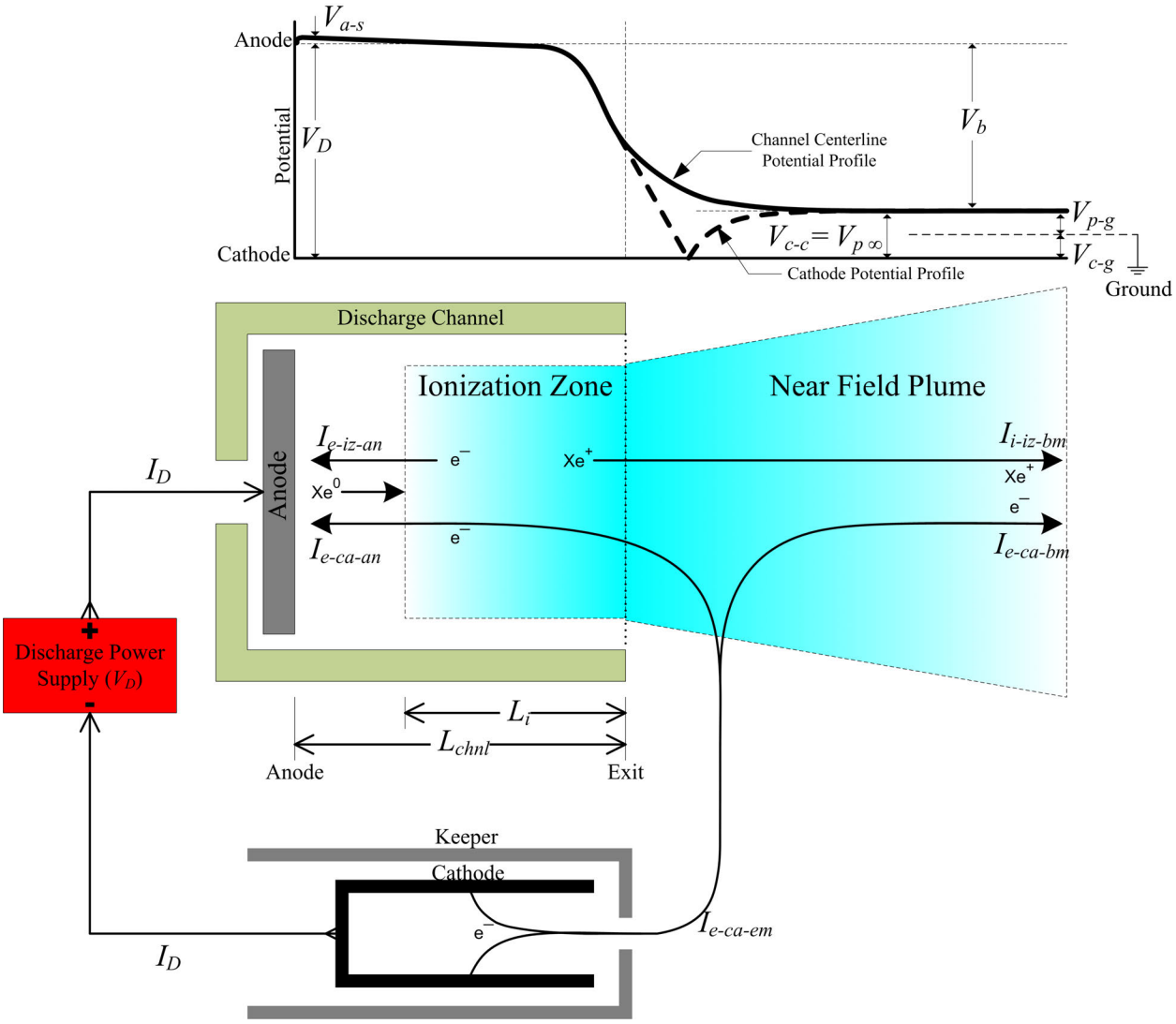

Figure 2.6: HET schematic showing the discharge channel, cathode on thruster centerline, ion and electron currents, and the discharge supply electrical schematic. The potential distribution is shown aligned with the channel. Based on Figure 5 of Ref. 29 and Figures 7-7 and 7-8 of Ref. 11.

the ion currents at both the anode and cathode and writing the emitted cathode current as the sum of anode and beam currents, the discharge current is

$$I_D \approx I_{e-iz-an} + I_{e-ca-an} \approx I_{e-ca-em} \approx I_{e-ca-an} + I_{e-ca-bm} \ . \tag{2.14}$$

The beam is neutral so the ion and electron currents must balance $I_{i-iz-bm} = I_{e-ca-bm}$. For every ionization event one or more electrons are generated in the ionization zone that diffuse to the anode while the ion accelerates downstream so $I_{i-iz-bm} = I_{e-iz-an}$. Therefore, the beam current is

$$I_b = I_{i-iz-bm} = I_{e-ca-bm} = I_{e-iz-an} \tag{2.15}$$

and using Equation 2.14 and 2.15 the discharge current can be written as

$$I_D \approx I_b + I_{e-ca-an} \ . \tag{2.16}$$

Equation 2.16 shows the discharge current is the sum of the ion beam current plus back-streaming electron current crossing the exit plane.

The current utilization efficiency is

$$\eta_b = \frac{I_b}{I_D} \approx \frac{I_b}{I_b + I_{e-ca-an}} \ . \tag{2.17}$$

Assuming the number density ionization fraction of neutrals is η_i and the ions have an average charge state Z, then the beam current can be written as

$$I_b = \frac{Zq}{m_i} \eta_i \dot{m}_a \ . \tag{2.18}$$

The discharge current can be written using Equation 2.17 and 2.18

$$I_D = \left(\frac{Z\eta_i}{\eta_b} \right) \frac{q}{m_i} \dot{m}_a \tag{2.19}$$

HETs have a high beam ionization fraction, so assume $\eta_i = 0.95$. From Table B-1 of Ref. [41] an average ion charge state of $Z = 1.14$ was experimentally found for $V_D = 300$ V and $I_D = 20.55$ A. The data presented in this work will show $I_D \approx 20$ A for $\dot{m}_a = 19.5$ mg/s. Using Equation 2.18 with $\eta_i = 0.95$ and $Z = 1.14$ yields $\eta_b = 0.78$. Combining these values in Equation 2.19 with $\dot{m}_a$ in mg/s yields a useful relationship for estimating discharge current for high-efficiency HETs operating on

Xe where the magnitude of the discharge current is approximately equal to the anode mass flow rate

$$|I_D| \approx |\dot{m}_a| \tag{2.20}$$

and the coefficient of 1.03 A/mg/s has not been explicitly written.

The thrust can be calculated from [11]

$$T = \gamma\sqrt{\frac{2m_i}{q}} I_b \sqrt{V_b} = 1.65\gamma I_b \sqrt{V_b} \tag{2.21}$$

where γ is the thrust correction factor due to beam divergence and multiply charged species and is typically $\gamma \sim 0.95$. The second equality in Equation 2.21 is for Xe in mN. When comparing performance between different thrusters, it is important to remember that phenomenological models may differ in their definitions of efficiencies or coefficients, but the scaling will remain the same as shown by comparing Equation 2.21 with Equation 33 of Ref. 38. Alternatively, the thrust can be measured on a thrust stand was done in this work. The discharge power is simply

$$P_D = I_D V_D \ . \tag{2.22}$$

The thrust to power and anode efficiency are defined as [30]

$$T/P = \frac{T}{P_D} \tag{2.23}$$

$$\eta_a = \frac{T^2}{2\dot{m}_a P_D} \tag{2.24}$$

where $\dot{m}_a$ is the anode mass flow rate. Anode efficiency is used in this investigation instead of total efficiency for ease of comparison with previous works. Total efficiency would also include the efficiencies of the cathode[2] and magnets, which do not directly affect thruster operation. Optimizing cathode and magnet efficiencies are important for flight systems, but not as critical for laboratory settings.

2.3.4 Magnetic Field

The magnetic field in a HET is arguably the most critical design element that directly impacts thruster performance and lifetime. The magnetic field topology shown in Figure 2.7(a) for the NASA-173Mv1 and Figure 3.2 for the H6 is that of a plasma lens where the magnetic field lines are concave and symmetric about the discharge channel centerline. This configuration focuses

[2]Cathode flow rates and location can affect thruster operation, but the efficiency of cathode operation does not.

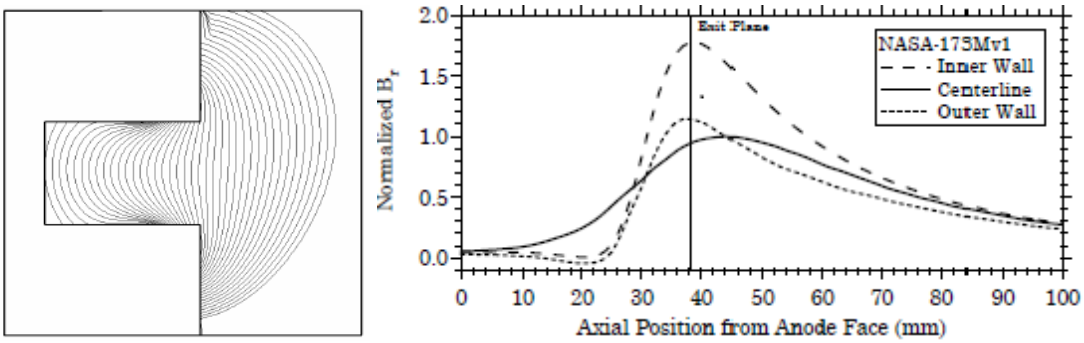

(a) Magnetic field topology show- ing the plasma lens. Reproduced from Figure 5-3.

(b) Radial magnetic field profiles normalized by maximum center- line value. Reproduced from Figure 5-4.

Figure 2.7: Magnetic field for the NASA-173Mv1 from Ref. 30.

plasma away from the walls to decrease plume impingement on the walls and increase lifetime by reducing erosion. [42] The fact that the magnetic field topology can influence the trajectory of ions to focus them onto channel centerline may seem contradictory to the fundamental design of HETs where ions are supposed to be non-magnetized. The reason is that the magnetic field lines are approximately equipotential lines called the "thermalized potential," so the direction of the electric field is tied to the shape of the magnetic field. The magnetic field impedes electron motion across field lines, but electrons can still flow freely along field lines. Therefore, along a line of force of index ψ, the electron temperature will be constant, $T_e = T_e(\psi)$. Integrating the electron momentum equation along that line of force yields the thermalized potential, V_{th} [2]

$$V_{th} = V_p - T_e \ln\left(\frac{n_e}{n_{e0}}\right) \tag{2.25}$$

where T_e is in eV and n_{e0} is the reference electron density at the reference potential. The natural log term will be of order unity, so the magnetic field lines are plasma equipotentials to an accuracy within the order of an electron temperature. [17]

The radial component of the magnetic field on channel centerline has the shape of a Gaussian function with different characteristic widths upstream and downstream from the peak as shown in Figure 2.7(b) for the NASA-173Mv1. Similarly, the radial magnetic field value on discharge channel centerline for the SPT-100 can be described as [33]

$$B_r(z) = \begin{cases} B_{r_0} \exp\left[-\left(\frac{z-L_{B_0}}{L_{B_{in}}}\right)^2\right] & z \le L_{B_0} \\ \\ B_{r_0} \exp\left[-\left(\frac{z-L_{B_0}}{L_{B_{out}}}\right)^2\right] & z > L_{B_0} \end{cases} \tag{2.26}$$

where the peak value is at L_{B_0}. The width of the magnetic field is described by characteristic lengths $L_{B_{in}}$ and $L_{B_{out}}$ for the upstream (anode side) region and downstream (exhaust side) region of the peak, respectively. As shown in Figure 2.7 for channel centerline, the outer magnetic field typically has a larger characteristic width than the inner, $L_{B_{out}} > L_{B_{in}}$, so it appears stretched downstream. Typically, the peak magnetic field occurs at or near the discharge channel exit $L_{B_0} \approx L_{chnl}$.

2.3.5 Electric Field and Potential

The magnetic field, $\vec{B}$, of an HET is carefully controlled with the magnetic circuit and the applied potential between the cathode and anode, V_D, is regulated by the power supply. The electric field, $\vec{E}$, however, is not directly controlled. Poisson's equation cannot be used to determine the electric field because of the assumption of quasi-neutrality

$$\nabla \cdot \vec{E} = -\nabla^2 \phi = \frac{q(n_i - n_e)}{\varepsilon_0} \approx 0 \tag{2.27}$$

Instead, consider the steady-state, perpendicular velocity component from the electron fluid equation of motion [43]

$$mn\frac{d\vec{v}_\perp}{dt} = -qn\left(\vec{E} + \vec{v}_\perp \times \vec{B}\right) - \nabla p_e - mn\nu\vec{v} = 0 \tag{2.28}$$

Without making any other assumptions except $d\vec{v}_\perp/dt \approx 0$ for steady-state, the perpendicular velocity component for electrons can be written from Equation 2.28

$$\vec{v}_\perp = -\mu_\perp \vec{E} - \mu_\perp \frac{\nabla p_e}{qn} + \frac{\vec{v}_{E\times B} + \vec{v}_D}{1 + 1/\Omega_e^2} \tag{2.29}$$

where quasi-neutrality has been assumed so $n \approx n_e \approx n_i$. The cross-field mobility, $\mu_\perp$ is defined as

$$\mu_\perp = \frac{\mu}{1 + \Omega_e^2} \tag{2.30}$$

and the mobility coefficient, μ, has the usual meaning

$$\mu = \frac{|q|}{m_e \nu_{ef}} \tag{2.31}$$

The $E \times B$ drift, $\vec{v}_{E\times B}$, (species independent) and the diamagnetic drift, $\vec{v}_D$, for electrons are

$$\vec{v}_{E\times B} = \frac{\vec{E}\times\vec{B}}{B^2} \tag{2.32}$$

$$\vec{v}_D = \frac{\nabla(p_e)\times\vec{B}}{qnB^2} \tag{2.33}$$

For the channel centerline, assume the electric field is purely axial $\vec{E} \approx E_z\hat{z}$ and the magnetic field is purely radial, $\vec{B} \approx B_r\hat{r}$. Assume axisymmetry so $\partial/\partial\theta \approx 0$ and uniformity across the discharge channel near centerline, $\partial/\partial r \approx 0$. The axial and azimuthal velocity components of the $E \times B$ drift velocity in Equation 2.32 are $\vec{v}_{E\times B}\cdot\hat{z} = (E_rB_\theta - E_\theta B_r)/B^2 \approx 0$ and $\vec{v}_{E\times B}\cdot\hat{\theta} = (E_zB_r - E_rB_z)/B^2 \approx E_z/B_r$. The axial and azimuthal velocity components of the diamagnetic velocity in Equation 2.33 are $\vec{v}_D\cdot\hat{z} \approx 0$ and $\vec{v}_D\cdot\hat{\theta} \approx (T_e/B_r)(1/n)(dn/dz) + 1/B_r dT_e/dz$. Writing the pressure as as $p_e = nqT_e$ for T_e in eV, the perpendicular velocity components of Equation 2.29 are

$$v_z = -\mu_\perp E_z - \frac{\mu_\perp}{n}\frac{d(nT_e)}{dz} = -\frac{1}{1+\Omega_e^2}\frac{q}{m_e\nu_{ef}}\left[E_z + \frac{T_e}{n}\frac{dn}{dz} + \frac{dT_e}{dz}\right] \tag{2.34}$$

$$v_\theta = \frac{1}{1+1/\Omega_e^2}\left[\frac{E_z}{B_r} + \frac{T_e}{B_r}\frac{1}{n}\frac{dn}{dz} + \frac{1}{B_r}\frac{dT_e}{dz}\right] \tag{2.35}$$

The electron current density to the anode is

$$j_z = -qnv_z \tag{2.36}$$

Figure 2.6 shows that the current collected at the anode is approximately the electron current from ionization events and cathode electrons crossing the magnetic field, which comprise the discharge current. Therefore, j_z is approximately the discharge current density, $j_z = j_D = I_D/A_{chnl}$ so the perpendicular electric field can be written as

$$E_z = \left(1+\Omega_e^2\right)\frac{m_e\nu_{ef}}{q^2n}j_D - \frac{T_e}{n}\frac{dn}{dz} - \frac{dT_e}{dz} \tag{2.37}$$

The density gradient peak is $dn/dz \sim 10^{20}$ #/m^3/m and a representative peak electron temperature is $T_e \sim 30$ eV from Ref. 44. The maximum value for the second term in Equation 2.37 is $(T_e/n)(dn/dz) \sim 3$ V/mm and is < 10% of the expected value for $E_z \sim 50$ V/mm. The maximum value for dT_e/dz is ~ 5 V/mm determined from Ref. 37, which is $\sim 10\%$ of the expected value for E_z. These pressure gradient terms are not negligible, but combined are less than 20% of the

expected peak axial electric field value. Neglecting the density and temperature gradient terms in Equation 2.37, the electric field can be written as

$$E_z \approx \eta_\perp \; j_D \approx \left(1+\Omega_e^2\right)\eta \; j_D \approx \frac{B_r^2}{m_e \nu_{ef} n} j_D \tag{2.38}$$

which is Ohm's law where the cross-field $\eta_\perp$ and classical η resistivities are

$$\eta_\perp = \left(1+\Omega_e^2\right)\eta \qquad \eta = \frac{m_e \nu_{ef}}{q^2 n} \tag{2.39}$$

The second approximation in Equation 2.38 uses the assumption that $\Omega_e \gg 1$, which is justified as the Hall parameter is known to be between 200 and 800 in the ionization region of HETs [3]. Equation 2.38 shows how the electric field is formed from the magnetic field which creates high cross-field resistivity in the plasma. The large resistance created by the magnetic field also heats the plasma through Joule heating. The peak electron temperature in a HET discharge is typically ~ 30 eV, while the the rest of the plasma is < 10 eV.

In order to check Equation 2.38, representative values can be used from previous works. A reasonable effective collision rate near the discharge channel exit from Ref. 3 is $\nu_{ef} \sim 10^7$ s^{-1} and Ref. 44 shows an electron density of $n_e \sim 10^{18}$ #/m^3. For a current density of $j_D \approx 130$ mA/cm^2, the resulting electric field is $E_z \approx 40$ V/mm and is the correct order of magnitude from Ref. 44 and Table 3.1.

Using the magnetic field approximation in Equation 2.26, the electric field in Equation 2.38 can be written as

$$E_z(z) = -\frac{d\phi}{dz} \approx \frac{j_D(z)}{m_e \nu_{ef}(z) n(z)} B_{r_0}^2 \exp\left[-2\left(\frac{z-L_{B_0}}{L_B}\right)^2\right] \tag{2.40}$$

The magnetic field length term L_B in Equation 2.40 is understood to be $L_{B_{in}}$ for $z \leq L_{B_0}$ and $L_{B_{out}}$ for $z > L_{B_0}$. Equation 2.40 is the form of a Gaussian that has a smaller width than the magnetic field (more sharply peaked), which in principle agrees with the empirical results discussed in Section 2.3.2 and shown in Figure 2.5.

Making the assumption that the term $j_D/(\nu_{ef} n)$ is nearly constant in the region of maximum magnetic field where the potential drop mostly occurs, Equation 2.40 can be integrated in z

$$\phi_b(z) \approx \left(\frac{\sqrt{\pi/2} L_B j_D B_{r_0}^2}{m_e \nu_{ef} n}\right)\left(\frac{1}{2} - \frac{1}{2}\,\mathrm{erf}\left[\frac{\sqrt{2}(z-L_{B_0})}{L_B}\right]\right) \tag{2.41}$$

where ϕ_b is the potential referenced to $V_{p\infty} = V_{c-c}$ in Figure 2.6 so the limits are $\phi_b(z=0) = V_b$ and $\phi_b(z \gg L_{chnl}) = 0$. The second bracketed term in Equation 2.41 varies from 1 at the anode to 0 in the far field plume, therefore the first term must be approximately the beam voltage. Using the

representative values listed above, the first term is ~ 500 V, which is large but the correct order of magnitude. This also agrees in principle with the shape of the empirical potential profile discussed in Section 2.3.2, Equation 2.10, and the data in Figure 2.5.

It is important to remember that these derivations are only meant to provide order of magnitude approximations and a mathematical construct for the qualitative shapes observed in the measured plasma property profiles. Simple models like Equations 2.40 and 2.41 will not predict a specific device performance, which even the most sophisticated numerical simulations cannot reproduce without empirical correction factors.

2.3.6 Hall Current and Azimuthal Drift Velocity

The azimuthal current, or Hall current, can be written as

$$j_H = j_\theta = -qn\mathrm{v}_\theta \tag{2.42}$$

Using the azimuthal velocity from Equation 2.35 with $\Omega_e \gg 1$ so $1/(1+1/\Omega_e^2) \approx 1$ yields

$$j_H = -qn\frac{E_z}{B_r} \approx -\frac{q}{m_e}\frac{B_r}{\nu_{ef}} j_D \tag{2.43}$$

The density gradient term and temperature gradient term in Equation 2.35 are both < 10% of the E_z/B_r term, so while not negligible they will not be considered for this approximation.

This also implies the ubiquitous $E \times B$ drift velocity in HETs scales as

$$\mathrm{v}_{E\times B} = \frac{E_z}{B_r} \approx \frac{B_r}{m_e \nu_{ef} n} j_D \tag{2.44}$$

The linear scaling between $\mathrm{v}_{E\times B} \propto B_r$ is counter to the inverse scaling that is intuitively expected $\mathrm{v}_{E\times B} \propto 1/B_r$ if E_z were controlled independently from B_r. The assumption of nearly constant j_D with varying B is justified in local mode as shown by Figures 4.2 and 4.3 where the discharge current is constant to within 5% before the mode transition to global mode. While the scaling of the $E \times B$ drift with B is counter intuitive, the neglected terms from the diamagnetic drift do scale as $\mathrm{v}_D \propto 1/B_r$.

2.3.7 Anomalous Electron Transport

Researchers have been attempting to understand cross-field electron transport since the inception of HETs and have various explanations including, but not exclusive to: classical cross-field diffusion, Bohm diffusion, turbulence, shearing, [45] near-wall conductivity [1] and azimuthal electric

fields. [46, 47] As Hofer noted, [3] the real cause is likely a combination of these mechanisms. An excellent summary of anomalous transport mechanisms is provided in Section 2.3 of Ref. 6. The term "anomalous electron transport" is used broadly in literature to describe the issue that is more appropriately term unresolved electron dynamics, because more mechanisms are not understood such as waves, instabilities, and movement along field lines (including electron "bounce" at a separatrix). This void of knowledge regarding electron motion in HETs is the reason why first-principle based predictive models have eluded researchers for decades. It is helpful to categorize the unknown electron dynamics and discuss how they affect HET operation: electron mobility in the discharge channel (in the near-anode, ionization and acceleration regions), electron mobility due to wall collisions (so called "near-wall conductivity"), azimuthal Hall current (how the electrons propagate around the discharge channel), and electron mobility in the plume (how the electrons get from the cathode to the discharge channel). Complicating matters are the different sources of electrons: emission from the cathode, ionization events (mostly in the ionization zone), secondary electron emission from the discharge channel walls, and secondary electron emission from other thruster or facility surfaces.

2.3.7.1 Electron Mobility in the Channel

Some models of the discharge channel will divide anomalous electron mobility coefficients into the near anode and ionization/acceleration region [3], but for the purposes of this qualitative discussion we treat the discharge channel as the entire region from the anode to the discharge channel exit plane. In the limit of $\Omega_e^2 \gg 1$, which is true in the channel but not necessarily the plume, Equations 2.6 and 2.37 can be used to show how j_D relates to ν_{ef} and the anomalous collision term, ν_a

$$j_D \approx \nu_{ef} \frac{m_e n}{B^2} \left[E_z + \frac{\nabla p_e}{qn} \right] = (\nu_{en} + \nu_{ei} + \nu_w + \nu_a) \frac{m_e n}{B^2} \left[E_z + \frac{\nabla p_e}{qn} \right] \tag{2.45}$$

Therefore, the discharge current increases as anomalous collisions increase. Higher electron mobility in the ionization zone and near-anode zone represents inefficiency, where it is desirable to minimize $I_{e-ca-an}$ in Figure 2.6 to increase the efficiency in Equation 2.17. The causes of ν_a are therefore critical to understanding the anomalous cross-field transport in the discharge channel, but it is likely caused by a combination of Bohm diffusion, turbulence, shearing, [45], azimuthal electric fields, [46, 47] and near-wall conductivity. A majority of the research into anomalous electron transport has focused on these areas with no consensus on the the relative importance of each mechanism. Ducrocq [48], Cavalier [49], and Adam [50] investigated high-frequency oscillations theoretically, numerically, and computationally, respectively, and determined that they could be a significant source of cross-field electron transport that resembles turbulence. An illustration of how collisions (anomalous or otherwise) propagate electrons towards the anode can be seen from

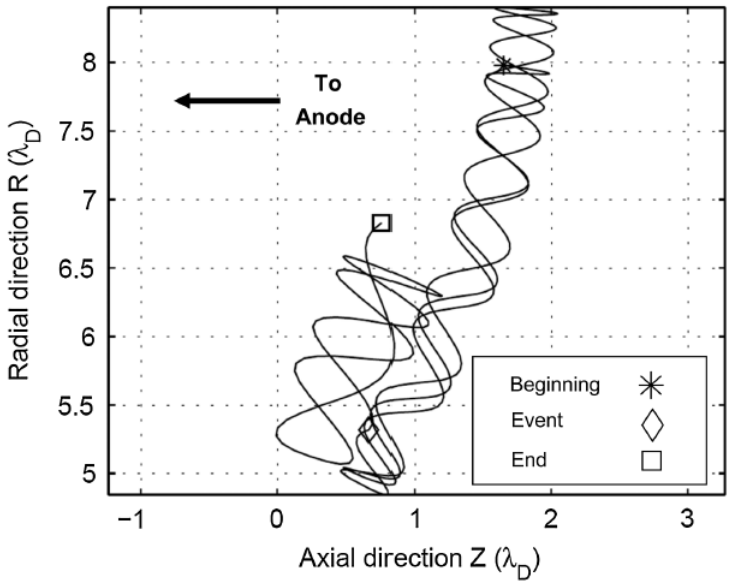

Figure 2.8: Electron trajectory in the discharge channel $r-z$ plane from fully-kinetic PIC simulation showing electron guiding center along the magnetic field line, reflection at the inner channel wall due to the magnetic mirror, and a collision event moving the electron to a new streamline closer to the anode. Reproduced from Figure 3 of Ref. 51.

Szabo's fully-kinetic, axi-symmetric Particle-In-Cell (PIC) model of a BHT-1000 discharge channel. [51] Figure 2.8 shows an example electron trajectory in the $r-z$ plane with its guiding center along a magnetic field streamline until a collision event moves it to a new streamline closer to the anode. The magnetic mirror effect turns the electron back into the channel at the inner wall while it remains on the new streamline.

Using the fluid approximation in Equation 2.45 assumes a Maxwellian energy distribution, which is not accurate based on measurements in the channel of an SPT. [1] Three distinct populations of electrons are shown in Figure 8 of Ref. 1 in the channel of an SPT: low-energy electrons (< 10 eV) that do not reach the walls and rotate about the thruster in the $E \times B$ drift, intermediate energy electrons ($\sim 10-20$ eV) that undergo inelastic collisions with the wall and are responsible for near-wall conductivity, and a high energy electron tail (> 25 eV) that undergo elastic reflections from the wall moving towards the anode with little energy loss. Therefore, some of the anomalous cross-field transport could be due to the deviations from an assumed Maxwellian energy distribution in most models.

2.3.7.2 Near-wall Conductivity

Near wall conductivity results from electron collisions with the walls as theorized by Morozov and summarized in Ref. 1 with other Soviet journal articles referenced therein. These collisions scat-

ter the electrons due to microscopic inhomogeneities or macroscopic structures on the discharge channel wall surface. The scattering collisions reduce the azimuthal drift velocity and allows the electrons to increase their net axial velocity towards the anode.

Figure 2.19 in Section 2.4.2 shows the magnetic field lines for an SPT type thruster. The magnetic field lines intersect the wall perpendicularly at the exit plane in the location of maximum radial magnetic field, but the magnetic fields have a large axial component parallel to the wall farther into the discharge channel where the field is weaker. Collisions allow electrons to "jump" magnetic field lines to ones that are closer to the anode, which progressively move the electrons upstream to eventually be collected by the anode.

Understanding plasma-surface interactions including collisions, secondary electron emission and sputtering are critical to determining the relative importance of near-wall conductivity in newer HETs, which Morozov states that it is "clear that this type of conductivity prevails in the SPT." [1] Also critical to this are the sheath conditions at the wall, which are strongly dependent on secondary electron emission.

2.3.7.3 Azimuthal Electron Motion

The Hall current is critical to HET operation and the force is transferred from the plasma to the thruster (and hence the spacecraft) by interactions between the Hall current and the magnetic field. [11] Yet the exact dynamics of how it propagates around the discharge channel are not known as discussed below. King [52] used single particle motion to show demonstrate that a radial electric field at the outer wall is required to keep the electrons on a nearly circular path in the discharge channel due to the cylindrical geometry as reproduced in Figure 2.9. Measured internal properties of the NASA-173Mv1 were used to calculate the trajectory of a single electron around the discharge channel and it was noted that the radial electric field force and magnetic mirror force ($1/10^{th}$ the electric field force) repels the electron at the outer wall towards channel centerline, while the magnetic mirror force predominantly reflects the electron at the inner wall. This motion is supported by the fully-kinetic PIC simulation of Szabo [51] and shown in Figure 2.8 where the electron guiding center follows the magnetic field lines as the electron "bounces" in the channel. Even though this model is axi-symmetric so azimuthal propagation is not modeled, it demonstrates the idea of electrons propagating around the discharge channel in a circular fashion akin to cars around a race track is overly simplistic and inaccurate. Considering the thermal velocities of 5-35 eV electrons, their bounce frequency between walls (across the channel width along a B-field stream line) would be 15-40 MHz.

Katz[3] pointed out that the sinusoidal motion suggested by King in Figure 2.9 is likely not accu-

[3]Personal correspondence, May 2013.

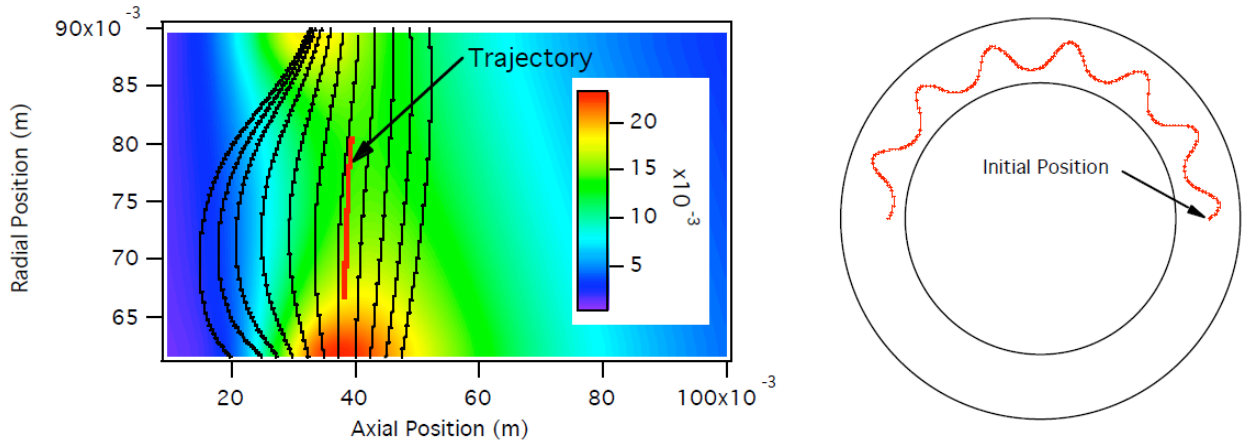

Figure 2.9: Guiding center trajectory of 20 eV electron in the discharge channel of the NASA 173Mv1. Motion in $r-z$ plane (left) with B-field streamlines and magnitude in Tesla. Motion in $r-\theta$ plane (right). Reproduced from Figure 10 of Ref. 52

rate because the electrons would spend more time at the extrema (inner and outer walls assuming all electrons have the same oscillation amplitude in r) causing the electron density to peak off-channel centerline which is not seen in experiments. We can calculate the electric field required to keep the electrons in a circular path following the discharge channel walls from simple centripetal acceleration. Considering the $E \times B$ drift velocity and the electron thermal velocity, the range of azimuthal electron velocities v_θ to consider is 1×10^4 to 5×10^6 m/s. Using the electron equation of motion, the radial electric field $E_r = (m_e/q)(v_\theta^2/R_{outer})$ required for the electron to maintain circular motion at the outer wall is 6 μV/mm to 1.5 V/mm. This is a small electric field that could be established by sheaths at the walls or internal to the plasma in order to maintain quasineutrality, so it could be assumed that electrons travel in nearly circular motion around the discharge channel. Regardless, a radial electric field is required to reflect electrons back into the channel per King or to keep electrons in a circular motion around the discharge channel per Katz.

Despite the fact that HETs are known as "closed-drift thrusters," [17] the details of the electron motion to make the closed-drift occur requires further research. The mechanisms that can reflect electrons back into the bulk plasma in order to continue azimuthal propagation for the Hall current are summarized below. Note that particle collisions are not considered as they act to change the guiding center gyration of electrons, but do not preferentially reflect them back into the bulk plasma.

1. **Electrostatic Sheaths at the Walls** An electron gyrating about a magnetic field line towards the wall will be reflected once the sheath potential is of order the electron temperature (5-35 V) or the radial electric fields are 6 μV/mm to 1.5 V/mm as calculated above.

2. **Magnetic Mirror Reflection** An electron gyrating about a magnetic field line towards the wall be reflected by the magnetic mirror effect (conserving the second adiabatic invariant) as the streamlines converge towards the wall in the ionization/acceleration as shown in Figures 2.7 and 2.11(left).

3. **Ambipolar Reflection** An electron gyrating about a magnetic field line towards the wall will be traveling through a field of essentially stationary ions (from the electron's perspective since $v_{th_e} \gg v_i$) whose density decreases closer to the discharge channel walls. As the electron attempts to stream out of the higher plasma density region to the lower density region, an ambipolar electric field will be self-generated within the plasma to maintain quasineutrality. As analyzed in Section 2.3.8 for magnetically shielded thrusters, the hot electrons could travel 100's μm or more out of the plasma before reflection.

4. **Electron Exchange** An electron gyrating about a magnetic field line towards the wall could penetrate the sheath and impact the wall. In steady state, the dielectric walls will have to give up an electron through secondary electron emission or ion neutralization to maintain a constant surface charge. Higher temperature electrons are more likely to penetrate the sheaths to reach the walls, but electrons emitted from the walls as secondary electrons are likely to be lower temperature so this effect will change the electron energy distribution in the bulk population.

2.3.7.4 Electron Mobility in the Plume

As shown schematically in Figure 2.6, the electrons must travel from the cathode to the plume for neutralization and to supply electrons in the channel. If the channel becomes starved of electrons because they cannot transit the plume, then an instability can occur. It is important to understand how electrons travel through the plume to ensure they can reach the discharge channel, which will differ in ground test facilities from in space due to the presence of background neutrals.

A 2-D map of electron density in the H6 plume at nominal conditions is shown in Figure B.5(a) of Appendix B, where the data are discussed in detail. Figure 2.10(a) shows this electron density map with magnetic field streamlines overlaid and labels of key features for the present discussion of electron motion in an HET plume. The very center B-field line on thruster and cathode centerline (through the center of the cathode orifice) for a center mounted cathode extends straight out into "infinity," which is the beam dump $\sim$ 6 m downstream in the Large Vacuum Test Facility (LVTF). An electron trapped gyrating about this field line will travel downstream to be collected by the beam dump and shunted to ground. Subsequently, an electron would have to be emitted from some grounded surface in the facility and re-enter the plume to maintain continuity. The B-field lines eventually reconnect at the separatrix starting at $r/R_{chnl} = 2$, $z/R_{chnl} = 0$ and extending at

a $\sim 40^\circ$ radially outward from thruster centerline. An electron guiding center following a field line emanating from the center of the thruster within the cathode keeper radius (but not exactly on cathode orifice centerline) would still travel downstream ($> 5z/R_{chnl}$) before curving in front of the discharge channel in the far-field plume. If it stays gyrating about the same field line it would travel radially out $> 2.5\ r/R_{chnl}$ before the field line curves upstream to encounter the separatrix. At the separatrix, if it does not encounter any collisions it would bounce off the separatrix like a magnetic mirror and begin the return trip to the origin near the cathode. However, it is more likely a collision in the plume emanating from the discharge channel would move the electron guiding center to a magnetic field line closer to the discharge channel.

One must consider the gyroradius or Larmor radius of the electrons about the field lines to determine the guiding center for the electron to reach the beam dump or extend far into the plume. The Larmor radius is $r_L = \mathrm{v}_{th_e}/\omega_{ce}$ where the thermal velocity is $\mathrm{v}_{th_e} = \sqrt{qT_e/m_e}$. The Larmor radius normalized by the channel radius in the plume is shown in Figure 2.10(b) using the electron temperature map in Figure B.5(d) of Appendix B. Figure 2.10(b) shows that an electron on the field line emanating from the thruster center would have a gyroradius $r_L/R_{chnl} \sim 0.01$ and 0.05 at $z/R_{chnl} \sim 1$ and 2, respectively, which is reasonable to assume the electron is trapped discounting collisions. The gyro radius increases to $r_L/R_{chnl} \sim 0.25$ at $z/R_{chnl} \sim 3$ and $r_L/R_{chnl} \sim 2.0$ at $z/R_{chnl} \sim 5$, which is unlikely to remain magnetized. Note this does not take into account the Earth's magnetic field, which is larger than the applied magnetic field for $z/R_{chnl} \gtrsim 3.5$.

Figure 2.10 shows the density over the inner-pole ($r/R_{chnl} = 0.50$) is less than 1×10^{17} #/m^3 for $z/R_{chnl} < 1$ and increases to match the density on thruster centerline for $z/R_{chnl} > 1.25$. The densities for all four locations in Figure B.4 converge at 1.5×10^{17} #/m^3 at $z/R_{chnl} = 2.75$. One can speculate that the "bridge" for electrons emitted from the cathode to the plasma emanating from the discharge channel begins before this axial distance. So electrons would on average travel $\sim\ z/R_{chnl} = 2$ downstream before entering the discharge channel plume for neutralization and electron supply for the discharge channel.

The external cathode configuration can present more challenges for the electrons to travel from the cathode to the discharge channel depending on the location and orientation with respect to the thruster and the magnetic field topology. Figure 2.10(a) shows that an external cathode on the H6 is outside the separatrix, although the cathode exit could be positioned inside the plume where some plasma impingement on the cathode keeper would occur. Several studies [53–58] have investigated cathode placement with thruster performance where some sensitivities were observed with discharge current and cathode-to-ground voltage. The critical factors were the conditions at the cathode exit including location inside or outside of the separatrix, axial and radial magnetic field, and local neutral density. Coupling of the plasma to the facility has also been proposed, which would reinforce the idea that the electrons travel far downstream on the B-field lines to

interact with vacuum chamber walls. The net results of these studies is that electron motion in the plume from the cathode to the discharge channel both parallel and perpendicular to the B-field is not well understood.

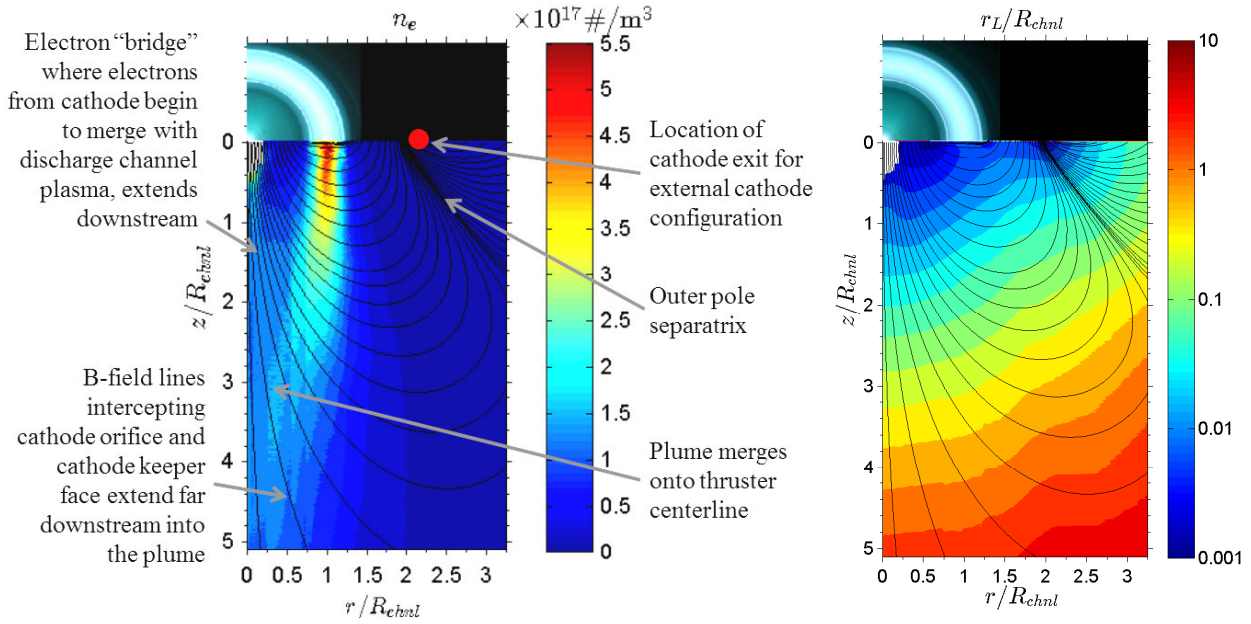

(a) Electron Density. (b) Normalized electron Larmor Radius

Figure 2.10: H6 plume maps at nominal conditions from Figure B.5 in Appendix B. Labels on n_e show the approximate region where cathode electrons begin to merge with the channel plume, central B-field lines extending far into plume, the outer separatrix and the location of the external cathode configuration. The electron Larmor radius map only considers the applied B-field, not the local Earth magnetic field which will in the far field.

2.3.8 Magnetic Shielding

Two problems in HET research remained unresolved for 50 years: 1) Cross-field electron mobility limiting performance and 2) Discharge chamber erosion limiting life. In particular, thruster life has been a major technological problem for all EP systems throughout their development history. While the problem of electron mobility as discussed in Section 2.3.7 remains unresolved, recent advancements in magnetic field design have potentially solved the issue of erosion limiting thruster life in HETs through a technique known as magnetic shielding [4, 22] that is shown in Figure 2.11.

Magnetic shielding was first observed in 2009 on a BPT-4000 during long-duration ground testing [21] in preparation for use on AEHF, where the thruster erosion decreased below the threshold of measurements after 5600 hours of operation. [59] The physics behind the decreased erosion were investigated through simulations [4, 21] and experiments [22] from 2010-2013 and demonstrated

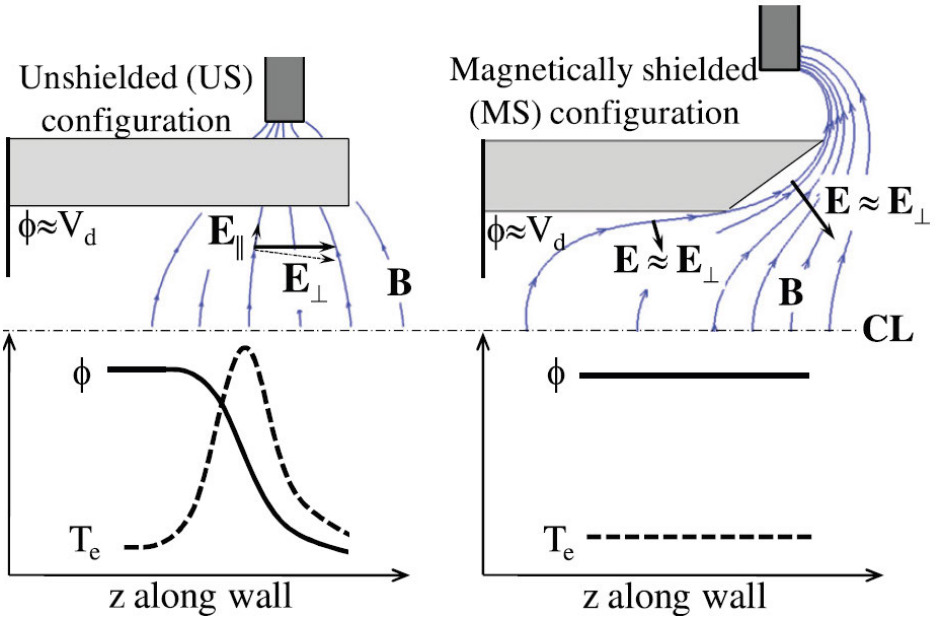

Figure 2.11: Magnetic field topology comparison between an unshielded thruster (left) and a magnetically shielded thruster (right). Reproduced from Figure 1 of Ref. 4.

on a modified H6 HET. The modified thruster reduced erosion below the threshold of detection by limiting plasma contact with the discharge channel walls. This has enabled the use of conductive discharge channel walls made from carbon [32] without significant performance degradation.

Erosion of the discharge channel walls can eventually expose the magnetic circuit and lead to system failure. The erosion is caused by ion bombardment with sufficient energy to sputter material. In an unshielded thruster as shown in Figure 2.4 with B-field topology of Figure 2.11(left) it can be seen that the electron temperature is high along the channel wall near the exit. This large T_e means the magnetic field lines are no longer equipotential lines from the thermalized potential in Equation 2.25 and large potentials form across the wall sheath that accelerates ions into the wall, sputtering material. In a magnetically shielded thruster as shown in Figure 2.11(right) and Figure 2.12, the near-wall electron temperature is kept low and the plasma potential adjacent to the wall is near anode potential along the entire length of the discharge channel. Maintaining a low electron temperature allows the magnetic field lines to be equipotential lines because the $T_e \log(n_e/n_{e0})$ term in the thermalized potential Equation 2.25 is small.

Comparison of Figure 2.4 and Figure 2.12 shows some important differences between unshielded and shielded thrusters. The ionization and acceleration regions are outside of the discharge channel, which *could* make magnetically shielded thrusters more susceptible to 1) facility effects and 2) instabilities or plasma oscillations without the walls to act as moderators. The peak electron temperature in magnetically shielded thrusters is higher. Performance between equivalent

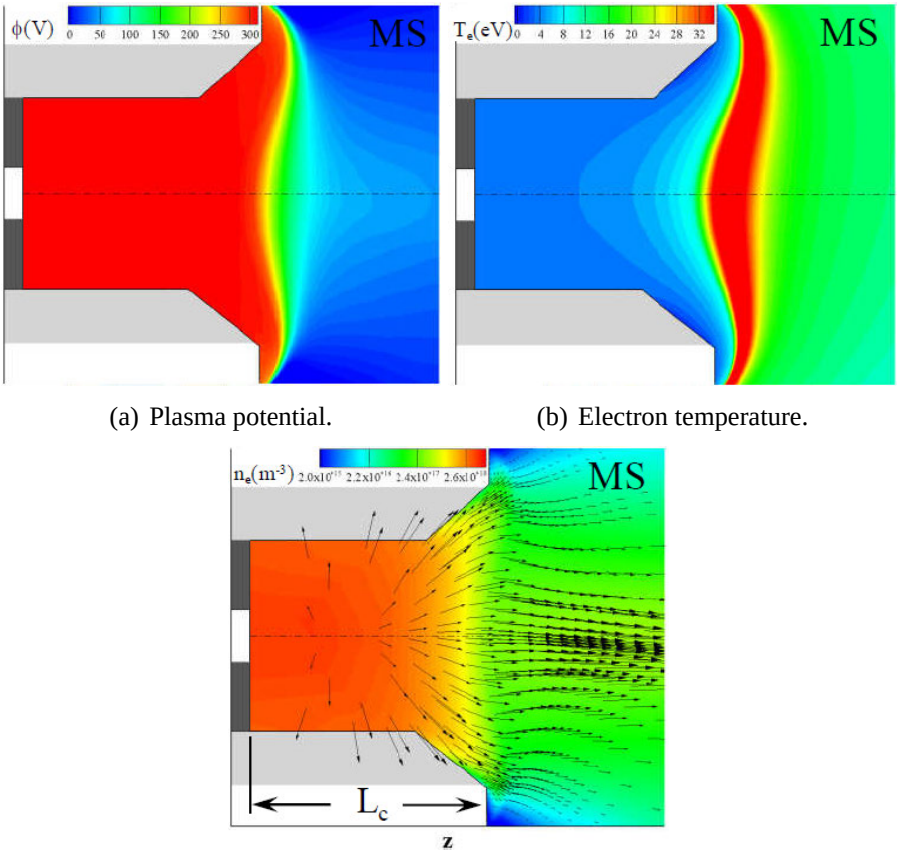

(a) Plasma potential. (b) Electron temperature.

(c) Electron density.

Figure 2.12: Plasma properties within the discharge channel of the magnetically shielded H6 from simulation: (a) plasma potential, (b) electron temperature, and (c) electron density with +1 ion current density vectors. The "MS" stands for "Magnetically Shielded.". Compare with the unshielded channel properties in Figure 2.4. Reproduced from Figure 4 of Ref. 36.

unshielded and magnetically shielded thrusters showed that the total efficiency decreased by 1.7% and the specific impulse increased by 2.9% in magnetically shielded thrusters. It is estimated that the life of a magnetically shielded thruster is 100,000 to 1,000,000 hours, [22] which is sufficient for any deep space missions under consideration.

The fully kinetic simulation of Szabo [51] in Figure 2.8 shows that the electrons bounce across the channel width along magnetic field lines reflecting at the walls until a collision knocks the electron to a different line closer to the anode. The single particle simulation of King [52] in Figure 2.9 showed that electric fields formed by sheaths on the outer wall and the magnetic mirror on the inner wall were primarily responsible for reflecting the electrons back into the channel to facilitate azimuthal electron motion. Both of these investigations show the important and complicated role the magnetic mirror and sheaths at the walls play in azimuthal electron motion to form the Hall current critical to HET function. In magnetically shielded thrusters, however, plasma contact with the

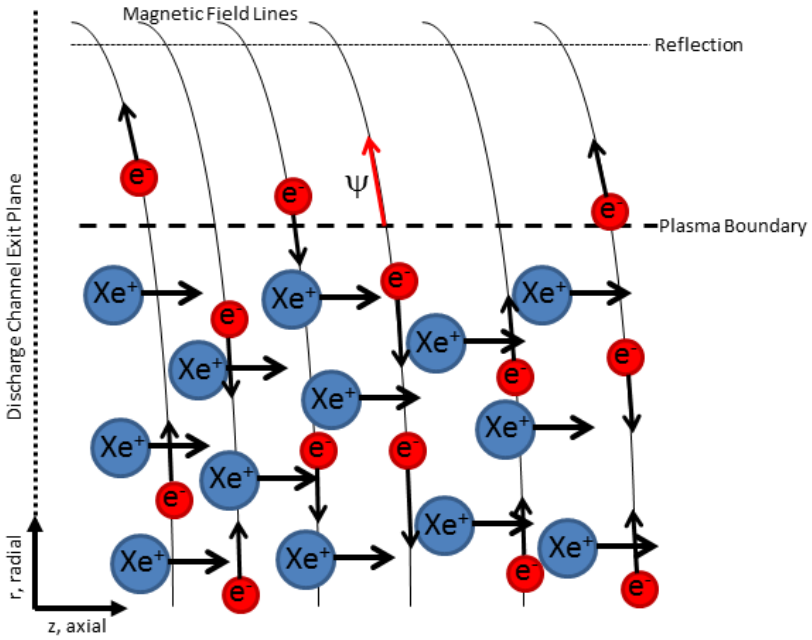

Figure 2.13: Diagram of the plasma outside of the discharge channel for a magnetically shielded thruster. Electrons are shown streaming radially along magnetic field lines while ions only have an axial velocity component. The electrons cross the quasineutral plasma boundary and are reflected by the self-generated ambipolar electric field.

wall is minimized so the role of sheaths at the wall will be fundamentally different. Figure 2 from Ref. 60 shows that the peak electron temperature and electric fields are now outside the channel at $z/L_{chnl} \sim 1.1$ instead of inside at $z/L_{chnl} \sim 0.95$ as shown in Figure 2.5 for the same unshielded thruster. There are still strong magnetic mirrors in magnetically shielded HETs, but they will be outside the discharge channel on the face of the magnetic pole piece instead of inside the discharge channel as shown in Figure 2.11.

An additional force to retain the electrons could be from ambipolar electric fields self-generated within the plasma if the ions are assumed to move purely axially and essentially stationary in compared to the electron thermal velocity. This assumption is not entirely true because plume divergence yields a small radial velocity component, but it is justified because the electron velocity along field lines will be orders of magnitude larger. One can consider a sheath formed by high energy electrons (~ 35 eV) trying to stream out of the bulk plasma along magnetic field lines that are retained by a sheath formed on the plasma boundary (not a material surface like a discharge channel wall) as shown in Figure 2.13. Consider a quasi neutral plasma ($n_0 \approx n_e \approx n_i \approx 10^{18}$ #/m^3) with a Maxwellian electron energy distribution ($T_e \approx 35$ eV) and a free boundary where ions are considered immobile.

Combining Gauss' law and the Boltzman relation for electron density assuming a Maxwellian velocity distribution [43] yields

$$\nabla \cdot \vec{E} = -\nabla^2 \phi = \frac{q(n_i - n_e)}{\varepsilon_0} \approx \frac{q n_e}{\varepsilon_0} = \frac{q}{\varepsilon_0} n_0 \exp\left[\frac{\phi}{T_e}\right] \tag{2.46}$$

Using a 1-D coordinate system along a magnetic field streamline, ψ, as shown in Figure 2.13 and using the non-dimensional parameter $\chi = \phi/T_e$, the non-linear, 2$^{\text{nd}}$ order, Ordinary Differential Equation (ODE) is

$$\frac{d^2\chi}{d\psi^2} \exp[-\chi] = \frac{q n_0}{\varepsilon_0 T_e} \tag{2.47}$$

This can be easily integrated numerically to yield $\phi(\psi)$ with the boundary conditions $\chi(0) = \chi'(0) = 0$ which implies no potential at the plasma boundary (i.e. the plasma potential is the reference potential) and no electric fields at the boundary. The electrons will be reflected when the average kinetic energy has been converted to potential energy in the ambipolar sheath, $1/2 m_e \mathrm{v}_{th_e}^2 = q\phi_{ref}$. The reflection distance is $\psi_{ref} \approx 63$ μm with the values listed above. Using the same integration trick found in derivation of the Child-Langmuir law [10] to integrate Equation 2.47, an approximate analytic expression for the reflection distance is $\psi_{ref} \approx \sqrt{2\varepsilon_0 T_e/(q n_0)}$. This is a very conservative estimate and the value of ψ_{ref} is likely to be larger since the ion density does not stop abruptly as depicted simplistically in Figure 2.13. The plasma sheath will be on the order of 10-100's μm thick or larger (possibly $\mathcal{O}$(1 mm)) before the average electron is reflected back into the main discharge plasma. The strength of the magnetic field will determine whether the electrons are primarily reflected by the magnetic mirror effect or the ambipolar effect. Therefore, the electrons could travel farther out (inside the inner channel wall radius and outside the outer channel wall radius) radially along the field lines reflecting near the magnetic field cusps at the poles or retained through self-generated electric fields. Although only a qualitative discussion, this difference between magnetically shielded thrusters and unshielded thrusters could be responsible for the different oscillations and lack of azimuthal spokes observed in Appendix C.

2.4 Mode Transitions

2.4.1 Definition of Mode Transition

HETs have been under development for over 50 years in Russia [1] and the United States with significant experimental and flight histories. Mode transitions have been commonly observed throughout their development as noted by some of the early pioneering Russian research. [61] HETs have several parameters that define a single operating point such as discharge voltage, mag-

netic field strength (or magnet coil current), anode mass flow rate and cathode mass flow rate. Laboratory HET discharge power supplies typically operate in voltage regulated mode where the discharge voltage between the anode and cathode is held constant and the discharge current is allowed to fluctuate. Generally, mode transitions are identified by changes in the discharge current characteristics including mean value and oscillation amplitude. Mode transitions can be caused by changes in discharge voltage, anode mass flow rate, cathode mass flow rate, magnetic field magnitude and/or shape, wall shape due to erosion, wall properties due to release of absorbed compounds or deposition, ambient neutral density in the near-field plume region between the cathode and discharge channel, cathode location, and deposition/oxidation on the anode. Note that changes in the magnetic field can be intentionally induced by changing the electromagnetic coil currents or unintentionally caused by degradation of the magnetic circuit or changes in the environment local to the thruster.

The most detailed delineation of operational modes for varying magnetic field strength was conducted by Tilinin [61] where six regimes were identified as shown in Figure 2.14. Note these definitions were developed using an older SPT type thruster almost 40 years ago and the term "loop" oscillations refer to what are currently called breathing mode oscillations.

I **Collisional (classical) conductivity:** The weak magnetic field causes the electron Larmour radius to be comparable to the effective dimensions of the channel and Coulomb collisions explain conductivity.

II **Regular electron drift wave:** Dominated by an azimuthal drift wave that propagates at $\sim 0.4 - 0.8 v_{E\times B}$.

III **Transition:** Moderate amplitude loop oscillations due to poor conductivity in the discharge channel.

IV **Optimal operation:** Discharge current and loop oscillations are minimized. The electron drift wave is detectable, but of lower amplitude.

V **Macroscopic instability:** Discharge current abruptly increases and loop oscillations become strong with visible instabilities in the thruster. Drift waves are absent.

VI **Magnetic saturation:** Discharge is again stabilized and loop oscillations are minimized. Transit time oscillations dominate.

The general shape shown in Figure 2.14 will be demonstrated repeatedly in the present work, but the description of oscillations and regimes are significantly different as described in Chapter 4

An investigation into the operational modes of an SPT-100ML was performed by Béchu in which four different modes were identified by varying discharge voltage. [62] The modes are

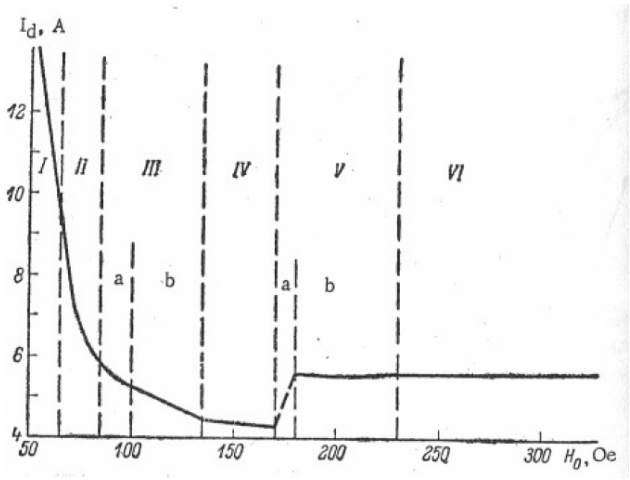

Figure 2.14: Discharge current as a function of magnetic field with constant discharge voltage showing the size operational regimes defined by Tilinin. Reproduced from Figure 5 of Ref. 61.

shown in Figure 2.15 with names that qualitatively describe the discharge current signal shape: irregular mode (100 V), fluctuating mode (300 V), oscillating mode (400 V) and pulsed mode (600 V). The shape of the discharge current trace for oscillating and pulsed mode are similar to global mode discussed in Chapter 4, as well as the marked increase in discharge current and decrease in thruster efficiency.

An ATON type thruster called the A53 was developed by SNECMA and used for characterization testing. [63] ATON thrusters are magnetic layer thrusters, but the gas is injected into a buffer chamber behind the anode instead of the anode acting as the gas distributor. The magnetic field shape is also different with a magnetic null point in the center of the channel cross section. This thruster has an external cathode similar to the SPT-100. By changing the magnetic coil currents to change the magnetic field strength, two different modes were induced called “spike” mode and “swallow tail” mode. [63] The names for these modes are inspired by the shape of the plume as shown in Figure 4.26 of Section 4.7.

These operational mode investigations and classifications are useful and underscore the importance of understanding the oscillatory characteristics of HETs. As noted by Zhurin [64]: “oscillations at conditions of otherwise poor electron mobility provides the necessary electric conductivity for operation.” However, modern HETs such as the H6 discussed in Section 3.3 have benefitted from a half century of research, development and flight history that has improved magnetic field topology, magnetic circuit design, and anode design (gas injection) amongst other improvements. In addition, significant advancements have been made in the field of high-speed diagnostics due to advances in electronics. All factors combined, a renewed investigation into oscillations and oper-

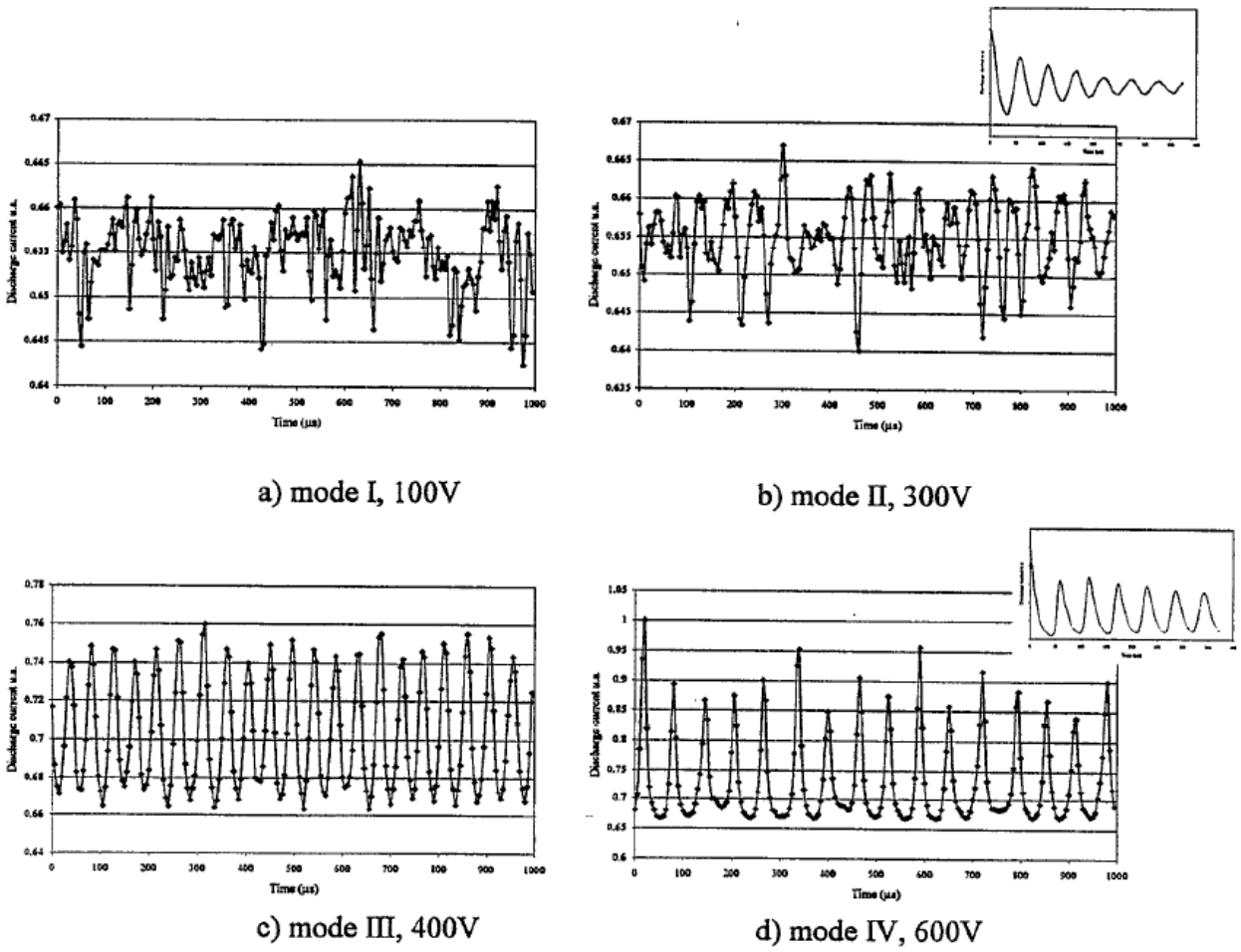

Figure 2.15: Discharge currents as a function of time at four discharge voltages for constant Xe gas flow of 3.5 mg/s in an SPT-100ML with 4.5 A coil current . Four modes are identified: I) Irregular at 100 V, II) Fluctuating at 300 V, III) Oscillating at 400 V, and IV) Pulsed mode at 600 V. Reproduced from Figure 6 of Ref. 62

ational modes using the latest advancements in time-resolved plasma measurements is warranted and presented here.

A general description of mode transitions can be deduced from the previous research as the point where a sharp discontinuity is observed in the mean discharge current, discharge current oscillation amplitude and plasma oscillations while varying one parameter and maintaining all others constant. More recent studies have identified two primary operational modes [41, 65–67] In one mode, the discharge current oscillation amplitude is small with respect to the mean discharge current value, while after the mode transition the mean discharge current rises sharply as well as the oscillation amplitude. Two mechanisms may play a role in mode transitions. The first idea involves wall effects and has been proposed with accompanying physical mechanisms and models. The second idea involves more recent investigations that suggest the plume physics in

the region immediately downstream of the discharge channel exit (near-field plume) has an influence on mode transitions, although the physical mechanisms were beyond the scope of that study. While the answer is likely a combination of the two ideas (and possibly other ideas not yet proposed), investigating the plasma oscillations during mode transition offers insight into the underlying mechanisms. This investigation only considers magnetic layer thrusters with deep discharge channels and non-conducting walls, but anode layer thrusters have exhibited similar mode transitions [68] to those described below.

2.4.2 Wall Effects

Gascon [65] investigated different wall material effects on SPT-100 thruster operation including borosil (BN-SiO_2), alumina (Al_2O_3), silicon carbide (SiC) and graphite (C). The significant differences among these materials include ion bombardment sputter yield, secondary electron emission yield coefficients, electrical conductivity (especially graphite), and thermal properties. Here we only discuss the borosil results as the closest to the Boron Nitride (BN) used in the H6. Varying the magnetic field by changing the magnetic coil current (I_B) as shown in Figure 2.16 results in a sharp mode transition between 3.5 and 4.0 A. Below the magnetic field transition threshold the mean discharge current (I_D) and discharge current oscillation amplitudes increase significantly. This work was related to a previous study by Gascon [69] where azimuthally spaced probes were used to investigate wave propagation and mode transitions were also observed.

In a companion paper to Gascons later work, Barral [66] expanded on the ideas of Baitin [70] and Jolivet and Roussel [71] who considered the effect of secondary electron emission on sheath potentials in HETs. A 1-D axial fluid model was developed that accounts for electron temperature anisotropy with different electron temperatures parallel, $T_{e\|}$, and perpendicular, $T_{e\perp}$, to magnetic field lines. The sheath potential, $\Delta\Phi_S$, from balancing ion and electron flux to the wall with effective total secondary electron emission yield, $\bar{\sigma}$, is

$$\Delta\Phi_S = \frac{k_B T_{e\|}}{q} \ln\left[(1-\bar{\sigma})\sqrt{\frac{m_i}{2\pi m_e}}\right] \tag{2.48}$$

where m_i is the ion mass, m_e is the electron mass, q is the elementary charge and k_b is Boltzmann's constant. Once $\bar{\sigma}$ approaches unity, Equation 2.48 results in a singularity and the sheath transitions to a Space Charge Saturation (SCS) regime where the potential is no longer monotonically changing from the plasma to the wall. This results in a potential well that traps electrons near the wall as shown in Figure 2.18. The mean energy of electrons at the wall, $\bar{\varepsilon}$, which is a function of $T_{e\|}$ and $T_{e\perp}$, determines $\bar{\sigma}$ and was based on a linear fit to experimental data.

The classical cross-field mobility for electron transport was used in the 1-D model so no ad-

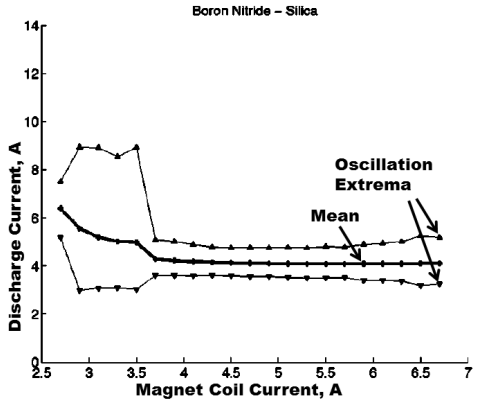

Figure 2.16: SPT-100 mean discharge current (crosses) and oscillation extrema (triangles) for anode flow rate of 5 mg/s and 300 V discharge voltage with variable magnetic field strength represented by magnetic coil current. Reproduced from Figure 2 of Ref. 65 for borosil.

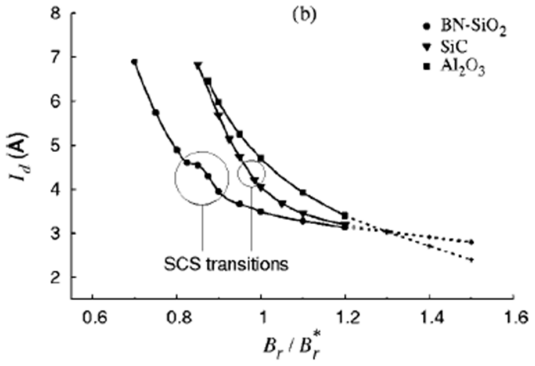

Figure 2.17: Simulated discharge current of an SPT-100 from 1-D fluid model with magnetic field variations for different wall materials. The steep rise in discharge current is attributed to the SCS transition. B_r is the maximum radial magnetic field and B_r^* is the nominal value. Reproduced from Figure 10(b) of Ref. 66.

justable parameters to account for anomalous electron transport were used to fit experimental data. [66] Therefore, the simulation results can only be qualitatively compared to experimental results. When the mean electron energy at the wall $\bar{\varepsilon}$ (a function of $T_{e\|}$ and $T_{e\perp}$) for a given axial position in the discharge channel exceeds a material dependent crossover energy ($\bar{\varepsilon} > \varepsilon^*$), then $\bar{\sigma} \to 1$ and that position on the discharge channel wall sheath is in SCS. As discharge voltage increases and more energy is available to increase $T_{e\|}$ and $T_{e\perp}$, or as the magnetic field strength decreases and energy is more easily transferred across magnetic field lines[4], $\bar{\sigma}$ increases and more of the channel length is in SCS. The SCS regime starts at the maximum radial magnetic field strength location where the electron temperature is highest, which is at the exit plane for the SPT-100, and migrates upstream in the discharge channel towards the anode as discharge voltage and magnet coil current change.

The magnetic lens topology in Figures 2.7 and 2.19 show the magnetic field lines converging towards the discharge channel walls. A trapped population of electrons near the walls would have greater access to field lines that extend deeper into the channel closer to the anode, thus facilitating cross-field transport. In addition, a higher electron density would increase collisions with the walls enhancing near-wall conductivity from scattering collisions as discussed in Section 2.3.7.2. The

[4]The decrease in B-field strength causes an increase in electron mobility such that higher temperature electrons in the ionization region can diffuse farther into the channel to propagate the SCS regime.

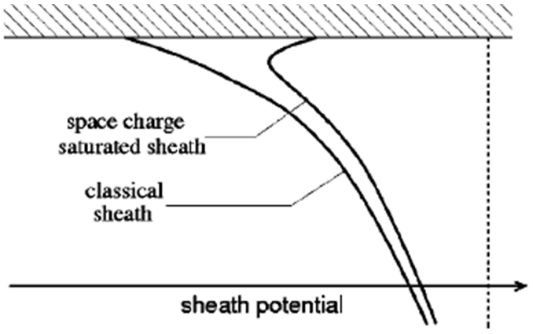

Figure 2.18: Sheath potential profiles at the wall with and without SCS. Reproduced from Figure 3 of Ref. 66.

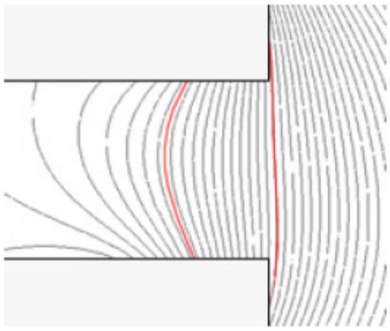

Figure 2.19: SPT-100B magnetic field lines. Reproduced from Figure 2a of Ref. 72.

implication is the potential well near the wall surface for regions in SCS provides the electrons an easier path across magnetic field lines. As the SCS region grows along the channel length, the low impedance path eventually reaches a region of lower magnetic field (increased mobility) or where the magnetic field lines are parallel to the wall and the electrons can easily reach the anode, resulting in a significant increase in discharge current. The magnetic field lines for the SPT-100B are shown in Figure 2.19. Note the magnetic field lines intersect the wall perpendicularly (almost purely radial in direction) at the exit plane in the location of maximum radial magnetic field, but the magnetic fields at the inner wall have a large axial component (parallel to the wall) farther into the discharge channel where the field is weaker. The model used in Ref. 66 is 1-D (axial) and only considers a radial magnetic field, while Figure 2.19 clearly shows the magnetic field has significant axial and radial components upstream from the exit plane. The qualitative shape of the transition between high-current to low-current is captured by the model and SCS theory as shown by comparing Figure 2.16 to Figure 2.17, however the quantitative magnitudes differ without empirical coefficients for electron transport.

2.4.3 Near Field Plume

Brown [41] showed that at low discharge voltages (100-120 V), the H6 thruster would operate either at a high-efficiency “low-current” mode with low mean discharge current values and low-amplitude oscillations, or low-efficiency “high-current” mode with high mean discharge current values and strong oscillations. It is important to note that the transition between modes occurred by making slight changes in either magnetic field settings, background vacuum chamber pressure, or cathode flow rate, or by introducing ambient gas near the center-mounted cathode. Varying discharge voltage for various Cathode Flow Fraction (CFF) in Figure 2.20 showed the discharge current decreased by approximately 10% when transitioning from “high-current” to “low-current”

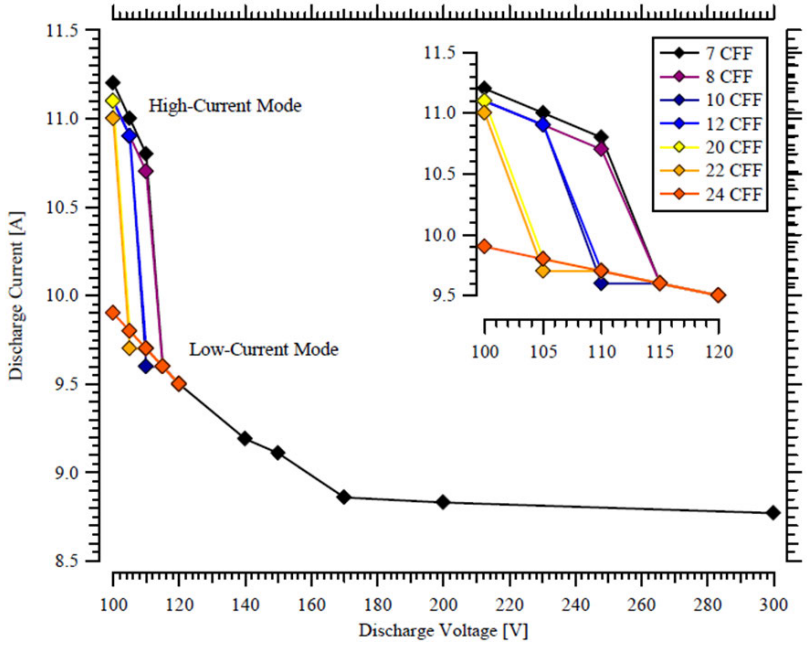

Figure 2.20: Change in discharge current between high-current mode and low-current mode for the H6 at low voltages. Reproduced from Figure 9 of Ref. 41.

mode. Figure 2.20 also shows the transition occurs at higher discharge voltage for lower CFF. From Figure 13 of Ref. 41 the discharge current Power Spectral Density (PSD) decreased by over two orders of magnitude when transitioning from the “high-current” mode to the “low-current” mode. Note that for this study, the magnetic field was varied in order to maximize thruster efficiency. This transition occurred at higher voltages (closer to nominal levels) and at lower chamber pressure, suggesting that the thrusters may operate differently in the space environment than in ground test facilities. During the transition from “high-current” to “low-current” modes, the thrust remained constant, but the decreased discharge current resulted in up to a 20% increase in thrust-to-power. Using an array of plume diagnostics including a nude Faraday probe, retarding potential analyzer and cylindrical Langmuir probe, Brown showed the transition from “low-current” to “high-current” modes corresponded to increased electron current to the anode and is therefore related to increased electron transport. Although no physical explanation is offered for the observed transitions, the effect of ambient chamber pressure, cathode flow fraction and augmented xenon flow at the cathode exit hint at a near-field plasma plume mechanism involving neutral density, collision rates and electron mobility for mode transitions without any consideration of wall effects, which is in contrast to the ideas of Gascon and Barral [66].

Further research by McDonald [67] using ultra-fast imaging on the H6 in low-voltage operation was the first to show the transition from “high-current” to “low-current” modes correlated with the formation of spokes. Figure 7 from Ref. 67 shows that strong discharge current oscillations or

strong azimuthal oscillations could both be achieved at a discharge voltage of 105 V by variation of CFF at constant magnetic field settings. Note that Brown [41] observed hysteresis at this condition where the thruster could be in either mode. Based on the parametric study, McDonald noted that the operating mode was a stronger function of magnetic field strength than discharge voltage.

2.4.4 Summary

In order to understand HETs and develop first-principles based models, the question of anomalous electron transport must be resolved. The transition between modes causes a change in electron current to the anode, implying that understanding mode transitions could offer insight into the unresolved question of anomalous electron transport. Furthermore, tens of kilohertz oscillations where breathing mode oscillations and azimuthal spoke oscillations dominate could play a critical role in electron transport. The previous research cited above suggests two completely different scenarios for mode transition: 1) Plasma interaction with the wall inside the discharge channel; and 2) Near-field plasma plume properties that affect the upstream discharge channel plasma. The research reported on below uses time-resolved plasma diagnostics to study plasma oscillations during induced mode transitions.

2.5 Oscillations

2.5.1 Oscillations Overview

Although HETs are steady-state devices, they contain a rich menagerie of plasma oscillations across the frequency spectrum from 1 kHz to 60 MHz [64, 73] and higher with the breathing mode and rotating spokes modes of primary interest. The so-called breathing mode, a global depletion and replenishment of neutrals akin to the predator and prey models of ecosystems, is commonly observed in HET operation [5, 74, 75] and numerical models [33, 34, 76, 77] from 15-35 kHz. The spoke modes are azimuthally propagating radially oriented disturbances (spokes) travelling within the channel in the $E_z \times B_r$ direction. Both phenomena are believed to be related to ionization processes and it is uncertain how they interact or feed off each other, however, it is strongly suspected these modes greatly affect anomalous electron transport. Janes and Lowder [47] first discussed oscillating azimuthal electric fields as the cause for spokes and electron transport. McDonald [6, 67, 78, 79] and Raitses et al [80–82] further explored whether so-called spokes (rotating azimuthal waves) could explain anomalous electron transport, but further conclusive evidence is needed. Many numerical models exist for Hall thrusters that focus on steady state operation and performance [3, 83, 84], but a few select models have focused on the oscillations present in Hall

thrusters. The breathing mode has been numerically modeled by Fife [77], Boeuf [76], Barral et al [33, 85], Hara [34, 86], Adam [50] and Szabo [51]. Additional azimuthal studies have been performed by Hirakawa [87, 88] and Lam et al [89].

2.5.2 Breathing Mode

The breathing mode oscillations are the most widely studied HET oscillation in the literature dating back to the pioneering work of early Soviet researchers, [61, 90, 91] where it is also known as the "current," "loop," or "contour"oscillation. The breathing mode did not gain acceptance as an ionization related instability until the 1990's [33]. The term "breathing" mode oscillation derives from the numerical studies cited here where the ionization front is shown to move back and forth in the discharge channel and the thruster appears to inhale neutrals and exhale plasma. This qualitative picture has been further visualized in the time-resolved plasma parameter measurements by Lobbia. [5, 74]

Fife [77] conducted a 2-D model in the axial and radial direction where the electrons are treated as a Maxwellian fluid and the ions and neutrals are modeled by PIC. The 2-D numerical simulations were able to reproduce a breathing mode of 11 kHz for an SPT-100 type thruster, which is close to the ~ 30 kHz typically seen during operation. A simple 0-D model was developed for the discharge channel based on influx of neutrals, n_n, outflow of ions, n_i, and ionization rate, k_i

$$\frac{\partial n_n}{\partial t} = -k_i n_n n_i + n_n \frac{v_n}{L_i} \tag{2.49}$$

$$\frac{\partial n_i}{\partial t} = k_i n_n n_i - n_i \frac{v_i}{L_i} \tag{2.50}$$

which is the form of the Lotka-Volterra predator-prey equations. To carry the predator-prey analogy further, the electrons act as the predators and neutrals as prey; quasi-neutrality is assumed so ion and electron density are equal ($n_i = n_e$). Linearizing and solving the undamped, harmonic oscillator equation yields an oscillation (breathing mode) frequency of

$$f_b = \frac{1}{2\pi L_i}\sqrt{v_i v_n} \tag{2.51}$$

Laser Induced Fluorescence (LIF) was used to measure a neutral velocity at the H6 exit plane of approximately 300 m/s with a 250 V discharge and 10 mg/s anode mass flow rate. [92] In addition, extensive thermal characterization was performed on a three-channel NHT [93] including simulation and measurements during operation. The results in Figure 5.6 and 6.17 of Ref. 93 show that most regions of the thruster near the anode (channel cups and magnets) were in the temperature

range of 200-400° C or 473-673 K. It is reasonable to assume the anode is in this temperature range so the neutral velocity is likely 280-330 m/s, which agrees with the H6 measurements. The fluid analysis of Barral [33] assumes 200 m/s neutrals, which is approximately room temperature. These velocities are all of the same order of magnitude and will not greatly affect the analysis.

Assume a thermal velocity of 300 m/s for gas entering the discharge channel of an SPT-100, the ions are accelerated through a 200 V potential, and the ionization region covers $L_i = 1.5$ cm, the breathing mode frequency from Equation 2.51 would be 24 kHz. Similarly, a neutral velocity of 200 m/s yields a frequency of 20 kHz. The breathing mode frequencies for these types of thrusters are typically a few to 10's kHz, so this simplistic model is of the correct order to capture what has been observed experimentally. Barral [94] pointed out that not only is the above model overly simplistic (assumes all neutrals are ionized and does not consider losses), but it is fundamentally flawed in that the influx of neutrals in Equation 2.49 is dependent on a priori knowledge of neutrals inside the chamber (the $n_n v_n / L_i$ term). This is not realistic because the influx of neutrals is constant without regard to the population of neutrals in the volume.

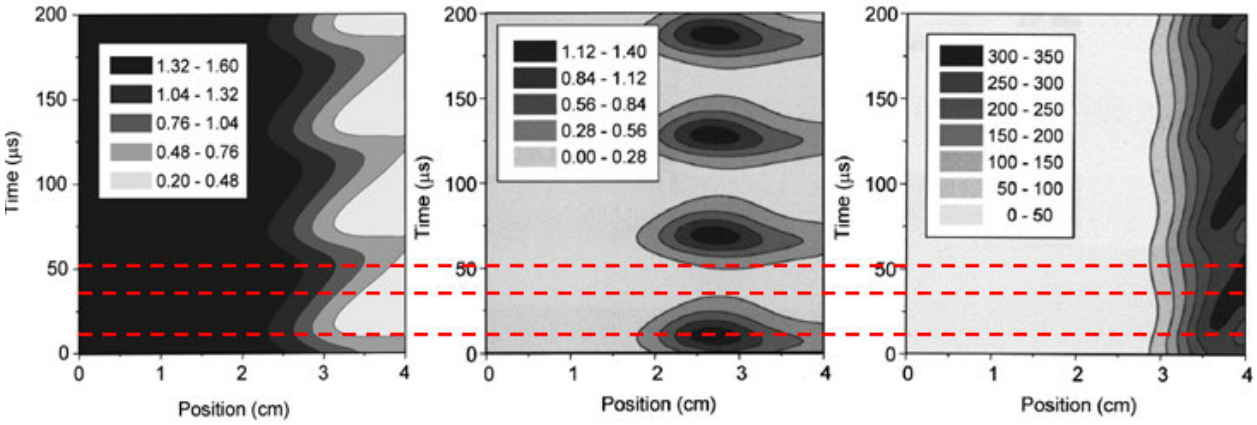

Figure 2.21: Time-resolved numerical simulations of the breathing mode. Left: neutral density with units of 10^{13} cm^{-3}, Center: ion density with units of 10^{12} cm^{-3}, Right: axial electric field with units of V/cm. Reproduced from Figure 8, 9 and 10 (left, center and right, respectively) of Ref. 76. Lines have been added to guide the eye for pre-avalanche ionization (top), post-avalanche ionization (bottom) and neutral refill (middle).

Boeuf [76] used a 1-D axial hybrid transport model where electrons are a fluid and ions are described by a collisionless kinetic equation with quasi-neutrality assumed throughout; the neutral density is modeled with the continuity equation. The computations were performed for an SPT-100, with an outer channel wall diameter of 100 mm and channel length of 4 cm. In performing a 1-D axial (z direction) simulation, the thruster discharge channel is assumed to be axisymmetric in the θ direction and uniform in the r direction. Results for neutral density, plasma density and

electric field are reproduced in Figure 2.21. The following is Bouef's description of the breathing mode: [76]

> "The current oscillations are associated with a periodic depletion of the neutral atom density near the exhaust of the SPT. The magnetic field is large in this region, and the resulting low electron conductivity leads ... to an increase of the electric field in order to maintain current continuity. The electron temperature and ionization rate are large in this region and the neutral flow tends to be quickly ionized by the electrons. This depletes the neutral atom density and the front of the neutral flow moves back upstream inside the column to a region where the electric field, mean electron energy and ionization rate are lower. The plasma density near the exhaust decreases drastically as the neutral atom density is depleted. Due to the corresponding decrease of the electron incoming flux at the exhaust the neutral atoms can flow again to the exhaust without substantial ionization, and the neutral density increases in this region. The increase of the xenon density in the large electric field region makes possible an increase of the ionization in this region, which leads to a depletion of the neutral atom density and so on."

Barral has done extensive simulations for the Hall thruster breathing mode with a series of publications [33, 85, 94, 95]. An SPT-100 type thruster was simulated with an outer channel radius of 5 cm, but a channel length of only 2.5 cm using fluid equations. The results from Ref. 33 are reproduced later in Figure 6.1. Section 6.5 will use this fluid model to investigate breathing mode triggers and damping. Hara [34, 86] uses a direct kinetic simulation for ions with comparison between direct kinetic and continuity models for neutrals and a simple fluid model for electrons. The approach has recovered the breathing mode for the SPT-100 of approximately 20 kHz. This work will also be discussed in more detail in Section 6.5. Adam [50] used a fully kinetic two-dimensional simulation ($z-\theta$) of an SPT-100 type thruster and one month of computation time which reproduced a 16-kHz oscillation in the axial direction that was identified as the breathing mode. Finally, Szabo [51] used a fully-kinetic, time-resolved, PIC simulation that reproduced the breathing mode and reasonably matched the plasma properties and performance of a BHT-1000.

The breathing mode oscillations originating in the discharge channel also affect the downstream plasma density as measured by the revolutionary HDLP and spatio-temporal data fusion techniques developed by Lobbia. [5, 96, 97] Figure 2.22 shows how the electron density varies throughout a breathing mode cycle in a planar region 2.5 mean channel diameters radially and 2.25 mean channel diameters axially beginning 2.5 mean channel diameters downstream from the thruster exit plane measured at 400 kHz. These measurements support the characterization of these discharge current oscillations as a "breath" of plasma exiting the thruster.

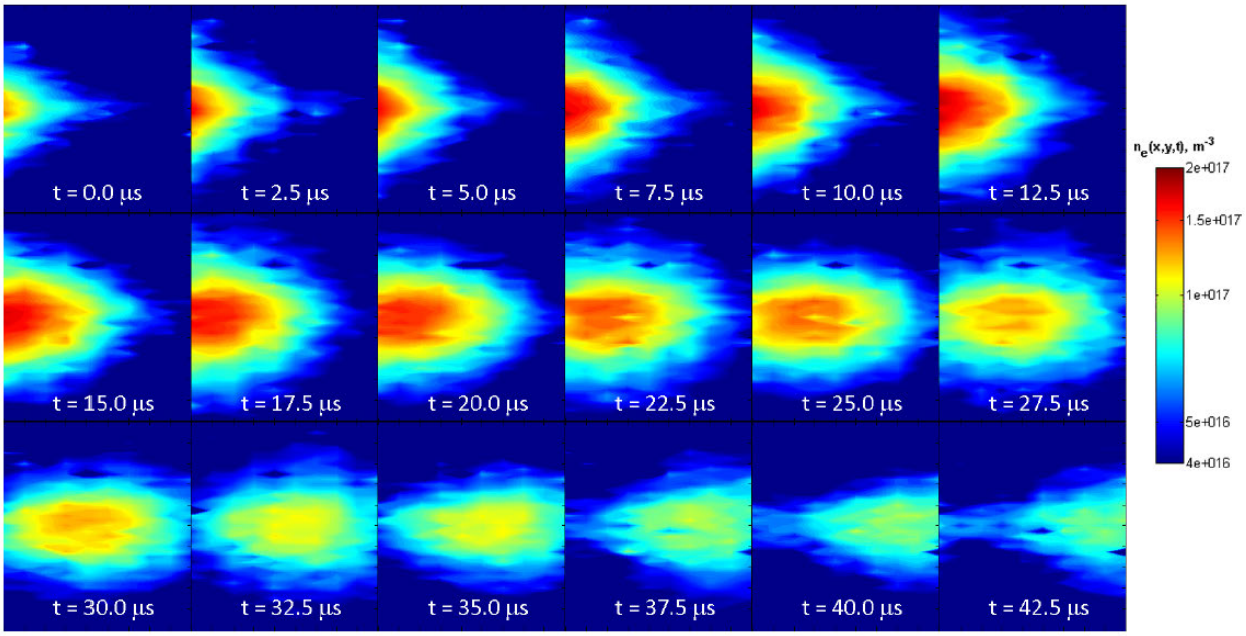

Figure 2.22: Breathing mode oscillations seen as electron density oscillations in the plume of a two-channel NHT measured with high-speed probes using spatio-temporal data fusion. For each of the 18 frames, the *x*-coordinate is axial extent from 2.5 to 4.75 mean channel diameters downstream from the exit plane, and the *y*-coordinate is radial extent from -1.25 to +1.25 mean channel diameters about thruster centerline. Reproduced from Figure 8 of Ref. 74.

The evolution of the breathing mode cycle from Figure 2.21 and Figure 6.1 will be discussed in more detail in Section 6.5.1. It is important to note the amplitude of oscillations in the plasma properties from these simulations. The change can be a factor of 2-3 up to an order of magnitude in plasma and neutral density as will be shown in more detail in Figure 6.6. This violates the assumptions used in typical linearized analysis for plasma waves where $\widetilde{n}/\overline{n} \sim \widetilde{n}_n/\overline{n}_n \sim 0.10 - 0.5$. In summary, the mechanism behind the breathing mode is reasonably supported from numerical simulations, but a fundamental theory for the initiation mechanism and stability analysis is lacking.

2.5.3 Azimuthal Spokes

A coherent theory with supporting experimental evidence for spoke propagation has yet to emerge, [73] and the location in the plasma of their formation and mechanism for propagation are unknown. However, there has been no shortage of research published on azimuthal oscillations since the early work of Morozov, Tilinin and Espipchuk [91] in the former Soviet Union and Janes and Lowder [47] in the United States. Recently, Escobar provided an excellent overview of experimental, theoretical and numerical research on azimuthal oscillations [98]. Spoke theories, mechanics and observations will be discussed in more detail in Chapter 5 with a brief summary presented here.

2.5.3.1 Experiments

The original work by Janes and Lowder [47] detected azimuthal oscillations with probes in the discharge channel where they even noted a spoke angle with respect to the walls. However, their experimental setup had significant differences from modern HETs. The experiments of Lomas [99] supported Janes and Lowder's original work, although it was conducted on a Hall accelerator using hydrogen.

Chesta [75] used probes downstream of the discharge channel exit plane and observed spokes propagating in the plume at least one channel diameter downstream. While investigating mode transitions, Gascon [69] used azimuthally space probes to investigate wave propagation in the Stanford Hall Thruster similar to the work presented here. McDonald [6, 67, 78, 79, 100] has done extensive work analyzing azimuthal spokes in the same H6 thruster used in the present investigation using the ultra-fast imaging techniques described in Section 3.5. McDonald's findings will be referenced for comparison throughout this work.

Recent work on a Cylindrical Hall Thruster (CHT) [80, 82] has demonstrated that 50% of the discharge current is carried through a single spoke. The CHT results have questionable relevance due to the significant difference in geometry (no inner channel wall) and magnetic field topology versus the H6, SPT-100 or other annular HETs.

2.5.3.2 Linearized Waves

The body of literature on dispersion relations for various waves is voluminous and the most relevant are presented here. A drift relation shown by Esipchuk [91] that accounts for density and magnetic field gradients has been used to reproduce azimuthal oscillations in the 10's kHz in the near-field plume of an SPT-100. [73] Kapulkin [101] developed a similar dispersion relation analysis for the near-anode region of an SPT-100, which is also very applicable to the H6 conditions tested here. Frias recently developed two new dispersion relations; one accounts for electron flow compressibility and the other includes temperature oscillations and gradients. [102, 103] The linearized 2-D axial-azimuthal models by Chesta [104] and Escobar [98] that account for ionization and neutral density are also relevant. A dispersion relation developed by Ducrocq [48] to study high-frequency azimuthal oscillations has been used by Cavalier [49] to numerically investigate azimuthal waves and found modes that resemble ion acoustic waves. Finally, Smoldevy [105] developed a dispersion relation with unstable modes that couples bulk plasma oscillations with the wall sheaths and bears resemblance to ion sound waves.

2.5.3.3 Simulations

Hirakawa conducted PIC simulations for ions and electrons with collisions and neutral density modeled by Direct Simulation Monte Carlo (DSMC). [87, 88] Azimuthal perturbations in plasma density were observed in the simulations with azimuthal electric fields peaking at 60 V/cm. Hirakawa noted from Janes and Lowder's original work [47] that if the oscillatory azimuthal E_θ field crossed with the steady radial magnetic field B_r are in the correct phase with the peaks in electron density n_e, then an $E_\theta \times B_r$ drift will be produced towards the anode which could account for the anomalous electron current.

Lam [89] published a $z-\theta$ fluid simulation that shows promise to numerically investigate the combined axial breathing mode and azimuthal spoke modes. Unfortunately, the simulations end at 1-3 μs due to computation difficulties, which is far too short to capture either mode which are expected to be of the order 10's kHz. The simulation duration must be of the order 100's μs with timesteps less than 1 μs to capture the oscillations of interest.

Adam [50] used a fully kinetic two-dimensional simulation ($z-\theta$) of an SPT-100 type thruster to reproduce a 16-kHz oscillation in the axial direction and high-frequency (low-wavelength) oscillations in the azimuthal direction. However, the azimuthal extent of the domain was too short to capture long-wavelength or low wave number oscillations. The azimuthal spokes observed here for various spoke orders have wave numbers in the range of $k_\theta = 30-80$ rad/m. This is two or more orders of magnitude lower than the findings of other work [48–50] that investigate short wavelength ($\sim r_{L_e}$), large wave number oscillations that resemble plasma turbulence and enhance cross-field electron transport.

What is needed is a $z-\theta$ simulation, which can be kinetic, fluid, PIC or a hybrid of any of these, that can resolve time steps of 1 μs or less (in order to resolve 10's kHz oscillation) and wave numbers less than 100 rad/m. The domain should be from the anode out at least one channel width downstream of the exit plane for a time duration of several hundred micro-seconds. Finally, in the limit of 1-D in the z-direction, it should recover the 10-30 kHz axial breathing mode.

CHAPTER 3

Experimental Setup and Analysis

"If a scientist is not befuddled by what they're looking at, then they're not a research scientist."

– Neil deGrasse Tyson

3.1 Introduction

This investigation uses the well-characterized H6 HET to study mode transitions by varying magnetic field strength for various operating conditions. High-speed diagnostics including ultra-fast imaging and probes provide valuable insight into plasma oscillation changes during mode transitions. The purpose of this chapter is to explain the experimental setup used for the testing including facilities in Section 3.2 and the thruster in Section 3.3. The analysis techniques that are at the heart of this investigation, the HDLP-ISR and HIA are discussed in detail in Sections 3.4 and 3.5, respectively.

3.2 Plasma Dynamics and Electric Propulsion Laboratory

3.2.1 Large Vacuum Test Facility

This investigation was conducted in the Large Vacuum Test Facility (LVTF) of the Plasmadynamics and Electric Propulsion Laboratory (PEPL) at the University of Michigan. The LVTF is a 200 m^3 stainless steel-clad vacuum chamber 9 m long and 6 m in diameter. Rough vacuum is achieved with two 57 m^3/min (2000 cfm) blowers backed by four 11 m^3/min (400 cfm) mechanical pumps with a final base pressure in the low 10^{-7} Torr achieved by seven CVI TM-1200 re-entrant cryopumps with LN_2 baffles and a nominal pumping speed of 500,000 L/s on air or 245,000 L/s on xenon. During thruster operation, the chamber pressure is measured with an external ion gauge

mounted at the top of LVTF above the thruster (~3 m away) and the pressure measurement uncertainty was estimated to be 20%. [106] Pressure varied for conditions based on anode flow rate but with a fixed chamber pumping speed. The xenon corrected chamber pressures were 8.5×10^{-6}, 1.1×10^{-5} and 1.4×10^{-5} Torr for 14.7, 19.5 and 25.2 mg/s anode flow rate, respectively. A more complete discussion of pressure measurements and pressure effects on HET operation is provided by Walker. [107] Using a gas kinetics relation for mass flux [108] $\dot{m}_a = 1/4 n_N m_N \mathrm{v}_{th_N} A_{chnl}$, an ambient pressure of 1×10^{-5} Torr and room temperature neutrals because they have thermalized with the chamber walls, the mass flow rate into the discharge channel from ambient neutrals is 0.06 mg/s, which is less than 0.5% of the lowest anode flow rate used in this investigation. Therefore, background gas should not significantly affect neutral densities within the channel, but may play a large role in processes that occur outside the channel.

Discharge voltage and current to the thruster were supplied with an Amrel 100-kW DC power supply across a 102 μF Maxwell Laboratories Caster Oil capacitor. Telemetry including mean discharge current, cathode-to-ground voltage, discharge voltage, inner and outer magnetic coil currents and voltages were measured at 1-s intervals with an Agilent 34970A Data Logger and recorded on a computer using Agilent Benchlink software. The discharge voltage, V_D, was measured using sense lines on the anode and cathode. Sense line raw voltage signals were sent to a 10,000:1 voltage divider that was calibrated with a BK Precision 5491A multimeter. Mean discharge current $\bar{I_D} = \langle I_D(t) \rangle$ where $\langle\rangle$ denotes the average was measured with an NT-50 FW Bell sensor. Magnet coil currents were measured with 10-mΩ shunt resistors. All currents were calibrated using a precision 10-mΩ resistor accurate to 0.1% and a BK Precision 5491A multimeter. Plume photographs were taken with a Nikon D80 digital camera with a DX AF-S Nikkor 18-135 mm lens set to f5.6, 1/100 s shutter speed and manual focus.

Xenon gas (Research Grade 99.999% pure) was used for the anode and cathode for all testing. The xenon propellant is delivered to the HET using Alicat Scientific MC Series mass flow controllers through electro-polished stainless steel lines. Mass flow calibration takes place through a Bios Definer 220L DryCal system plumbed in parallel to the anode and cathode feed lines with a measurement accuracy of 1% of the reading between 5 and 500 sccm. Mass flow calibrations are taken for each mass flow controller at several flow rates and a linear fit is used to determine the flow produced at any arbitrary set point. The AC component of the thruster discharge current, $I_{D_{AC}}(t)$ was measured either with a Tektronix TCP 312 (DC to 100-MHz bandwidth) or TCP 303 (DC to 15-MHz bandwidth) split-core Hall current sensors through a Tektronix TCPA 300 current probe amplifier. The signal was measured on the discharge current line external to the chamber on the anode side and was acquired simultaneously with Langmuir probe (HDLP-ISR) signals on

the same Data Acquisition (DAQ) system described later. The total discharge current, time history signal is the combination of the two measurements

$$I_D(t) = \bar{I}_D + I_{D_{AC}}(t) \tag{3.1}$$

Discharge current oscillation amplitude will be defined here as the root-mean-square (RMS) of the AC component of the discharge current time history signal in amperes

$$\tilde{I}_D = \sqrt{\left\langle \left(I_D(t) - \bar{I}_D \right)^2 \right\rangle} = \sqrt{\langle I_{D_{AC}}(t) \rangle^2} \tag{3.2}$$

Note that Equation 3.2 is the square root of the sample variance for a sample size N and not the square root of the bias-corrected variance which would have $\sqrt{N-1}$ in the denominator. The difference is negligible for the discharge current signal where the sample size N is between 1×10^6 and 45×10^6 points. The relative discharge current oscillation amplitude is the RMS value fraction of the mean discharge current $\tilde{I}_D / \bar{I}_D$. The normalized, AC component of the discharge current, $\hat{I}_D(t)$, is calculated from the discharge current time-history signal, by

$$\hat{I}_D(t) = \frac{I_D(t) - \bar{I}_D}{\tilde{I}_D} \tag{3.3}$$

Discharge current density average $\bar{j}_D$ and time history $j_D(t)$ values are defined as

$$\bar{j}_D = \frac{\bar{I}_D}{A_{chnl}} \tag{3.4}$$

$$j_D(t) = \frac{I_D(t)}{A_{ch}} = \frac{\bar{I}_D + I_{D_{AC}}(t)}{A_{ch}} \tag{3.5}$$

where $A_{ch} = \pi \left(R_o^2 - R_i^2 \right) = 2\pi R_{ch} W_{ch}$ is the area of the discharge channel with outer and inner radius, R_o and R_i, respectively. R_{ch} is the mean channel diameter and W_{ch} is the channel width.

3.2.2 Motion Tables

Two perpendicularly-mounted motion stages, one radial and one axial, were used to acquire plasma plume data in a 2-D plane. The radial stage is a 1.5 m long Aerotech ATS62150 ball screw stage driven by a stepper motor as shown in Figure 3.1. It is used in open loop position feedback mode with a 15-V string potentiometer to monitor the radial stage position during movement. The axial stage is a 0.5 m long Parker Trilogy T2S I-Force Ironless Motor Positioner, a linear motor capable of a maximum of 6 g acceleration and 5 m/s velocity. This stage is better known as the High-

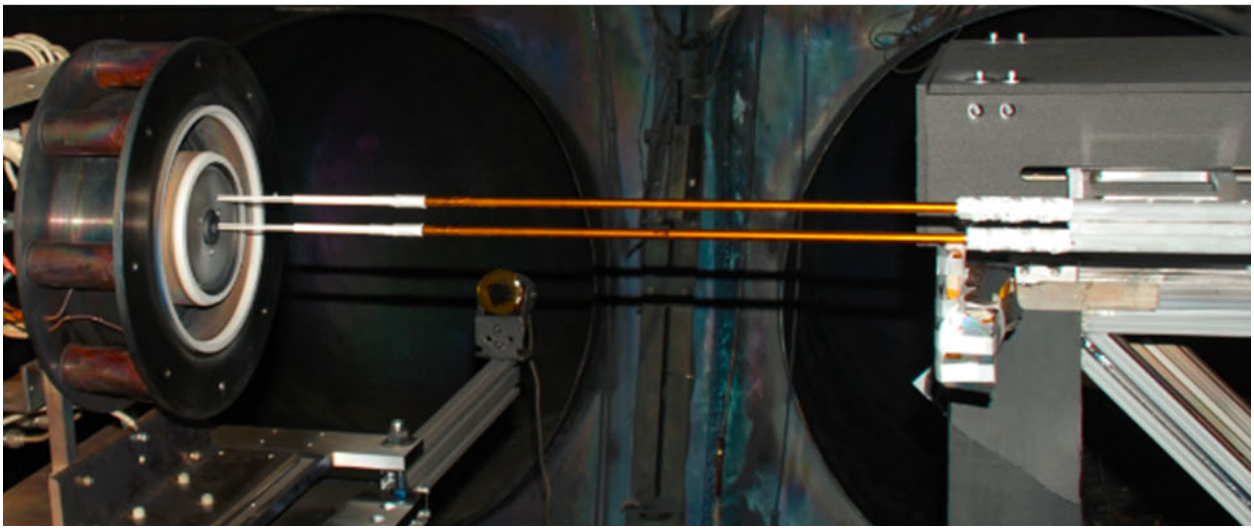

Figure 3.1: HDLP-ISR mounted on HARP shown at full extension to the discharge channel exit plane ($z/R_{chnl} = 0$) on cathode centerline ($r/R_{chnl} = 0$). Note the ISR probe is over the outer pole. This configuration was used to generate the plume maps in Appendix B.

speed Axial Reciprocating Probe (HARP) and is used for axial injection of plasma probes into the thruster plume as shown in Figure 3.1. It operates in a closed loop position feedback mode with 5 μm resolution Renishaw LM10 encoder. Both stages are operated by Aerotech motion controllers, an Aerotech MP10 for the radial stage and an Aerotech CP20 for the axial HARP stage, that are both automated from LabView.

3.2.3 Thrust Stand

PEPL uses an inverted pendulum thrust stand based on the NASA Glenn Research Center (GRC) design of Haag [109] to measure thruster performance. This design has extensive heritage for testing electric propulsion devices. [44, 110, 111] In summary, the inverted pendulum thrust stand operates in null mode using a Proportional, Integral, Derivative (PID) controller and a solenoid actuator to maintain the pendulum in a vertical position based on feedback from a Linear Variable Differential Transformer (LVDT). The thrust stand tilt must remain constant throughout operation, which can shift during pump down and thruster operation due to thermal expansion of structural components. An inclinometer is used to monitor thrust stand tilt and manual adjustments are made with a control motor as necessary. A cooling loop with glycol powered by a Polyscience Durachill 6860T chiller with 5.2 kW cooling capacity is used to thermally regulate the thrust stand. The thruster was operated for over three hours before any data were acquired in order for the thruster and thrust stand to reach thermal equilibrium. Even if the thrust stand were not at complete thermal equilibrium, this is accounted for by taking zero values at regular intervals where

the thruster is briefly turned off and the zero output is recorded. The thrust stand was calibrated by lowering and raising a series of high-precision weights to ensure a linear response. Calibration was performed before thruster operation, two times during testing when the thruster was briefly turned off, and once again after testing was complete. All calibrations showed a linear response and were combined to generate the thruster calibration curve to convert PID controller output in volts to thrust in mN.

3.3 H6 Thruster

The H6 Hall thruster shown in Figure 3.2 is a 6-kW class Hall thruster with a nominal design voltage of 300 V and a 7% CFF. CFF is the mass flow rate of gas through the cathode divided by the mass flow rate of gas through the anode, CFF = $\dot{m}_c/\dot{m}_a$. It uses a hollow cathode with a lanthanum hexaboride (LaB_6) insert that can either be mounted centrally (on thruster centerline which is the nominal configuration) or mounted externally. The inner magnet coil is one, continuously wound solenoid core while the outer coil consists of eight discrete solenoid cores wound in series and separated by 45°. The outer pole is designed such that inside the discharge channel the magnetic field shown in Figure 3.2 (Right) is azimuthally uniform to less than one Gauss. Note that the magnetic field within the discharge channel cross-section is radially symmetric about (mirrored above and below) discharge channel centerline from the anode to the exit plane, [42] whereas the SPT-100 magnetic field shown in Figure 2.19 is not. The H6 was a joint development effort of the University of Michigan, the Air Force Research Laboratory (AFRL) at Edwards Air Force Base (AFB), and the NASA Jet Propulsion Laboratory (JPL). A separate copy of the thruster is maintained at each institution. It is notable for its high total efficiency; e.g., 64% at 300 V (6 kW) with a specific impulse of 1950 s, and 70% at 800 V (6 kW) with a specific impulse of 3170 s. [37] Slightly different nominal operating conditions are used between institutions.

At the University of Michigan, work by Reid [44], Shastry [110], Huang [112] and McDonald [6] studied H6 operation between 5 and 30 mg/s flow rates, but primarily focused on 20 mg/s for ~ 6-kW operation at 300 V. Work by Hofer at JPL has tuned the H6 to even discharge currents and power levels; i.e., 20 A for exact 6 kW operation at 300 V. For xenon these operating conditions vary only by a few percent in current or mass flow rate (1 mg/s Xe ~ 1 A discharge current), but peak magnetic field strengths between the two cases may vary by up to 15%. At the 300 V, 20 mg/s, 6.1 kW Michigan operating condition, the H6 has a 20.3 A discharge current and produces 397 mN of thrust at a specific impulse of about 1900 s. [44] At the nominal 300 V, 20 A, 6 kW JPL condition, the specific impulse is 1950 s with a thrust of 401 mN. [37]

Since first firing in 2006, the H6 has been well characterized by a variety of diagnostic and modeling techniques at Michigan, AFRL and JPL. Six experimental doctoral dissertations have

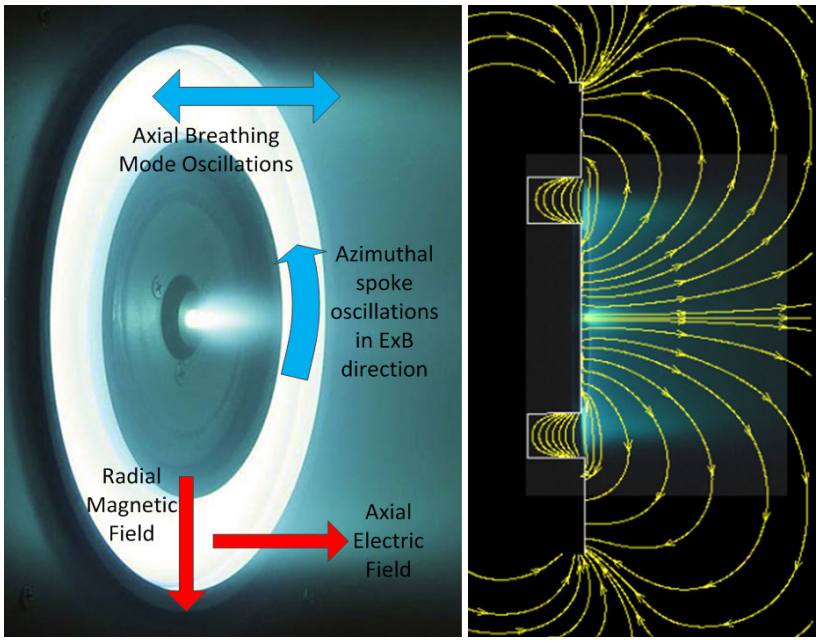

Figure 3.2: (Left) H6 with direction of magnetic field and $E \times B$ shown. (Right) Profile picture of the H6 operating at nominal conditions with magnetic field stream lines overlaid and discharge channel outlined.

focused on the thruster to date, [6, 44, 110, 112–114] which have spawned numerous associated conference and journal articles. Modeling of the H6 has been performed using the hybrid PIC simulation HPHall-2 [115] and the more recently developed fluid code Hall-2De. [83] The H6 is a well-characterized HET with multiple references for steady-state values and provides an ideal platform for high-speed investigations of oscillatory plasma phenomena.

The flow rate of 19.5 mg/s is the nominal setting used for comparison in this work and the cathode flow fraction of 7% was maintained for all conditions. Centerline cathode mounting is the nominal configuration of the H6 as shown in Figure 3.2 and Figure 3.3 (Left), but an external cathode configuration was also tested as shown in Figure 3.3 (Right). The only data presented here for the external configuration are for the nominal 300-V, 19.5-mg/s case. Unless explicitly stated, all data shown below are for the centerline-mounted cathode configuration.

The magnetic field shape shown in Figure 3.2 (Right) was kept constant during testing, though the magnitude, noted by B_r/B_r^*, was varied throughout the testing in order to induce a mode change within the H6. The quantity B_r/B_r^* is the maximum radial magnetic field value at a particular setting of inner magnet (I_{IM}) current and outer magnet (I_{OM}) current (I_{IM}/I_{OM} = 1.12) divided by the reference maximum radial magnetic field. The reference magnetic field (B_r^*) strength at 300 V and 20 A discharge current was I_{IM} = 3.50 A and I_{OM} = 3.13 A, which maximizes *total* efficiency according to Hofer. [22] This magnetic field strength was used as the non-magnetically shielded

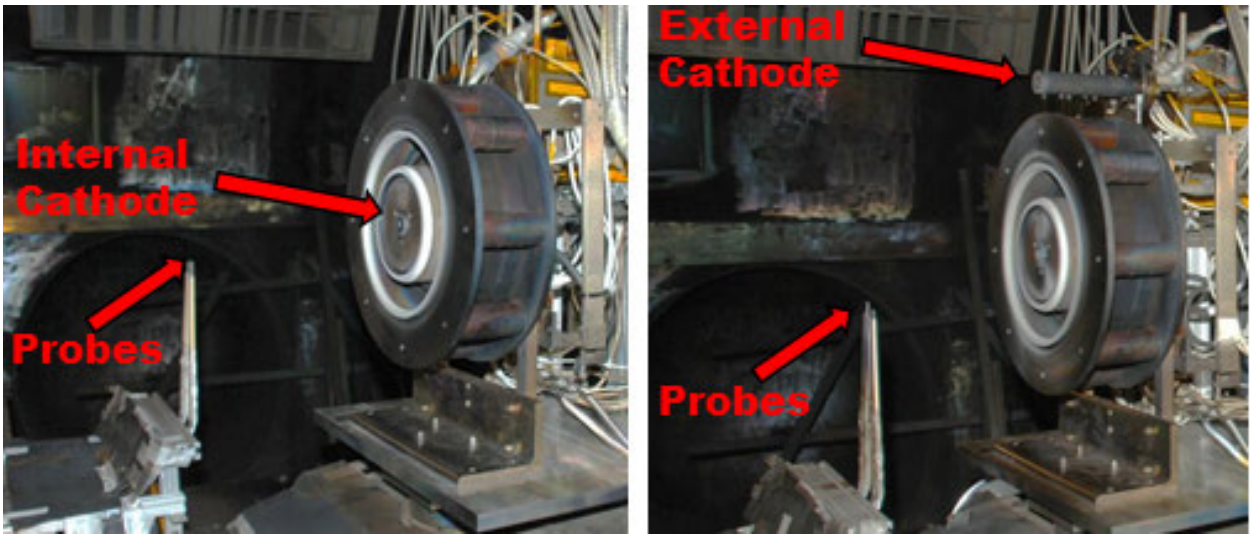

Figure 3.3: Internal cathode (Left) and external cathode (Right) configurations shown with probes.

thruster baseline to compare with a magnetically shielded thruster equivalent during their initial development. [22,37] Therefore, this setting has been well characterized and is used for the plume maps presented in Appendix B. However, as will be shown later in Figure 4.30 of Section 4.8, this reference magnetic field strength does not coincide with maximum thrust to power and anode efficiency or minimum mean discharge current.

In order to confirm the magnetic field magnitude was varied and not topology, magnetic field simulations of the H6 were performed using MagNet Version 7.4.1.4 (32-bit) from Infolytica Corporation for all magnet settings used during B-field sweeps. The peak magnetic field value varied linearly with inner magnet current from the minimum of 1.45 A to approximately the reference setting of 3.5 A as shown in Figure 3.4. However, a second order, least squares fit best represents the peak B-field value across the range of magnet coil currents used with the equation shown in Figure 3.4. This captured the deviation from linearity for the peak B-field that occurred for $I_{IM} \gtrsim 3.5$ A. In practice, deviations in the magnetic lens symmetry for the H6, which is an important assumption in this investigation, begins at $I_{IM} \sim 4.5 - 5.0$ A.[1] The axial location of the peak B-field did not change to within the 2 mm grid used in simulations. Noting that L_{ch} is the channel length, the maximum deviation of B-field direction within $L_{ch}/2$ axial distance from the exit plane along the outer wall, channel centerline and inner wall was 6.3, 0.9 and 5.9 degrees, respectively. For $\pm L_{ch}/4$ axial distance from the exit plane the maximum deviations were 1.8, 0.3 and 1.9 degrees, respectively. Based on the internal measurements of Reid, [44] most of the ionization and acceleration occurs within the axial region approximately $\pm L_{ch}/4$ from the exit plane. Therefore, the magnetic field shape shown in Figure 3.2 can be considered constant throughout

[1] Personal correspondence with R. Hofer, September 2013.

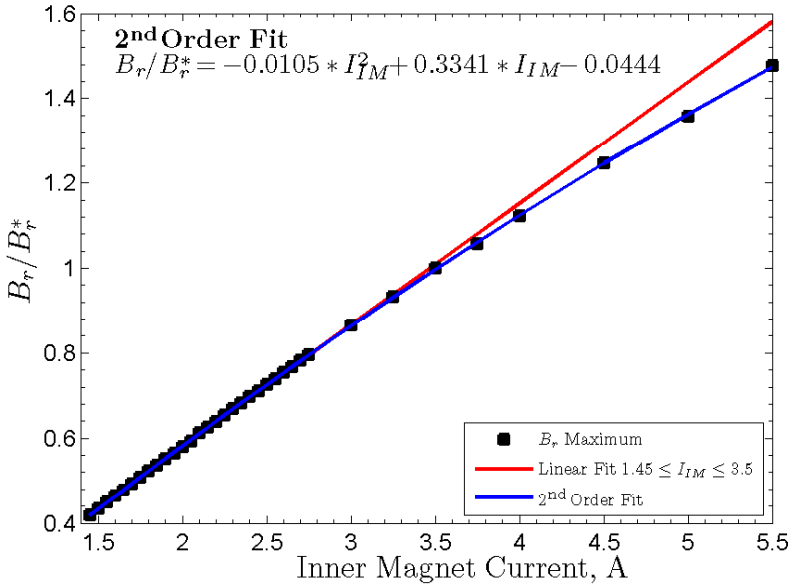

Figure 3.4: Normalized maximum radial magnetic field (B_r/B_r^*) on channel centerline as a function of inner magnet current (I_{IM}). A linear least squares fit from the minimum current to the reference setting is shown as well as a 2nd order least squares fit over the entire range.

sweeps (validated for $B_r/B_r^* < 1.2$) and the resulting mode transitions are due solely to the magnitude change. This conclusion will be further supported by the fact that mode transitions across different operating conditions do not occur at any one preferential magnetic field setting.

3.4 High-speed Dual Langmuir Probe with Ion Saturation Reference (HDLP-ISR)

The purpose of this section is to explain the techniques used for the time-resolved probe measurements using the HDLP-ISR. The High-speed Dual Langmuir Probe (HDLP) was developed by Lobbia [96] and used successfully to measure plasma oscillations in the plume of an HET as the world's fastest fully swept Langmuir probe. [74] The work presented here expands on the HDLP by adding an Ion Saturation Reference (ISR) probe to provide the Direct Current (DC) reference needed by the HDLP, serve as an electrostatic probe for monitoring oscillations, and enable ion density calculations that are typically corrupted in HDLP signals due to noise. When used as a simple electrostatic probe, the ISR signal is not dependent on the HDLP signal, so at times it will be used independently to monitor plasma oscillations. Calculating plasma properties from the HDLP signal does require the ISR signal. A new method for calculating ion density from a flowing plasma with a cylindrical Langmuir probe aligned with the flow is reserved for a detailed

discussion in Appendix A. The time-resolved techniques shown here can also be used to calculate time-averaged plasma properties as well, which are discussed and shown in Appendix B.

3.4.1 Principles of Langmuir Probes

The first technique for measuring plasma properties was the electrostatic probe developed by Irving Langmuir circa 1924 [116] and remains one of the most fundamental diagnostics for plasma measurements today. The Langmuir probe consists of a small metallic electrode, usually a wire, inserted into a plasma and biased at various voltages to measure the current response known as I-V traces (for current-voltage). The plasma properties including density, plasma potential and electron temperature or Electron Energy Distribution Function (EEDF) can be calculated with the voltage-current traces. Due to their ubiquitous use, Langmuir probe theory has enjoyed considerable attention within the literature [116–123] so only the relevant basics will be recapitulated here.

Langmuir probe voltages can be varied slowly to generate time averaged measurements of plasma properties or can be swept fast to measure plasma transients, exemplified by [74] where the plasma properties and EEDFs were measured at a remarkable 400 kHz. Such measurements were made possible using the HDLP [5, 96, 124] developed by Lobbia shown schematically in Figure 3.5. The HDLP uses an active and null probe to cancel the capacitive current, I_{cap}

$$I_{cap} = C\frac{dV}{dt} \tag{3.6}$$

generated by rapid, high amplitude (i.e. large dV/dt) voltage sweeps with the resulting plasma currents measured by a wideband current transformer manufactured by Pearson Electronics (Pearson coil) in the vacuum chamber. However, the current transformer cannot measure DC currents so either a shunt resistor must be used or another reference to the low frequency current is necessary.

3.4.2 Ion Saturation Reference

The null probe in the HDLP is meant to cancel capacitive current due to stray and line capacitance as well as cancel noise incident on both probes, but the plasma sheath capacitance is of order 10's pF [125]. Consider a ±50 V, 200 kHz sine voltage signal, the maximum dV/dt yields a peak capacitive current from Equation 3.6 of 630 μA assuming a 10 pF sheath capacitance. This current overwhelms the plasma current in the ion saturation region where the current is also of the order 100 μA. Therefore, an alternative, reliable measurement of the ion saturation current is needed that fluctuates with the plasma. The solution is to use a second Langmuir probe several millimeters or more away, far enough not to disturb the swept probe, but close enough to maintain reasonable

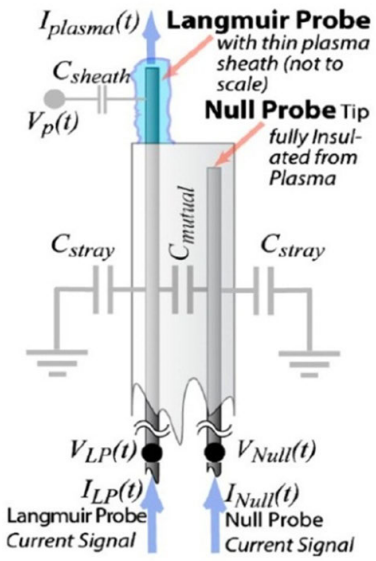

Figure 3.5: Diagram of HDLP adapted from Lobbia [124] showing active and null probes with capacitances represented schematically.

spatial resolution. This probe is maintained at a continuous negative bias for time resolved ion saturation measurements. Additionally, this probe is able to provide the ion saturation portion of the I-V trace which acts as the DC reference necessary for the HDLP probe which was not provided by the current transformer. The resulting system is hereby known as the HDLP-ISR.

The ISR signal alone can provide useful information for identifying plasma oscillations without actually calculating plasma properties. From Equation 3.10 for thin sheath Langmuir probe theory, I_{ISR} is linearly related to ion density at constant electron temperature if the probe is operated in ion saturation

$$n_i = \frac{I_{ISR}}{0.605 A_p e \sqrt{e T_e / m_i}} \tag{3.7}$$

Note that ion density calculations in a flowing plasma where the ion velocity is larger than the Bohm velocity is discussed in Appendix A. Figure B.5 shows a plasma plume map of the H6 with a discharge voltage of 300 V and discharge current of 20 A for the reference magnetic field, $B_r/B_r^* = 1$. Using the plume information from Figures B.5(c) and (d), the plasma potential and electron temperature are 30 V with respect to ground and 3.7 eV, respectively. In order to ensure the ISR probes are in ion saturation, they must be biased well below the floating potential, which from Equation 3.15 is $V_f \approx V_p - 5.8T_e$. The ISR probes were biased to -30 V with respect to ground, which is more than 16 T_e below the plasma potential and therefore are safely in ion saturation. During this investigation, the magnetic field, discharge voltage and flow rate were varied, so the plume properties will differ from those shown in Figure B.5. However, with a factor of 3 margin

(16 T_e versus 5.8 T_e) at nominal conditions, the probes are still expected to be in ion saturation at the off-nominal conditions.

3.4.3 Linear Correlation

The Pearson linear correlation coefficient or product-moment coefficient of correlation ρ_{xy} is used to quantify how well two signals, x and y, are linearly correlated [126]

$$\rho_{xy} = \frac{\sum_N (x_i - \langle x \rangle)(y_i - \langle y \rangle)}{\sqrt{\sum_N (x_i - \langle x \rangle)^2 \sum_N (y_i - \langle y \rangle)^2}} \tag{3.8}$$

This technique will be used to show the correlation between the discharge current with the ISR probe signals and between probe signals. The coefficient ranges from $-1 \leq \rho_{xy} \leq 1$ where 1 means the signals are perfectly correlated ($x = y$), -1 means they are inversely correlated ($x = -y$) and 0 means they are not correlated. Additionally, the cross-correlation is used extensively to calculate the time-offset between two signals. The cross-correlation function is [126]

$$R_{xy} = \lim_{T \to \infty} \frac{1}{T} \int_0^T x(t) y(t + \tau) dt \tag{3.9}$$

Signal delays for non-frequency dispersive propagation can be identified by peaks in R_{xy} as is done with discharge current and probe signals. When calculating R_{xy} from Equation 3.9, the AC component is isolated by subtracting the mean and then normalized by dividing by the RMS value; the time delay is determined from the largest peak in R_{xy}.

3.4.4 Temporal Limits

Lobbia discussed the temporal limits of Langmuir probes in Ref. 124 and only the important results will be discussed here. A full set of frequency limitations were developed for Langmuir probe measurements based on plasma properties and probe characteristics. As summarized in Table 1 of Ref. 124, the near-field region for a typical HET has the frequency limits in the single to hundreds of MHz, which are well above the sweep frequency used here of only 200 kHz. The stray capacitance is mitigated by the HDLP configuration which uses a null probe. The mutual capacitance limitation is avoided with the HDLP-ISR because shunt resistors are not used since the ISR provides the DC reference.

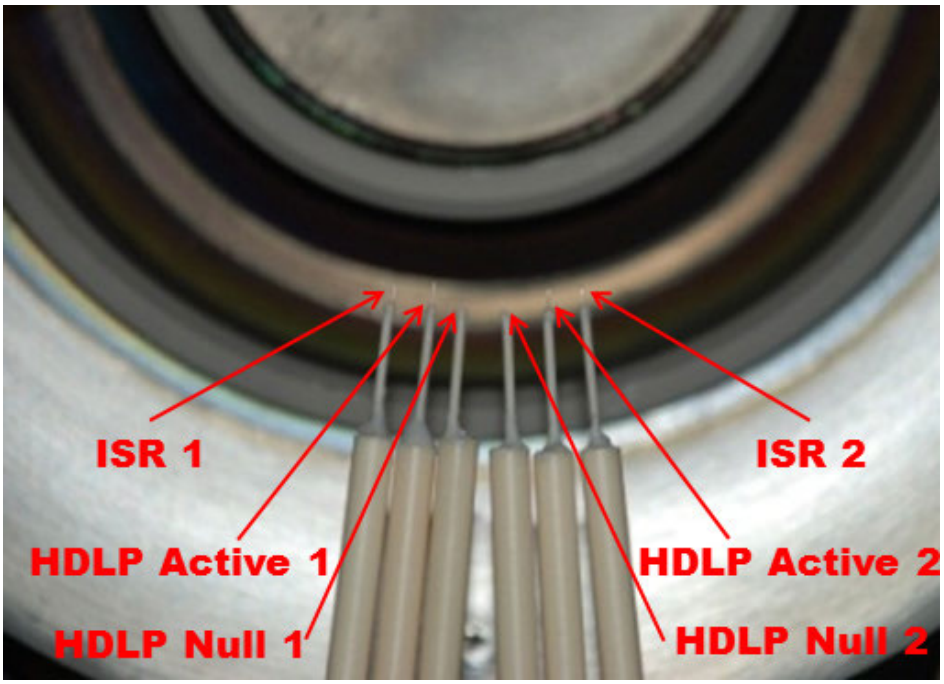

Figure 3.6: Two HDLP-ISR probes in position at the 6 o'clock location. A complete HDLP-ISR consists of an active probe, a null probe and an ISR probe. The exposed Tungsten wire is only near the arrow tip for the ISR and active probes. This configuration was used for the mode transition investigations of Chapter 4.

3.4.5 Hardware

A 200-kHz sinusoidal signal generated by a Tektronix AFG3101 is amplified using a Krohnhite 7500 wideband power amplifier capable of DC to 1 MHz output with ±200-V range to generate the probe bias. The DAQ system consists of eight channels sampled at 180 MHz with 16-bit AlazarTech ATS9462 digitizers. The HDLP current is measured with the active and null probe lines wound in opposite directions through a model 6585 Pearson coil protectively mounted inside LVTF with less than 2 m of cable length from the probe tip to current measurement location to minimize capacitance. The ISR current is measured external to LVTF across a $100-\Omega$ shunt resistor through an Analog Devices AD 215 120 kHz low distortion isolation amplifier where the $2-\mu$s offset has been accounted for. The $2-\mu$s offset was specified on the data sheet and verified using the AFG3010 and a Tektronix digital oscilloscope.

The probes consist of 0.38 mm diameter pure tungsten wire with 3.2 mm exposed for the active HDLP probe and 3.3 mm exposed for the ISR probe. For the mode transition investigation of Chapter 4, the probes in Figure 3.6 were positioned using the 1.5-m-long Aerotech ATS62150 ball screw stage driven by a stepper motor and controlled with an Aerotech MP10 controller. The probe table was used in open loop position feedback mode with a 15−V string potentiometer to

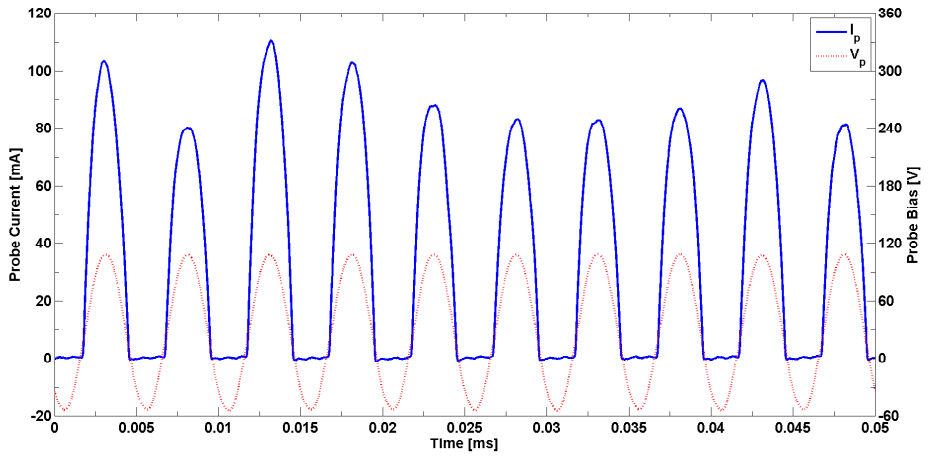

Figure 3.7: Example time history of probe bias and probe current for the first 0.05 ms of the channel centerline ($R/R_{ch} = 1$) shot. Each half-cycle of the probe bias was "chopped" into an individual I-V trace for calculating plasma properties.

monitor the stage position during movement and ensure proper positioning in front of the thruster to within 5 mm radially. Figure3.6 shows the two HDLP-ISRs in position in front of the thruster 1.5 mean channel radii downstream in the 6 o'clock position on discharge channel centerline (within ±5 mm). The ISR probe gap was 29.5 ± 0.5 mm apart, which corresponds to $21.4^\circ \pm 1.7^\circ$ of azimuthal spacing; i.e., $\sim 11^\circ$ on either side of 6 o'clock.

For the plume maps in Appendix B, the thruster was moved on the Aerotech motion table and the HDLP-ISRs in Figure 3.1 were injected into the plume using the HARP. In Figure 3.1, the bottom probe was the HDLP and the top probe was the ISR, which were separated by 26.5 mm. This gap is larger than preferred for HDLP-ISR operation since the ISR probe will be sampling a different segment of plasma and will not provide the correct ion saturation current to correct the HDLP trace. However, the fluctuations in ion saturation current are 10's to 100's of μA and the rest of the I-V trace is 10's to 100's of mA as seen in Figure 3.7 so the effect on electron density calculations is negligible.

The voltage range swept for the HDLP varied based on radial location, but in general ranged from -50 to +150 V around the floating potential. At each radial location, the probes were first injected to generate a floating potential profile for each shot. The probes were subsequently injected again while sweeping around the floating potential. Figure 3.7 shows an example segment of the time history trace for the probe bias and probe current. Note that each half-cycle of the probe bias and corresponding probe current form one complete I-V trace.

3.4.6 Automated I-V Trace Processing

3.4.6.1 Regions of I-V Trace

As will be shown later for this testing, time-resolved plasma measurements require processing of 10^5 to 10^6 I-V traces, which is impractical to do by hand. Therefore, an automated technique that was initially developed for HDLP [5, 74, 96] has been adapted for HDLP-ISR automated I-V trace processing. The premise of HDLP analysis is the standard collisionless, thin-sheath Langmuir probe theory which has been discussed in literature [116–123] with the basics outlined below. Note that all electron temperatures, T_e, in the equations below, are in eV. The criteria for thin-sheath is the probe radius to Debye length (λ_D) should be greater than 1. A typical I-V trace for a cylindrical Langmuir probe is shown in Figure 3.9 and consists of three regions:

1. Ion saturation region where the probe is biased negative to repel most electrons and collect ions.

2. Electron retarding region approximately between the floating potential and the plasma potential where the probe is collecting both ions and electrons.

3. Electron saturation region where the probe is biased positive with respect to the plasma potential to repel ions and collect electrons.

3.4.6.2 Probe Current and Electron Density

Not accounting for flowing plasma as discussed in Appendix A, the ion current to a probe accounting for the Bohm criteria and assuming only singly charged ions is [117]

$$I_+ = 0.61 n_\infty q A_s \mathrm{v}_B \tag{3.10}$$

where n_∞ is the plasma density outside of the sheath, q is the fundamental charge, A_s is the sheath area and v_B is the Bohm velocity given by

$$\mathrm{v}_B = \sqrt{\frac{qT_e}{m_i}} \tag{3.11}$$

The electron current to a probe biased at ϕ in the electron retarding region, assuming a Maxwellian velocity distribution, is

$$I_e = -\frac{1}{4} A_{pr} n_\infty q \mathrm{v}_{th} \exp\left[\frac{\phi - V_p}{T_e}\right] \tag{3.12}$$

where A_{pr} is the area of the probe, V_p is the plasma potential and v_{th} is the thermal velocity

$$v_{th} = \sqrt{\frac{8qT_e}{\pi m_e}} \tag{3.13}$$

The electron density can be calculated from Equation 3.12 with the electron saturation current, , the point at which the probe enters electron saturation

$$n_e = \frac{I_{e_{sat}}}{0.25 A_{pr} \mathrm{v}_{th}} \tag{3.14}$$

3.4.6.3 Plasma Potential

While not as precise as emissive probes, plasma potential can be determined from Langmuir probe I-V traces by identifying the "knee" in the curve identifying the transition from electron retarding to electron saturation. As noted frequently in the literature, determining the plasma potential from the "knee" in the I-V curve is imprecise because the "break in the characteristic is frequently far from abrupt," [122] especially for a cylindrical probe where the transition from electron retarding to electron saturation is gradual even in the best of circumstances (c.f. Fig. 5 from Ref. 116).

The slope of the electron current, $dI_e/d\phi$, is exponentially related to the probe bias and T_e as seen from the derivative of Equation 3.12; therefore $dI_e/d\phi$ should be increasing with ϕ until the electron saturation region is reached where the slope will then decrease significantly. Therefore, the peak in $dI_e/d\phi$ is a reasonable measure for plasma potential [121, 123]. As noted in Ref. 30, this method tends to under-predict the plasma potential where +2/-1 V error was assumed on V_p calculations in that work. An example of detecting the $dI_e/d\phi$ peak value is shown in the lower-left plot of Figure 3.9.

Testing with various methods of fitting lines to the electron retarding and electron saturation regions to determine V_p from the intersection yielded unsatisfactory results because the electron saturation region was not well represented by a straight line. Therefore, the method of determining V_p, and hence $I_{e_{sat}}$ from the peak of $dI_e/d\phi$ will be employed in this work. The electron saturation current is the electron current at V_p and is then used to calculate n_e from Equation 3.14. Using this technique yielded more consistent results, which is critical for autonomous analysis of hundreds of thousands of I-V traces for time-resolved plasma property calculations.

3.4.6.4 Electron Temperature

The electron temperature with an assumed Maxwellian energy distribution for traditional, collisionless, thin-sheath Langmuir probe analysis is found from the inverse of the slope of $\ln(I_e)$ versus ϕ in the electron retarding region from the floating potential, V_f, to V_p (from taking the natural log of Equation 3.12). However selecting all points between V_f and V_p will include the

gentle transitions (the gradual "knee") between the regions and thus skew the slope of the line, so only the linear points in the center between V_f and V_p should be selected. This process is simple to perform manually, but to automate analysis for 100,000's I-V traces, a reliable selection method is necessary. The slope of a line can be determined from as few as two points, so the selection criteria for what datum to include from the tens to hundreds in the electron retarding region during a single I-V sweep could be stringent. However, the maximum number of reliable points are desired because Lobbia [5] points out the non-systematic T_e uncertainties are reduced by a factor of $1/\sqrt{N_{T_e}-1}$ where N_{T_e} is the number of I-V points used to calculate T_e. Before a point selection method can be considered, V_p and V_f need to be determined.

The floating potential, V_f, is the point of zero crossing for the I-V trace; however, the ion saturation current portion of the trace is so small compared to the electron retarding and electron saturation currents that noise often corrupts the signal introducing significant error in determining the probe bias for zero current. This is a peculiarity to high-speed Langmuir probe data because the floating potential is the characteristic typically easiest to measure with low speed I-V sweeps. For the HDLP-ISR system, the purpose of the ISR reference is to give a reliable ion saturation current to calculate ion density and compensate for this noise, but since the ISR bias is not varied V_f cannot be determined reliably.

The total current to the probe is the sum of Equations 3.10 and 3.12. When the probe is at V_f the total current is zero because the ion and electron currents balance. Equating 3.10 and 3.12 and assuming $A_s \approx A_{pr}$ for thin sheath yields a relationship for V_f, V_p and T_e [120, 122] where the coefficient has been calculated for xenon

$$V_p = V_f + T_e \ln\left[\frac{1}{0.61}\sqrt{\frac{m_i}{2\pi m_e}}\right] \approx V_f + 5.8T_e \tag{3.15}$$

The importance of Equation 3.15 is to show that the floating potential should be several electron temperatures below the plasma potential.

The value of $dI_e/d\phi$ up to electron saturation should be approximately 0 for the entire ion saturation region since negligible electron current is collected and then from Equation 3.12 it should become exponential after V_f up to V_p and $I_{e_{sat}}$. The lower left plot in Figure 3.9 shows this to be accurate except close to V_p, which is clearly no longer exponentially increasing. Very near the plasma potential the I-V curve does not follow the simple, collisioinless, thin-sheath model. A consistent and robust method for setting the lower bound of points to select for the T_e calculation is when $dI_e/d\phi$ rises above some constant threshold value, which should be somewhat close to V_f. Subsequently, select a certain fraction of points between that threshold value and V_p starting with the threshold value. This will ensure that no points are selected near the gentle transition region to electron saturation near V_p. An example of this threshold value is shown in the lower-left plot of

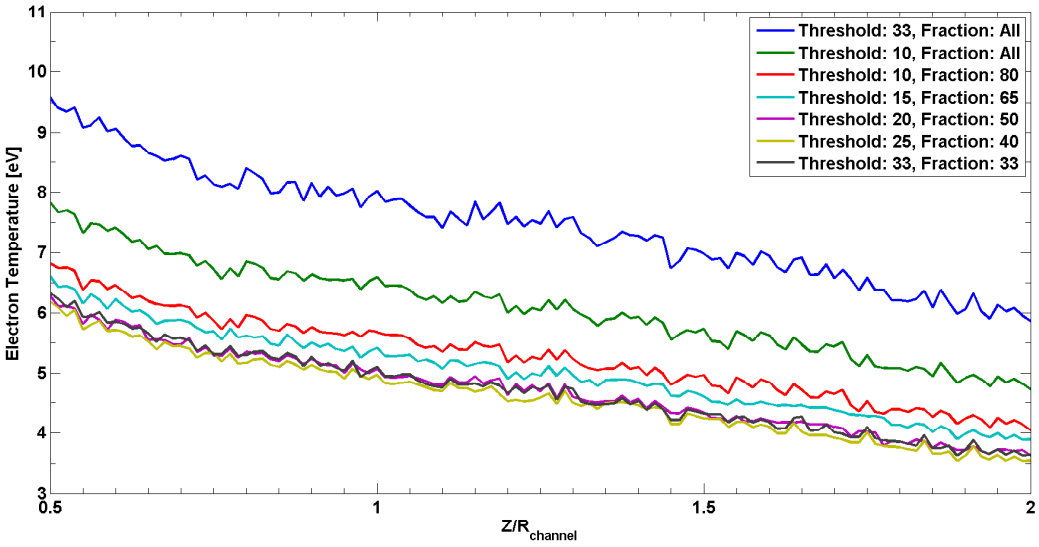

Figure 3.8: Parametric variation of the threshold value and fraction of points used in calculating T_e for the time-averaged results at $R/R_{ch} = 1$ and a range Z/R_{ch} from 0.5 to 2.

Figure 3.9. To illustrate this concept, consider a single I-V sweep with 50 datum points between V_f and V_p. Using a threshold value of 25% and an inclusion fraction of 40%, 15 of those points would be used to fit a straight line whose slope yields the electron temperature.

A parametric study was conducted by varying the threshold value (percentage of $dI_e/d\phi|_{peak}$ to begin selecting points) and the fraction of points to select between that threshold value and V_p as shown in the time-averaged results of Figure 3.8. The results were insensitive (T_e varying by less than ~ 0.1 eV) to the threshold value as long as it was 15-33% of $dI_e/d\phi|_{peak}$, which according to (7) should be $\sim 1-2\ T_e$ above V_f. Selecting a fraction of points between the threshold value and V_p was insensitive until the fraction was large enough (75-100%) to include the electron saturation transition. This caused the electron temperature to be artificially increased as seen in Figure 3.8 by decreasing the slope of the fitted line. In fact, the values for threshold 20/fraction 50, threshold 25/fraction 40 and threshold 33/fraction 33 all lie on top of one another. Therefore, a threshold value of 25% $dI_e/d\phi|_{peak}$ was the start and 40% of the $\ln(I_e)$ points from there towards V_p were selected to conduct a linear fit to determine T_e with an example shown in the upper-right of Figure 3.9.

3.4.6.5 Quality Control

Figure 3.9 shows a typical I-V trace and resulting analysis. The $dI_e/d\phi|_{peak}$ is well defined and is clearly below the peak probe bias which ensures electron saturation is achieved. Also shown is the linear fit to the selected electron retarding region to calculate electron temperature. The validity

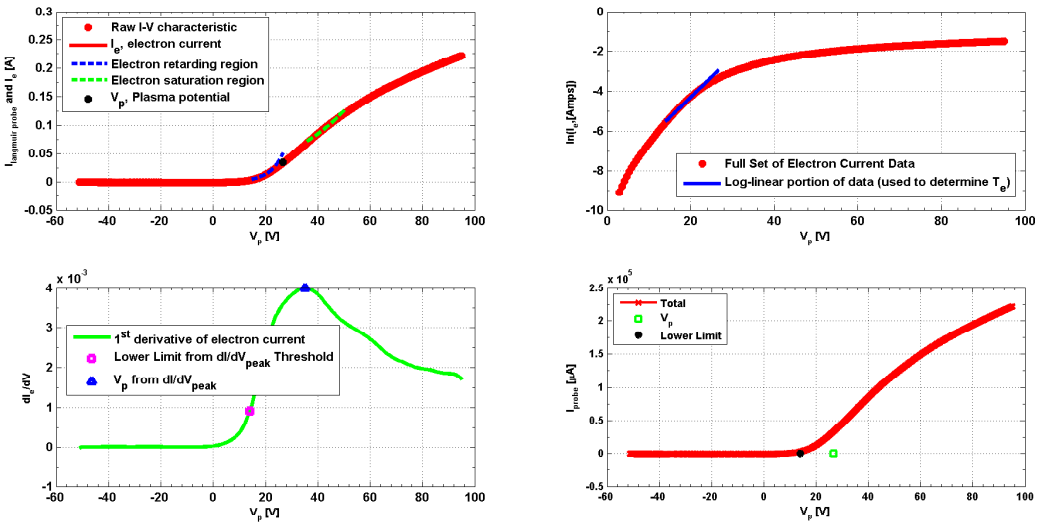

Figure 3.9: Example I-V analysis at $R/R_{ch} = Z/R_{ch} = 1$ showing the I-V trace, the natural log of electron current and the linear fit for T_e calculation, and $dI_e/d\phi$ with the peak identified for V_p and $I_{e_{sat}}$.

of results from automated data processing can be questionable without adequate quality controls in place to build confidence. In order to maximize the reliability of results from automated data processing, automatic reject criteria were developed for each I-V trace:

1. If $R_P \leq \lambda_D$ then the probe was no longer in thin sheath regime.
2. If the potential for the $dI_e/d\phi$ peak was within the last 10% of the I-V sweep, then the probe bias may not have reached plasma potential and entered electron saturation.
3. If the R^2 value for the linear fit to $\ln(I_e)$ versus ϕ was less than 0.990, then the electron energy distribution may not have been Maxwellian or the data contained noise.

Finally, a manual auditing process was also used whereby traces were selected at random or odd features were examined on a trace-by-trace basis to determine regions of rejected data. An entire radial shot was rejected if the ISR current was of the wrong sign, which most likely resulted from experimental setup and operator error where the ISR bias was not applied. Additional entire radial shot rejection criteria were plasma properties not conforming to adjacent radial shots. These situations only occurred in 4 out of 61 shots.

3.4.6.6 Uncertainty Analysis

A critical component of any experimental investigation is an uncertainty analysis of measurement accuracy (error with respect to true value) and precision (error in repeatability). While Langmuir probe measurements are not renowned for their accuracy, the measurements presented here appear precise as demonstrated in the time-resolved plasma properties of Figure B.3. If the oscillations were entirely due to inaccurate measurements, then the points would simply oscillate approximately every other point about the mean bouncing up and down. The time-resolved data shows the properties appear to have a sinusoidal nature with three to four points together above or below the mean before transitioning. As shown in Figure B.3, the electron temperature and the plasma potential oscillate by less than 2 eV and 4 V, respectively. If the uncertainty on the measurements were conservatively estimated to be 1 eV and 3 V, which are reasonable values for Langmuir probe measurements, then the time-resolved data would be rendered nearly meaningless. Therefore it is important to distinguish the uncertainty in the mean values (time-averaged) and uncertainty in the oscillatory values (time-resolved).

During development of the HDLP [5], Lobbia included a detailed discussion and analysis of error. Comparative measurements were made of averaged results from rapidly swept probes (100 kHz) to slowly swept probes (100 Hz) with a difference in measured plasma properties of approximately 23%. Error analysis of the thin sheath relations yielded approximate errors of $\partial n_e/n_e \approx \partial T_e/T_e \approx$ 10-20% and $\partial V_p/V_p \approx$ 10-40%; however, these are dependent on the local plume conditions tested in Ref. 5. This represents the error in time-resolved values to time-averaged values (error in oscillatory values to the mean). As noted in the numerous Langmuir probe theory reviews [116–123], interpretation of I-V traces to plasma properties is difficult and error prone. Sheath limited electrostatic probe theory has an error on the order of 50% [5] with electron density possibly in error by a factor of 2 or 3 [127]. Based on the preceding discussion, the uncertainty in time-resolved, oscillatory plasmas value to the local mean value will be assumed as 25% and the uncertainty in time-averaged, mean value of a plasma property to the true local value will be assumed as 50%.

3.5 High-speed Imaging Analysis (HIA)

A HIA technique was developed by McDonald [6, 78, 79, 100] to investigate azimuthal oscillations from videos. Here the McDonald technique has been adapted to transform the videos into measurements of discharge current density distribution in the discharge channel in order to quantify oscillations. These techniques will be referred to as HIA throughout the following discussion.

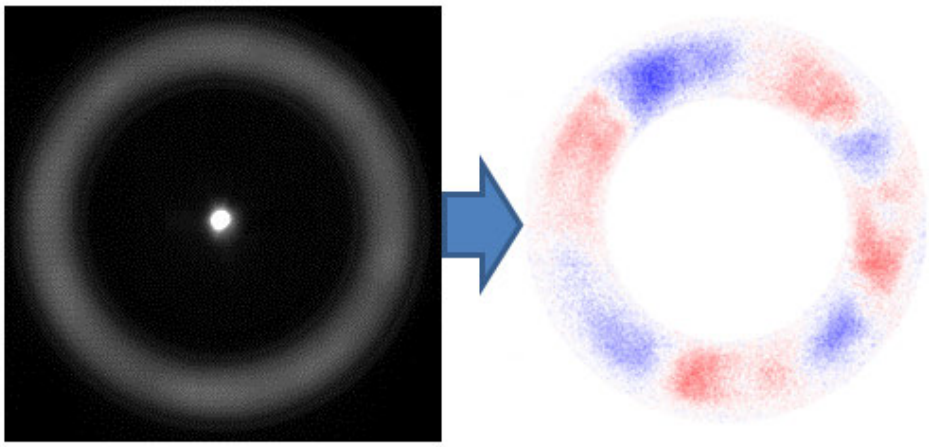

Figure 3.10: Raw FastCam video frame and subsequent enhancement with the McDonald technique to visualize spokes.

3.5.1 FastCam

High-speed imaging was acquired with a Photron SA5 FASTCAM with a Nikon ED AF Nikkor 80-200 mm lens at its maximum aperture f/2.8. The SA5 is capable of up to 1,000,000 fps with 12816 pixel resolution, but was used at 87,500 fps with 256×256 pixel resolution for this testing. The camera was 6 m downstream from the thruster outside LVTF with a view of the thruster through a viewport. The image enhancement technique developed by McDonald [79] allows for easy visualization of rotating spokes as shown in Figure 3.10. When watching the raw FastCam video the rotating spokes are very clear to the casual observer; the visualization technique shown in Figure 3.10 is only meant to enhance what is unambiguously present. Here small fluctuations in light intensity from a mean value can be seen and have been shown to rotate in the $E \times B$ direction as azimuthally propagating spokes. It is important to note that the pixel value corresponding to light intensity is not a direct measure of plasma properties. However, if light is assumed to be produced primarily by collisional processes or spontaneous emission then the brightness should be related to collision rates and densities as will be discussed later. Also important is that the camera records an integrated light intensity through the plume to the anode, meaning it cannot distinguish where the brightest regions of the plume are located axially.

3.5.2 HIA Processing Steps

The Fourier analysis techniques developed by McDonald [78, 100] have been adapted to process the FastCam videos to determine breathing and spoke mode frequencies. The high-speed imaging technique consists of the following eight steps:

1. Import the raw video file into MatLab as a $p(x,y,t) = 256 \times 256 \times N_f$ matrix, where N_f is the number of frames in the video. The Photorn SA5 has a 12-bit sensor, so each pixel, p, has $2^{12} = 4096$ possible values assumed to linearly represent light intensity. McDonald notes that raw pixel output is non-linear at high incident fluxes to the camera, but by design the "high frame rates used [imaging HETs] are sufficient to keep the light intensity reaching the camera well inside the linear regime." [78] The cathode region saturates and becomes non-linear, but that is not used in this analysis so it is negligible. The light from the discharge channel critical for this analysis remains within the linear region of pixel output and the assumption is justified as discussed in Ref. 100.

2. Calculate and subtract the mean image $\bar{p}(x,y)$ from each frame in order to isolate the AC component of the video $\tilde{p}(x,y,t) = p(x,y,t) - \bar{p}(x,y)$. The mean image is a 256×256 matrix where each pixel has been averaged across all N_f frames. Subtracting the mean image to isolate the AC component removes any DC bias for pixel values and is discussed in more detail at the end of this section with an example shown in Figure 3.13.

3. Automatically identify the center of the circular discharge channel using a Taubin circle fit [100] and isolate the annular region of the discharge channel in each frame.

4. Convert the pixels into cylindrical coordinates $\tilde{p}(x,y,t) \rightarrow \tilde{p}(r,\theta,t)$, divide the annulus into $N_b = 180$ two-degree bins, b, and determine which pixels from the 256×256 array belong to each bin. The number of pixels per bin, M_b, is $120 \leq M_b \leq 160$.

5. Average the pixel value for each bin to generate a 180×1 vector of light intensity values for each frame.

$$a(b,t) = \frac{\sum_{r=r_i}^{r_o} \sum_{\theta=\theta_b}^{\theta_{b+1}} \tilde{p}(r,\theta,t)}{M_b} \tag{3.16}$$

6. Calculate the $m = 0$ or m_0 spoke order, which is the entire channel added together.

$$m_0(t) = \sum_{b=1}^{N_b} a(b,t) \tag{3.17}$$

7. The discharge current is linearly related to the $m_0(t)$ spoke order as first shown by Lobbia [128] and will also be shown later in Figure 4.8. The discharge current sampled at 1 MHz or higher is down-sampled to the camera frame rate of 87.5 kHz using an 8^{th} order Chebyshev Type 1 filter to smooth and resample. Apply a linear, least squared fit to relate I_D to m_0, where c_1 and c_2 are the resulting linear coefficients. Note, the total discharge current $I_D(t)$

can be written as the sum of the discharge current through each bin, $I_{D_b}(t)$. Assuming the offset coefficient, c_2, can be equally distributed amongst the bins allows it to be included in the summation. The discharge current can then be written as

$$I_D(t) = \sum_{b=1}^{N_b} I_{D_b}(b,t) = c_1 m_0(t) + c_2 = \sum_{b=1}^{N_b} \left(c_1 a(b,t) + \frac{c_2}{N_b} \right) \tag{3.18}$$

Assuming that local light intensity is linearly related to local discharge current, each element of the summation in Equation 3.18 can be equated. The local discharge current density j_{D_b} for bin b is then

$$j_{D_b}(b,t) = \frac{I_{D_b}(b,t)}{A_b} = \frac{c_1}{A_b} a(b,t) + \frac{c_2}{A_b N_b} \tag{3.19}$$

While the linear relation in Equation 3.18 between the global variables I_D and m_0 are well supported in the results, the assumption of a linear relation between local light intensity and local discharge current at present only has indirect support. The discharge current density surface is a $180 \times N_f$ matrix for the angular discharge current density over time as shown in Figure 3.13(c) and discussed in more detail below with uncertainty analysis.

8. Perform a 2-D Discrete Fourier Transform (DFT) on the discharge current density surface to compute frequency and order number. The magnitude of the 2-D DFT generates a PSD surface map of frequency (1/s) versus 1/deg or 1/rad using Equation 3.41 as discussed below. The angular location is converted to spoke order, m, which are the number of spokes present in the channel.

The light observed by the FastCam is integrated through the plume and through the discharge channel to the anode at the back of the discharge channel. Photographs from angles nearly orthogonal to thruster centerline (e.g. Figure 4.24 and Figure 4.25 in Chapter 4.7) show the plasma in the discharge channel is significantly brighter than the plume. Even though the path length through the plume is longer than the path length through the discharge channel, the brighter discharge channel generates most of the light recorded by the FastCam. The camera is vertically level with the thruster and offset horizontally with an angle of 2.5° to the left of thruster centerline and has a more direct view of the 6 to 12 o'clock side of the channel. Even though the view of the discharge channel 3 o'clock region will be integrated through more of the plume, part of the discharge channel will be masked and could appear dimmer to the camera. The inner channel wall and near-anode region within ~ 2 mm of the thruster inner diameter will be blocked from the camera at 3 o'clock, which is less than 3% of the discharge channel radial-axial cross-section. However, light producing collisions and plasma oscillations are not expected to be significant in these masked areas compared to the discharge channel exit plane where the bulk of ionization and other collisional processes occur.

Isolating the AC component of pixel value as in Step 2 will remove any constant pixel brightness differences that may occur due to these offset or other factors.

The spoke surface is discussed in detail in Section 3.5.5 where examples are shown in Figure 3.13. Figure 3.13(a) shows an example plot of average pixel value per bin, $a(b,t)$ from Equation 3.16, that would be produced in Step 5 without executing Step 2 to isolate the AC component. Figure 3.13(b) shows the average pixel value per bin when all steps are executed and very little difference is observed with Figure 3.13(a) other than scale change. Figure 3.13(c) shows an example current density plot that is produced in Step 7, which also retains all of the same features as Figure 3.13(a) and (b) with only a scale change. It is important to note that the calculation of discharge current density does not alter the features of the Spoke Surface plots that McDonald originally developed during his analysis so those techniques for calculating PSDs remain valid and comparable.

3.5.3 Local Discharge Current to Local Light Intensity

The assumption in Section 3.5.2 that local light intensity is linearly related to local discharge current density to allow Equation 3.19 from 3.18 will be justified in three different ways:

1. Segmented anode experiment from McDonald [78] comparing local discharge currents to HIA;

2. Linearized fluid analysis and optical emission theory to relate discharge current density to particle density to light intensity; and

3. Hybrid direct kinetic simulations from Hara [34] that include an excited neutral state and light emission from de-excitation.

3.5.3.1 Segmented Anode

The most direct evidence for the assumption that local light intensity is linearly related to local discharge current density would be a direct, linear correlation between FastCam images and local discharge current measurements from a segmented anode. McDonald [78] conducted an investigation using a 12-segment anode in the H6 and used the same Photron SA5 FastCam where he concluded that "visible rotating spokes detected via high speed camera correspond to azimuthally localized electron current deposition to the anode." Unfortunately, the experiment experienced technical difficulties with electrical isolation, thermal control and sense circuits, so the experiment did not allow for the desired level of correlation.

Figure 3.11 reproduces two important figures from Ref. 78. Figure 3.11(a) shows HIA PSD from the segmented anode experiment exhibiting the broad breathing mode at ~ 10 kHz and spoke

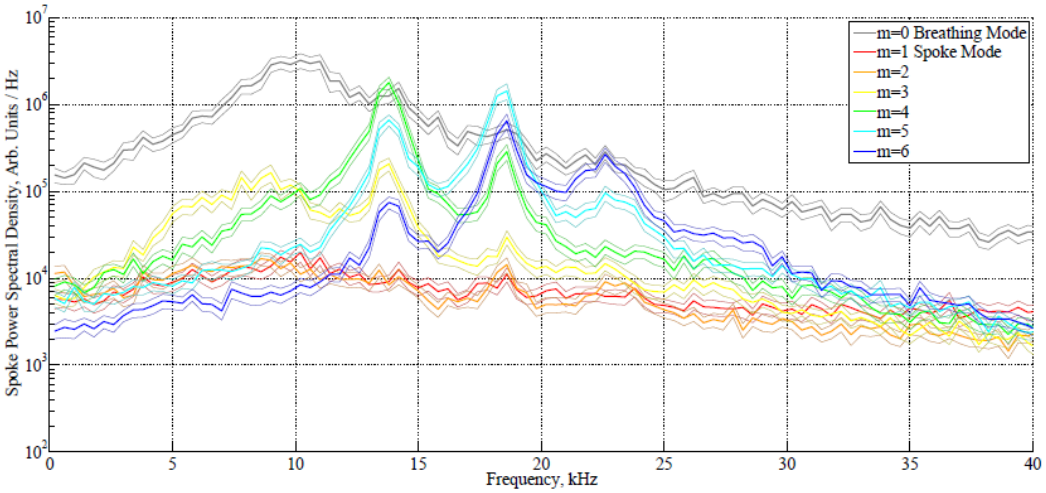

(a) HIA PSD from reproduced from Figure 12 of Ref. 78.

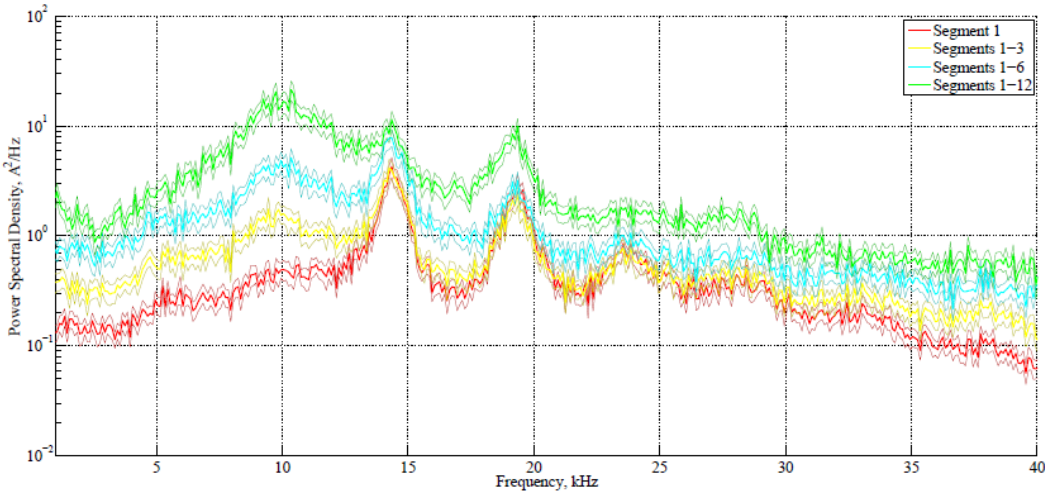

(b) Discharge current PSDs from anode segments reproduced from Figure 13 of Ref. 78.

Figure 3.11: H6 segmented anode PSDs from HIA and segment discharge currents.

orders $m = 4$ at 14 kHz, $m = 5$ at 18 kHz and $m = 6$ at 23 kHz. Figure 3.11(b) shows the PSDs from an individual segment (red), three segments added together (yellow), six segments (blue), and eventually all of the segments (green) which is the total discharge current. The single segment PSD shows strong peaks at 14, 18 and 23 kHz matching the HIA PSD in Figure 3.11(a). In contrast, all of the segments added together show the same shape as the breathing mode, because the individual segment current oscillations constructively and destructively interfere. This indicates the anode segments are observing local current oscillations that are not present in the global discharge, but are observed as azimuthal oscillations with the FastCam.

Figure 9 from Ref. 78 shows the time history of discharge current signals from three segments where the time delay between signals of adjacent segments is interpreted to be the result of passing

spokes. The time delay between signals can be estimated as approximately ~ 0.05 ms to travel 3 segments which corresponds to 1/6 - 1/4 of the discharge channel circumference. This yields a very reasonable spoke velocity between 1700 and 2500 m/s.

While not direct evidence that local light intensity is linearly related to local discharge current, matching PSDs and discharge current peaks moving from segment to segment like spokes provides evidence that the local discharge current oscillations are related to azimuthal light fluctuations in the discharge channel. Repeating this experiment with improved electrical isolation, thermal control and electronics is recommended in Section 7.2.4.

3.5.3.2 Linearized fluid analysis and optical emission theory

This method will show that oscillations in light intensity, L, are approximately linearly related to oscillations in electron and neutral density in the discharge channel, which are approximately linearly related to oscillations in discharge current density

$$\widetilde{j_D} \propto \widetilde{n_e}, \widetilde{n_n} \propto \widetilde{L} \tag{3.20}$$

noting that the tilde indicates an oscillatory component of a quantity and the bar indicates the steady-state value.

The first step will correlate downstream density in the plume to light in the discharge channel. In a study using a Busek BHT-600 thruster, Lobbia [128] correlated high-speed imaging results with downstream high-speed Langmuir probe measurements of electron density, plasma potential and electron temperature. This analysis showed total light intensity for the portion of the discharge channel imaged with a Photron FastCam-1024-PCI (only ~ 50% of the discharge channel is imaged) at 109,500 fps was correlated to discharge current and electron density oscillations downstream using linear, frequency domain transfer functions. In processing the FastCam images, Lobbia used an integrated, normalized image intensity which effectively gives the $m = 0$ order described here. The correlation was observed at the strong 18.4 kHz breathing mode and no attempt was made to analyze azimuthal variations although they were qualitatively noted. The location of the probes was varied from 3 to 11 thruster diameters downstream with a linear relation shown throughout.

In Section 4.5, Figures 4.13, 4.14, and 4.20 will all show that downstream probes measuring density are strongly correlated to the discharge current in global mode. More importantly, in Section 4.6, Figures 4.21 and 4.22 will both show that the downstream probes measure density oscillations that are linearly correlated to the light oscillations from passing spokes in the discharge channel that is immediately upstream from the probes. Although very conclusive, these examples only show that light in the discharge channel is linearly related to plume density, not the density

inside the discharge channel. The assumption can be made that the increased electron and ion density are produced in the discharge channel which then propagates axially downstream, so the light intensity correlates to electron density oscillations in the channel. This assumption makes physical sense as Lobbia [128] noted that in the discharge channel the "unsteady emission of photons generated by increased atomic state transitions [are] associated with the bursts of ionization."

Having made the reasonable assumption that light intensity fluctuations are linearly correlated to density oscillations in the channel, an argument can be made that oscillations in local discharge current density, j, are linearly related to electron density n_e and neutral density n_n fluctuations to first order with a common relation

$$j_D = -qn_e \mathrm{v}_z \tag{3.21}$$

where v_z is an effective cross-magnetic field, axially directed, electron velocity. This makes the reasonable assumption that discharge current is mostly ($\gtrsim 90\%$) composed of electron current to the anode. [11] However, v_z is a complicated and unknown function of density, magnetic field and other parameters. Indeed, researchers have been attempting to understand cross-field electron transport since the inception of HETs and have various explanations including, but not exclusive to: classical cross-field diffusion, Bohm diffusion, turbulence, shearing, [45] near-wall conductivity [1] and azimuthal electric fields. [46,47] Linearizing Equation 3.21 with mean (bar) and oscillatory values (tilde) and neglecting second order terms the local discharge current density can be written as

$$j_D = \bar{j}_D + \widetilde{j}_D = -q\bar{n}_e\bar{\mathrm{v}}_z - q\bar{n}_e\widetilde{\mathrm{v}}_z - q\widetilde{n}_e\bar{\mathrm{v}}_z \tag{3.22}$$

In order to justify the assumption that $\widetilde{j}_D \sim \widetilde{n}_e, \widetilde{n}_n$ to first order, Equation 3.22 shows that $\widetilde{\mathrm{v}}_z$ must also be linearly related to $\widetilde{n}_e$ and $\widetilde{n}_n$ to first order.

The axial velocity Equation 2.34 derived in Section 2.3.5 can be written as

$$\mathrm{v}_z = -\frac{q}{m_e}\frac{\nu_{ef}}{\nu_{ef}^2+\omega_c^2}\left(E_z + \frac{dT_e}{dz}\right) - \frac{qT_e}{m_e}\frac{\nu_{ef}}{\nu_{ef}^2+\omega_c^2}\frac{d}{dz}\ln(n_e) \tag{3.23}$$

where it has been noted that $1/n_e dn_e/dz = d/dz \ln(n_e)$. The effective collision frequency, ν_{ef}, can be broken down into electron-neutral collisions, electron-ion collisions, wall collisions and turbulence as discussed in Ref. 3. However, for this first order derivation only electron-neutral and electron-ion collisions will be considered. The generalized collision frequency for electrons with neutrals is [123]

$$\nu_{e-n} = k_m n_n \tag{3.24}$$

where n_n is the neutral density and k_m is a rate coefficient that is generally a function of electron

temperature, but will be assumed as constant here. The collision frequency for electrons with +1 ions is [43]

$$\nu_{e-i} = \beta n_e \tag{3.25}$$

$$\beta = 2\times 10^{-12}\frac{\ln(\Lambda)}{T_e^{3/2}} \tag{3.26}$$

for T_e in eV, n_e in m^{-3} and noting $\ln(\Lambda) \cong 10$. Using Equations 3.24 and 3.25, the simplified effective collision frequency is

$$\nu_{ef} \cong k_m n_n + \beta n_e \tag{3.27}$$

Neglecting oscillations in electron temperature that change k_m and β, the effective collision frequency in Equation 3.27 can be linearized as

$$\nu_{ef} = \overline{\nu}_{ef} + \widetilde{\nu}_{ef} = k_m\overline{n}_n + k_m\widetilde{n}_N + \beta\overline{n}_e + \beta\widetilde{n}_e = \overline{\nu}_{ef} + k_m\widetilde{n}_N + \beta\widetilde{n}_e \tag{3.28}$$

Linearizing Equation 3.23 using Equation 3.28 and neglecting oscillations in electric field and electron temperature, the effective cross-field velocity is

$$\mathrm{v_z} = -\frac{q}{m_e}\left(E_z + \frac{dT_e}{dz}\right)\left(\frac{\overline{\nu}_{ef}}{\overline{\nu}_{ef}^2+\omega_c^2} + \frac{\beta\widetilde{n}_e}{\overline{\nu}_{ef}^2+\omega_c^2} + \frac{k_m\widetilde{n}_n}{\overline{\nu}_{ef}^2+\omega_c^2}\right) - \frac{qT_e}{m_e}\left(\frac{\overline{\nu}_{ef}}{\overline{\nu}_{ef}^2+\omega_c^2} + \frac{\beta\widetilde{n}_e}{\overline{\nu}_{ef}^2+\omega_c^2} + \frac{k_m\widetilde{n}_n}{\overline{\nu}_{ef}^2+\omega_c^2}\right)\left(\frac{1}{\overline{n}_e}\frac{d\widetilde{n}_e}{dz} - \frac{\widetilde{n}_e}{\overline{n}_e^2}\frac{d\overline{n}_e}{dz}\right) \tag{3.29}$$

where $d\widetilde{n}_e/dz$ has been neglected and the assumption of $\widetilde{n}_e/\overline{n}_e \ll 1$ has been used to justify a binomial expansion

$$\frac{d}{dz}\ln(\overline{n}_e + \widetilde{n}_e) \;\sim\; \frac{1}{\overline{n}_e}\left(1 - \frac{\widetilde{n}_e}{\overline{n}_e}\right)\frac{d\overline{n}_e}{dz} \tag{3.30}$$

Additional assumptions in Equation 3.29 while expanding the denominator include neglecting second order terms and assuming the oscillatory component in the denominator can be been neglected since $\overline{\nu}_{ef}^2 + \omega_c^2 \gg 2\overline{\nu}_{ef}\beta\widetilde{n}_e + 2\overline{\nu}_{ef}k_m\widetilde{n}_n$. The effective cross-field velocity $\mathrm{v_z}$ can now be written in the linearized form of steady $\overline{\mathrm{v}}_z$ and oscillatory $\widetilde{\mathrm{v}}_z$ components

$$\overline{\mathrm{v}}_z = -\frac{q}{m_e}\frac{\overline{\nu}_{ef}}{\overline{\nu}_{ef}^2+\omega_c^2}\left(E_z + \frac{dT_e}{dz}\right) - \frac{qT_e}{m_e}\frac{\overline{\nu}_{ef}}{\overline{\nu}_{ef}^2+\omega_c^2}\frac{1}{\overline{n}_e}\frac{d\overline{n}_e}{dz} \tag{3.31}$$

$$\widetilde{v}_z = -\frac{\widetilde{n}_e}{\overline{n}_e}\left[\frac{q}{m_e}\frac{\beta\overline{n}_e}{\overline{\nu}_{ef}^2+\omega_c^2}\left(E_z+\frac{dT_e}{dz}\right)+\frac{qT_e}{m_e}\frac{k_m\overline{n}_n}{\overline{\nu}_{ef}^2+\omega_c^2}\frac{1}{\overline{n}_e}\frac{d\overline{n}_e}{dz}\right]- \\ \frac{\widetilde{n}_n}{\overline{n}_n}\left[\frac{q}{m_e}\frac{k_m\overline{n}_n}{\overline{\nu}_{ef}^2+\omega_c^2}\left(E_z+\frac{dT_e}{dz}\right)+\frac{qT_e}{m_e}\frac{k_m\overline{n}_n}{\overline{\nu}_{ef}^2+\omega_c^2}\frac{1}{\overline{n}_e}\frac{d\overline{n}_e}{dz}\right] \quad (3.32)$$

Equation 3.32 shows that given the lengthy list of assumptions and simplifications used above, the oscillatory component of the cross-field velocity is linearly related to electron and neutral density oscillations. Inserting Equations 3.31 and 3.32 in Equation 3.22 validates $\widetilde{j_D} \propto \widetilde{n}_e, \widetilde{n}_n$.

Variable	Value	Source
$\overline{n}_e$	2×10^{18} m^{-3}	Figure 7-10 for 20 mg/s from Ref. 44, assumed from $\overline{n}_i$ and quasi-neutrality
$\overline{n}_n$	2×10^{19} m^{-3}	Figure 3-12 from Ref. 44 (simulation)
E_z	40 V/mm	Figure 7-21 for 20 mg/s from Ref. 44
T_e	30 eV	Figure 7-14 for 20 mg/s from Ref. 44, Figure 15 from Ref. 37
$d\overline{n}_e/dz$	10^{20} m^{-3}/m	Figure 7-10 for 20 mg/s from Ref. 44, estimated from change in from $\overline{n}_i$ over $\sim L_{chnl}/2$. Positive (directed downstream) for $z < L_{chnl}$, negative (directed upstream) for $z > L_{chnl}$.
dT_e/dz	5 V/mm	Figure 15 from Ref. 37
k_m	2.5×10^{-13} m^3/s	From Ref. 33

Table 3.1: Sample H6 properties used to calculate cross-field current density.

In order to validate this approach, sample values for the H6 can be used to calculate steady state current density, j_D, by inserting Equations 3.31 and 3.32 in Equation 3.22 to ensure the correct order of magnitude is obtained. Table 3.1 contains representative discharge channel plasma properties for the H6. The calculated current density is 167 mA/cm^2 where 149 mA/cm^2 is from the axial electric field with electron mobility term and 18 mA/cm^2 is from the electron density gradient and temperature gradient terms. Although the signs of $d\overline{n}_e/dz$ and dT_e/dz are dependent on location ($d\overline{n}_e/dz > 0$ for $z < L_{chnl}$ and $d\overline{n}_e/dz < 0$ for $z > L_{chnl}$), the difference is not significant since the gradient terms are ~ 10% of the discharge current density. This result is the correct order of magnitude for discharge current density which is ~ 130 mA/cm^2 at nominal conditions. Assuming small oscillations in electron and neutral densities, $\widetilde{n}_e/\overline{n}_e \sim \widetilde{n}_n/\overline{n}_n \sim 0.10$, using Equations 3.31 and 3.32 in Equation 3.22 with the values in Table 3.1 yields an oscillation amplitude of ±17 mA/cm^2 which is ~ 10% of the mean value. A less conservative assumption of $\widetilde{n}_e/\overline{n}_e \sim \widetilde{n}_n/\overline{n}_n \sim 0.20$ yields ±34 mA/cm^2 or ~ 20% of the mean value. This simple model calculates the correct order of

magnitude steady-state current density and yields reasonable oscillation amplitude, so it supports the idea that oscillations in density are linearly related to discharge current oscillations.

For azimuthal electric fields, E_θ, the derivation of Yoshikawa [46] as discussed by McDonald [78] derived an analytical expression for the local current density due to $E_\theta \times B_r$ drifts

$$j(\theta) = \frac{e\pi}{4B} E_z \left(\widetilde{n}_e \sin(\theta) + \frac{\widetilde{n}_e^2}{\overline{n}_e} \sin^2(\theta) \right) \tag{3.33}$$

where the linearized density is $n_e = \overline{n}_e + \widetilde{n}_e \sin(\theta)$. Equation 3.33 also shows that local discharge current density is linearly related to $\widetilde{n}_e$ to first order after neglecting the second order $\widetilde{n}_e^2$ term. When integrating Equation 3.33 around the discharge channel from $0 \rightarrow 2\pi$ to calculate the average current density over the entire channel due to azimuthal electric fields, the $\sin(\theta)$ integrates out and the result is

$$\overline{j} = \frac{e\pi}{8} \frac{E_z}{B} \frac{\widetilde{n}^2}{\overline{n_e}} \tag{3.34}$$

Therefore the *average* discharge current density is related to the square of the oscillation amplitude for cross-field current due to azimuthal electric fields.

It is very important to note the derivation shown above and the relation from Yoshikawa are not meant to be all-inclusive models of electron transport in the discharge channel of a HET, which even far more sophisticated models cannot reproduce accurately. Also when considering near-wall conductivity, turbulence and shearing, the relation may not be linear between $\widetilde{v}_z$, $\widetilde{n}_e$ and $\widetilde{n}_n$. The sole purpose of this derivation and discussion is to reasonably justify the assumption that to first order the local discharge current density oscillations are linearly related to local density oscillations which are linearly related to light intensity oscillations in order to support the assumption used to derive Equation 3.19 from Equation 3.18.

Now consider the relation between optical emission (light) intensity and the physical processes occurring in the discharge channel. Plasma spectroscopy can be used to calculate neutral densities and electron densities [128] using a given plasma model (e.g. thermal equilibrium, coronal equilibrium, collisional-radiative, etc). Assume the plasma is in coronal equilibrium where all upward transitions in atomic energy state (excitations) are collisional and all downward transitions are radiative. Also assume the plasma is optically thin so all emitted photons escape the plasma and are not reabosrbed. [120] Finally, assume the time constant, τ, for this equilibrium is faster than the 10's kHz oscillations considered here so $\tau \ll 100\ \mu$s. In equilibrium, the emission of radiation from atoms or ions in an excited state will balance the collision frequency that produced the excited state. [120] This means light emission will be related to electron density, neutral density, ion density, and electron temperature. Ref. 123 shows that optical emission intensity due to excitation from ground state is linearly related to the free radical density and in Ref. 129 continuum emission

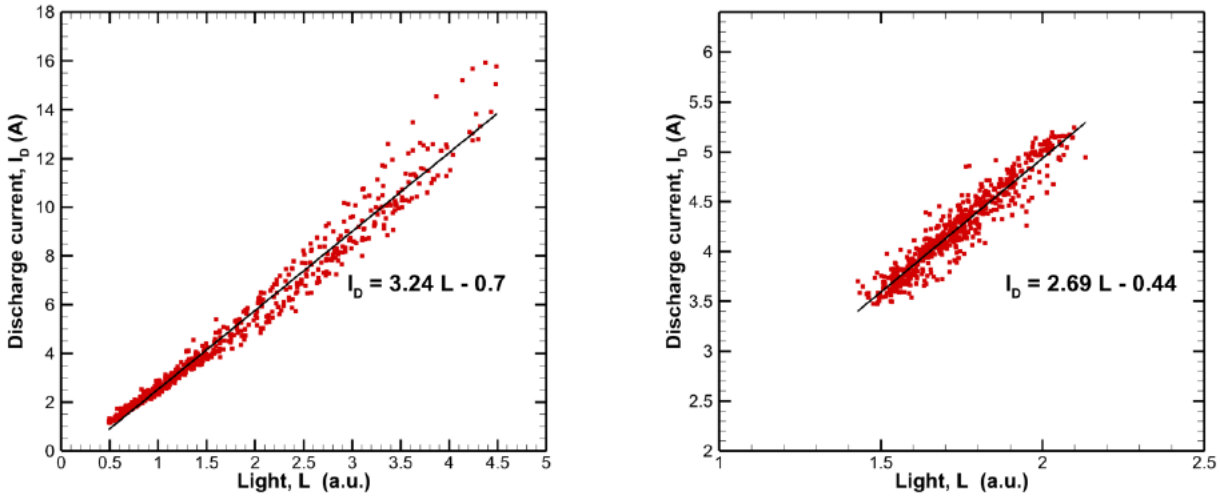

(a) Breathing mode: B = 120 G

(b) Stable mode: B = 180 G

Figure 3.12: Correlation between light intensity and discharge current in (a) breathing mode and (b) stable mode from simulations. Reproduced from Figure 10 of Ref. 34.

coefficients are linearly related to electron and ion densities. We assume that fluctuations in optical emissions are linearly related to oscillations in electron and neutral densities to first order. This assumption implies that the electron energy distribution is Maxwellian and remains constant during plasma oscillations. From this discussion the assumption can be reasonably made that $\widetilde{L} \propto \widetilde{n}_e, \widetilde{n}_n$.

In summary, the linear correlation of light intensity to downstream density is conclusive as well as downstream density to discharge current in global mode. Reasonable assumptions and simple calculations support that local light intensity is correlated to density in the channel which is correlated to the local discharge current, thus supporting Equation 3.20.

3.5.3.3 Light Intensity from Simulation

The most direct support for the assumption that local light intensity is linearly related to local discharge current density is provided by a hybrid-direct kinetic simulation by Hara. [34] The model solves the kinetic equations to obtain the velocity distribution function and considers three heavy species, neutrals, electronically excited neutrals, and +1 ions while treating electrons as a fluid. The result is a time-resolved 1-D model of the plasma properties on channel centerline of an SPT-100. The work in Ref. 34 was inspired by the work presented here where the magnetic field strength was varied to initiate mode transition in the simulations which observed a breathing mode oscillation (global mode) and a stable mode (local mode).

By including electronically excited states, light is emitted each time an excited state decays back to the ground state. [34] These optical emissions are summed in the simulation to give the

total light intensity. Using a 1-D axial simulation to calculate total discharge current effectively calculates a local discharge current at one point in the thruster and integrates it over the discharge channel assuming axisymmetry and no radial dependence. Figure 9 from Ref. 34 shows the time history of the metastable density compared to the discharge current, which demonstrates a strong linear correlation. Figure 10 from Ref. 34 is reproduced in Figure 3.12 which quantifies the linear relationship between local light intensity (i.e. metastable density) and local discharge current. This supports the assumption made in Equation 3.19 in order to calculate discharge current density surface plots. While light intensity is linearly correlated to discharge current as seen in Figure 3.12, the correlation coefficient is different between the modes indicating the stable mode more efficiently generates excited states. [34]

3.5.4 Error Calculation

Three primary sources of uncertainty will be considered, other sources of uncertainty such as probe resolution, calibration uncertainty, model uncertainty and linearity of camera response are assumed to be of lower order. The three sources of error considered here are:

1. Standard deviation of pixel values in bin b from the mean pixel value, a. This will be different for each bin b and time t.

2. Error from the linear fit of $m_0(t)$ to $I_D(t)$, which will vary in time but be applied equally for each bin b.

3. Difference between $I_D(t)$ at the native sampling rate or full bandwidth of the current probe (whichever is lower) and $I_D(t)$ down-sampled to the camera frame rate. This will vary in time but also be applied equally for each bin b.

The total error in j_D is estimated as the sum of the three error sources considered above:

$$\sigma_{j_{D_b}}(b,t) = \sigma_{j_{D_b}1}(b,t) + \sigma_{j_{D_b}2}(t) + \sigma_{j_{D_b}3}(t) \tag{3.35}$$

The standard deviation for the pixel value in bin b is computed similar to how the average value is calculated in Equation 3.16.

$$\sigma_a(b,t) = \left[\frac{1}{M_b - 1} \sum_{r=r_i}^{r_o} \sum_{\theta=\theta_b}^{\theta_{b+1}} \left(\tilde{p}(r,\theta,t) - a(b,t)\right)^2 \right]^{1/2} \tag{3.36}$$

Using the error propagation equation [130] on Equation 3.19 yields

$$\sigma_{j_{D_b}1}(b,t) = \frac{\partial j_{D_b}}{\partial a}\sigma_a(b,t) = \frac{c_1}{A_b}\sigma_a(b,t) \tag{3.37}$$

where the error in c_1 and c_2 will be accounted for in $\sigma_{j_{D_b}2}$.

The error in linear fit between I_D and m_0 is estimated using built in MatLab functions (`polyfit` and `polyval`) while calculating the least-squared coefficients c_1 and c_2. The estimate of the standard deviation of the error at each point is calculated using the triangular factor of the Vandermonde matrix, the degrees of freedom and the norm of the residuals. [131] Assuming the error in measurements is independent with constant variance, the uncertainty estimates $\Delta I_D(t)$ will encompass 50% of predictions in I_D from m_0. The uncertainty $\sigma_{j_{D_b}2}$ introduced by the linear fit between I_D and m_0 is

$$\sigma_{j_{D_b}2}(t) = \frac{\Delta I_D(t)}{A_{chnl}}. \tag{3.38}$$

The discharge current I_D is filtered and down-sampled to correlate with m_0 as described in Step 7. It is then up-sampled using interpolation to calculate the difference with the original I_D. The difference is re-sampled at the camera frame rate without smoothing or filtering in order to determine the difference between the original and down-sampled discharge current. An example of this is shown later in Figure 4.8.

$$\sigma_{j_{D_b}3}(t) = \frac{\left|\{I_D(t)\} - \{I_D(t)\}_{DownSampled}\right|}{A_{chnl}} \tag{3.39}$$

For a mean discharge current of $\bar{I}_D = 20$ A the average discharge current density is $\bar{j}_D = 133$ mA/cm^2. An error of 1 A in discharge current for Equations 3.38 or 3.39 yields an uncertainty of 6.6 mA/cm^2 for $\sigma_{j_{D_b}2}$ or $\sigma_{j_{D_b}3}$. Regardless of the uncertainty introduced, the method outlined above provides meaningful quantification of FastCam images to discuss oscillation amplitudes during mode transitions.

3.5.5 Spoke Surface Plots

An example of a discharge current density surface plot calculated from Equation 3.19 is shown in Figure 3.13(c) with the uncertainty calculated from Equation 3.35 shown in Figure 3.13(d). In the discharge current density surface plot, the ordinate is azimuthal location around the discharge channel in clock positions and the abscissa is time with each vertical column of values representing one frame of video. Vertical features in the discharge current density surface plot represent extremes in discharge current density that occur everywhere in the channel simultaneously. Horizontal features would be discharge current values that remain constant at a fixed azimuthal location, which

is not typically observed because they are removed in Step 2. Diagonal features are perturbations in discharge current density that propagate azimuthally around the discharge channel. Lines from upper-left to lower-right are propagating counter-clockwise around the discharge channel and lines from the lower-left to upper-right are propagating clockwise. The $E \times B$ direction in the H6 is counter-clockwise since the B-field direction is radially out. It will be shown later that all azimuthally propagating features are in that direction represented by lines from upper-left to lower-right with the slope corresponding to propagation velocity in deg/s, which will be exploited to calculate the spoke velocities. While in global mode, the discharge current rises in approximately 20-40 μs as shown in Figure 4.13, but the FastCam frame rate of 87,500 fps yields a resolution of 11.4 μs which introduces error while matching m_0 and I_D in Equation 3.38. The surface plots of discharge current density (e.g. Figure 3.13(c)) have the same features and look identical to the spoke surface plots developed by McDonald [78] due to the linear scaling. However, the scaling adds physical units and is useful to investigate and visualize global discharge channel oscillations as well as azimuthally rotating spokes.

3.5.6 Power Spectral Density (PSD)

Several methods can be used to describe the frequency response of a signal, so here we define the methods and formulas used below. If $X(f)$ is the 1-D DFT of a time-series signal $x(t)$ with length N, then the periodogram spectral estimate $S_N(f)$ of the signal, [132] which is an estimate of the PSD without scaling, [132] is

$$PSD_{1D}(f) = S_{N1D}(f) = \frac{1}{N} X^*(f) \cdot X(f) \tag{3.40}$$

where $X^*(f)$ is the complex conjugate. A 2-D DFT of the discharge current density surface plot $j_{D_b}(t,\theta)$ produces $J_{D_b}(f,\gamma)$ where γ is in units of 1/deg. Fourier transforms can be extended to multiple dimensions, so by analogy to Equation 3.40 the 2-D PSD is

$$PSD_{2D}(f,\gamma) = S_{N2D} = \frac{1}{N_f N_b} J^*_{D_b}(f,\gamma) \cdot J_{D_b}(f,\gamma) \tag{3.41}$$

The analysis of PSDs below only compares the change in relative magnitude of the PSDs through mode transitions, so without proper scaling on Equations 3.40 and 3.41 the units will be listed as Arbitrary Units/Hz. In a 2-D Fourier transform of a surface where one axis is time and the other is angle (degrees), one axis of the transformed surface will be similar to a typical 1-D Fourier transform of a time history signal with units of f = 1/s or Hz and the other will yield γ = 1/deg. Multiplying γ by 360 deg/circle yields the spoke order m or number of segments per circle (e.g. m = 3 means three segments or three spokes). As described by McDonald in his original

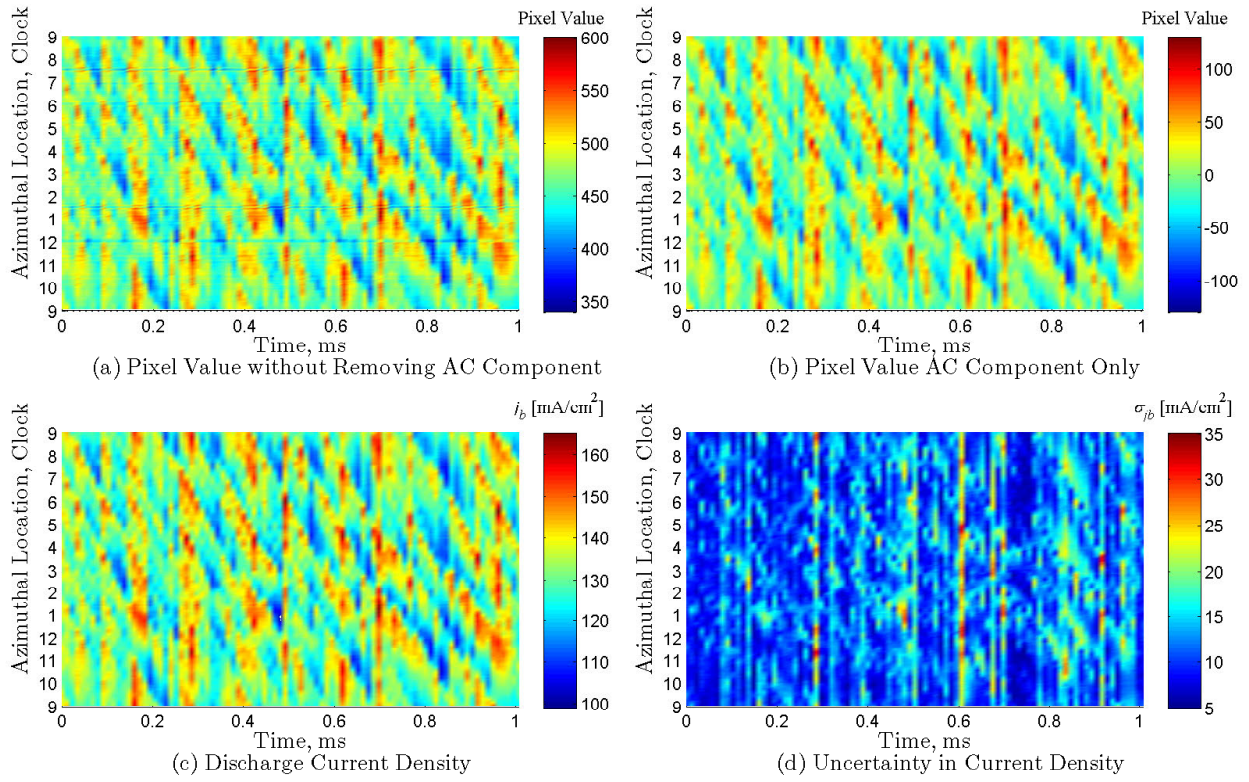

Figure 3.13: Surface plots for 300 V, 19.5 mg/s, $B_r/B_r^* = 1$. (a) Average pixel values from Equation 3.16 without executing Step 2 to isolate the AC component; note the horizontal lines present for some bins, (b) AC component of average pixel values calculated in Step 5; the pixel values oscillate about zeros but all features and amplitudes are retained from (a), (c) Discharge current density plot calculated in Step 7 from Equation 3.19 which retains all features of (c), (d) Uncertainty in discharge current density calculated from Equation 3.35.

derivation, m is analogous to number of wavelengths per channel circumference. [78] Hence $m = 0$ or m_0 is no wave in the channel (the entire channel is dark or bright), $m = 1$ means one wave in the channel (one half bright, the other dark), $m = 2$ is two waves per channel (two bright regions, two dark regions), $m = 3$ is three waves per channel (three bright regions, three dark regions), etc. In the literature m is often called the wave mode, but here it is called spoke order to avoid nomenclature confusion with the HET operational modes discussed later. The azimuthal wave number, k_θ, is calculated from the spoke order by $k_\theta = m/R_{ch}$. Equation 3.40 is used to calculate the PSDs for the AC components of discharge current and ISR probe current, which removes large values at $f = 0$ when there is a DC offset. When computing the 1-D DFT for I_D and I_{ISR} a Blackman window is used and when computing the 2-D DFT of j_D a Hamming window is used.

The 2-D Fourier transforms show the peak frequencies for each spoke order. Harmonics are noted at higher frequencies than the dominant frequency due to the Fourier decomposition when

the azimuthal bin intensity has a sharp edge that cannot be resolved as a single frequency. If a spoke order has a very strong peak, then other spoke orders often show smaller peaks at the same frequency, which are noted to be non-physical artifacts of the processing techniques. [100] As discussed by McDonald [100], the absolute peak values for HIA PSDs should only be compared within a given parameter study with the same experimental setup because the 2-D Fouier transform values are sensitive to camera CCD quantum sensitivity, lens aperture size, shutter speed or exposure time, vacuum chamber viewport optical quality, operating condition and other post-processing variables. In this investigation, all setup and processing parameters were held constant.

3.5.7 Upper Limit of Observations

Each spoke order represents the number of light and dark regions in the thruster so the wavelength is $\lambda = 2\pi R_{chnl}/m$. If the spoke travels 1/2 wavelength during the period of time the shutter is open, then the bright region will travel over the dark region rendering the spoke unobservable by the camera. Assuming the open period of the shutter is $\tau_s = 1/f_c$ where f_c is the camera frame rate, then the observable spoke velocity is

$$v_{sp} < \frac{\pi R_{chnl} f_c}{m} \tag{3.42}$$

For m = 3, 5, 7 and 9, Equation 3.42 yields maximum observable spoke velocities of 7300, 4400, 3100 and 2400 m/s, respectively. This is within all of the spoke velocities for each spoke order as shown in Figure 5.7; however, the highest spoke orders are close to the limit.

CHAPTER 4

Mode Transitions

"The most exciting phrase to hear in science, the one that heralds new discoveries, is not 'Eureka!' but 'That's funny...' "

– Isaac Asimov

4.1 Introduction

This chapter shows how the measurement tools and data analysis techniques described in Chapter 3 were used to analyze mode transitions induced in the H6 by varying magnetic field magnitude. Magnetic field sweeps, or B-field sweeps denoted by B_r/B_r^*, were conducted with all other parameters including discharge voltage, flow rate and chamber pressure, held constant until the thruster transitioned modes and eventually became unstable for low enough B-field values. For reasons that will be made clear and discussed in great detail, the B_r/B_r^* region of decreased discharge current mean and oscillation amplitude will be called local oscillation mode and the B_r/B_r^* region of increased discharge current mean and oscillation amplitude will be called global oscillation mode. Section 4.2 describes the test matrix of discharge voltages and flow rates investigated. Section 4.3 details how mode transitions are identified including quantitative metrics. Section 4.4 shows how mode transitions change the discharge current characteristics. The changes to plasma oscillations in the plume are discussed in Section 4.5 and Section 4.6 and the changes in visible plume structure are discussed in Section 4.7. Of critical importance, the thruster performance change through mode transition is shown in Section 4.8. The modes are formally defined in Section 4.9 and the impact of this investigation to thruster characterization testing is discussed in Section 4.10. A similar investigation was conducted with magnetically shielded thrusters (H6MS and NASA-300MS) and the results are discussed in Appendix C.

4.2 Test Matrix

Table 4.1 shows the test matrix for the H6 used in this investigation. Discharge voltages of 300, 400 and 450 V were applied between the anode and cathode. Propellant mass flow rates tested were 25.2, 19.5 and 14.7 mg/s through the anode and 1.8, 1.4 and 1.0 mg/s (7% CFF) through the LaB_6 cathode. The flow rate of 19.5 mg/s is the nominal setting used for comparison in this work and the cathode flow fraction of 7% was maintained for all conditions. Unless explicitly stated, all data shown below are for the centerline-mounted cathode configuration. The only data presented here for the external cathode configuration are for the nominal 300-V, 19.5-mg/s case.

	14.7 mg/s	19.5 mg/s	25.2 mg/s
300 V	1	4	2
400 V	0	2	0
450 V	0	1	0

Table 4.1: Test matrix showing discharge voltage and anode flow rate variations for the internal cathode configuration. Green: tested, Red: not tested. Number indicates the number of sweeps at the condition.

4.3 Identification of Mode Transitions

The transition point is identified starting from the strong global oscillation mode where the entire channel is oscillating in unison shown by vertical stripes in the spoke surface plot. The transition point, $B_r/B_r^*|_{trans}$, is qualitatively identified when the entire channel oscillations begin to break up, become irregular and spokes begin to form sporadically as shown in Figure 4.1 ($B_r/B_r^* = 0.58$ for (a) and $B_r/B_r^* = 0.67$ for (b)). The quantitative transition criteria from global mode to local mode are listed in Table 4.2.

In Table 4.2, $PSD_{m_{max}}$ is the peak PSD for any spoke order $m > 1$, PSD_{m_0} is the peak for $m = 0$ and $\bar{I}_{D_{min}}$ is the minimum discharge current during the sweep. The criteria of Table 4.2 are guidelines and not absolute cutoffs. The transition point is associated with the destabilization of global mode because typically that is the clearest to identify. This marks the lower limit of the transition region. The upper limit of the transition region where the spokes dominate and global oscillations are absent or negligible is not as easy to identify. The strong global oscillations begin to lose coherency at $B_r/B_r^*|_{trans}$, but the plasma oscillations are typically seen to alternate between global mode and local mode for $B_r/B_r^*|_{trans} \leq B_r/B_r^* \lesssim 1.1 B_r/B_r^*|_{trans}$. This is considered the transition region where the discharge channel displays both oscillatory modes.

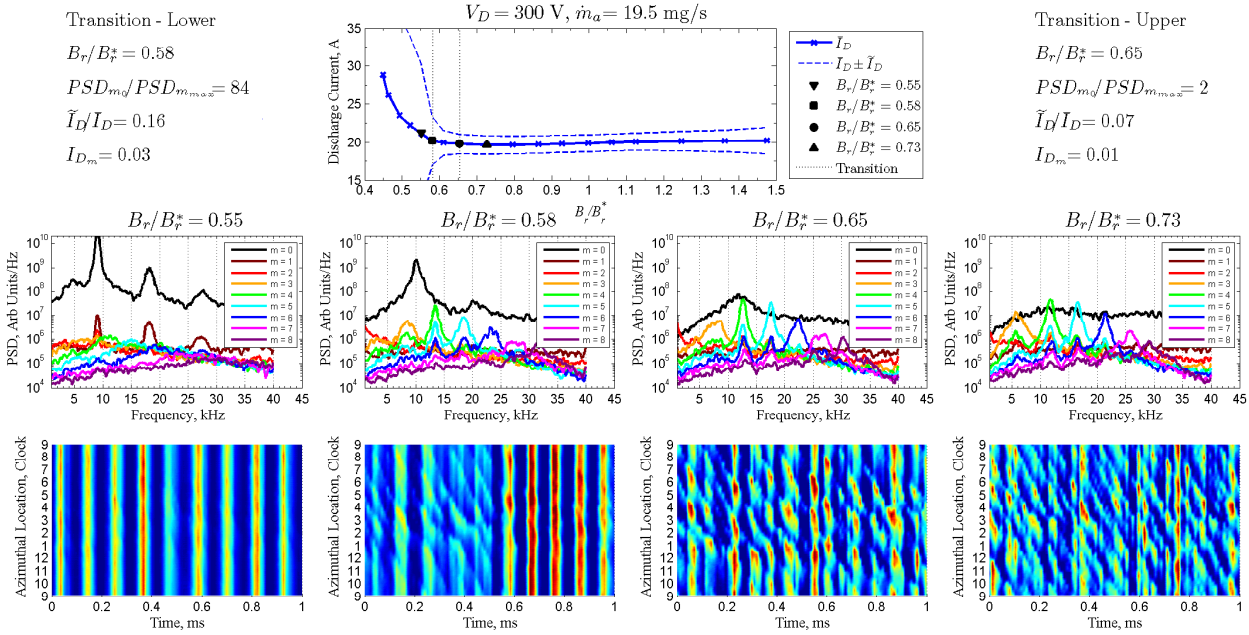

(a) Mode transition region for 300 V, 19.5 mg/s

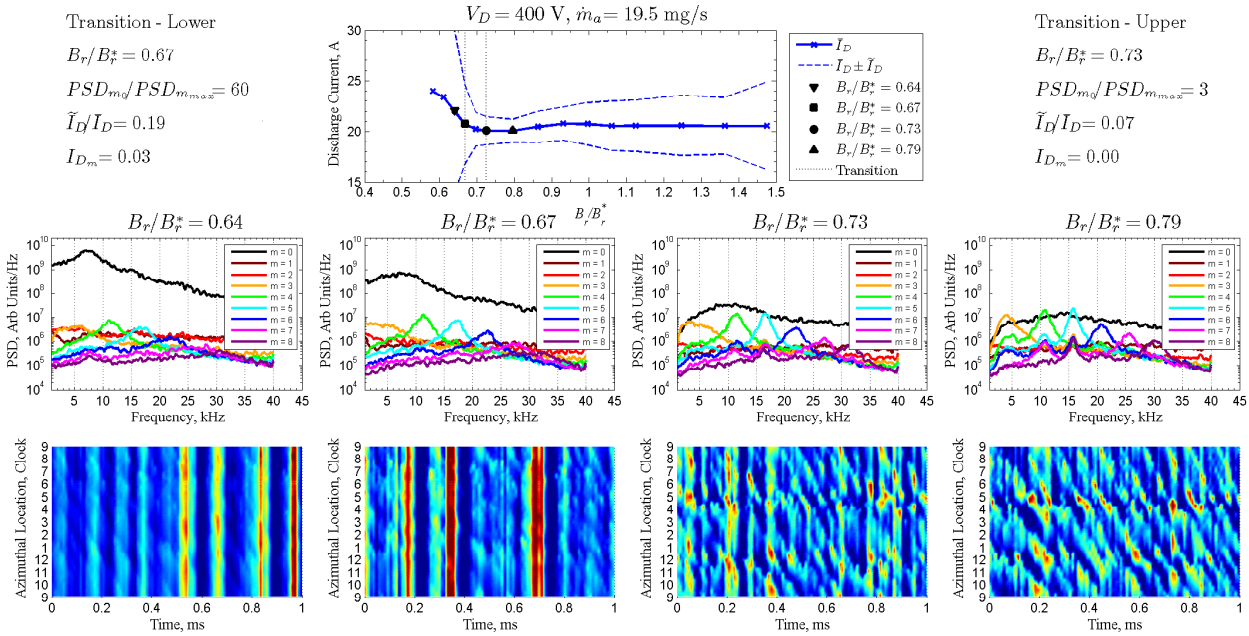

(b) Mode transition for 400 V, 19.5 mg/s

Figure 4.1: Example mode transition regions showing global mode($B_r/B_r^* = 0.55$ and 0.64), the initial breakup of global mode ($B_r/B_r^* = 0.58$ and 0.67), global mode intermixed with local mode ($B_r/B_r^* = 0.65$ and 0.73), and fully local mode ($B_r/B_r^* = 0.73$ and 0.79).

Criteria	Global Mode	Local Mode
$\frac{PSD_{m_0}}{PSD_{m_{max}}}$	$\gtrsim 50$	$\lesssim 10$
$\frac{\widetilde{I_D}}{\bar{I}_D}$	$\gtrsim 0.15$	$\lesssim 0.10$
$I_{D_m} = \frac{\bar{I}_D - \bar{I}_{D_{min}}}{I_{D_{min}}}$	$\gtrsim 0.02$	$\lesssim 0.02$

Table 4.2: Transition criteria between global and local oscillation mode based on HIA PSD and discharge current PSD.

Figure 4.1(a) and (b) shows example mode transition regions for 300 V and 400 V, respectively. The lowest setting, $B_r/B_r^* = 0.55$ and 0.64, shows global mode for both cases. The global channel oscillations are seen to begin breaking up and becoming more sporadic for $B_r/B_r^* = 0.58$ and 0.67. For $B_r/B_r^* = 0.65$ and 0.73 the diagonal lines indicate spoke propagation intermixed with entire channel oscillations. The thruster is fully in local mode with strong azimuthal spokes for $B_r/B_r^* = 0.73$ and 0.79.

4.4 Discharge Current Response to Mode Transition

4.4.1 Magnetic Field Sweeps

The magnetic field was varied by changing the inner and outer magnet coil currents in a constant ratio with all other parameters held constant including flow rates, discharge voltage, and chamber pressure. Maintaining a constant 1.12 ratio of inner to outer coil current allowed the magnetic field magnitude to be varied without significantly changing the shape shown in Figure 3.2; i.e. the B-field topology was nearly constant as discussed in Chapter 3.3.

Magnetic field sweeps were typically started from $B_r/B_r^*|_{max}$ and decreased until the thruster discharge was unstable as indicated by an uncontrolled increase or "run-away" discharge current as discussed in Section 4.4.3. However, a sweep at 300 V was conducted starting from $B_r/B_r^*|_{max}$ decreasing until thruster instability and then increased returning to $B_r/B_r^*|_{max}$ in order to demonstrate directionality independence and the absence of hysteresis. The thruster was operated for approximately 3-5 minutes at each B_r/B_r^* setting during a sweep. In order to ensure thermal equilibrium, the thruster was operated for a minimum of 3 hours before conducting B-field sweeps and when changing conditions (discharge voltage or flow rates) it was operated for 0.5 to 1 hour prior to sweeps. All flow rates at 300 V discharge voltage were repeated during different pump downs

where the thruster was exposed to atmosphere between tests. Tests were also repeated with and without the probes present in order to ensure the probes were not significantly altering the thruster operation.

Decreasing B_r/B_r^* below a certain threshold was shown to repeatedly induce a mode transition similar to those discussed in Chapter 2.4, where the mean discharge current increased and the discharge current amplitude increased. This was shown consistently for the three different voltages (300, 400 and 450 V) and three different flow rates (14.7, 19.5 and 25.2 mg/s) as shown in Figure 4.2 and Figure 4.3 where the plots of $\bar{I_D}$ and $\widetilde{I_D}/\bar{I_D}$ vs. B_r/B_r^* show two distinct regions with a transition line. The thruster is considered to be more sensitive to mode transitions if the transition $B_r/B_r^*|_{trans}$ occurs at higher B_r/B_r^* values. Because $B_r/B_r^*|_{max}$ is an upper limit due to thruster design, if the transition point occurs at higher B_r/B_r^* then the range of B-field values where the thruster operates in local mode is diminished. As was discussed in Section 4.3, defining a single transition value for the B-field is misleading because there is a transition region where the plasma exhibits both types of oscillations, however the transition typically occurred over only $\sim 10\%$ change in B_r/B_r^*. The transition line shown is where global oscillation behavior begins to dominate and the transition region typically extends from 0.9 $B_r/B_r^*|_{trans}$ to $B_r/B_r^*|_{trans}$. The estimated uncertainty in transition point is ± 0.1 A for I_{IM} which corresponds to ± 0.03 for $B_r/B_r^*|_{trans}$.

Figure 4.2 and Figure 4.3 show that increasing discharge voltage or flow rate makes the thruster more sensitive to mode transitions. The transition points from Figure 4.2 and Figure 4.3 have been summarized in Figure 4.4 in order to highlight the trends. Figure 4.2(a) and (b) show the discharge current mean and oscillation amplitude, respectively, for discharge voltages of 300, 400 and 450 V. The parenthetical numbers in the legend show the number of sweeps where the 300 V condition was repeated four times (one sweep was a continuous decreasing then increasing sweep and one sweep was with probes) and the 400 V condition was repeated twice (once with probes and once without). The different sweeps showed remarkable consistency with deviations less than 3% of the mean indicating the transitions were not caused by transient thruster properties such as out-gassing or thermal dis-equilibrium.

Figure 4.3 and Figure 4.4 show that increasing anode flow rate with a constant 7% CFF makes the thruster more sensitive to mode transitions. Figure 4.3(a) and (b) show the discharge current mean and oscillation amplitude, respectively, for anode flow rates of 14.7, 19.5 and 25.2 mg/s. Only 1 sweep at 14.7 mg/s is shown, although a second was conducted before all current sensors were calibrated and it yielded identical results. A second sweep at 25.2 mg/s was also conducted and not shown where the thruster was not operated at that flow rate for adequate time to reach thermal equilibrium, which caused a shift in mode transition. After adequate equilibrium time, the transition region stabilized. The higher discharge voltages of 400 V and 450 V in Figure 4.2 showed a steadily increasing oscillation amplitude as B_r/B_r^* was increased for $B_r/B_r^* \geq 1$, yet the

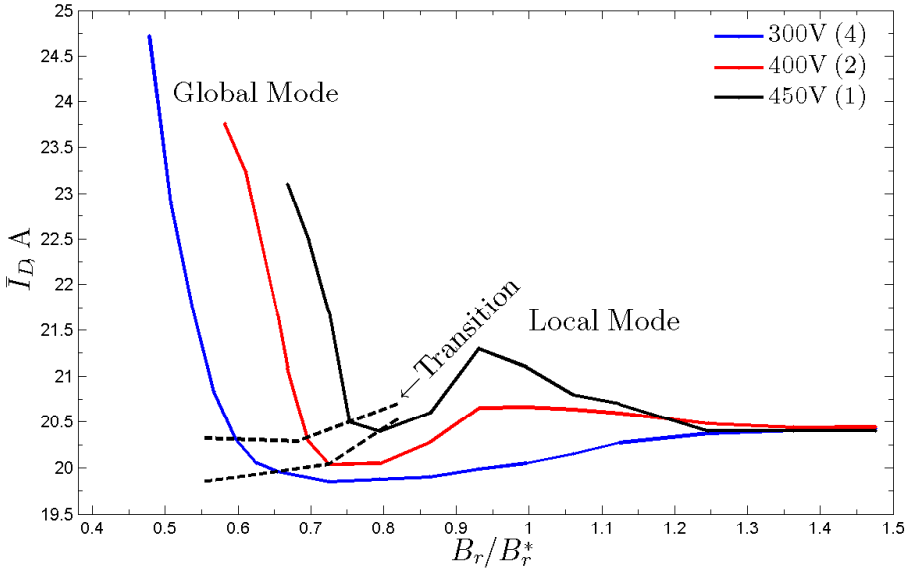

(a) Mean Discharge Current

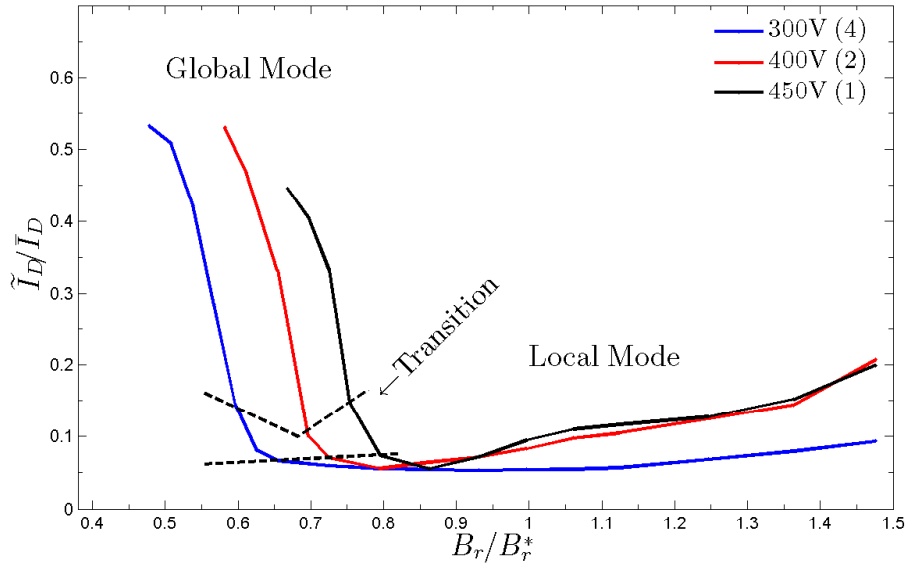

(b) Discharge Current Oscillation Amplitude

Figure 4.2: Discharge current mean (a) and oscillation amplitude (b) variation with constant 19.5 mg/s anode flow rate and variable discharge voltages of 300, 400 and 450 V. The upper and lower bounds for the transition region are shown. The number in parenthesis is the number of sweeps averaged together.

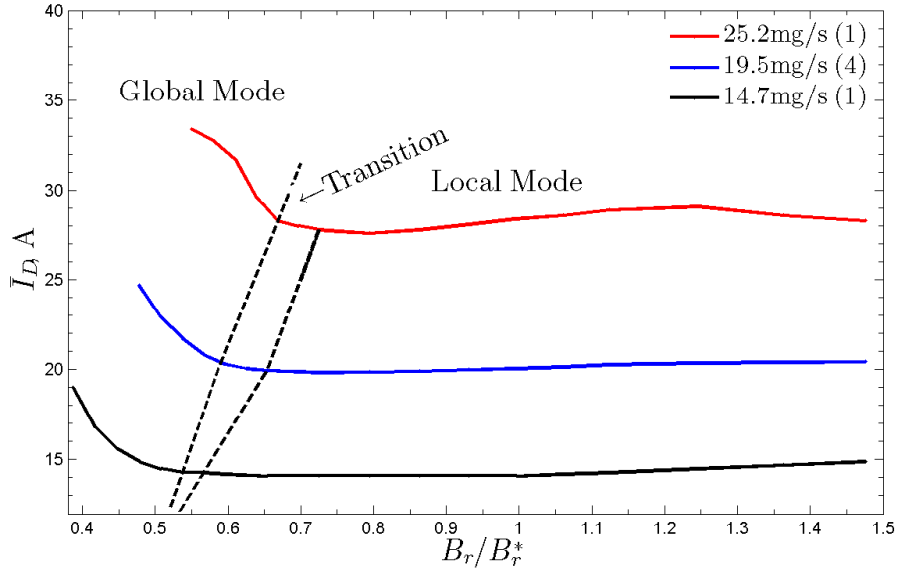

(a) Mean Discharge Current

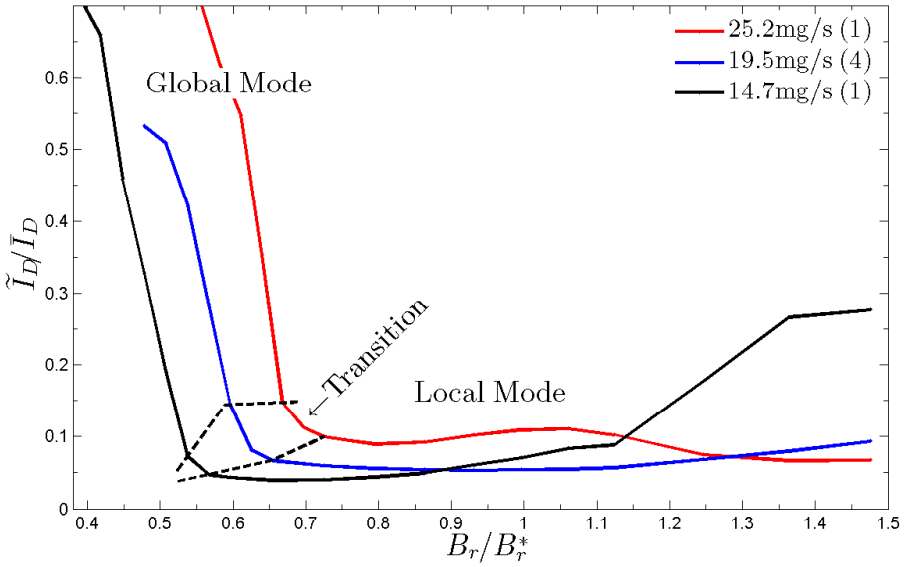

(b) Discharge Current Oscillation Amplitude

Figure 4.3: Discharge current mean (a) and oscillation amplitude (b) variation with constant 300 V discharge and variable anode flow rates of 25.2, 19.5 and 14.7 mg/s. The upper and lower bounds for the transition region are shown. The number in parenthesis is the number of sweeps averaged together.

mean discharge current remained the same. Additionally, the lowest flow rate case of 14.7 mg/s for 300 V showed significantly higher oscillation amplitude in Figure 4.3 for $B_r/B_r^* > 1.2$ than the other flow rates indicating a possible transition to an entirely different mode than the transition between global and local mode at $B_r/B_r^* = 0.53$.

4.4.2 Transition Point Characterization

Figures 4.2 and 4.3 show that mode transition occurs at higher magnetic field strength for increasing discharge voltage and mass flow rate. The lower limit of the transition region, $B_r/B_r^*|_{trans}^{lower}$ is plotted versus anode mass flow rate and discharge voltage in Figure 4.4. The lower transition point can be characterized as functions of discharge voltage and mass flow rate using linear and power approximations.

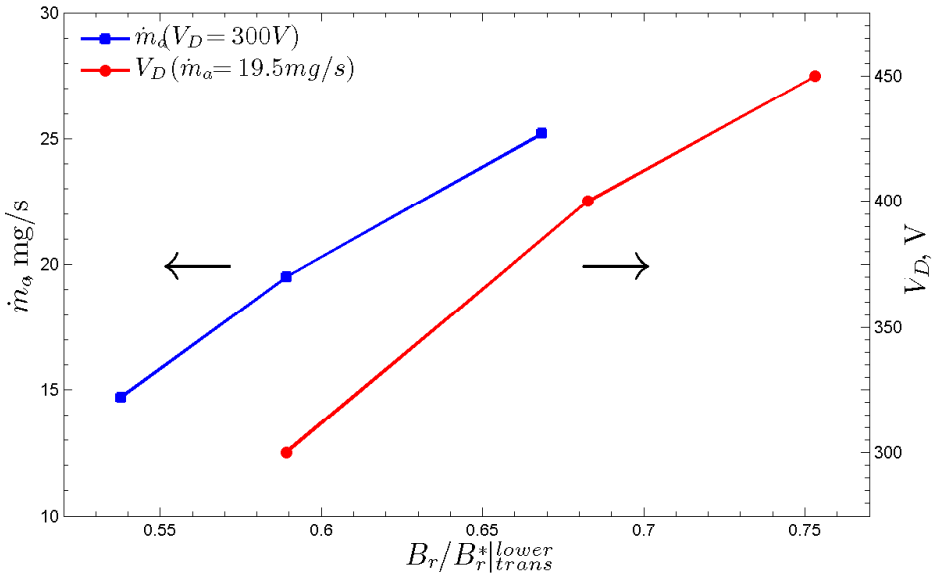

Figure 4.4: Mode transition point as a function of anode flow rate (left axis) at constant discharge voltage (300 V) and a function of discharge voltage (right axis) at constant anode flow rate (19.5 mg/s). The lower bound of the transition region is shown with an uncertainty in $B_r/B_r^*|_{trans}$ of ±0.03 The multiple sweeps for 300 V and 400 V have been averaged together.

For the linear approach, a least squares fit was performed between $B_r/B_r^*|_{trans}^{lower}$ and $(V_D/V_D^*)(\dot{m}_a/\dot{m}_a^*)$ where V_D^* = 300 V and $\dot{m}_a^*$ = 19.5 mg/s. The resulting fit is shown in Figure 4.5 and Equation 4.1.

$$B_r/B_r^*|_{trans}^{lower} = 0.284\frac{V_D}{V_D^*}\frac{\dot{m}_a}{\dot{m}_a^*} + 0.309 \tag{4.1}$$

A "transition surface" can also be plotted using Equation 4.1 as shown in Figure 4.6. More testing is required to validate the accuracy of the transition surface over the entire range, but the

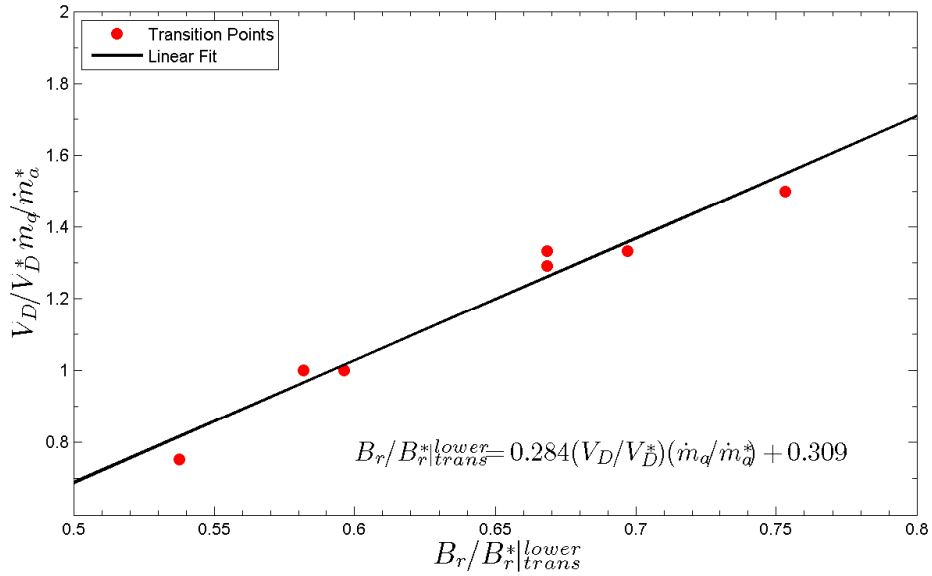

Figure 4.5: Lower transition point as a linear function of normalized discharge voltage and normalized anode mass flow rate. The resulting least-squares fit is shown. The multiple sweeps for 300 V and 400 V at 19.5 mg/s remain as separate data points.

surface in Figure 4.6 demonstrates a new technique for defining the operational modes of an HET. Using experimental data or an empirical relation the transitions points can be determined a priori over a prescribed range of discharge voltages and mass flow rates in order to avoid thruster operation near those settings.

A power law approach for the relation between $B_r/B_r^*|_{trans}^{lower}$ has the form

$$B_r/B_r^*|_{trans}^{lower} = C\left(\frac{V_D}{V_D^*}\right)^{\beta}\left(\frac{m_a}{m_a^*}\right)^{\gamma} \tag{4.2}$$

Equation 4.2 can be written in matrix form and the coefficients can be solved according to

$$\log\left(B_r/B_r^*|_{trans}^{lower}\right) = \begin{bmatrix} \log C \\ \beta \\ \gamma \end{bmatrix}\begin{bmatrix} 1 & \log\left(\frac{V_D}{V_D^*}\right) & \log\left(\frac{\dot{m}_a}{\dot{m}_a^*}\right) \end{bmatrix} \tag{4.3}$$

$$\begin{bmatrix} \log C \\ \beta \\ \gamma \end{bmatrix} = \log\left(B_r/B_r^*|_{trans}^{lower}\right)\begin{bmatrix} 1 & \log\left(\frac{V_D}{V_D^*}\right) & \log\left(\frac{\dot{m}_a}{\dot{m}_a^*}\right) \end{bmatrix}^{-1} \tag{4.4}$$

Equation 4.4 can be solved using the same data used to calculate Figure 4.5, which yields more

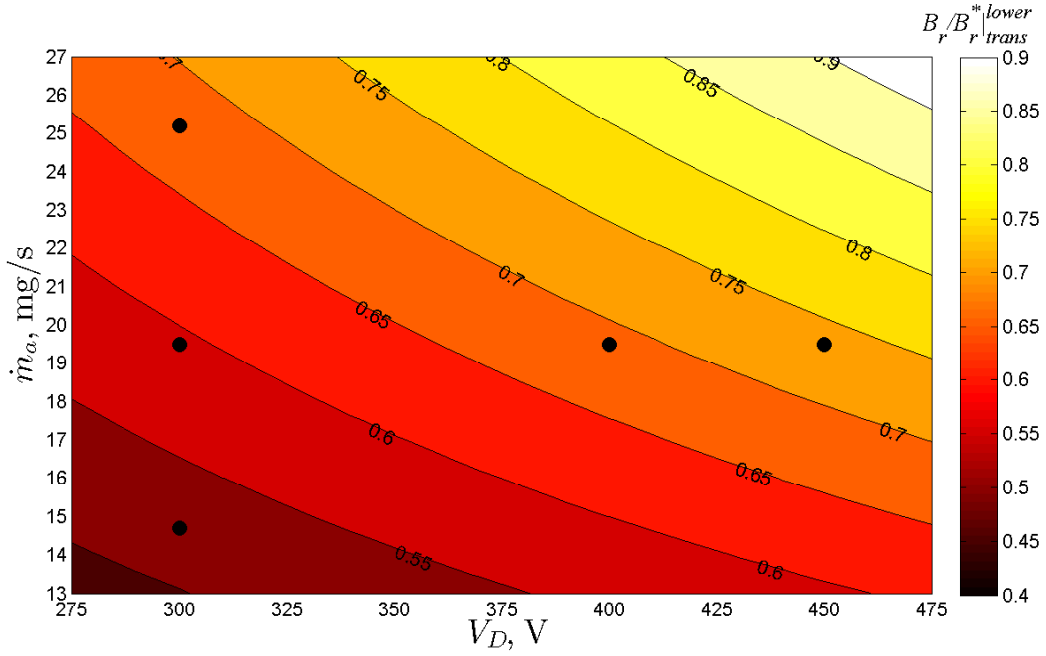

Figure 4.6: Transition surface generated from Equation 4.1 for $B_r/B_r^*|_{trans}^{lower}$ for a range of discharge voltages and anode mass flow rates. Black dots represent the conditions tested in Table 4.1.

equations than unknowns. Therefore the Moore-Penrose pseudoinverse matrix is used which is the least-squares solution to the over-determined problem. The solution is

$$B_r/B_r^*|_{trans}^{lower} = 0.593\left(\frac{V_D}{V_D^*}\right)^{0.401}\left(\frac{\dot{m}_a}{\dot{m}_a^*}\right)^{0.541} \tag{4.5}$$

Noting that β and γ are close to 1/2, the power law in Equation 4.5 can be approximated as

$$B_r/B_r^*|_{trans}^{lower} \approx 0.6\sqrt{\left(\frac{V_D}{V_D^*}\right)\left(\frac{\dot{m}_a}{\dot{m}_a^*}\right)} \tag{4.6}$$

There are not enough different conditions tested to conclusively determine which approximation is correct. However, over the range of V_D and $\dot{m}_a$ shown in Figure 4.6, the difference between Equation 4.1 and 4.6 is less than 7% so both approaches are equally valid pending further investigation.

In order to theoretically investigate the physics behind the transition, Equation 4.6 should be formulated as a function of quantities that appear in continuity equations. The ion velocity can be related to the discharge potential using conservation of energy

$$V_D = \frac{m_i v_i^2}{2q\eta_V} \tag{4.7}$$

where η_V is the voltage utilization efficiency in Equation 2.12 (fraction of the discharge potential the average ion is accelerated through). The mass flux of particles through the discharge channel of area A_{chnl} is

$$\dot{m} = An_N m_N \mathrm{v}_{th_N} \tag{4.8}$$

where n_N is the neutral particle density and $\mathrm{v}_{th_N} = \sqrt{8k_B T_N/(\pi m_N)}$ is the thermal velocity for neutrals of temperature T_N in K and mass m_N. Using Equations 4.7 and 4.8, Equation 4.6 can be written as

$$B_r/B_r^*|_{trans}^{lower} \approx \Psi \mathrm{v}_i \sqrt{n_N \mathrm{v}_{th_N}} \tag{4.9}$$

$$\Psi = 0.6 m_i \sqrt{\frac{A_{chnl}}{2V_D^* \dot{m}_a^* q \eta_V}} \tag{4.10}$$

Equation 4.9 shows that the transition point scales linearly with ion velocity and as the square root of neutral density and neutral velocity for the very limited number of data shown in Figure 4.6. More data are required over a large range of V_D and $\dot{m}_a$, but the techniques presented here, especially the idea of a transitions surface, are still valid.

4.4.3 Highly Oscillatory versus Unstable Operation

A distinction needs to be drawn between oscillatory operation in global mode and unstable operation. An increase in mean discharge current and oscillation amplitude is often labeled as unstable operation; however the thruster shows no sign of run-away behavior. Here we define unstable operation as the condition where discharge current begins to rise uncontrollably at a constant B-field setting. Figure 4.7 shows a typical B-field sweep at 300 V, 19.5 mg/s, lasting less than 1 hour with approximately 3 minutes at each setting. The continuously recorded values for inner magnet current I_{IM} and mean discharge current $\bar{I_D}$ are shown in Figure 4.7 with the discrete values used in later plots shown as symbols. Inner magnet current is decreased from the max of 5.5 A in discrete steps until the thruster goes unstable at 1.65 A. From 5.5 A until 2.1 A, the thruster is in local mode and transitions to global mode below 2.1 A. From 2.1 A to 1.75 A the thruster is more oscillatory in global mode, but is stable at higher mean discharge current values. Below 1.75 A, the discharge current begins to steadily rise and significant fluctuations are seen even on the 1-Hz telemetry in Figure 4.7 without any thruster setting changes, which is unstable operation.

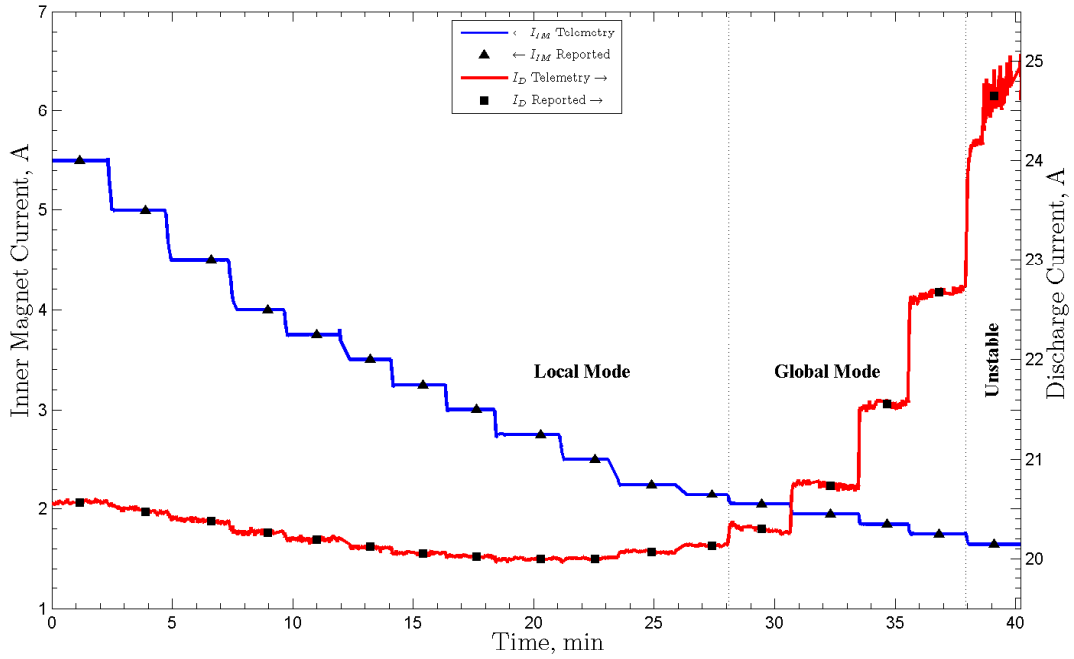

Figure 4.7: Telemetry for discharge current (right axis) and inner magnet current (left axis) for a B-field sweep at 300 V, 19.5 mg/s recorded at 1 Hz. The reported values used in Figure 4.2(a) and Figure 4.3(a) are shown as symbols. The B_r/B_r^* regions of local mode, global mode and unstable operation are noted.

4.5 Plasma Oscillations Response to Mode Transition

4.5.1 Discharge Current Density

FastCam videos of the thruster were acquired at all B_r/B_r^* settings during a B-field sweep and were time synchronized with discharge current measurements. All videos were processed as described in Chapter 3.5 in order to generate a discharge current density surface as shown in Figure 3.13(c). Figure 4.8 (a) compares a 0.5 ms sample of a $\hat{I}(t)$ signal and the $\hat{I}(t)$ signal filtered and down-sampled to the camera frame rate of 87.5 kHz with a normalized, AC component only m_0 from the FastCam. The discharge current sampled at $f_s > 1$ MHz in Figure 4.8(a) shows higher frequency discharge current oscillations that are not captured with FastCam. The difference between the original $\hat{I}(t)$ signal and $\hat{I}(t)$ signal filtered and down-sampled yields the uncertainty $\sigma_{j_{D3}}(t)$ in Equation 3.39. The correlation is visually apparent in Figure 4.8(a) with a linear correlation coefficient of 0.92 between the down-sampled $\hat{I}(t)$ signal and m_0. This matches the result first reported by Lobbia. [128] A linear correlation coefficient of $\rho > 0.8$ is always observed between I_D and m_0, supporting the assumption made in Chapter 3.5 that the time varying light intensity within the

discharge channel is linearly related to the discharge current. The PSD of the down-sampled $\hat{I}(t)$ and m_0 are nearly identical as shown in Figure 4.8(b). Therefore, PSDs of the discharge current from the split core Hall probes and m_0 spoke order from HIA are excellent proxies for each other and are important comparisons during mode transitions.

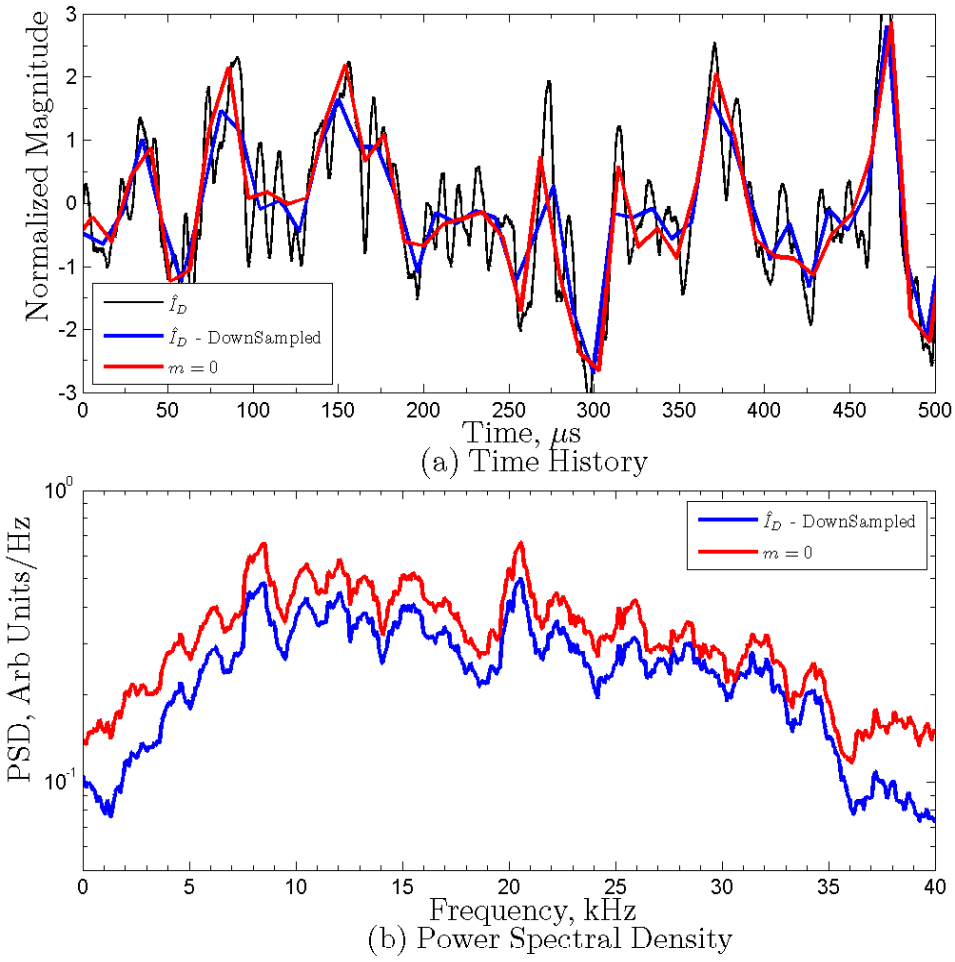

Figure 4.8: Comparison of normalized, AC component of the discharge current measurements to $m = 0$ spoke order from HIA. (a) The time history of the discharge current signal shows higher frequency components than the $m = 0$ signal, but the down-sampled discharge current and the $m = 0$ signal are well correlated, $\rho = 0.92$. (b) PSD of the down sampled discharge current and $m = 0$ signal also match well. A 1-kHz moving average filter has been applied to smooth both PSDs.

During B-field sweeps, HIA of the discharge current density surface shows a distinct change in the discharge channel oscillations in Figure 4.9 where the transition point is $B_r/B_r^* = 0.61$. While in local mode ($B_r/B_r^* > 0.61$), the spoke surfaces in the right plots show clear diagonal stripes, indicative of strong, coherent spokes or azimuthally propagating perturbations. Figure 4.9

shows the discharge current mean and RMS values with HIA during the B-field sweep and mode transition for 300 V, 19.5 mg/s, where the nominal discharge current is 20 A or 133 mA/cm^2 average discharge current density.

Several important features can be distinguished on the discharge current density surface plots, beginning with the low magnetic field setting of $B_r/B_r^* = 0.52$. Vertical stripes of constant current density indicates the entire discharge channel is acting in unison with minimal azimuthal non-uniformities, as shown clearly in $B_r/B_r^* = 0.52$. The fluctuations are large with the entire discharge channel at 70 mA/cm^2 (10.6 A) or approximately half of the nominal value at the minima and then rising to over 300 mA/cm^2 (45 A) during the peak. In 1 ms of the discharge current density surface shown in Figure 4.9, 8.5 cycles are visible. This corresponds to a frequency of 8.5 kHz, which is clearly seen as a peak for $m = 0$ in the HIA PSD with corresponding harmonics at 17 and 25.5 kHz. The $m = 1$ spoke order peak is just an artifact from $m = 0$ which McDonald [78] describes as "smearing." No spokes are observed to have any significant peaks for $B_r/B_r^* = 0.52$. The PSD peak in m_0 is over 10^7; two orders of magnitude higher than at the transition point ($B_r/B_r^* = 0.61$) or higher B_r/B_r^* values.

At the transition point, $B_r/B_r^* = 0.61$ in Figure 4.9, strong vertical stripes are seen between 0.46 and 0.73 ms as well as 0.9 ms, indicating an oscillation in the entire channel from 110 to 160 mA/cm^2. These entire channel oscillations are significantly lower than the global oscillations seen at $B_r/B_r^* = 0.52$. The three oscillations seen between 0.46 and 0.73 ms correspond to 11 kHz oscillations. However, diagonal stripes are clearly visible from 0 to 0.4 ms with oscillations between 120 to 150 mA/cm^2, which are symmetric about the mean of 133 mA/cm^2 for the discharge current of 20 A. These diagonal stripes represent azimuthal spokes propagating around the channel counter-clockwise, which is the $E \times B$ direction for the H6. The spokes extend for 1/4 to 1/2 of the discharge channel before dissipating and last from 100 to 200 μs in duration. The existence of spokes and global channel oscillations simultaneously indicates the thruster is switching or "bouncing" between the different oscillatory modes. The PSD shows the magnitude of the global mode has decreased by 2 orders of magnitude and is now the 11 kHz noted above. Spoke orders $m = 3-6$ are present, with 4 and 5 the most dominant at 13 and 18 kHz, respectively.

For the reference magnetic field of $B_r/B_r^* = 1.00$ in Figure 4.9, very few global oscillations are seen as evidenced by the very flat m_0 in the PSD and only hints of vertical lines in the spoke surface. Spoke orders $m = 3-6$ are also present with 4 and 5 still the most dominant, but they have shifted down to 10 and 15 kHz, respectively. The spokes are stronger as evidenced by the higher PSD peaks, but the length of the diagonal lines in the spoke surface has also increased. Spokes typically propagate over 1/2 to sometimes even the entire discharge channel lasting for several 100's μs. The local oscillations represented by spokes are from 115 to 150 mA/cm^2, which is about the mean of 133 mA/cm^2 or 20 A.

For the high magnetic field of $B_r/B_r^* = 1.48$ in Figure 4.9, the entire discharge channel occasionally oscillates in unison or "flickers" (i.e., 0.35 ms and 0.65 ms), but is not nearly as periodic as $B_r/B_r^* = 0.52$. The current density during these peaks can be as high as 180 mA/cm^2. Therefore, the m_0 mode is stronger than at $B_r/B_r^* = 1.00$, but the PSD peak is much broader than at $B_r/B_r^* = 0.60$ or 0.51 since the "flicker" is more sporadic and not at one frequency. The spoke orders $m = 4-8$ are nearly the same level, with 4 and 5 shifting down again to 9 and 14 kHz, respectively. The spoke peaks are an order of magnitude lower than $B_r/B_r^* = 1.00$ indicating weaker spokes. As seen qualitatively in the spoke surface, the spokes are shorter in duration so more spokes are present (higher spoke order), but propagate for shorter periods (lower PSD peaks).

In a study with data acquired before the present work, but published after the results shown here, McDonald [100] varied magnetic field strength for the H6 and noted an optimum B-field where discharge current was minimized. Below this optimum the discharge current oscillation amplitude increased significantly. Using different metrics for spoke strength, it was noted that spoke strength was maximized when discharge current oscillation strength was minimized.

In summary, B-fields below the transition thresholds do not support spoke propagation or local oscillations and the entire discharge channel oscillates in unison. At the transition points, spokes are able to propagate but the channel occasionally reverts to global oscillation mode. At the reference B-field strength of $B_r/B_r^* = 1$, spokes that are able to propagate over large regions of the discharge channel dominate and global oscillations are minimized. For higher B-field more spokes are present (higher m number in plots), but are less stable (occur for less time before disappearing in spoke surface). As the B-field increases, the peak frequency of each spoke order decreases, which supports an inverse relation between the spoke frequency (i.e., spoke velocity) and B-field as noted in Ref. 67, 100.

4.5.2 Probe Response in Local Mode

The value of high speed probes is displayed by the ability to extract oscillatory plasma behavior through PSD analysis or transient properties through time history analysis. Appendix B shows maps of plasma plume properties for the H6 at reference conditions, which were acquired with HDLP-ISR injected into the plume. The plume maps and oscillation content will be reserved for detailed discussion and analysis in Appendix B, but Figure B.3 shows a sample time history of plasma properties during probe injection over the discharge channel centerline exhibiting plasma oscillations. The PSD was calculated for both ion and electron density and compared to discharge current for the channel centerline ($R/R_{ch} = 1$). Approximately 2/3 of the time history signal was used for the PSD shown in Figure 4.10, which was a majority of the axial extent. However, even using a small selection of time history yields the same results.

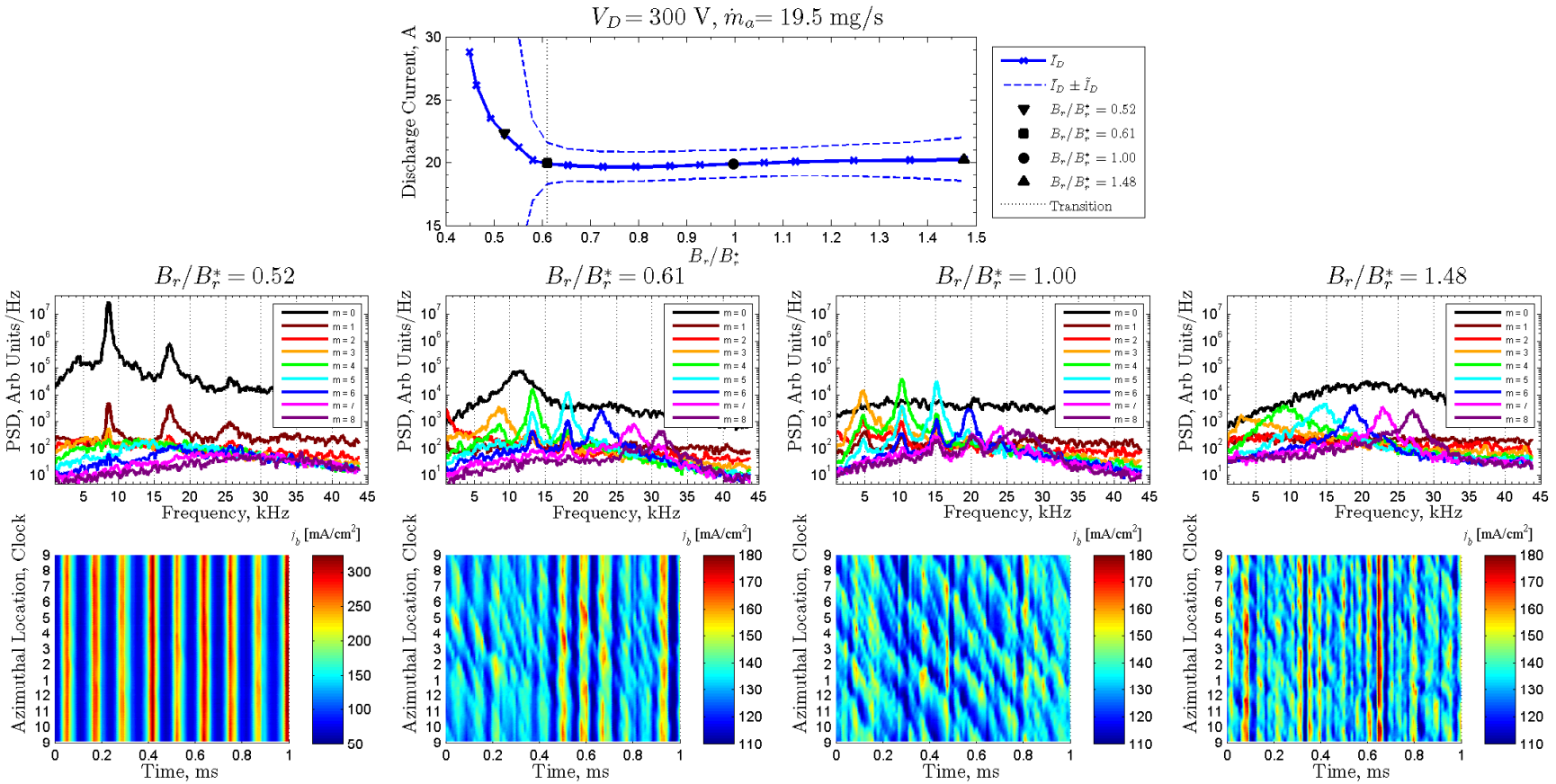

Figure 4.9: B-field sweep for 300 V, 19.5 mg/s showing transition at $B_r/B_r^* = 0.61$. The discharge current mean and oscillation amplitude are shown with the transition and for B_r/B_r^* settings selected for further analysis. The middle row plots are HIA PSDs and the bottom row plots are discharge current density. The scale range for $B_r/B_r^* = 0.52$ discharge current density is larger due to the magnitude of oscillations. A 500-Hz moving average filter has been applied to smooth all PSDs.

The distinguishing features in Figure 4.10 are the frequency peaks in both ion and electron density. The peaks correspond to oscillations at 16, 20, 24 and 28 kHz, which agrees with the rough observation in Figure B.3. What is also immediately obvious is the lack of corresponding peaks in the thruster discharge current, which only displays the broad breathing mode peak between approximately 10-15 kHz. Previous high-speed investigations [74] on different HETs have noted the electron density oscillations to follow the discharge current (with an appropriate time-of-flight delay), which showed a more distinctly peaked breathing mode. However, those measurements were farther out in the plume and did not approach the channel exit plane as closely as this investigation.

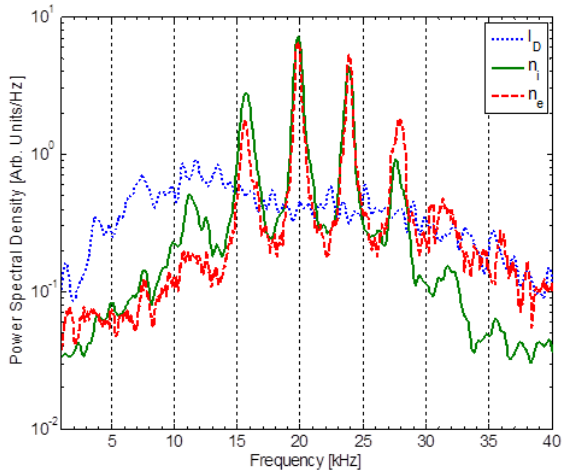

Figure 4.10: Power Spectral Density for thruster discharge current, ion density and electron density for $R/R_{ch} = 1$. Frequency peaks match those identified with HIA in Figure 4.11.

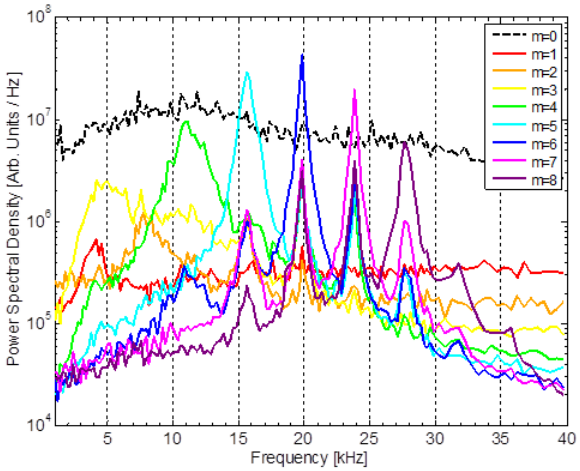

Figure 4.11: Power Spectral Density for plasma oscillations from HIA showing strong $m = 6$ spoke order. The spoke order peaks match the frequencies observed by probes in Figure 4.10.

Density oscillations with peaks in frequencies that differ from the breathing mode are confirmed from the HIA PSD shown in Figure 4.11 calculated using the methods described in Section 3.5. The frequencies of a 2-D PSD correspond to a local frequency that would be measured in a fixed location within the thruster. The $m = 0$ order in Figure 4.11 corresponds to the breathing mode, which is a global brightening and dimming of the entire thruster discharge channel and was shown to closely correlate to the discharge current in Figure 4.8. The shape matches the discharge current in Figure 4.10 (note the ordinate axis units are arbitrary) as expected from previous investigations [78]. The orders for $m \geq 1$ correspond to the number of spokes present. As seen in Figure 4.11 the modes can "smear" into each other due to the turbulent discharge [78] where they exhibit the same peaks, so the important peak for each spoke order is the value where it dominates: $m = 5$ peaks at 16 kHz, $m = 6$ peaks at 20 kHz, $m = 7$ peaks at 23 kHz and $m = 8$ peaks at 28 kHz.

As shown in Figure 4.11, the HIA detected the exact same frequency peaks as noted in the ion and electron density. This exciting result provides confirmation that observed spokes have a direct correlation to transient plasma properties in the thruster downstream plume. One possible interpretation is that the spokes (bright regions in the discharge channel) correspond to increased ionization zones and increased plasma density moving azimuthally in the discharge channel. These regions of increased density would produce density peaks that would then move axially outward (downstream) into the plume where probes in a fixed plane would measure them as plasma oscillations, but could not determine whether they were generated from the global breathing mode (axial oscillations) or from azimuthally moving spokes (azimuthal oscillations). If the spokes are indeed azimuthally moving regions of increased ion density, then azimuthally spaced probes should detect a time of arrival difference in density measurements that would correlate to the spoke velocity.

4.5.3 ISR Probe Response to Mode Transition

The two HDLP-ISRs were positioned in front of the thruster at 6 o'clock for a B-field sweep at 400 V, 19.5 mg/s as shown in Figure 3.6 with the results shown in Figure 4.12. The mode transition occurs at $B_r/B_r^* = 0.70$, below which oscillation amplitude increases greatly. Unlike the 300 V case, for the high magnetic field setting of $B_r/B_r^* = 1.48$ the oscillation amplitude $\widetilde{I_D}$ is also quite large at 5 A or 25% of $\bar{I_D}$. The results reported below only use the ion saturation current signals from the ISR probes (I_{ISR}), although high-speed data were also collected from the HDLP and will be presented in Section 4.5.4. Simply looking at signal correlation and PSDs, the ISR signals are easier to use with less noise and uncertainty than the high-speed electron density, electron temperature or plasma potential results. The same scale factor of 10^5 used later in Figure 4.13 will be applied to the I_{ISR} signal before calculating PSDs in Figure 4.12 for a direct comparison to discharge current PSDs.

For the global oscillation mode, $B_r/B_r^* = 0.61$ in Figure 4.12, the discharge current and $m = 0$ PSDs have a flat peak between 6.6 to 8.5 kHz. This peak is over one order of magnitude larger than at $B_r/B_r^* = 0.70$ for $m = 0$ in the HIA PSD and almost two orders of magnitude larger for the discharge current. Both the HIA PSD and discharge current PSD are over two orders of magnitude larger than at $B_r/B_r^* = 1.00$. No spokes are present from HIA or the ISR signals. The discharge current signal peak is larger than the ISR signals, indicating the dominance of the global oscillations. At the transition point, $B_r/B_r^* = 0.70$, spokes are present with $m = 4$ and 5 dominant at 12 and 17 kHz, respectively. Spoke order $m = 6$ is present at 22 kHz and $m = 7$ order is present at 27 kHz one order of magnitude lower in signal strength than $m = 4$ or 5. The discharge current and m = 0 peaks have shifted to a sharp peak at 9 kHz. The ISR signals show the same peaks as the HIA spokes at 17, 22 and 27 kHz (the 12-kHz peak is weakly present), but the discharge current

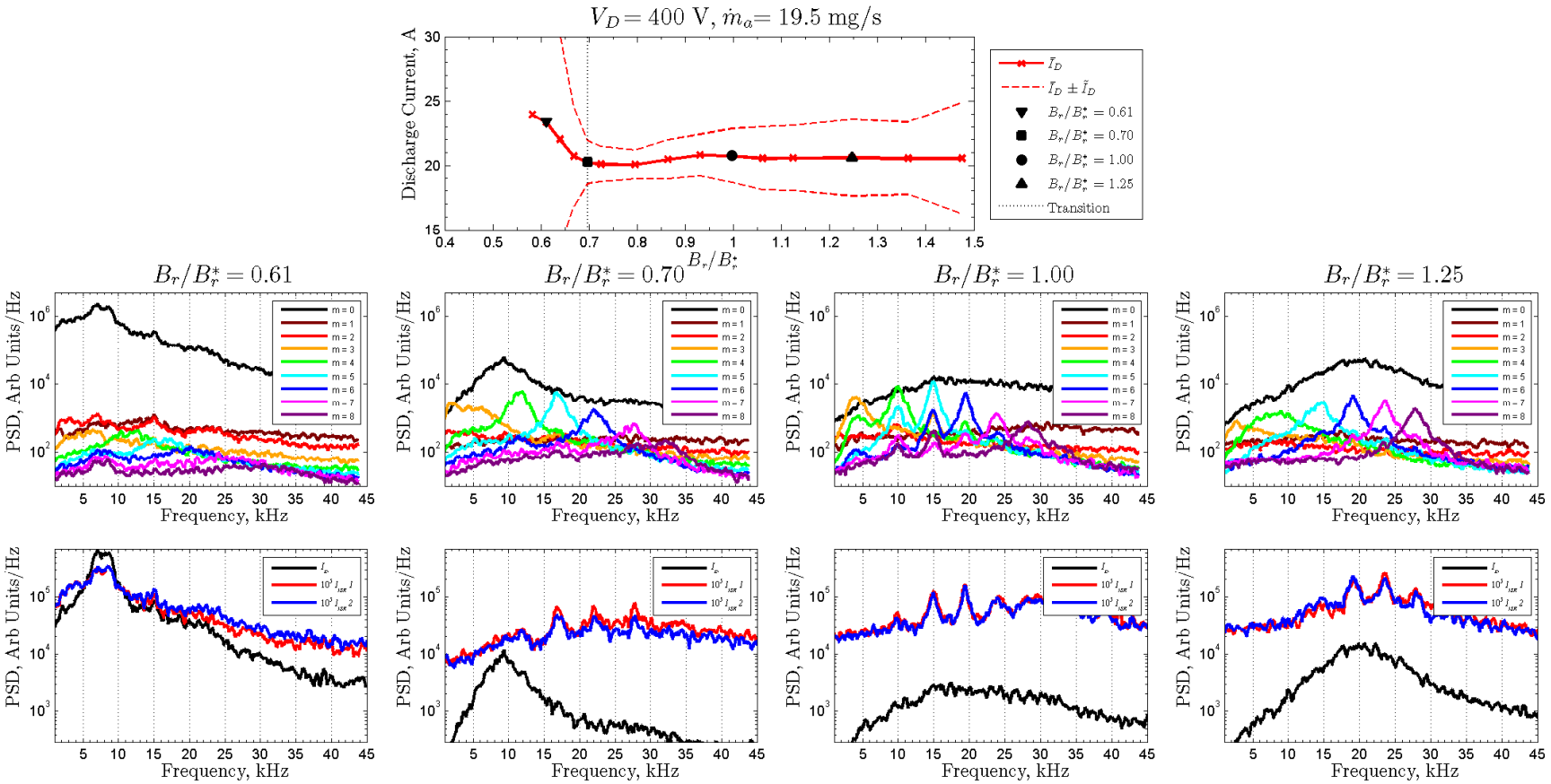

Figure 4.12: B-field sweep for 400 V, 19.5 mg/s with probes in place showing transition at $B_r/B_r^* = 0.69$. The discharge current mean and oscillation amplitude are shown with the transition and for B_r/B_r^* settings selected for further analysis. The middle row plots are HIA PSDs and the bottom row plots are discharge current and ISR signal PSDs. A 500-Hz moving average filter has been applied to smooth all PSDs.

peak at 9 kHz is entirely absent. This shows local plasma oscillations due to spokes dominate over the global discharge current oscillations. The HIA spoke signals are an order of magnitude lower than the discharge current signal at $B_r/B_r^* = 0.70$.

At the reference magnetic field, $B_r/B_r^* = 1.00$ in Figure 4.12, the discharge current and $m = 0$ signals have a very broad peak between 15 and 20 kHz. On the HIA PSDs, the dominant spoke orders are $m = 3$, 4, 5 and 6 at 4, 10, 15 and 19 kHz, respectively, with the $m = 7$ order at 24 kHz and $m = 8$ order at 28 kHz also weakly present. The ISR signals have strong peaks at 15, 20 and 24 kHz matching the $m = 5$, 6 and 7 spoke orders well. For a higher magnetic field, $B_r/B_r^* = 1.25$, the discharge current oscillations increase, as evidenced by a large (same magnitude as transition) and more peaked discharge current and $m = 0$ order at 20 kHz. On the HIA PSDs, the $m = 4$ spoke order has faded, but $m = 5$, 6, 7 and 8 have peaks at 15, 19, 24 and 28 kHz, respectively. The ISR signals show the same peaks with the strongest peaks at 19 and 24 kHz matching the $m = 6$ and 7 spoke orders. The peaks have shifted to lower frequencies, but by less than 0.5 kHz and all frequency peaks are rounded to the nearest kHz.

In summary, the PSDs for ISR 1 and 2 consistently match, indicating that they record the same plasma oscillations. This is important when doing the correlation later as it is shown they do not record the plasma oscillations at the same time. The ISR signal PSDs have peaks matching the HIA PSD peaks for spokes with the strongest peaks corresponding to the higher spoke orders. As with the 300 V case, the peak spoke orders m increase with increasing B_r/B_r^* but the frequency of the peaks gradually decreases. No spokes are present in global oscillation mode for ISR signals or HIA PSDs. This indicates that in local oscillation mode, the plasma density fluctuations are determined by local oscillations within the discharge channel and not a global phenomenon. In global oscillation mode, the entire channel is oscillating in unison.

In order to further investigate local and global oscillations, a time history segment of the discharge current and ISR signals is shown in Figure 4.13 for local oscillation mode ($B_r/B_r^* = 0.73$) and global oscillation mode ($B_r/B_r^* = 0.61$). The ISR current (I_{ISR}) which is typically of order 100's μA has been scaled by 10^5 with the mean subtracted (leaving the AC component only) in order to match the discharge current AC component $I_{D_{AC}}$ for $B_r/B_r^* = 0.61$. The difference in the discharge current between the two modes in Figure 4.13(a) and (b) is also apparent with the local oscillation mode exhibiting lower mean and oscillation amplitude (RMS value) as shown in Table 4.3. The peak-to-peak value for the time segment shown in Figure 4.13(a) is less than 6 A for local mode, while the peak-to-peak value for the time segment shown in Figure 4.13(b) is ~ 35 A for global mode.

For local oscillation mode, Figure 4.13(a), the linear correlation coefficient, ρ, between $I_{ISR\,1}$ and $I_{D_{AC}}$ is only 0.23, whereas in global oscillation mode, Figure 4.13(b) $\rho = 0.77$. This means $I_{ISR\,1}$ tracks $I_{D_{AC}}$ very well in global oscillation mode, but not in local oscillation mode. In other

	Local Mode	Global Mode
B_r/B_r^*	0.73	0.61
$\bar{I}_D$ [A]	20.1	23.4
$\widetilde{I}_D$ [A]	1.4	11.0

Table 4.3: Summary of discharge current mean and oscillation amplitude for Figure 4.13.

words, the plasma oscillations in local oscillation mode are less dependent on the discharge current oscillations, but are strongly dependent in global oscillation mode. The time delay calculated by cross-correlation from $I_{ISR\,1}$ to $I_{ISR\,2}$ is 14.7 μs, with an estimated uncertainty of 1 μs based on the width of the correlation function or 10% (1-2 μs) as discussed in Ref. 34. Figure 4.13(c) shows $I_{ISR\,2}$ shifted to match $I_{ISR\,1}$, demonstrating the signals are very well correlated; the correlation coefficient before the time shift was -0.28 and after was 0.52. This means the ISR2 probe records the same plasma oscillations as ISR1 probe, but delayed by 14.7 μs. The ISR2 probe signal delay is in the spoke propagation direction ($E \times B$ direction) from ISR1 leading to the conclusion that the plasma oscillations are caused by the passage of azimuthally propagating spokes as discussed in Chapter 5.

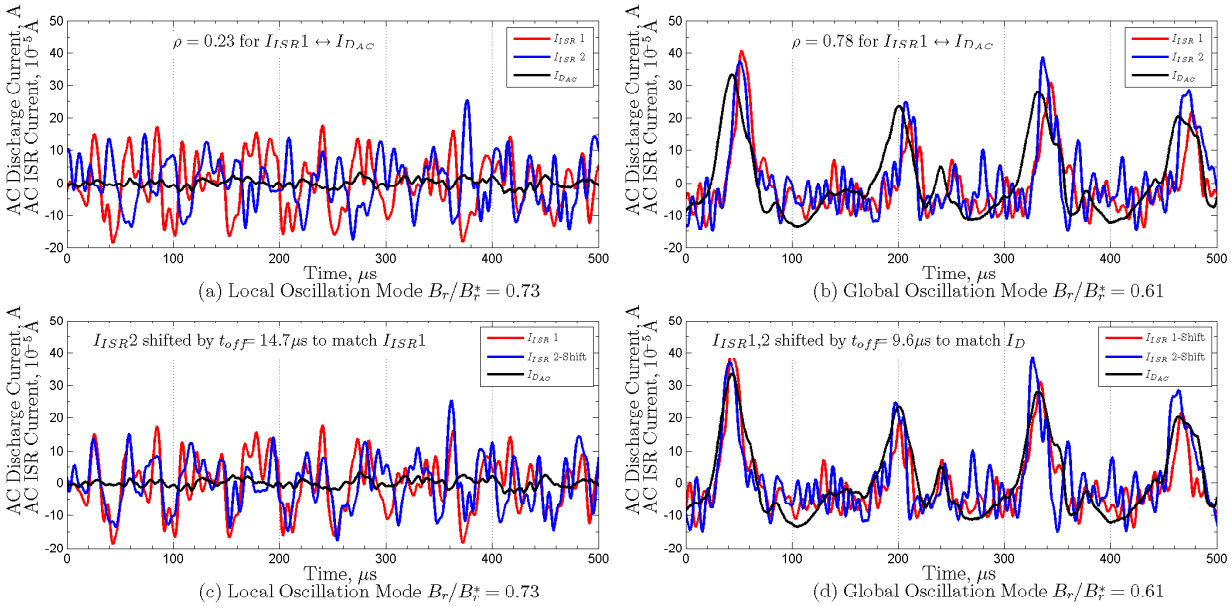

Figure 4.13: Comparison between the AC component of discharge current ($I_{D_{AC}}$) to ISR current ($I_{ISR\,1}$ and $I_{ISR\,2}$) for 400 V, 19.5 mg/s in local and global mode. Note the I_{ISR} signals have been scaled by 10^5, the $I_{D_{AC}}$ signals are true scale. The ISR signals were low-pass filtered at 150 kHz using a Butterworth 3rd order filter to reduce noise.

For global oscillation mode, Figure 4.13(b), the time delay calculated by cross-correlation from

$I_{ISR\,1}$ to $I_{ISR\,2}$ was $-1.4\,\mu$s, near the margin of error and the correlation coefficient ρ without time shifting was 0.75 so effectively there was no delay between ISR signals. However, the time delay calculated by cross-correlation from $I_{ISR\,1}$ to $I_{D_{AC}}$ was 9.7 μs, which can be construed as the ion time of flight from the discharge channel to the probes. This means the plasma oscillations occurred uniformly within the discharge channel during surges in discharge current and propagate downstream to be detected by both probes simultaneously.

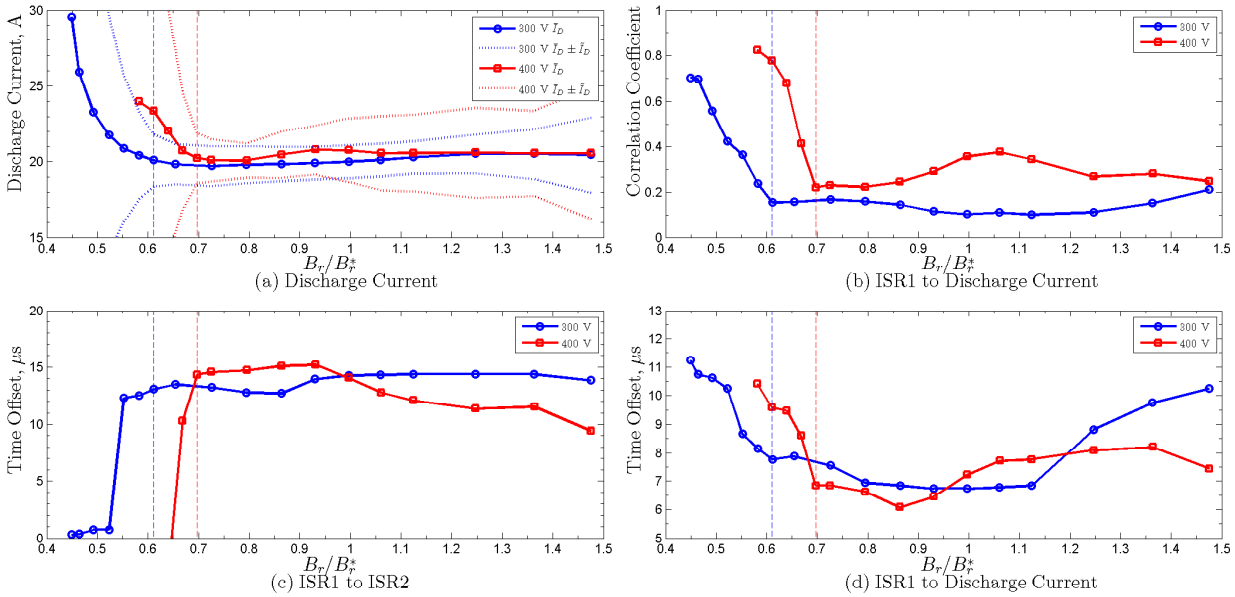

Figure 4.14: B-field sweeps at 19.5 mg/s for 300 V (blue) and 400 V (red) with ISR probes; transition points are shown as vertical dashed lines. (a) Discharge current mean values with oscillation amplitude in dotted lines. (b) Correlation coefficient from ISR1 to discharge current. (c) Time offset from ISR1 to ISR2 calculated from cross-correlation (d) Time offset from ISR1 to discharge current calculated from cross-correlation.

Key features identified in Figure 4.13 are time offsets from discharge current to ISR probes with correlation coefficients and time offsets between ISR probes. These quantities are shown in Figure 4.14 for 300 V and 400 V, 19.5 mg/s during B-field sweeps. Figure 4.14(a) shows the discharge current mean and oscillation amplitude with transition points during B-field sweeps, noting that 400 V transitions at a higher B_r/B_r^*. The correlation coefficients ρ in Figure 4.14(b) are between the AC components of I_{ISR1} and $I_{D_{AC}}$ after time shifting $I_{ISR\,1}$ by the offset times shown in Figure 4.14(d) calculated from cross-correlation. Figure 4.14(b) clearly shows for all B_r/B_r^* values in local oscillation mode, the ISR signal is not well correlated with the discharge current signal, as was shown in Figure 4.13. Below the transition value for B_r/B_r^* the signals become well correlated in global oscillation mode with $\rho > 0.3$. The offset time increases below the transition point for both 300 V and 400 V as shown in Figure 4.14(d) indicating a longer integrated ion time-

of-flight from the discharge channel to the probes in global mode. It is important to remember that global oscillations exist in local mode, but they are not dominant. There are still oscillations in discharge current that will correspond to global fluctuations in plasma density downstream. These oscillations are not dominant in local mode, but are significant enough for a linear cross-correlation between I_{ISR1} and I_D. Figure 4.14(b) shows the correlation coefficient between I_{ISR1} and I_D is low ($0.1 < \rho < 0.4$) in local mode, but the time offset is still an averaged ion time-of-flight with the same meaning as in global mode.

The time offset from ISR1 to ISR2 calculated from cross-correlation is shown in Figure 4.14(c) where above the transition point the time delay is between 10 and 15 μs. The time delay is generally decreasing with increasing B_r/B_r^* for 400 V, but is relatively constant for 300 V. For both discharge voltages, below the transition point the offset time drops to within ± 3 μs of 0 μs indicating the probes are measuring plasma oscillations nearly simultaneously. Combined with the high correlation coefficient between ISR1 and the discharge current, this indicates the plasma is oscillating in unison within the discharge channel and propagating downstream to be detected by the probes. For 300 V, the offset time does not immediately go near zero indicating some spoke propagation in the transition region of $B_r/B_r^* = 0.57$ to 0.61.

The specific impulse at the nominal conditions ($B_r/B_r^* = 1$) for the H6 at 300 V discharge is 1950 s, [37] which corresponds to an expected ion velocity of 19.1 km/s. From Figure 4.14(d), the time offset at 300 V discharge for $0.8 < B_r/B_r^* < 1.1$ is approximately 7 μs. The corresponding ion velocity is 17 ± 3 km/s using the fixed probe position 1.5 mean channel radii downstream and an uncertainty of ± 1.5 μs in the time offset. Note that this is an average ion velocity in the region between the discharge channel exit plane and the probes and not an instantaneous velocity. In global oscillation mode the time offset is 10 μs which corresponds to an average ion velocity of $\sim 12 \pm 2$ km/s. While both values are lower than expected, the nominal condition is within uncertainty of the expected ion velocity. As Lobbia points out, using linear cross-correlation to determine ion time-of-flight is less accurate than determining the phase delay from frequency domain transfer functions. [128] Therefore, the lower than expected average ion velocity may be the result of experimental uncertainty. It may also be indicative of changes in the plasma properties in global oscillation mode. The ion time-of flight from creation in the ionization zone to observation by ISR probes is calculated by integrating the ion position using the equation of motion for a particle in the axial electric field (assuming the ions are unmagnetized). The instantaneous ion velocity at the probes may be higher in global mode than the average ion velocity of 12 km/s calculated by simple ion time-of-flight, but the time for an ion to travel from the ionization zone to the probes may be longer due to a different plasma potential profile. Assuming conservation of energy, if the plasma potential at the probes is the same in global mode and local mode and if the ions are created at the same potential, then they should have the same instantaneous velocity. These subtleties mean that

using the simple linear cross-correlation time offsets in Figure 4.14(d) to calculate ion velocity can be misleading.

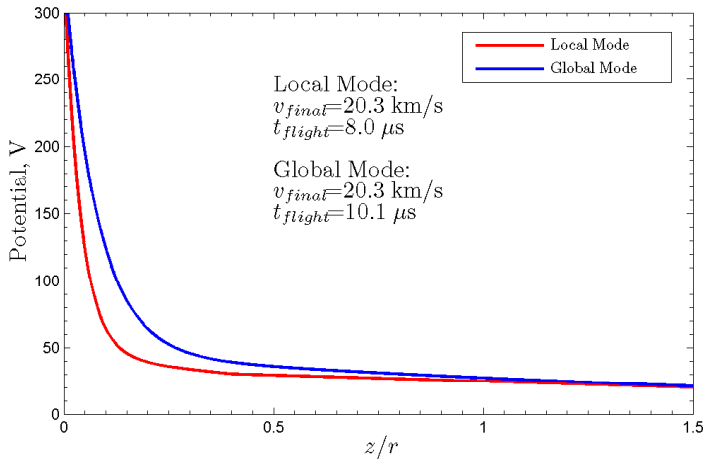

Figure 4.15: Plasma potential profiles with respect to ground to calculate ion time-of-flight. Local mode profile is based on measurements from Ref. [37]. Global mode is based on a modified version of local mode for demonstrative purposes only. The calculated final velocity and time-of-flight are shown.

An example has been created using a measured plasma potential profile and an altered plasma potential profile to illustrate this hypothesis. The measured plasma potential profile with respect to the cathode has be extracted from Figure 15 of Ref. 37 and has been linearly extrapolated to the probe distance at $z/r = 1.5$ as shown in Figure 4.15. This is for the nominal H6 conditions which is local mode. A second plasma potential profile has been created by "stretching" the measured profile downstream, but the plasma potential at the probe location remains the same. This has been labeled as global mode in Figure 4.15 but does not represent a measured plasma potential profile. The equation of motion for a singly charged ion has been numerically integrated using energy conservation with distance increments of 1 μm to calculate the final velocity and total time of flight to reach the probes with the results shown in Figure 4.15. The calculated final ion velocities of 20.3 km/s are reasonable estimates of expected ion velocities from measurements and both time-of-flights fit with the data shown in Figure 4.14(d). As expected, the final velocities are the same since they have been accelerated through the same potential, but the time of flight from $z/r = 0$ to $z/r = 1.5$ has increased by 2 μs for global mode to 10 μs. At present there are no direct measurements of plasma potential profile changes between local mode and global mode for the H6 and the global potential profile shown in Figure 4.15 is purely hypothetical. However, it does quantitatively demonstrate how the downstream probes could measure different time offsets and yield different average velocities when the ion instantaneous velocities are the same.

4.5.4 HDLP-ISR Probe Response to Transition

4.5.4.1 Introduction

Time-resolved probe measurements were made using the HDLP-ISR probes shown in Figure 3.6 to quantify changes in plasma properties between modes. This allowed observation of oscillations in normalized density, plasma potential and electron temperature. The probes are located 1.5 R_{ch} downstream on channel centerline near the 6 o'clock position. It is important to note that these are near-field plume measurements and not internal discharge channel measurements. The probe area decreased during the hours of testing, but not significantly within the less than 1 second of data acquisition so the density oscillations are normalized and not absolute values. The probes are not aligned with the plasma flow so the ion density calculations of Appendix A do not apply.

The HDLP-ISR data were processed using the techniques described in Chapter 3.4. The voltage was swept at 200 kHz and every two traces were averaged together so the plasma properties are also sampled at 200 kHz or 5 μs intervals. For automated I-V trace processing, a threshold value of 25% $dI_e/d\phi|_{peak}$ was the start and 40% of the $\ln(I_e)$ points from there towards V_p were selected to conduct a linear fit to determine T_e. The time-resolved plasma properties were smoothed with a 7 point wide, third order Savitzky-Golay filter. The raw signal from HDLP 2 exhibited irregularities in the ion saturation portion of the trace indicating it may have been corrupted by noise or the Pearson coil was damaged so only the time-resolved results from HDLP-ISR 1 will be shown. Note that ISR2 was unaffected. The 400 V, 19.5 mg/s case was tested first and the HDLPs failed during the magnetic field sweep for the 300 V, 19.5 mg/s condition so only the results from the 400 V case are shown. Time averaged plasma property values are calculated using the same automated I-V processing scripts on an I-V trace trace that is the average of multiple other I-V traces.

The difference between average of time-resolved results and time-averaged results needs to be addressed, which will be discussed in more detail in Appendix B. The average of time-resolved results is the mean value of a time-history trace for a time-resolved plasma property. Time-averaged results are obtained when many I-V traces (enough to be much more than one oscillation period) have been averaged together and the resulting plasma properties calculated from that averaged I-V trace using the processing techniques discussed in Section 3.4. For example, in this section 10,000 I-V traces acquired at 400 kHz are averaged together (25 ms of plasma data) to create one I-V trace, whereas the typical plasma oscillations of interest here are $\sim$ 10 kHz or $\sim$ 100 μs. As will be shown, the average of time-resolved results and time-averaged results match well when the oscillations are sinusoidal in nature, but do not match as well when the oscillations take on a different functional form.

The plasma oscillations are qualitatively and quantitatively different in both modes. In local mode, the plasma properties oscillate in a sinusoidal fashion as shown in Figure 4.13(a,c).

The mean of a sinusoidal function is the DC or offset value. Therefore, the average of the time-resolved plasma proprieties corresponds well to time-averaged results calculated from an averaged I-V trace. However, in global mode the discharge current oscillations are not sinusoidal as shown in Figure 4.13(b,d), but are closer to a periodic or repeating narrow, Gaussian function. The oscillation frequency in global mode is typically ~ 8 kHz so an oscillation period is ~ 125 μs. Even though the cycle may be 125 μs, the rapid rise and decay of the peak lasts less than 50 μs as shown in Figure 4.13. A time step of less than 25 μs is necessary to capture the oscillations accurately. Without the brief peaks, the time-averaged results from an I-V trace that has been averaged over many cycles will tend towards the lower value of the signal. This shows the benefit of time-resolved probes, because time-averaging misses important details.

4.5.4.2 Cathode-to-Ground Voltage

All plasma potential values presented are with respect to cathode potential as determined from a time-averaged cathode-to-ground measurement. The time-resolved plasma potential is initially calculated with respect to ground and then adjusted with a DC offset to account for the measured time-averaged cathode-to-ground potential shown in Figure 4.16. By convention, the cathode potential is below ground when $V_{cg} < 0$ and above ground when $V_{cg} > 0$. The time-averaged cathode-to-ground potential is measured as a single value simultaneous to HDLP-ISR data acquisition. During later testing at 300 V and 19.5 mg/s without the HDLP-ISR, time-resolved cathode-to-ground measurements were acquired with a high-speed voltage probe using the same DAQ as the HDLP-ISR and it was observed that V_{cg} oscillations also change significantly during mode transition as shown in Figure 4.17. These results will be discussed to highlight how the lack of time-resolved cathode-to-ground measurements for the 400-V case creates significant uncertainty in global mode, but not local mode.

Figure 4.17 shows the discharge current and oscillation amplitude (RMS) in the upper left plot with the transition region identified by dashed vertical black lines. The cathode-to-ground voltage is shown in the upper right where the blue line is the time-averaged $\bar{V}_{cg}$ value recorded by the 1-Hz telemetry and has an uncertainty of ±0.1 V. The red line shows the mean value of the time-resolved cathode-to-ground voltage $\langle V_{cg}(t) \rangle$ and the dashed red lines are the RMS value calculated using Equation 3.2. Other than a ~ 0.25 V vertical offset for $\langle V_{cg}(t) \rangle$, the two results from these independent measurements agree well. Three magnetic field settings have been selected, B_r/B_r^* = 0.54, 0.60 and 0.73, to show 500 μs segments of $V_{cg}(t)$ and $I_D(t)$ in global mode, transition and local mode, respectively. A 1-μs wide moving average window has been applied to $V_{cg}(t)$ to smooth the data.

In global mode at $B_r/B_r^* = 0.54$, the peak cathode-to-ground voltage during an oscillation cycle is ~ 9 V *above* ground, while the mean value is 6.7 V *below* ground, a ~ 16 V difference. The 4.1 V

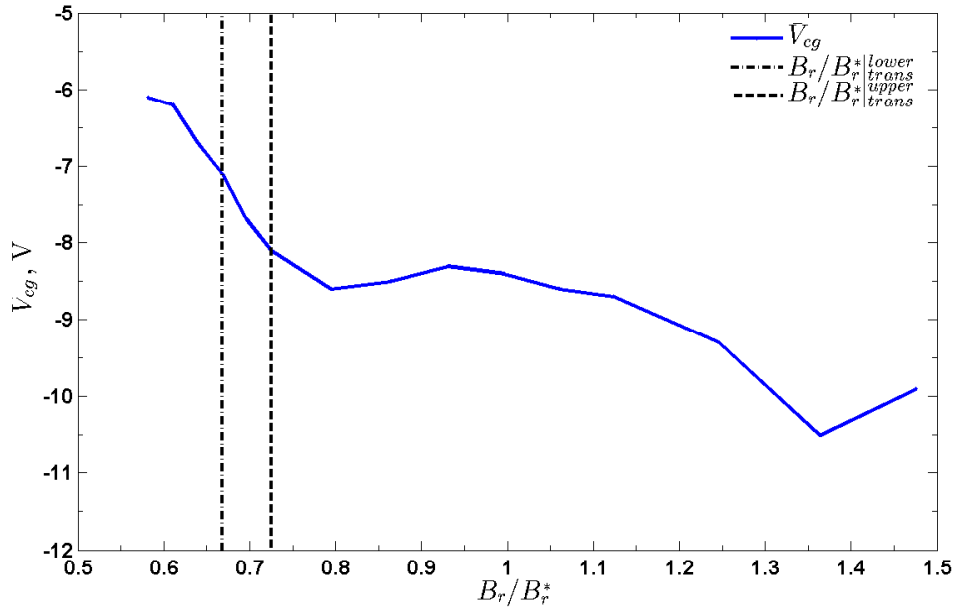

Figure 4.16: Cathode-to-ground voltage during a B-field sweep for 400 V and 19.5 mg/s with the HDLP-ISR. Negative values indicate the cathode potential is below ground. Black vertical lines identify the transition region.

RMS value bounds the most negative value in the oscillation cycle at ~ 10 V below ground, but does not capture the high-amplitude peak approximately 4 times the RMS value above the mean. The peak-to-peak value in global mode is ~ 20 V or +16/-4 V about the mean, so the error in plasma potential when converting from ground to cathode potential reference can be significant. As shown in Figure 4.17, the cathode-to-ground voltage follows the discharge current breathing mode cycle with a ~ 15 μs delay calculated from linear cross-correlation. Figure 4.14(d) shows the plasma density oscillations in global mode are offset ~ 10 μs from the discharge current oscillations due to ion time-of-flight. Assuming the plasma potential is correlated to the plasma density (supported later in Figure 4.20), the cathode-to-ground voltage ~ 10 μs after a discharge current peak is ~ 0 V, so using the -6.7 V mean value will overestimate the plasma potential by 6.7 V in this example. It is uncertain how large the error will be for the plasma potential results at 400 V presented in this section, but the plasma potential in global mode could be in error by up to 10's of V.

In local mode at $B_r/B_r^* = 0.73$, Figure 4.17 shows the RMS value of 2.1 V reasonably represents the oscillation amplitude and the -8.4 V mean value is a very representative cathode-to-ground voltage. The transition condition at $B_r/B_r^* = 0.60$ shows occasional breathing mode oscillations mixed with lower amplitude oscillations associated with local mode. Aside from the occasional large amplitude breathing mode oscillations, the 2.3 V RMS value reasonably represents the oscillation amplitude and the -7.8 V mean value is a representative cathode-to-ground voltage. In summary,

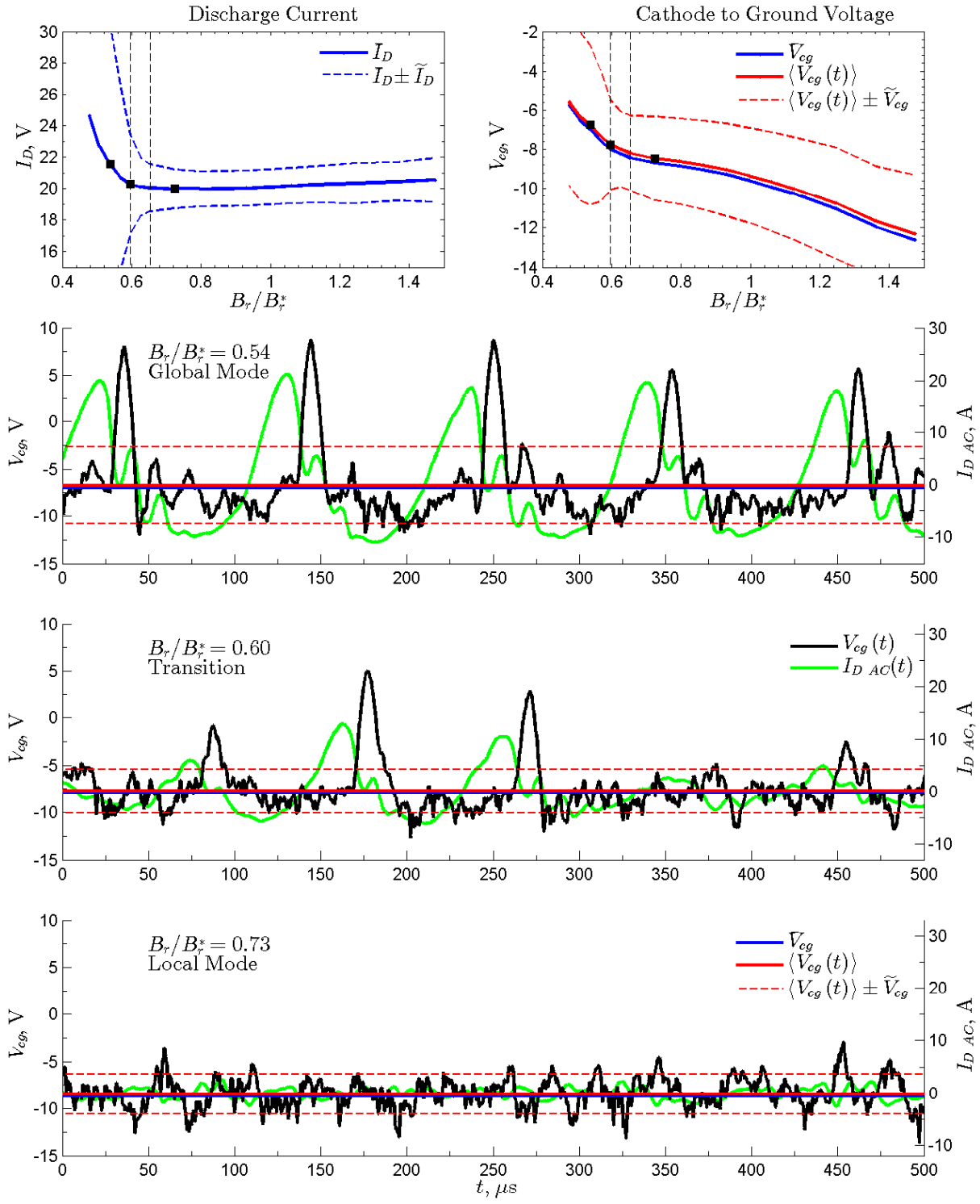

Figure 4.17: Cathode-to-ground voltage at 300 V and 19.5 mg/s. Upper left: discharge current and RMS values with the mode transition region identified by vertical lines. Upper right: cathode-to-ground voltage from time-averaged values, $\bar{V}_{cg}$, in blue and the average of time resolved, $\langle V_{cg}(t)\rangle$, in red bounded by RMS values. 500 μs segments of $V_{cg}(t)$ and $I_D(t)$ are shown for B_r/B_r^* = 0.54, 0.60 and 0.73 corresponding to global mode, transition and local mode, respectively. The $V_{cg}(t)$ signal has been smoothed by a 1-μs wide moving average window.

converting the time-resolved plasma potential reference from ground to cathode can be accomplished with minimal error in local mode using a DC measurement for cathode-to-ground voltage, but cannot in global mode. Time-resolved cathode-to-ground measurements synchronized to the discharge current and HDLP-ISR measurements are necessary for accurate, time-resolved plasma potential calculations in global mode. Future tests will record time-resolved, cathode-to-ground potential to correctly calculate the time-resolved plasma potential with respect to cathode.

4.5.4.3 Plasma Potential

Figure 4.18 shows the plasma potential with respect to cathode for the 400 V, 19.5 mg/s condition throughout a B-field sweep. The time-resolved plasma potential is initially calculated with respect to ground and a single, time-averaged cathode-to-ground voltage is measured at each B-field setting. Combining these measurements for each point yields the plasma potential with respect to cathode. As discussed in Section 4.5.4.2, this approach is accurate in local mode, but can induce 10's of V error in global mode. Adding further error to the plasma potential results for global mode in Figure 4.18, the time-resolved plasma potential signal in global mode exhibits the same shape as the plasma density and discharge current signals in Figure 4.13 for B_r/B_r^* = 0.61 and the cathode-to-ground voltage in Figure 4.17 for B_r/B_r^* = 0.54. Therefore, the mean plasma potential value in global mode for Figure 4.18 will significantly underestimate the plasma potential peaks as discussed in Section 4.17 for the cathode-to-ground voltage.

For $B_r/B_r^* > 0.9$ in Figure 4.18 the plasma potential is 40-43 V, and for $B_r/B_r^* < 0.9$ decreases with decreasing B_r/B_r^*. The plasma potential is 33-35 V in the transition region and drops below 30 V in global mode $B_r/B_r^* < 0.66$. The oscillation amplitude is the RMS value calculated from the 200 kHz data and is shown above and below the 200 kHz results. The oscillation amplitude is 3-4 V in local mode and increases to $\sim$ 16 V in global mode. The difference between the average of time-resolved and time-averaged calculations is apparent in global mode, where the time-averaged results calculated by combining 10,000 I-V curves yields a V_P that is 5 V too low. As discussed above, this is because the time-averaged results miss the high-amplitude, short-duration peaks in potential.

Decreasing plasma potential in local mode with decreasing B_r/B_r^* indicates the acceleration zone is moving further into the channel or is becoming more compressed near the exit plane. The $\sim$ 4 decrease in mean plasma potential after the transition to global mode is likely an artifact of how the mean is not a reliable metric for global mode oscillations due to the shape of the signal. The fact that the RMS value approximately doubles in global mode (where it underestimates the peak value) compared to local mode (where it is representative of oscillation amplitude) indicates the plasma potential has large amplitude peaks downstream. During these peaks the acceleration zone extends far outside of the discharge channel. In summary, the acceleration zone recedes into

the channel with decreasing magnetic field in local mode until the mode transition point where the acceleration zone (and possibly the ionization zone) will have large amplitude peaks that extend out of the discharge channel into the near-field plume. These bursts may be responsible for the increased brightness discussed in Section 4.7 and should be further investigated.

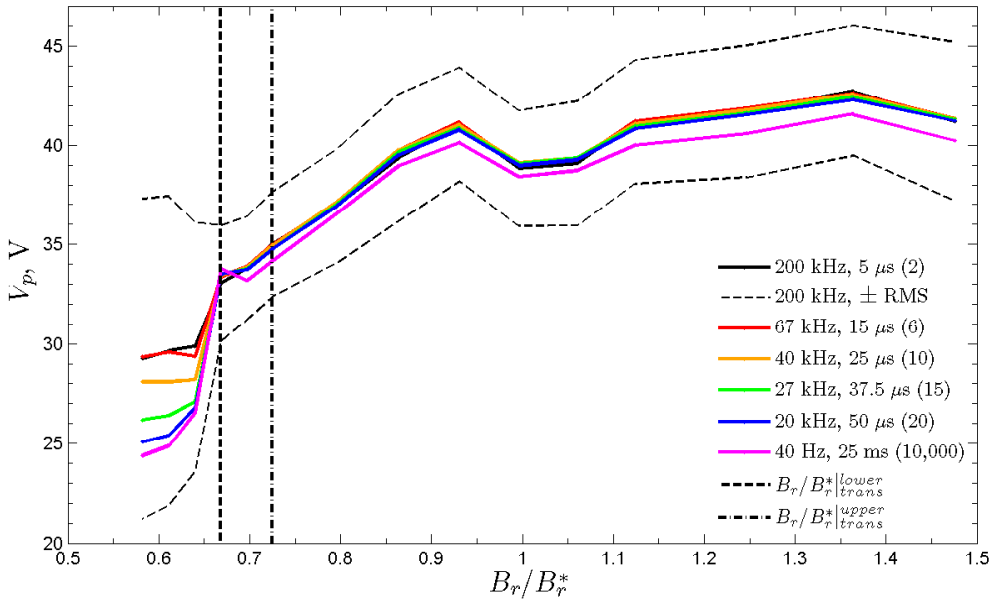

Figure 4.18: Plasma potential with respect to cathode for 400 V, 19.5 mg/s measured by probes 1.5 R_{chnl} downstream. The plasma potential has been calculated at 200 kHz, 67 kHz, 40 kHz, 27 kHz, 20 kHz and 40 Hz by averaging a different number of I-V traces together indicated by the parenthetical numbers. The transition region is shown with the oscillations in global mode ($B_r/B_r^* < 0.66$) average of time-resolved differs from time-averaged calculations.

4.5.4.4 Electron Temperature

Figure 4.19 shows the electron temperature for the 400 V, 19.5 mg/s condition throughout a B-field sweep. The temperature is between 4.5 and 5.5 eV for all local oscillation mode conditions. There is a general decreasing trend where the highest temperatures are observed at the highest B_r/B_r^* and decreasing until transition with a slight dip at $B_r/B_r^* = 1.00$ and 1.05. The electron temperature in global mode is between 4 and 4.75 eV, although that is mean value is likely not a representative metric as discussed in Sections 4.5.4.2 and 4.5.4.3. As with the plasma potential, the time-averaged results miss the high-amplitude, short-duration bursts in electron temperature. The oscillation amplitude (RMS) is ~ 1 eV in local mode and increases to ~ 2.5 eV in global mode. As with the plasma potential measurements, further work is needed to characterize the electron temperature oscillations in global mode.

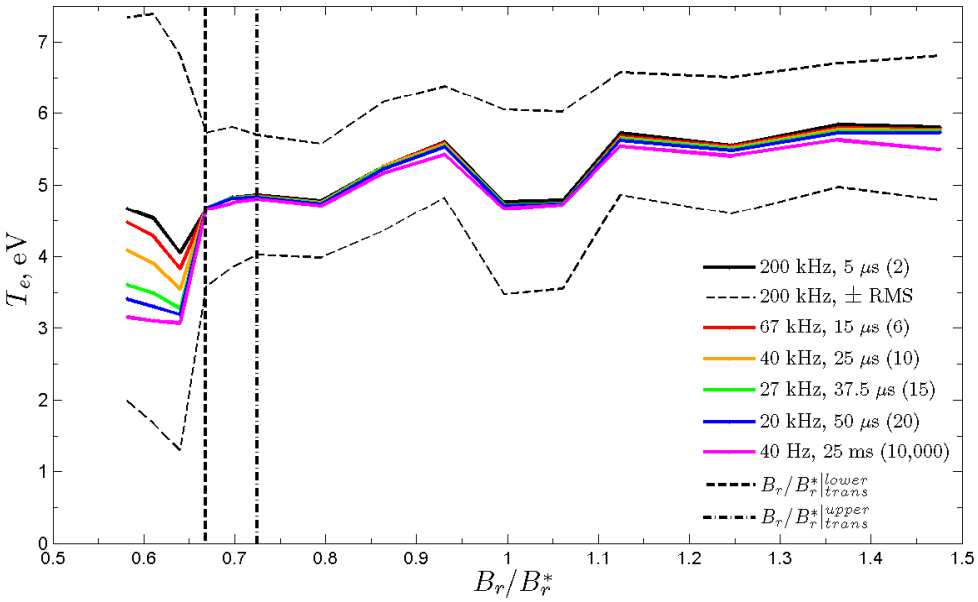

Figure 4.19: Electron temperature for 400 V, 19.5 mg/s calculated at 200 kHz, 67 kHz, 40 kHz, 27 kHz, 20 kHz and 40 Hz by averaging a different number of I-V traces together indicated by the parenthetical numbers. The transition region is shown with the oscillations in global mode ($B_r/B_r^* < 0.66$) average of time-resolved differs from time-averaged calculations. Measured by probes 1.5 R_{chnl} downstream.

4.5.4.5 Correlation of Plasma Properties

Linear correlation analysis is performed with the time-resolved plasma properties to look for trends in oscillatory parameters. Figure 4.20 shows the correlation between discharge current, ion density, electron density, plasma potential, and electron temperature during a B-field sweep for 400 V, 19.5 mg/s from HDLP-ISR measurements. Compare Figure 4.20(left) with Figure 4.14(b), with the inclusion of electron density correlation in addition to ion density. The same trends are shown where the density oscillations are not well correlated in local mode but they are well correlated in global mode. In Figure 4.20(right) the ion density and electron density are closely correlated, $\rho > 0.4$, for all settings indicating quasi-neutral plasma, as expected. The electron density and plasma potential are also closely correlated, $\rho > 0.6$ showing that the high density plasma bursts that emanate from the thruster are also higher potential. Note the correlations with plasma potential are calculated with the time resolved plasma potential-to-ground measurement since time-resolved cathode-to-ground measurements were not taken. The cross-correlation from ion density to electron temperature and electron density to electron temperature shows no correlation in local mode, $|\rho| < 0.2$. However, in global mode both are negatively correlated indicating that bursts of plasma density have lower electron temperatures.

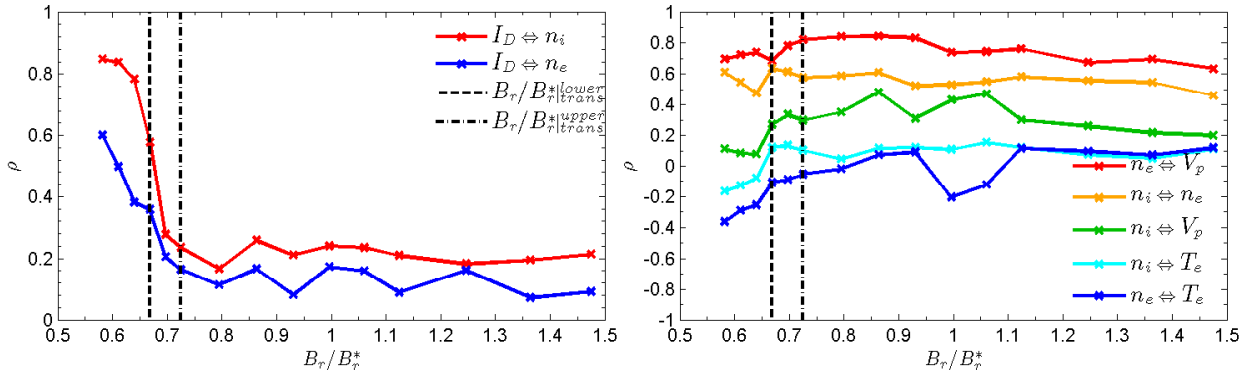

Figure 4.20: Correlation between discharge current, ion density, and electron density (left) and ion density, electron density, plasma potential, and electron temperature (right) during a B-field sweep for 400 V, 19.5 mg/s from HDLP-ISR measurements.

In summary, for local mode, oscillations in plasma density are quasi-neutral with increased density associated with increase plasma potential; density oscillations are not well correlated with discharge current oscillations and are not correlated with electron temperature. In global mode, oscillations in plasma density are quasi-neutral with increased density associated with increase plasma potential and decreased electron temperature; density oscillations are well correlated with discharge current oscillations.

4.6 Spoke Correlation to Probes

In this section the time-resolved correlation between azimuthal spokes in the discharge channel and downstream probe measurements are shown. It will be shown that the passage of a bright region called a "spoke" in front of the probe produces an increase in plasma density measured by the probe after ion time-of-flight is accounted for. In local mode, the density oscillations are correlated to the discharge channel region upstream from the probe while in global mode the density oscillations are correlated to the entire discharge channel with no localized effects.

The linear cross-correlation, ρ, is calculated between the normalized plasma density signals, $\hat{n}_i(t)$ and $\hat{n}_e(t)$, from each probe and each of the 180 azimuthal bins using Equation 3.9. The HIA process described in Chapter 3.5 discusses how the discharge channel is divided into 180 two-degree wide azimuthal bins where the light is averaged over that bin for each FastCam frame. This creates 180 time-resolved light intensity signals for the discharge channel; examples of which are shown later in Figure 5.4 when describing the spoke velocity correlation method in Chapter 5.5.2. Peaks in the cross-correlation ($\rho > 0$) indicate when the plasma density correlates well with brightness fluctuations at a particular angular location in the discharge channel. A valley ($\rho < 0$) in

the cross-correlation will indicate that the plasma density correlates well but is 180° out-of-phase with a particular angular location in the discharge channel. When $\rho \sim 0$ then no correlation exists between the density measured by that probe and a particular angular location in the discharge channel.

The light from the discharge channel travels to the FastCam and is recorded nearly instantaneously on the timescales of interest here ($\ll 1\,\mu$s). The plasma produced in the discharge channel, however, requires time to travel from the discharge channel to the probe to be measured. This time of flight, t_{TOF}, for each B_r/B_r^* is calculated from the peak cross-correlation between the discharge current and the ISR probe signal as discussed in Section 4.5.3 and shown in Figure 4.14(d). The typical time offset from I_D to $\hat{n}_i$ is 6 to 11 μs.

While the plasma is traveling downstream to the probes, the spoke that generated the plasma is continuing to propagate around the discharge channel at the spoke velocity, v_{sp}. The spoke velocity for each B_r/B_r^* is calculated in Chapter 5.5.2 using the correlation technique and is between 1500 and 2000 m/s for the cases considered here. In the time t_{TOF} that is required for the plasma to travel from the discharge channel to the probe, the spoke will have rotated Δd degrees around the discharge channel according to

$$\Delta d = \frac{t_{off} v_{sp} 180}{\pi R_{chnl}} \tag{4.11}$$

For example, Probe 1 is located 10.7° Clockwise (CW) from the 6 o'clock position of the discharge channel as shown in Figure 3.6. If the time of flight is $t_{TOF} = 8\,\mu$s and the spoke velocity is $v_{sp} =$ 1800 m/s, then according to Equation 4.11 the spoke that produced the plasma being measured at time t will have moved Counter Clockwise (CCW) by 10.3°, or almost exactly to 6 o'clock of the discharge channel by the time the signal arrives at the probe. However, if the spokes are an angularly periodic structure (a regular series of bright and dim regions) propagating around the discharge channel at the spoke velocity v_{sp}, then the probe signal will be correlated to other regions around the discharge channel that are integer wavelengths away from the probe location.

A typical global mode oscillation frequency is ~ 8 kHz as shown previously, which corresponds to a period of 125 μs. From Figure 4.14(d) the typical ion time-of-flight in global mode is $\sim 10\,\mu$s. Therefore, the probe signal will be delayed by $\sim 10\%$ of the period from the plasma oscillations observed in the FastCam, but the correlation coefficient is still expected to be greater than 0.3 even without accounting for t_{TOF}. The correlation coefficient for I_D to $\hat{n}_i$ in global mode is $\rho > 0.3$ in Figure 4.14(b) which does account for t_{TOF} by shifting $\hat{n}_i(t)$ in time to $\hat{n}_i(t - t_{TOF})$.

Figure 4.21 shows $B_r/B_r^* = 0.46$, 0.86 and 1.12 settings for the 300 V, 19.5 mg/s condition. Figure 4.22 shows $B_r/B_r^* = 0.61$, 0.93 and 1.12 settings for the 400 V, 19.5 mg/s condition. Time-resolved electron density, $\hat{n}_e(t)$, is not shown from HDLP 2 for 300 or 400 V due to signal corruption. HDLP 1 failed halfway through the the 300 V testing so $\hat{n}_e(t)$ is only shown for the 400 V

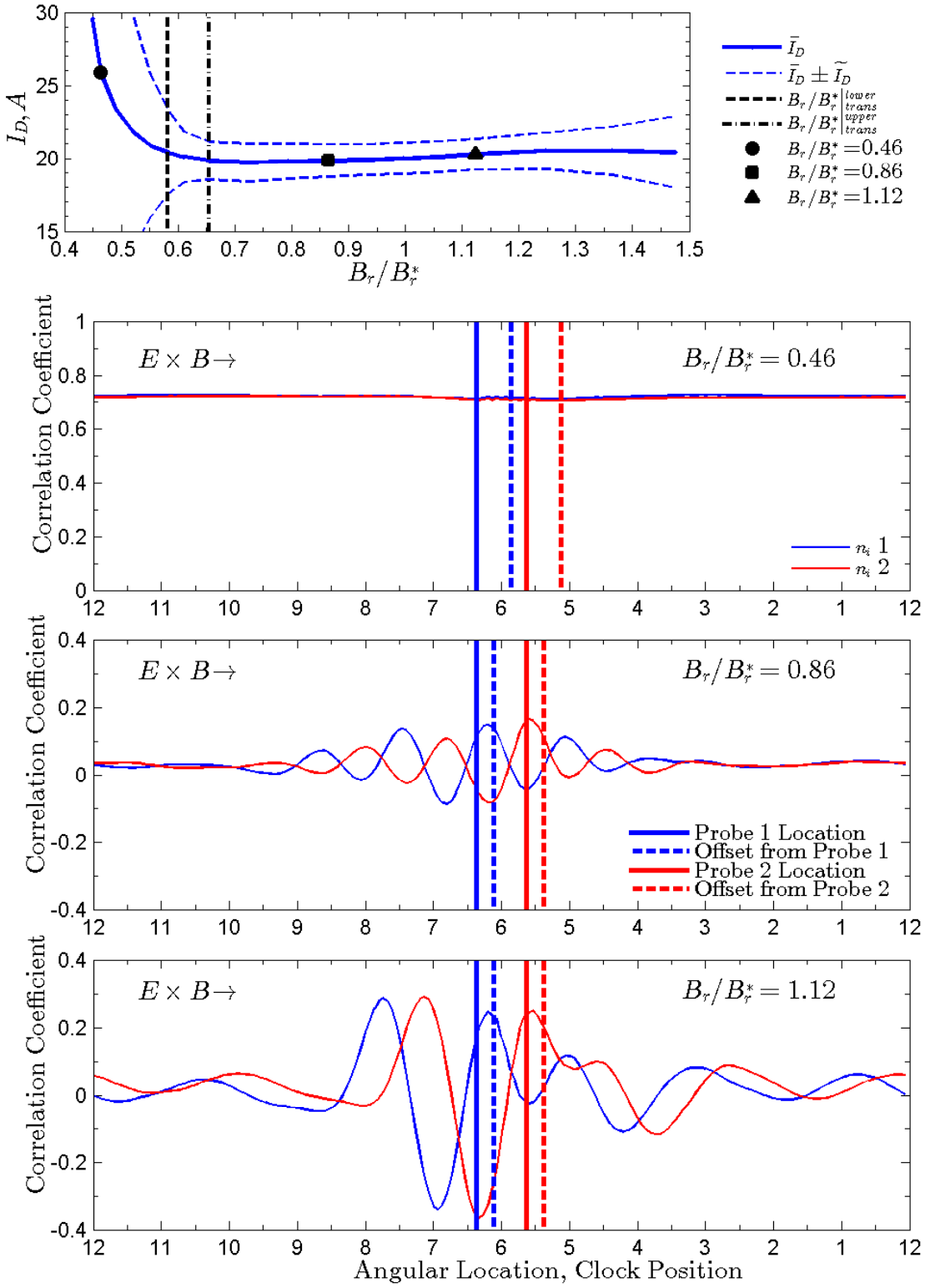

Figure 4.21: Probe to FastCam correlation at 300 V, 19.5 mg/s for B_r/B_r^* = 0.46, 0.86, and 1.12. Probe 1 is in blue and Probe 2 is in red. Ordinate is correlation coefficient, ρ, for $\hat{n}_i$ to each of the 180 azimuthal bins from the FastCam videos spoke surfaces. Solid vertical lines are probe locations and dashed vertical lines are offset locations.

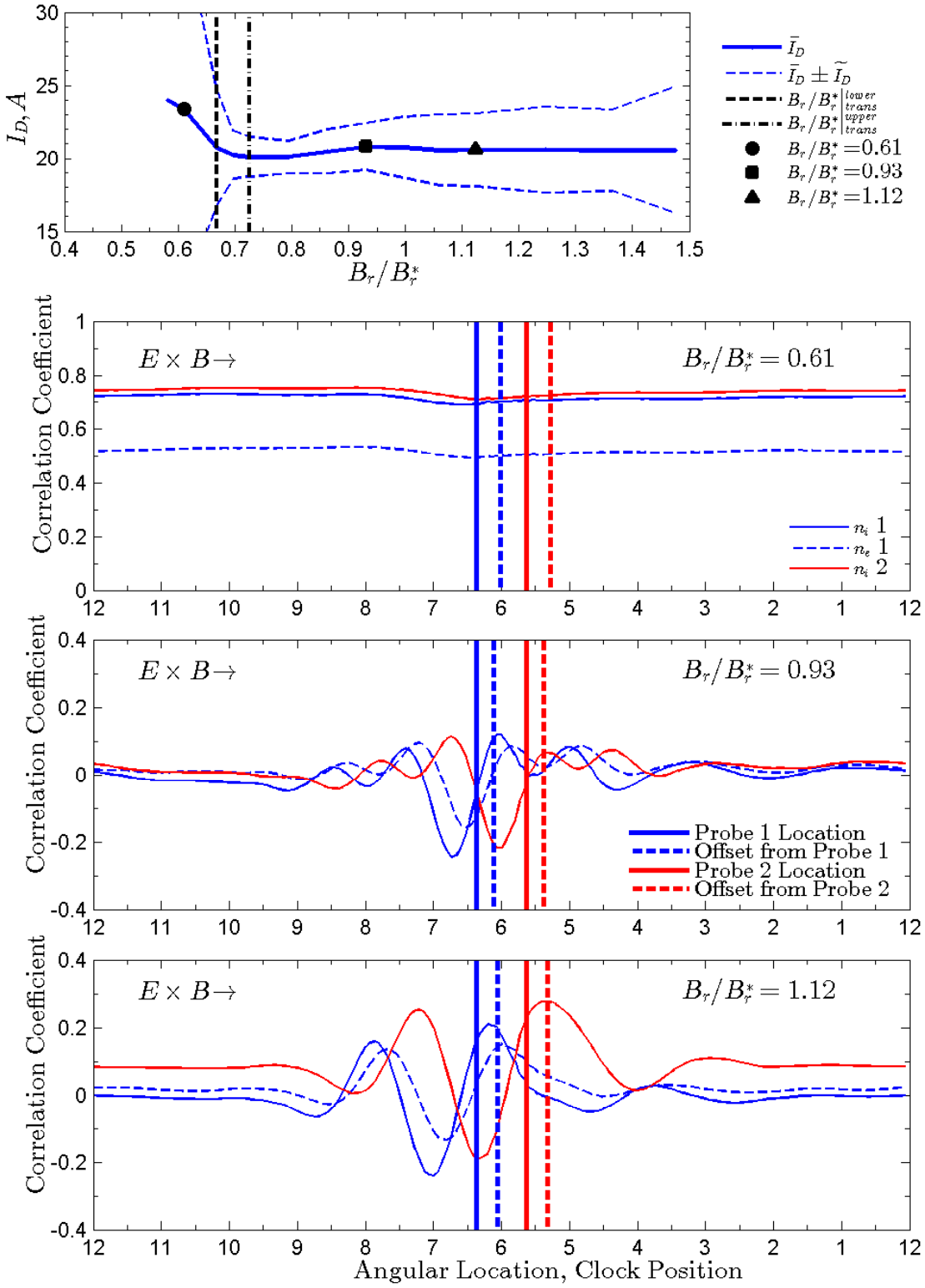

Figure 4.22: Probe to FastCam correlation at 400 V, 19.5 mg/s for B_r/B_r^* = 0.61, 0.93, and 1.12. Probe 1 is in blue and Probe 2 is in red. Ordinate is correlation coefficient, ρ, for $\hat{n}_i$ or $\hat{n}_e$ to each of the 180 azimuthal bins from the FastCam videos spoke surfaces. Solid vertical lines are probe locations and dashed vertical lines are offset locations.

case in Figure 4.22, which was completed first. The spokes propagate in the $E \times B$ direction which is CCW in the H6. In Figures 4.21 and 4.22, the discharge channel has been "unwrapped" onto the abscissa with the discharge channel 6 o'clock position in the center and the 12 o'clock position at the extrema. The CCW or $E \times B$ direction is from left to right as shown on the plots. The probe locations are denoted by solid vertical lines in Figures 4.21 and 4.22 and the offset locations Δd from the probes calculated from Equation 4.11 are denoted by dashed vertical lines. As discussed above, the spoke will continue to propagate in the $E \times B$ direction by Δd degrees in the time required for the plasma to travel to the probe. Therefore, the $\hat{n}_i$ and $\hat{n}_e$ signals are more strongly correlated to locations in the discharge channel offset from the probe locations (offset to the right in Figures 4.21 and 4.22).

The lowest B_r/B_r^* settings in Figures 4.21 and 4.22 are in global mode where the entire discharge channel is oscillating in unison. The downstream density oscillations $\hat{n}_i$ and $\hat{n}_e$ are well correlated at $\rho > 0.7$ and 0.5, respectively, to the discharge current and the FastCam signal at all azimuthal locations. Therefore, the correlation coefficient is nearly constant and shows no preference for the discharge channel region in front of the probe. This characteristic is what motivated the nomenclature of "global mode" for this type of oscillation.

In Figures 4.21 and 4.22, the higher settings of B_r/B_r^* = 0.86 and 1.12 for 300 V and B_r/B_r^* = 0.93 and 1.12 for 400 V are in local oscillation mode. They are correlated to the region of the discharge channel immediately upstream of the probes or the region upstream and slightly CW by $\sim 45-60°$. The plasma density $\hat{n}_i$ and $\hat{n}_e$ is not correlated ($\rho \sim 0$) in the rest of the discharge channel. A peak in ρ is observed near the probe location (solid lines) or offset from the probe (dashed lines). The uncertainty in the azimuthal locations is $\pm 5°$ and the typical shift is $\Delta d \sim 10°$ so an exact matching of correlation peaks to probe or offset location is not within the uncertainty, however, the trends are clear. The consistent result is that ρ peaks at the probe or offset location indicates that a peak in brightness in the discharge channel at time t produces an increase in plasma density that propagates downstream to be measured by the probe at time $t + t_{TOF}$. This trend was observed for all magnetic field settings in local mode except for those near the transition region to global mode. Close to the transition the correlation peaks do not line up with the probe locations or offset locations, which is another indicator that the plasma oscillations begin to fundamentally change in mode transition. This observation requires further study to quantify and determine the physical meaning.

In local mode the signal is not as well correlated ($\rho < 0.3$) as the global mode ($\rho > 0.7$), which is likely related to the turbulent nature of the plasma plume. In global mode only one dominant oscillation exists, but in local mode many different oscillations likely exist in addition to the azimuthal spokes. Figures 4.21 and 4.22 shows that $\hat{n}_i$ and $\hat{n}_e$ are well correlated to light intensity in the discharge channel one wavelength of the dominant spoke order in the CW or $-E \times B$ direction.

This could be indicative of the ions being slightly magnetization so that the plasma spirals out of the thruster in a helical pattern and could be the source of the so-called “swirl torque” observed by flight systems. [35]

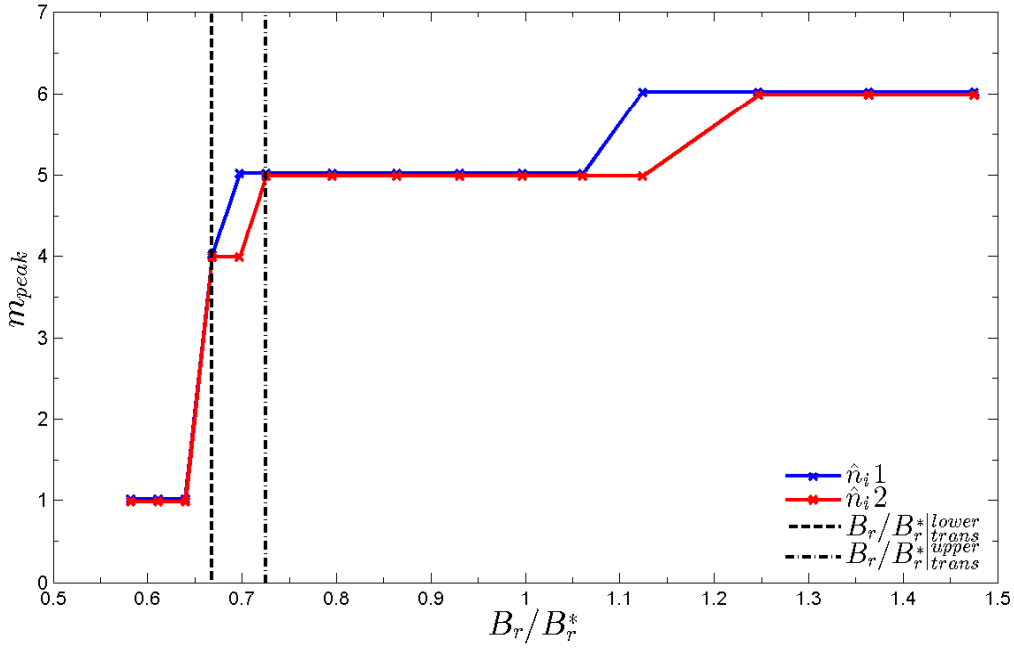

Figure 4.23: Dominant spoke order from the peak in PSD of the correlation between $\hat{n}_i$ 1 and 2 to FastCam for 400 V, 19.5 mg/s. The dominant spoke order is $m = 6$ for the higher magnetic field in local mode and $m = 5$ before the transition region. The dominant spoke order decreases through the transition region $0.67 < B_r/B_r^* < 0.73$ and is not applicable in global mode ($B_r/B_r^* < 0.67$).

The distance between peaks in ρ observed for local mode in Figures 4.21 and 4.22 indicate the dominant spoke wavelength or spoke order for that B_r/B_r^*. The wavelength for a given spoke order, λ_m, must be an integer factor of the discharge channel mean circumference, $\lambda_m = 2\pi R_{chnl}/m$. Calculating the PSD of ρ using Equation 3.40 will yield the relative strength of each m and the peak in PSD will be the dominant spoke order. Figure 4.23 shows the dominant m for the 400 V condition for each B_r/B_r^*. It was previously shown in Figures 4.9 and 4.12 that higher spoke orders are dominant at higher B_r/B_r^*. Figure 4.23 confirms this finding where $m = 6$ is dominant for $B_r/B_r^* > 1.25$ and $m = 5$ is dominant for $0.73 < B_r/B_r^* < 1.06$. The spoke order decreases in the transition region and is not applicable for global mode $B_r/B_r^* < 0.67$.

In conclusion, the correlation between $\hat{n}_i$ and $\hat{n}_e$ and the FastCam generated spoke surface has shown that peaks in light intensity in the discharge channel create increases in plasma density that propagate downstream. The plasma density is also correlated to the discharge channel one

wavelength in the $-E \times B$ direction. Identifying the most significant sine wave by calculating the PSD of $\rho(\theta)$ yields dominant spoke order and is typically $m = 5$ or 6.

4.7 Plume Brightness Response to Mode Transition

4.7.1 Plume Shape and Brightness Contours

Digital photographs of the plume were taken from a view port at a nearly 90° angle with respect to thruster centerline. Photographs at different B_r/B_r^* settings in Figure 4.24 qualitatively show the plasma plume evolution during mode transitions. The viewing angle was slightly upstream so the discharge channel was visible very obliquely. The photos with accompanying contours were modeled after Figure 1 of Brown [41] which also qualitatively showed plume shape changes between modes. The contours show relative light intensity calculated from a grayscale version of the image where 1 is the brightest and 0 is dark. Note the probes can be seen as vertical lines of intensity ~ 0.2 in the plume at 1.5 channel radii downstream near the bottom of the picture and should be disregarded. Visible brightness is important because it indicates excited energy states caused by collisions. So although qualitative, the brightness of the plume is representative of the plasma physics occurring in the near-field region. Here we define the near-field plume region as the plasma directly downstream from the discharge channel to a few channel widths; the far-field plasma is the plasma outside of the near-field region.

In global oscillation mode where $B_r/B_r^* = 0.46$ in Figure 4.24, the discharge channel is very bright with relative intensity 1 and the center spike of plasma extending along thruster centerline. The spike extends downstream over 1 channel diameter and dominates the plume. As B_r/B_r^* is increased to 0.61 at the transition point, the center spike recedes, but the discharge channel is still very bright at 1. At the reference magnetic field setting, $B_r/B_r^* = 1.0$, where the thruster is in localized oscillation mode, the center spike is not present although the plasma from the cathode is still visible on centerline. The relative light intensity visible in the channel is only 0.6 to 0.7, which means the near-field plasma is less collisional and the collisions are likely occurring deeper within the channel where they are not visible to the camera. At $B_r/B_r^* = 1.48$, the discharge current oscillation amplitude is greater and the plume is again brighter downstream, but the channel relative brightness is still only 0.6 to 0.7. In general, the plume recedes as B_r/B_r^* is increased and the transition from global oscillation mode to local oscillation mode occurs. This may indicate fewer collisions and other processes are occurring in the near-field plume and are more confined to within the discharge channel. These observations seem to contradict the results in Figure 4.18 where plasma potential measurements indicate the acceleration zone is moving farther into the channel or compressing more in global mode where one would expect the brightness to decrease. However,

as discussed in Section 4.5.4.3, there are large amplitude plasma potential peaks that coincide with the discharge current peaks so during a burst of plasma in global mode the acceleration zone is stretched further downstream and may be responsible for the increased brightness.

The same B-field sweep was conducted with the cathode mounted externally, as shown in Figure 4.25. The cathode was mounted above the thruster at the 12 o'clock position with cathode centerline 32 mm above the outer pole radius. For the low magnetic field setting, $B_r/B_r^* = 0.48$, the plume brightness extends downstream with the central spike dominating the plume structure. As B_r/B_r^* is increased to 0.57, the plume recedes towards the channel with some vestige of the center spike remaining. Both settings are in the global oscillation mode and the discharge channel relative brightness is 1. Increasing B_r/B_r^* above the transition point into local oscillation mode the center spike disappears and the discharge channel relative brightness is only 0.6 to 0.7. The transition point for the external cathode case is higher $B_r/B_r^* = 0.65$ (not shown in Figure 4.25) than the internal case, where $B_r/B_r^* = 0.61$. The plume now extends out primarily along the channel indicating the plasma is well focused from the discharge channel downstream. Note the probes are present at the bottom and a reflection from the LVTF viewport sacrificial glass is visible as a vertical perturbation 1 channel radii downstream; both should be disregarded. For the external cathode case at 300 V, 19.5 mg/s, B_r/B_r^* was first swept from 1.48 to minimum and then increased again showing repeatability; the photos shown in Figure 4.25 are during the down sweep portion.

4.7.2 Optical Spectroscopy

Despite differences between the A53 thruster discussed in Section 2.4 and the H6 or SPT-100, the changes in plume shape shown in Figure 4.25 from global mode to local mode are remarkably similar to the "spike" mode and "swallow tail" mode, respectively, shown in Figure 4.26 reproduced from Ref. 133. Two different operating conditions were tested for the A53 and the mode transition from swallow tail to spike mode caused a 16% increase in mean discharge current for both conditions, which also agrees with the local to global mode transitions discussed in Section 4.4. In swallow tail mode, the ionization zone is deeper in the channel with fewer neutrals observed by the channel exit. Spike mode is noted to be visibly brighter similar to global mode here. Images with different filters in Figure 4.26 show that the increased brightness on thruster centerline in spike mode is primarily due to excited Xe ion states and the increased brightness by the thruster exit plane is associated with both excited neutrals and ions. The plume has larger divergence in spike mode so the point where ion trajectories converge on thruster centerline is closer to the channel exit (75 mm instead of 125 mm) and creates the bright central region (i.e. spike). Using optical spectroscopy and Abel inversion, Roche [133] was able to quantify the light intensity increase of the center spike for Xe +1 ions using the 529.2 nm line as shown in Figure 4.27.

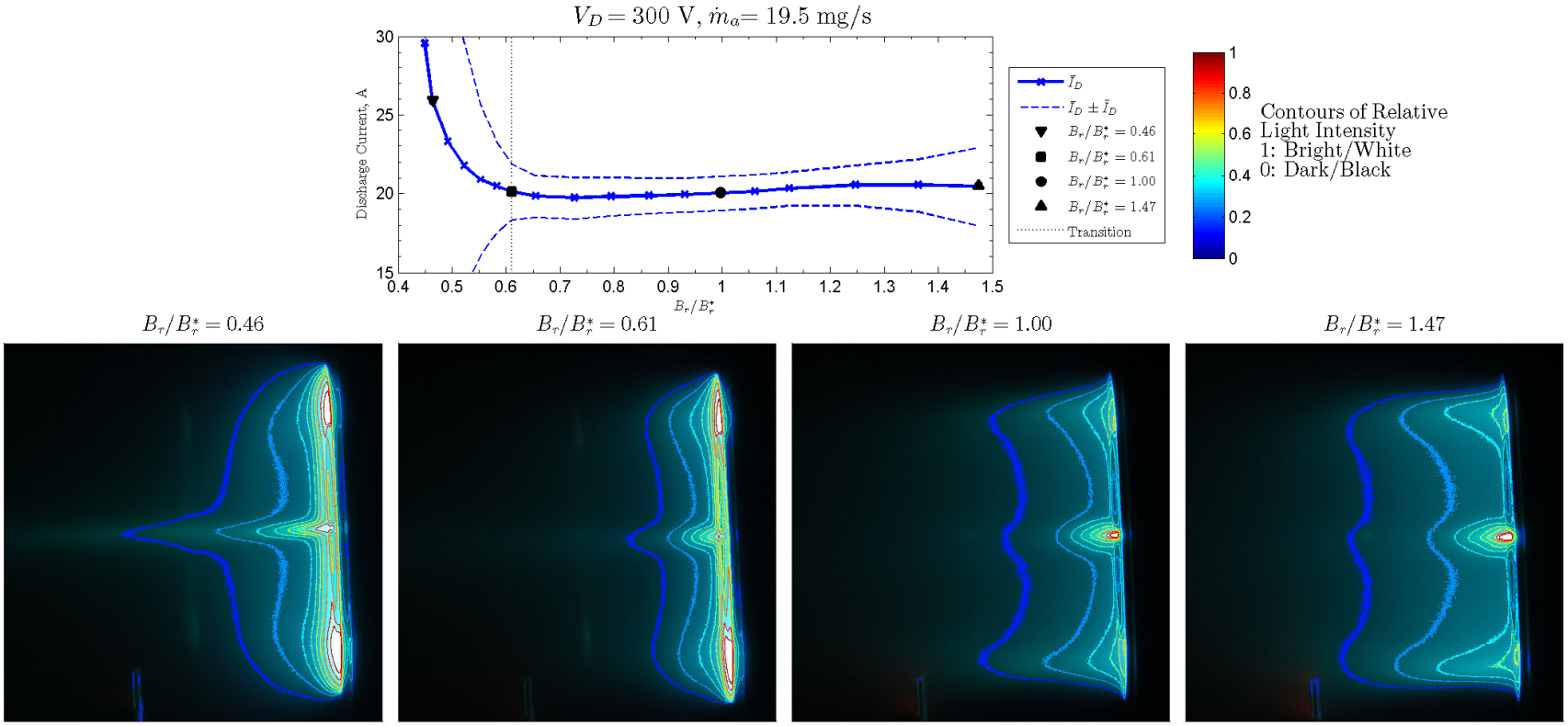

Figure 4.24: Plume photos showing light intensity during B-field sweep with the internal cathode at 300 V, 19.5 mg/s. Contours of relative intensity are shown to qualitatively illustrate the change in plume shape. Note the probes are present 1.5 channel radii downstream at the bottom and should be disregarded.

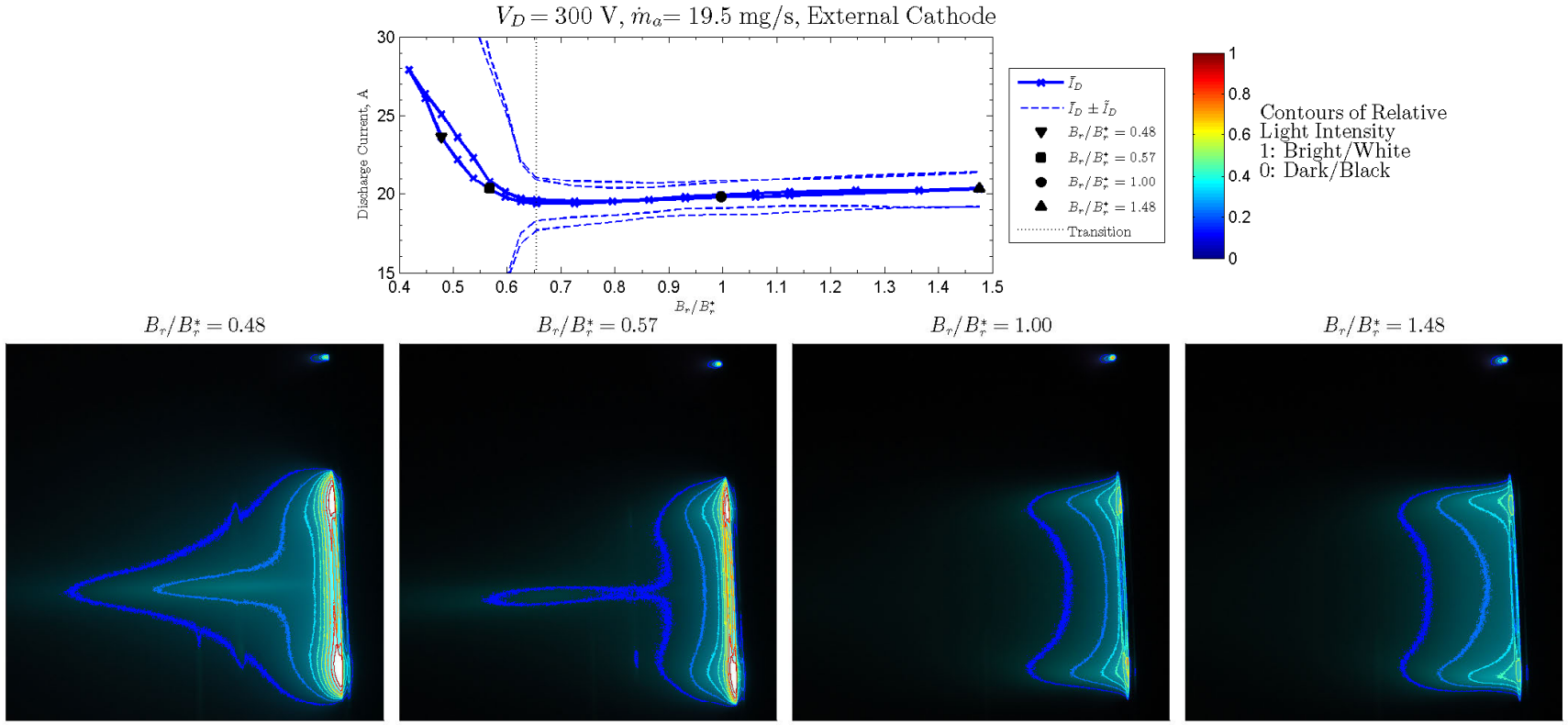

Figure 4.25: Plume photos showing light intensity during B-field sweep with the external cathode at 300 V, 19.5 mg/s. Contours of relative intensity are shown to qualitatively illustrate the change in plume shape. The probes are present at the bottom and a reflection from the LVTF viewport sacrificial glass is visible as a vertical perturbation 1 channel radii downstream, both should be disregarded. B_r/B_r^* was first swept from 1.48 to minimum and then increased again. The cathode is visible above the thruster at the 12 o'clock position.

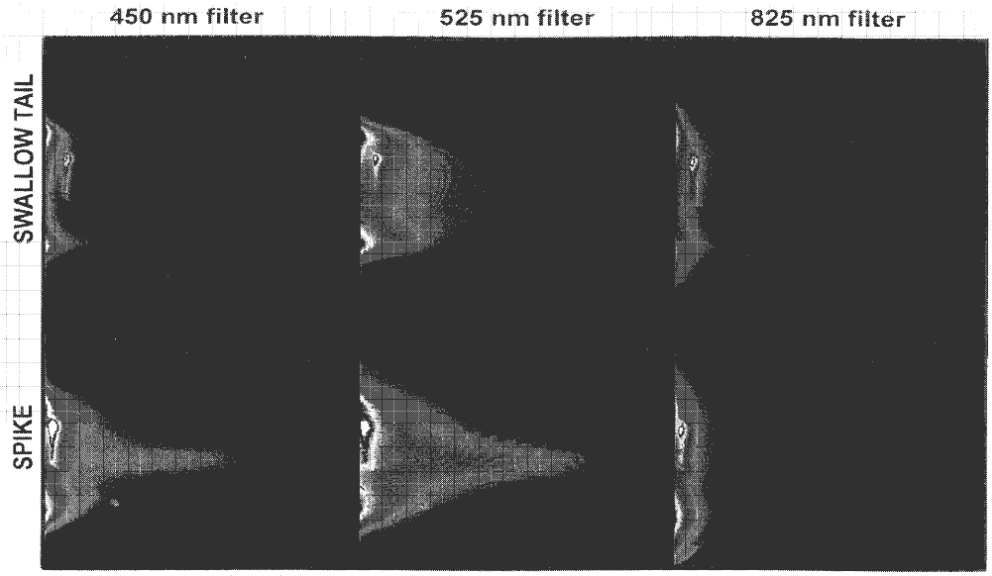

Figure 4.26: A53 plume images with three different filters (450, 525 nm: Xe ion excited states; 825 nm: Xe neutral excited states) in swallow tail mode (top) and spike mode (bottom). Reproduced from Figure 9 of Ref. 133

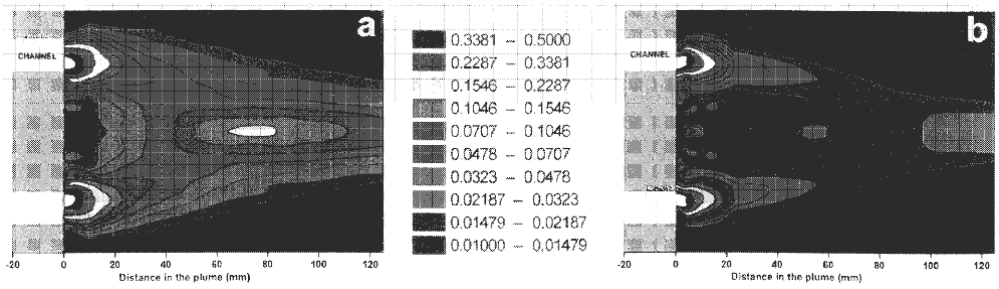

Figure 4.27: A53 plume light intensity for Xe+1 529.2 nm in the plume obtained from Abel inversion for (a) spike mode and (b) swallow tail mode. The scale is logarithmic. Reproduced from Figure 10 of Ref. 133

The photographs of Figures 4.24 and 4.25 clearly show a change in light intensity in the near-field plume region after mode transition. Referencing optical emission characteristics for xenon in arbitrary units, [134] neutral xenon dominates in the light blue to cyan portion of the visible spectrum (approximately 470 to 500 nm) with lines of 500+ intensity at 473, 481 and 492 nm. Xenon +1 ions dominate in the violet to blue portion of the spectrum (approximately 430 to 470 nm) with lines of 1000 intensity at 433 and 446 nm. Xenon +1 ions also have a strong 1000 intensity line at 508 nm in the cyan to green portion of the spectrum. Xenon +2 ions do not have any lines greater than 100 intensity in the 430 to 520 nm bandwidth. Neither the human eye nor a standard digital camera are a calibrated optical spectrograph, but the plume is clearly blue in hue showing the combination of xenon neutral and +1 ions wavelengths. The blue hue of the plume extends outward (farther downstream) after the transition to global mode indicating that increased collisionality is occurring outside of the discharge channel. The luminosity is determined by collision rates (here we assume electron to neutral or electron to ion), which are functions of the particle densities (neutral, electron or ions) and collision cross-sections (determined by electron temperature). Therefore, increased brightness after mode transition may indicate increased densities outside the channel or a change in electron temperature (increase or decrease depending on how cross section varies with electron temperature). However, the results in Figure 4.19 show that electron temperatures decrease after mode transition, so increased density is likely the cause. If the increased luminosity is neutral lines (light blue to cyan), this may result from more neutral atoms escaping the discharge channel, indicating the ionization zone is pushed out from the channel. If the ionization zone and plasma potential are pushed outside of the channel in global mode then the possibility exists that ions could be accelerated at nearly the discharge potential to very large incidence angles (up to $\sim 90^{\circ}$ degrees) from thruster centerline.

4.7.3 Differential Brightness

The change in light intensity with respect to magnetic field streamlines can yield qualitative information about the plume change between transitions. Photographs of the thruster in the external cathode configuration are shown in local mode ($B_r/B_r^* = 1.00$) and global mode ($B_r/B_r^* = 0.47$) in Figure 4.28(a) and (b), respectively. Magnetic field streamlines are shown overlaid in Figure 4.28 for reference. Figure 4.28(a) shows the plasma in local mode is well columnated on discharge channel centerline with negligible brightness on thruster centerline. Figure 4.28(b) shows the plasma in global mode where the bright centerline spike appears with additional brightness extending radially out from the discharge channel along the outer-pole.

To accentuate the differences in plume brightness between modes, the images are loaded into Matlab, converted to gray scale values, and subtracted. The resulting relative brightness difference

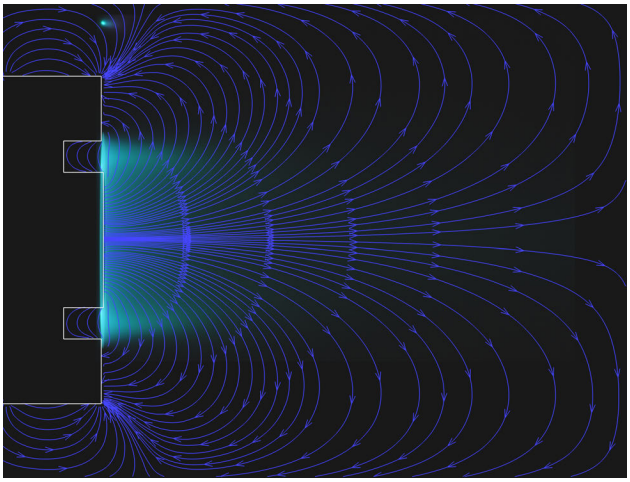

(a) Local Mode: $B_r/B_r^* = 1.00$

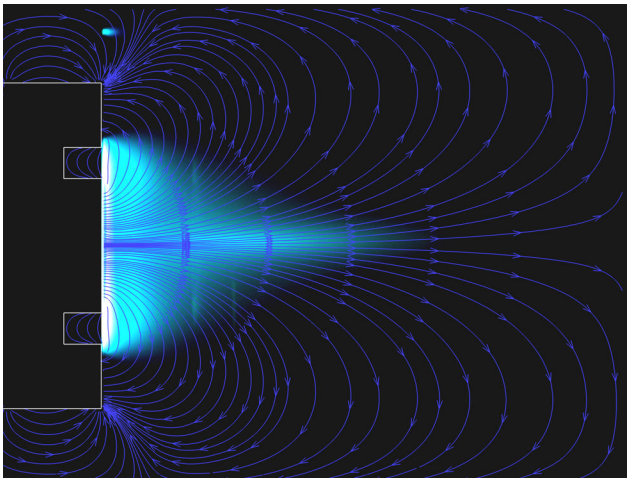

(b) Global Mode: $B_r/B_r^* = 0.47$

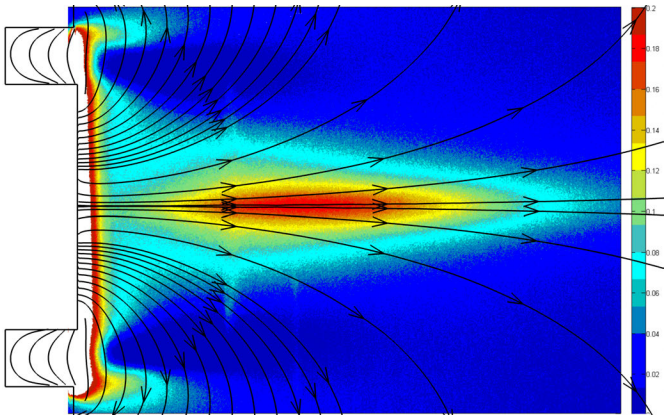

(c) Difference in light intensity.

Figure 4.28: Light intensity for 300 V, 19.5 mg/s with an external cathode in global and local mode. Magnetic field stream lines shown for reference.

is shown in Figure 4.28(c) with magnetic field streamlines overlaid. The brightness contour values are percent difference between modes where the red region indicates the global mode is 20% brighter than local mode. The anomalous vertical distortion is from light reflection on the LVTF view port and should be disregarded. Figure 4.28(c) clearly shows the spike on thruster centerline that appears approximately $z/R_{chnl} \sim 1$ downstream and extends to $z/R_{chnl} \sim 3$. The upstream shape of the spike (the end pointing towards the thruster) is approximately defined by the magnetic field stream lines emanating from thruster centerline. There is very little change in plume brightness on discharge channel centerline more than one channel width downstream from the exit plane. "Wings" of brightness emanate from the discharge channel radially outward. This likely represents plasma that is exiting the channel with large divergence or a significant velocity component in the radial direction. This increased divergence would represent a decrease in thruster efficiency. Increased divergence between modes for low-voltage operation of the H6 was noted in Table 2 of Ref. 41 where the plume half-angle increased by as little as 1° to as much as 5° from "low-current" (local) to "high-current" (global) mode.

The center spike could possibly be explained by far-field electrons on thruster centerline entering the near field plasma realm. Consider far field electrons ($z/R_{chnl} > 5$) that are trapped on the magnetic field lines from the center of thruster, which extend far downstream and meet back up at the separatrix ($r/R_{chnl} > 1$). As the electron approaches the thruster, the magnetic field strength increases very similar to a magnetic mirror. If on average the electrons are reflected before any significant collisional processes can occur, then no light will be emitted on thruster centerline. However, as the magnetic field is decreased, the strength of the magnetic mirror decreases and electrons on average will be reflected closer to the thruster. If the electrons do encounter significant collisions due to increased neutral or plasma density closer to the thruster, then light will be emitted and a center spike will be visible. Therefore, this could be evidence of electrons "bouncing" on magnetic field lines far downstream, but further investigation is required and suggested in Section 7.2.

4.8 Performance Response to Mode Transition

Thrust was measured during B-field sweeps at 300 V for anode mass flow rates of 14.7, 19.5 and 25.2 mg/s. Thrust-to-power and anode efficiency are calculated with Equations 2.23 and 2.24, respectively. For the 14.7 mg/s case shown in Figure 4.29, the mean value for the thrust is 281 mN with a standard deviation of 3 mN, which is within the uncertainty of 7 mN or 2.5% of the mean value. Therefore, the thrust was constant within experimental error during the B-field sweep at this condition. The discharge current, however, increased below the transition point at $B_r/B_r^* = 0.54$ from 14 A to 19 A at $B_r/B_r^* = 0.39$. With a constant discharge voltage of 300 V, the increase

in discharge current indicates an increase in power to the thruster so the thrust-to-power, T/P, decreases significantly in global oscillation mode. The peak T/P of 67 mN/kW occurs between $B_r/B_r^* = 0.64$ and 0.79 and decreases to 50 mN/kW at the minimum magnetic field, representing a 25% decrease in T/P.

Since thrust is constant or nearly constant, the increased discharge current is almost entirely excess electron current to the anode. This is supported by low-voltage H6 operation in Table 2 of Ref. 41 where the current utilization efficiency decreased by as little as 0.04 to as much as 0.1 from "low-current" (local) to "high-current" (global) mode. As the B-field is decreased, the cross field resistivity decreases, therefore increased current across the magnetic field lines is expected. However, the mode transition marks a percentage of discharge current increase that is disproportionate to the B-field decrease. While the discharge current increase as B-field decreases is expected, the difference in plasma oscillations may be responsible for the significant increase in discharge current i.e. increased electron transport across magnetic field lines.

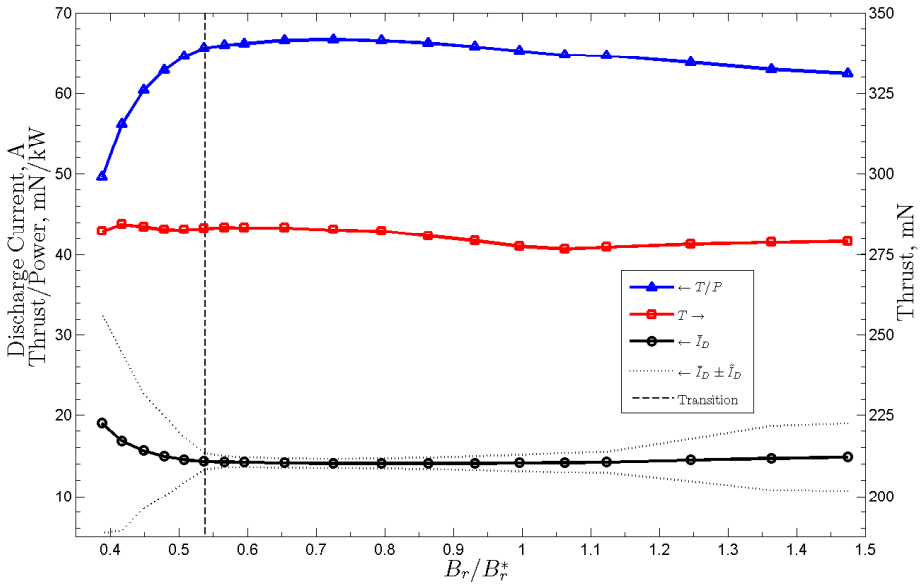

Figure 4.29: Thrust and T/P for 300 V, 14.7 mg/s during B-field sweep. The thrust is constant at 281 mN within experimental error, but the T/P decreases below the transition point as the discharge current increases.

Figure 4.30 shows all flow conditions for 300 V with transition regions as shaded areas on all plots. Figure 4.30(b) shows the mean thrust was 281, 379 and 507 mN for 14.5, 19.5 and 25.2 mg/s, respectively. Figure 4.30(c) shows the peak thrust-to-power was 67, 64 and 61 mN/kW for 14.5, 19.5 and 25.2 mg/s, respectively. Figure 4.30(d) shows the peak anode efficiency was 65%, 63% and 63% for 14.5, 19.5 and 25.2 mg/s, respectively. The uncertainty on the thrust measurements

shown as error bars in Figure 4.30(b) for the 14.7 and 25.2 mg/s case is conservatively estimated to be 7 and 10 mN, respectively. Unfortunately, for the 19.5 mg/s case a zero point was not acquired after the thruster reached equilibrium and before data acquisition, but a zero was acquired immediately after data acquisition. This condition was a down and back B-field sweep where the B_r/B_r^* was decreased from 1.48 through mode transition and then increased back to 1.48. The discharge current tracked during the down sweep and up sweep with a less than 4% difference at any one point in global mode and less than 1% difference at any one point in local mode as shown in Figure 4.30(a). Therefore, the zero before data acquisition was estimated using the post data acquisition zero and the assumption that the thrust was the same for the down sweep and up sweep (similar to discharge current), with a conservatively estimated 20 mN uncertainty. As shown in Figure 4.30(b), this yielded a constant thrust throughout the sweeps (in local and global mode) to within 3% which is very similar to the 14.7 mg/s condition. The thrust for the 25.2 mg/s condition increased with decreasing magnetic field from 482 to 518 mN, which is a ~7% change. Figure 4.30(b) shows that the thrust was not affected by mode transition. Zero points were appropriately taken before and after the B-field sweeps so the increase in thrust is likely not a thermal drift.

Figure 4.30(d) shows that from $B_r/B_r^*|_{trans}^{lower}$, the anode efficiency for 14.7 mg/s decreases from 64% to 48%, for 19.5 mg/s decreases from 62% to 50% and for 25.2 mg/s decreases from 62% to 53%. While significant, these numbers are a worst case because the percentage decrease is related to how deep into global mode the thruster is operated. The most important aspect of this analysis is the observation in Figure 4.30(c) and (d) that the peak in thrust-to-power and anode efficiency typically occurs at B_r/B_r^* just larger than $B_r/B_r^*|_{trans}^{upper}$ and not the reference magnetic field setting of $B_r/B_r^* = 1$. Therefore, thruster performance is typically maximum near the transition point, but once the thruster transitions from local mode to global mode the performance decreases significantly with a further decrease in B_r/B_r^*.

4.9 Definition of Modes

Here we define the modes by their plasma oscillation characteristics, where most conditions should be satisfied to represent either mode. An attempt is made to quantify the mode metrics, but the criteria values are meant only as a guide and not rigid discriminators. These criteria are based on the above observations of the H6 and are likely different for other HETs, but since mode transitions have been observed in other thrusters a subset of the criteria below should apply. These definitions delineate the thruster behavior when in either mode, but a less well-defined transition region exists from $B_r/B_r^*|_{trans}^{lower}$ to $B_r/B_r^*|_{trans}^{upper}$. In this transition region, the thruster does not meet all of the cri-

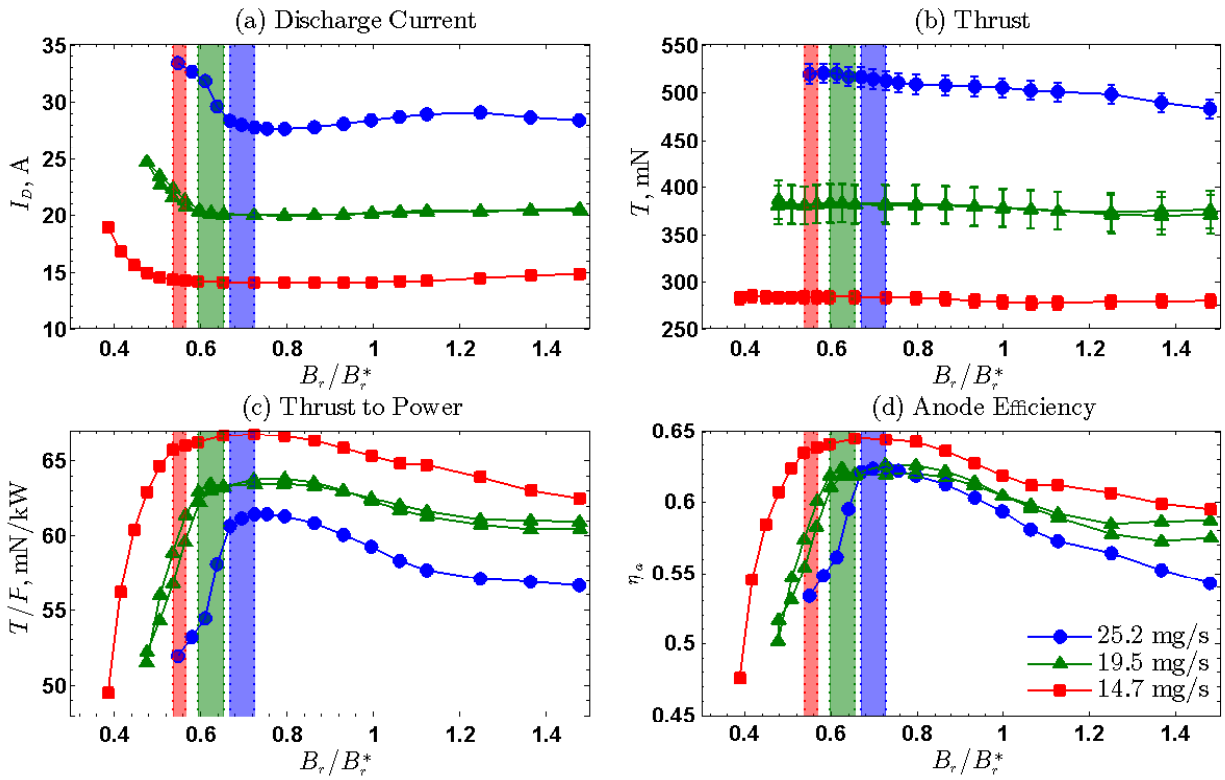

Figure 4.30: (a) Discharge current, (b) thrust, (c) thrust-to-power, and (d) anode efficiency for 300 V discharge and anode flow rates of 25.2 (blue), 19.5 (green) and 14.7 (red) mg/s. The shaded regions are the transition regions for a particular anode mass flow rate. The error bars on the thrust measurements in (b) are estimated uncertainties.

teria for either mode and the HIA clearly shows the thruster jumping between modes as evidenced from $B_r/B_r^* = 0.61$ in Figure 4.9. The criteria for identifying modes are given in Table 4.2.

4.9.1 Global Mode

The discharge current density in the entire channel is oscillating in unison with peak values of order 100% of the mean value and azimuthally propagating perturbations are either entirely absent or of negligible magnitude with respect to the discharge current density peaks. The m_0 mode of the HIA PSD has a clearly defined peak value and spoke orders $m > 1$ do not have peaks more than an order of magnitude above the general noise floor. Azimuthally spaced probes do not observe delays in plasma property oscillations indicative of the entire channel luminosity or current density oscillating in unison, and are well correlated to the discharge current with $\rho > 0.3$. The discharge current oscillation amplitudes (RMS) are well above 10% of the mean discharge current value and the mean discharge current is over 15% higher than the minimum discharge current

value obtained in a sweep. The discharge channel and near-field plume regions are observed to be brighter, indicative of increased collisions in the plume; a spike of bright plasma is visible on thruster centerline.

4.9.2 Local Mode

The discharge current density oscillations are dominated by localized perturbations that are less than 25% of the mean value and propagate in the $E \times B$ direction. Oscillations may be present where the entire channel luminosity or discharge current increases or decreases in unison, but they are sporadic and do not dominate the azimuthal propagations. The m_0 mode of the HIA PSD has a very broad peak value and spoke orders $m > 1$ have peaks more than an order of magnitude above the general noise floor. Azimuthally spaced probes observe clear delays in plasma property oscillations indicating localized regions of increased ionization within the discharge channel propagating downstream. The probe signals are not well correlated to the discharge current with $\rho < 0.3$. The discharge current oscillation amplitudes (RMS) are less than approximately 10% of the mean discharge current value and the mean discharge current is within 15% of the minimum discharge current value obtained in a sweep. The discharge channel and near-field plume regions are observed to be dimmer, indicative of decreased collisions in the plume and collisional processes more confined to within the discharge channel. The plasma is well focused on discharge channel centerline and the center spike of plasma is absent for an external cathode or greatly diminished for an internal cathode. Note that an internal cathode will always produce a spike on thruster centerline because it is a plasma source.

4.9.3 High B-field Mode

The plasma oscillations in the discharge channel show different characteristics for high magnetic fields that may be indicative of yet another operational mode. Previous simulations and experiments have observed changes in oscillations at high magnetic fields. In recent hybrid direct-kinetic simulations on an SPT-100, increasing the magnetic field oscillation above a threshold induced oscillations that Hara called the strong ionization mode. [34] In the first classification of modes, Tilinin [61] also noted larger oscillations in discharge current at high magnetic field settings that he called macroscopic instability or magnetic saturation regimes. It should be noted the device used in Tilinin's study pre-dated the SPT-100 and these results may have limited applicability.

Figure 4.9 shows that as the magnetic field is increased, the spoke order increases, the spoke duration decreases and low-amplitude oscillations occur throughout the channel. Additionally, Figures 4.2 and 4.3 show the discharge current RMS increases at high magnetic field settings for all conditions except 300 V, 25.2 mg/s. Finally, as will be shown later in Figure 5.11, the spoke

velocity becomes independent of magnetic field for $B_r/B_r^* \gtrsim 1$. The transition to this mode is not as sharp as the distinct transition between global and local mode. A qualitative explanation can be offered if collisional drift waves are responsible for azimuthal spokes. In discussing collisional drift waves, Bellan notes [135] "plasmas with strong magnetic fields tend to have turbulent, short perpendicular wavelength drift waves, whereas plasmas with weak magnetic fields have coherent, long perpendicular wavelength drift waves." However, the differences in magnetic field strength we are considering are factors of 2 or less and not orders of magnitude different. Regardless, this could indicate that the high magnetic field settings are a turbulence dominated oscillation mode.

4.9.4 Magnetically Shielded Thrusters

The modes described in this section and criteria listed in Table 4.2 apply to non-magnetically shielded thrusters. Using HIA techniques only, a similar investigation to the one detailed in this chapter was performed on two magnetically shielded thrusters with the results presented in Appendix C. Detailed analysis and discussion is reserved for that section where the oscillatory modes of magnetically shielded thrusters show similar mode transition to global mode, but no spokes are observed in the equivalent local mode. Spokes do not appear until the equivalent of the high B-field mode for non-shielded thrusters. The cathode oscillation that is identified in Appendix B and is barely perceptible in non-shielded thrusters is dominant in magnetically shielded thrusters.

4.10 Impact to Thruster Characterization

4.10.1 Thruster Characterization Testing

The 25% decrease in thrust-to-power during mode transition for the 14.7 mg/s case was similar to the results of the low voltage investigation of Brown. [41] The minimum mean discharge current typically occurred in local mode right before the transition region as shown in Figures 4.2 and 4.3. Similarly, the peak T/P and anode efficiency occurs near the transition point in Figure 4.30 where the thruster is on the verge of entering global oscillation mode. If one were to choose magnetic field settings for flight operation based on maximizing T/P or minimizing $\bar{I}_D$, then the thruster would be operating near the transition point where any perturbation in magnetic field (due to pole piece B-H properties changing over time, magnetic coils degrading, etc.) or changes in wall geometry and properties (due to erosion, coating from sputtered material, etc.) during the mission could cause the thruster to be more sensitive to transitioning from local oscillation mode to global oscillation mode. The B-field sweeps shown in Figures 4.2 and 4.3 were constant and repeatable across several pump downs, but will likely change during the life of the thruster. This is more likely to be true if the

transitions are related to wall effects where the plasma properties near the wall (i.e., susceptibility to space charge saturation) may change as the wall erodes. Therefore, discharge current versus B-field curves, while very repeatable during this test campaign, are likely only snapshots and may change after thousands of hours of operation. The most important take-away from this investigation is a new perspective on performance mapping of thrusters. Figure 4.4 shows that the transition point occurs at higher B-field for increased anode flow rate or discharge voltage. Discharge current versus discharge voltage mapping ($I_D - V_D$) are commonly performed on thrusters at beginning of life or after thousands of hours of operation. However, more insight into thruster performance and stability margins is gained by also mapping B-field to generate or $I_D - V_D - B$ maps for different flow rates and possibly even different facility background pressures over the entire range of I_D and V_D. Using these results it can be assured that thrusters are not operated near a transition point where the thruster unintentionally enters global oscillation mode and decreases thruster performance. In general, the thruster is more sensitive to mode transitions caused by magnetic field changes for *higher* mass flow rate or *higher* discharge voltage. As discussed in Section 2.4, there can be many causes for mode transition besides magnetic field variations used in this investigation, including CFF variations. Based on Brown's work for low-voltage operation, [41] the thruster is more senstitve to mode transitions caused by CFF changes for *lower* mass flow rate or *lower* discharge voltage.

The body of research presented here underscores the importance of knowing where transition points are and how to control the mode of operation. It also highlights that optimal thruster operation is obtained when the ionization front is stabilized in the discharge channel (i.e. breathing mode is damped), which will be discussed in Chapter 6. Below is a list of recommended improvements for thruster design and for more comprehensive thruster characterization to compare ground test performance to in-flight performance.

1. New thruster designs should have magnetic circuits with more capability and not be designed near saturation for the pole pieces. This will allow a wide range of variation in the magnetic field magnitude without altering the shape.

2. A transition surface should be empirically determined similar to Figure 4.6 for a range of expected operating conditions. This should be performed at beginning-of-life and at regular intervals.

3. $I_D - V_D - B$ surfaces should be calculated for each flow rate similar to Figure 4.31. This should be performed at beginning-of-life and at regular intervals. Determine the values of $\bar{I}_D$ and $\widetilde{I}_D/\bar{I}_D$ that are representative of stable regions that can be used as metrics for thruster operation.

4. Each condition should be characterized on the ground by high speed probes and ultra-fast imaging to comprehensively understand the oscillatory characteristics. This will provide a large parameter space for thruster operation where the oscillations are characterized and correlated to discharge current (and any other diagnostics that are anticipated to be available in flight).

5. High-speed diagnostics will likely not be available on a flight systems, but thruster oscillatory mode can be determined from time-resolved discharge current measurements in-flight. Build capability into the Power Processing Unit (PPU) to burst sample discharge current at ≥ 200 kHz for periods ≥ 10 ms. This will allow PSD calculations to quantify and characterize discharge current oscillations and compare with the detailed ground measurements.

4.10.2 Flight System Design Recommendations

Typical operating parameters for laboratory HETs include: propellant gas, discharge voltage, anode mass flow rate, cathode mass flow rate, separate magnet coil currents (inner magnet, outer magnet and trim coil), and facility background pressure. Typical operating parameters for flight HETs only include: discharge voltage, power level and magnet settings. A closed-loop, automated control system varies mass flow rate to maintain constant power for a set discharge voltage and a proportional flow controller regulates CFF. [24] Note the BPT-4000 xenon flow controller varies CFF from 5-9% depending on operating condition. [136] Flight systems typically power the inner and outer electromagnets with one power supply with the magnetic coils connected in series, therefore only the magnet current I_M can be varied. The magnetic field should be the symmetrical, lens topology described in Ref. 42 or magnetically shielded [4] where the shape and symmetry are maintained to within a few percent from $0.5I_{M0} \lesssim I_M \lesssim 1.5I_{M0}$ and I_{M0} is the reference design setting. This will provide significant dynamic range to adjust the magnitude of B without changing the shape for optimal performance. This range has been suggested based on the investigation presented here without comparison to other HETs and may impose impractical requirements on a flight system. It is likely that a smaller range such as $0.25I_{M0} \lesssim I_M \lesssim 1.25I_{M0}$ would also provide adequate range, which can be determined during testing since no first-principles based models can predict HET performance let alone mode transitions.

A flight system such as the BPT-4000 will communicate State-of-Health (SOH) information in the telemetry to the flight computer at a rate of 10 Hz or less [137], so at best ground stations will receive SOH information at a sample rate of only a few samples per second during standard operation. New flight system designs should build in capabilities to capture short segments of time-resolved discharge current (and voltage if not regulated). Real-time, time-resolved data do NOT

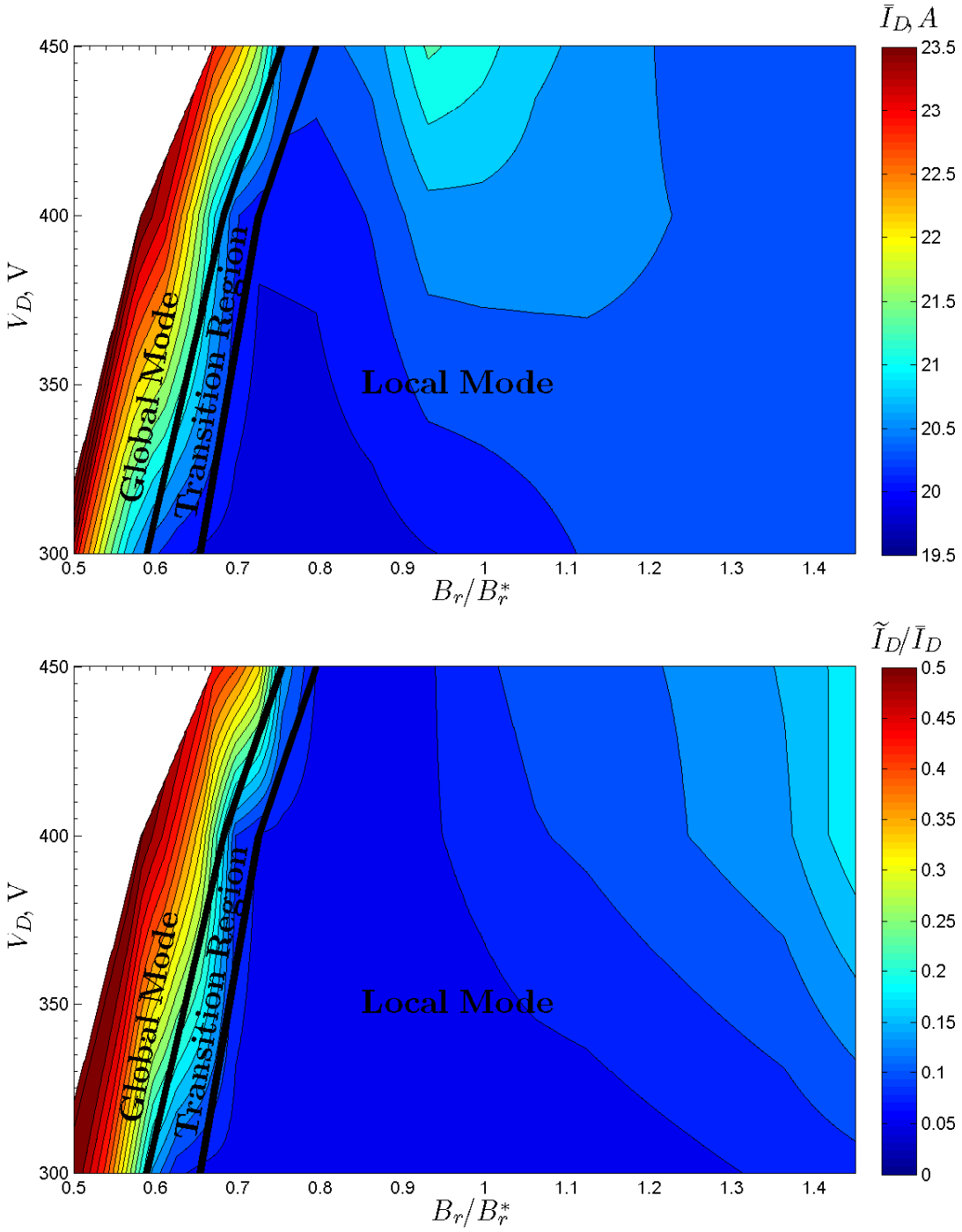

Figure 4.31: Example $I_D - V_D - B$ surface for $\bar{I}_D$ (top) and $\widetilde{I}_D/\bar{I}_D$ (bottom) generated from the data in Figure 4.2(a) for V_D = 300, 400 and 450 V. This graphic is meant to illustrate the utility of an $I_D - V_D - B$ plot to identify minimum discharge current, but is not intended for operational use since the data has been linearly interpolated between only three discharge voltages tested.

need to be streamed to ground control stations. The critical values of interest are discharge current mean value $\bar{I}$, RMS and peak-to-peak values (sometimes called "swing current") $\widetilde{I}$, and the PSD form 0-100 kHz. These can be calculated on-board and transmitted to ground stations or a segment of a discharge current time-history $\geq$ 10 ms long sampled at $\geq$ 200 kHz can be transmitted to the ground, from which $\bar{I}$, $\widetilde{I}$ and the PSD can be calculated in post-processing. Time-averaged values for mass flow rate, discharge voltage and magnet current measured simultaneously with the time-resolved discharge current should also be provided by the system. The time-resolved discharge current needs measured downstream from any filters in the PPU so the actual current to the anode is measured.

The mass flow rates in flight systems may be varied to maintain constant power, [24] while in laboratory systems the flow rates are held constant. Although this parameter varies in time, the time-scales for gas flow response are much slower than the expected 10's kHz oscillations in the discharge current. The response time from when a command is sent to the mass flow controller in the gas feed system to when increased neutral density is observed in the discharge channel needs to be measured and characterized (which is likely a function of temperature). It can be assumed that this response time is likely to be in the seconds, so a $\sim$ 1 Hz SOH measurement is likely accurate enough for characterization purposes, especially within the 10 ms of sample duration for the time-resolved discharge current.

Similar to the examples in Figure 4.31, it is recommended to make $x - V_D - I_M$ plots at different power levels P where the variable x could be $\bar{I}$, $\widetilde{I}$, $\dot{m}$, T, T/P or η. A detailed thruster characterization should be performed with the techniques developed in this work. Create a parameter space volume of P, V_D and I_M (or whatever independent variables are inherent in the system) where the thruster is characterized over the parameter space with time-resolved I_D, HIA, and probes in the plume. This characterization should include time-averaged discharge current, thrust, thrust-to-power and efficiency as well as time-resolved discharge current oscillation amplitude obtained with commercial high-speed current monitors, peak plasma oscillation frequencies in the plume from HDLP-ISR, and discharge current density oscillation characteristics in the discharge channel determined from HIA. This will provide identification of operational mode and mode transition regions within the expected thruster operational parameter space. This parameter space characterization should be done during qualification life testing in a ground test facility at the beginning-of-life and then middle ($\sim 5,000$ hrs) to end-of-life ($> 10,000$ hrs) to note changes due to erosion or material aging. In flight, when a ground operator sets the discharge voltage, power level and magnet current, a single burst sample of time-resolved discharge current (or $\bar{I}$, $\widetilde{I}$ and PSD from 0-100 kHz) from the flight system combined with this extensive characterization data set will most likely allow the thruster operational mode on-orbit to be determined. Part of initial checkout for the spacecraft and propulsion system after launch should include a re-characterization of the parameter space volume

as best as possible to quantify the differences between operation in a ground-test facility (which has higher background pressure) and on-orbit.

4.11 Conclusions

Previous researchers have identified mode transitions in HETs where a small change in a thruster operating parameter such as discharge voltage, magnetic field or mass flow rates causes the thruster discharge current mean and oscillation amplitude to increase significantly. Mode transitions in the H6 were induced by varying the magnetic field intensity while holding all other operating parameters constant and measurements were acquired with ion saturation probes and ultra-fast imaging.

The modes are described here as global oscillation mode and local oscillation mode. In global mode the entire discharge channel is oscillating in unison and spokes are either absent or negligible with discharge current oscillation amplitude (RMS) greater than 10% of the mean value and can even be as high as 100%. Downstream azimuthally spaced probes show no signal delay between each other and are very well correlated to the discharge current signal. In local oscillation mode perturbations in the discharge current density are seen to propagate in the $E \times B$ direction with clear spokes shown in a HIA PSD. Spokes are localized oscillations that are typically 10-20% of the mean discharge current density value. The discharge current oscillation amplitude and mean values are significantly lower than global mode. Downstream azimuthally spaced probes show a clear signal delay between each other indicating the passage of spokes but are not well correlated to the discharge current indicating localized plasma oscillations within the discharge channel. The mode transitions were consistent across different tests and showed no hysteresis, but did change at different operating conditions. The transition between global mode and local mode occurred at higher relative B-field strengths for higher mass flow rate or higher discharge voltage. The thrust was approximately constant through the mode transition, but the thrust-to-power ratio and anode efficiency decreased significantly in global mode. The peaks in thrust-to-power and anode efficiency typically occurs near the transition point. Plume images showed marked differences between modes with the global mode was brighter in the channel and the near-field plasma as well as exhibiting a plasma spike on thruster centerline. For the external cathode case the plasma spike disappeared in local oscillation mode.

This investigation describes techniques for identifying thruster operational mode using discharge current monitoring, high-speed probes and ultra-fast imaging. Based on the research presented here, the H6 and likely any similar thruster should be operated in local oscillation mode to minimize discharge current and maximize performance. Thruster performance maps should include variation in discharge current, discharge voltage, magnetic field, known as $I_D - V_D - B$ maps,

at different flow rates to identify transition regions throughout the life of a thruster. These results are used to calculate a transition surface for use by operators to keep the thruster operating in an optimal mode. New thruster designs should have magnetic circuits with more capability and not be designed near saturation. These techniques are naturally extendable to comparing ground-test operation with on-orbit operation.

CHAPTER 5

Local Mode and Azimuthal Spokes

"The journey from ignorance to wisdom demands not only curiosity, but the ability to change one's mind."

– Elbert Hubbard

5.1 Introduction

This chapter summarizes findings on the characterization of azimuthal oscillations known as spokes that are observed in local oscillation mode and discusses mechanisms for their propagation. The mode transitions investigated in Chapter 4 showed the presence of spokes is associated with improved thruster performance without determining causality, which motivates an investigation into the underlying fundamental physics. Section 5.2 discusses the possible mechanisms for spoke formation. Section 5.3 discusses the relation between spokes and electron transport and Section 5.4 discusses spoke location within the discharge channel and plume. Section 5.5 develops and compares multiple techniques for calculating spoke velocity and describes an empirical dispersion relation for spoke propagation. The results are shown for spoke velocity variation with magnetic field strength, discharge voltage and mass flow rate. These measurements identify important characteristics of spoke propagation and develop a set of observations that any theory for spoke propagation must explain. Section 5.6 investigates plasma waves as a possible spoke formation mechanism using time-averaged plasma measurements inside the H6 discharge channel at $B_r/B_r^* = 0.86$ from a previous investigation [44]. Section 5.7 discusses spokes as a sequential breathing mode and Section 5.8 considers wall effects.

5.2 Spoke Mechanisms

A coherent theory with supporting experimental evidence for spoke propagation has yet to emerge, [73] and the location in the plasma of their formation and mechanism for propagation are unknown.

In searching for the origin for spokes, we will consider the plasma in three different regions similar to that used in simulations [3]: near-anode region, the ionization/acceleration region near the channel exit, and near-field plasma plume. HETs have steep gradients in all relevant plasma parameters: density, electron temperature, electric field and magnetic field. However, the largest gradients occur near the channel exit where the magnetic field peaks, the ionization rate is highest, and most of the ion acceleration occurs. We will begin our discussion of the origin and mechanism for spokes by broadly considering these different mechanisms:

1. **Plasma Waves** The values for the magnetic field, plasma density, neutral density, plasma potential and electron temperature vary in space throughout the discharge channel as will be shown later in Figures 5.13 and 5.14 and . However, if they are constant in time, slowly varying on time-scales longer than spoke propagation time-scales or have a small oscillation amplitude, then any number of plasma waves can propagate that can be described by a dispersion relation. Chapter 6 discusses the implications of this in more detail where the presence of spokes could be an indicator of breathing-mode damping. We can subdivide the plasma wave mechanisms into three categories:

   (a) **(Nearly) Homogeneous Plasma Waves**. The gradients in the near-anode region or near-field plasma plume may be sufficiently small such that elementary, homogenous plasma waves may exist. These are discussed and analyzed in Section 5.6.3.

   (b) **Drift Waves Driven by Gradients in the Plasma**. The ionization and acceleration region near the discharge channel exit has steep gradients in all plasma parameters and provides fertile ground for drift waves without considering ionization effects or neutral densities. A preliminary investigation for this is conducted in Section 5.6.4 and a more comprehensive analysis of the plethora of drift dispersion relations, including shear driven instabilities, is reserved for future work as discussed in Section 7.2.5.

   (c) **Azimuthal Ionization Instability**. The spokes are bright regions moving azimuthally in the discharge channel as seen in high-speed imaging analysis, which would indicate spokes are regions of increased collisionality leading to more excited states that decay to release photons. From downstream ISR probes in the plume the spokes are observed as increased regions of plasma density. Together this may indicate that spokes are related to ionization processes. Chesta's [104] and Escobar's [98] linear analyses showed oscillations due to ionization and the work presented here suggests that spokes represent increased ion production zones. These waves are dependent on ionization frequencies and neutral density, which in general are not captured in the dispersion relations analyzed in Section 5.6. Analysis and discussion of these important mechanisms are reserved for future work as discussed in Section 7.2.5.

2. **Localized Breathing Mode**. The same fundamental mechanism may exist between the spokes and breathing mode, where the breathing mode (global mode in Chapter 4) exhibits a uniform channel discharge and replenishment process while the spoke mode (local mode in Chapter 4) exhibits an azimuthally local discharge and replenishment process. The ionization zone could propagate around the channel at $\sim v_{E\times B}\sqrt{m_e/m_i}$ from ambipolar effects. Discussed in Section 5.7.

3. **Wall Effects**. Spokes propagate in the $E\times B$ direction and electron interaction with the walls may be necessary for azimuthal propagation as discussed in Section 2.3.7.3, so spokes may be related to sheaths or interactions with the discharge channel walls. Additionally, previous research suggests that plasma contact with the wall [65, 66] or potentially wall heating could be related to spoke propagation and mode transition. Finally, spokes are generally not observed in magnetically shielded thrusters where plasma-wall contact is reduced. Discussed in Section 5.8.

5.3 Spokes and Electron Transport

Spokes have been thought of as possible current carrying mechanisms to explain anomalous electron transport. Janes and Lowder [47] suggested that azimuthal electric fields from spokes could produce $E\times B$ drift in the axial direction and could account for anomalous electron transport. Recent work on a Cylindrical Hall Thruster (CHT) [80, 82] has demonstrated that 50% of the discharge current is carried through a spoke (only one spoke is observed in the CHT). While CHT results have questionable relevance due to the significant difference in geometry (no inner channel wall) and magnetic field topology versus the H6, SPT-100 or any traditional annular discharge channel, they do reinforce the idea that significant current can pass through a spoke. Unfortunately, it was also reported that the CHT performance (measured by discharge current) increased when the spoke was not present, [81] which is opposite of what has been clearly shown in this work. Here electron transport decreases when spokes are present; based on these results, thrusters should be operated in local oscillation mode. Spokes cannot be the sole cause for anomalous electron transport because they are not present in global mode where electron transport is higher. Spokes are localized oscillations that are typically 10-20% of the mean discharge current density value while the global oscillation mode can be 100% of the mean value as shown in Figure 4.9. It is difficult to explain how a 10-20% oscillation can cause the order of magnitude higher electron transport than predicted by classical theory or Bohm diffusion [138]. A one-size fits all description for causes of anomalous electron transport is improbable and likely several different mechanisms are at work. [3]

As shown in Figure 4.29, thrust is constant but $\bar{I}_D$ increases, so extrapolating from Brown's work [41] the electron transport and electron current to the anode increases during transitions from local mode to global mode. The implication is that the presence of spokes indicates decreased electron transport to the anode. This raises an interesting causality question of whether the presence and mechanics of propagating spokes reduces electron transport to the anode or the plasma conditions that decrease electron transport also allow spokes to propagate. Regardless, the presence or disappearance of spokes is related to electron transport through the discharge channel to the anode and strong spoke behavior is a symptom of higher efficiency operation and should be sought after. Caution should be used when discussing electron transport as a global parameter when in actuality it will vary in different regions of the plasma with different effects on performance. As discussed in Ref. 3, electron transport in numerical models is often considered separately in different regions: near-plume, acceleration and near-anode. The near-field region mobility describes the ability for electrons to traverse through the plume from the cathode to supply electrons to the ionization zone, which is critical for HET operation. The acceleration region mobility describes how well electrons are retained to undergo ionization collisions. The near-anode mobility describes the ability for electrons to reach the anode once they have escaped the acceleration/ionization region and influences the formation of the acceleration region. The combination of different electron mobilities through the regions play a complex role in defining thruster stability and performance.

5.4 Spoke Locations

The location within the discharge channel where spokes originate is unknown and previous experiments have detected azimuthal oscillations throughout the plasma from the anode out into the plume. The original work by Janes and Lowder [47] detected azimuthal oscillations with probes in the discharge channel where they even noted a spoke angle with respect to the walls. However, significant differences exist between their experimental apparatus in 1966 and the modern H6 including a longer discharge channel length, $\sim 1/2$ discharge voltage than nominal H6 values, chamber pressure two orders of magnitude higher, use of filament cathode, radially inward magnetic field with over $2\times$ larger peak value, and quartz walls instead of boron nitride.

In a more recent investigation, Chesta [75] used probes downstream of the discharge channel exit plane to observe spokes propagating at least one channel diameter downstream, similar to the results described in Section 4.5. Figures B.9 and B.10 of Section B.4 in Appendix B shows that oscillations related to azimuthal spokes are observed and dominant in some regions of the plume, particularly on discharge channel centerline.

Work by McDonald [78] with a segmented anode discussed in Section 3.5.3.1 showed PSD frequency peaks for the discharge current from individual anode segments matched spoke frequen-

cies from HIA PSDs. In a time history trace (Figure 9 from Ref. 78) local discharge current peaks are observed propagating from segment to segment at a velocity between 1700 and 2500 m/s. In addition, Ellison [82] observed a 1200-2800 m/s spoke propagating in a cylindrical Hall thruster with a segmented anode. This shows direct detection of the spokes at the anode itself, and by association the near-anode region.

High-speed imaging of the discharge channel along thruster centerline is a line-integration of all light emitted in the plume and discharge channel from the camera to the anode. Qualitatively, most light will be emitted in the region of highest collision frequency, which will be the ionization and acceleration region. This is substantiated by the profile photographs shown in Figures 4.24 and 4.25 of Section 4.7 where the channel is significantly brighter than the plume when viewed from the side. One can reasonably assume that the HIA techniques described in Section 3.5 are primarily imaging the ionization and acceleration region. Since spokes are readily observed with HIA, the assumption can be made that spokes exist in the ionization and acceleration region, however time-resolved internal measurements are needed for verification.

Spokes have been directly detected in the near-anode (segmented anode) and near-field plume (downstream probes), and are strongly suspected to exist in the ionization and acceleration region from HIA. Therefore, the presence and propagation of azimuthal oscillations are detectable from the anode out into the plasma plume of HETs with no agreement on where they originate. Time-resolved internal measurements as discussed in Section 7.2.1 will be critical to answering the question of spoke origin.

5.5 Spoke Velocity

The spoke velocity can be calculated from either the high-speed imaging or the azimuthally spaced probes using several different methods. Spokes are observed to propagate at a range of velocities, so there is a distribution associated with the speed akin to a distribution function. The methods below will identify one representative velocity for spoke propagation. McDonald has previously proposed a simpler method for calculating spoke velocity [67,100] $v_{sp} = 2\pi f_m R_{chnl}/m$, that yielded similar results and trends to the far more rigorous approach and analysis provided here.

As stated in Section 3.5, spokes are visible to even the casual observer. Figure 5.1 shows three false-colored frames 45.7 μs apart from HIA where red are the bright regions (spokes) and blue are the dim regions. FastCam frames are every 11.4 μs with the frame rate of 87.5 kHz, so there are 2 frames between each of the frames shown. The spoke can be seen to move approximately $\sim 45°$ in ~ 45 μs, which corresponds to an approximately spoke velocity of ~ 1400 m/s.

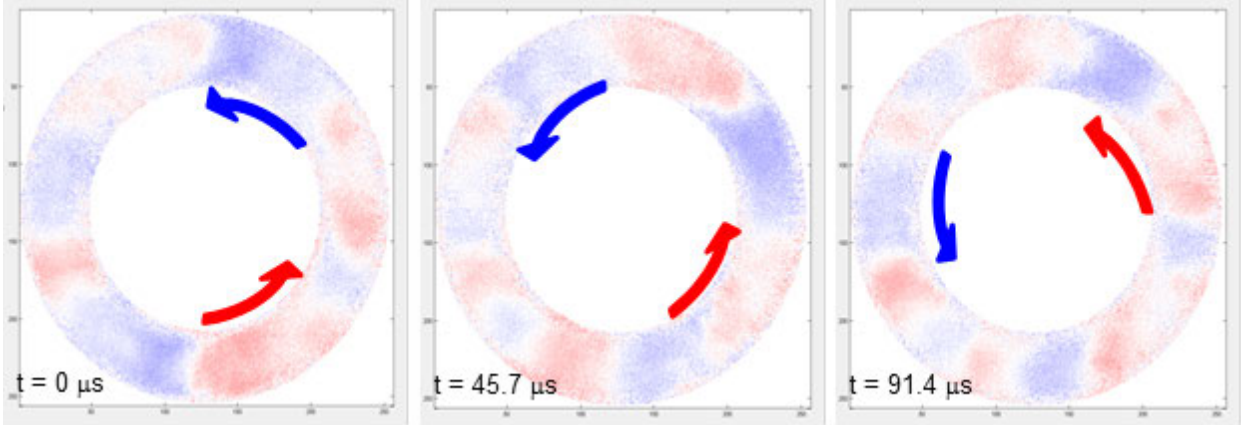

Figure 5.1: Three false-colored FastCam frames 45.7 μs apart from a seven frame series showing azimuthal spoke propagation. Red are bright regions (spokes) and blue are dim regions of the discharge channel.

5.5.1 Manual Method

Spokes are unambiguously observed in the FastCam videos and are obvious even to the casual observer as bright regions rotating azimuthally around the discharge channel. Using the techniques described in Section 3.5 to create a spoke surface, the spokes appear as diagonal stripes in the spoke surface as shown in Figure 3.13. This technique divides the discharge channel into 180 two-degree bins of averaged light intensity and a video consisting of N_{fr} frames will yield a $180 \times N_{fr}$ spokes surface.

The most obvious technique to calculate spoke velocity is to fit lines to the diagonal stripes on the spoke surface; the slope of which represent spoke angular velocity $\dot{\theta}_{sp}$ in deg/s. In the FastCam videos and subsequent video enhancement (c.f. Figure 5.1 and Figures 2 and 3 from Ref. 79), spokes are observed to fill the entire channel width. Therefore, spoke angular velocity is converted to a linear velocity using the mean channel radius, R_{chnl}

$$\mathrm{v}_{sp} = (2\pi R_{chnl}/360)\dot{\theta}_{sp} \tag{5.1}$$

In order to determine an average spoke angular velocity, 45 to 50 lines are manually fitted to a normalized spoke surface as shown in Figure 5.2 for $B_r/B_r^* = 1.00$, 300 V and 19.5 mg/s. A normalized spoke surface shows the spokes more clearly without altering their characteristic slope. To normalize a spoke surface, each frame (vertical line) has its mean value subtracted and is divided by its RMS value. In order to test the uncertainty due to human error and repeatability, 50 lines were fitted to the same propagating spoke with a standard deviation of 39 m/s; this will be shown to be within the standard deviation of a typical velocity distribution. The velocity distribution

for the spoke surface example of Figure 5.2 is shown in Figure 5.3 where the spoke velocity is 1530 $\pm$ 180 m/s and the uncertainty is the standard deviation of the distribution.

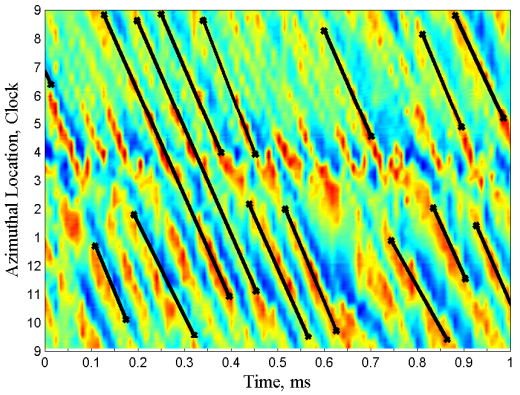

Figure 5.2: One millisecond segment of a normalized spoke surface showing 14 of 47 manually fitted lines for $B_r/B_r^* = 1.00$. Values in a normalized spoke surface range from -1 (blue) to 1 (red).

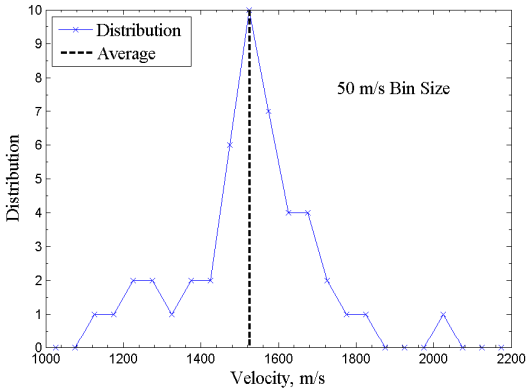

Figure 5.3: Velocity distribution for the manually fitted lines in Figure 5.2. The black dashed line is the mean of the 47 measurements.

More sophisticated techniques will be introduced in later sections, but those results should be within the range of this straightforward, yet labor-intensive approach. Representative uncertainties for the manual method are the mean uncertainties in Figure 5.9 of 190 m/s and 180 m/s for 300 V and 400 V, respectively.

5.5.2 Correlation Method

The correlation method uses linear cross-correlation to determine the time delay between oscillations in light intensity at different azimuthal locations in the discharge channel. The time delay represents transit time for a spoke to travel from one azimuthal location to another and is used to calculate angular and linear velocity. By comparing a large quantity of azimuthal locations ($\mathcal{O}10^3$) a representative spoke velocity can be calculated.

Starting with the normalized spoke surface as discussed above, the time-history signal of light intensity for each bin is a $1 \times N_{fr}$ vector representing light fluctuations at that azimuthal location for the duration of the video, which is typically 150 to 250 ms ($N_{fr} \sim 13 \times 10^3$ to 22×10^3). A 1 ms segment of four normalized light intensity traces are shown in Figure 5.4 for reference. A linear cross-correlation analysis of the signals between two bins, b_j and b_k, at different azimuthal

locations with an angular difference of $\Delta\theta_{j,k}$ degrees will yield the time, $t_{j,k}$, it took on average for a spoke to propagate around the channel from b_j to b_k. The cross-correlation function is [126]

$$R_{jk} = \lim_{T\to\infty} \frac{1}{T} \int_0^T b_j(t)\, b_k(t+\tau) dt \tag{5.2}$$

Signal delays for non-frequency dispersive propagation can be identified by peaks in R_{jk} where the highest peak is the time offset, $t_{j,k}$. Figure 5.4 shows an example of the time offset for three azimuthal locations (30°, 50° and 70°) referenced to 12 o'clock on the thruster face calculated from linear cross-correlation. Five peaks in light intensity (spokes) are selected and shown how they propagate around the thruster in Figure 5.4. The spoke velocity, $v_{spj,k}$, from b_j to b_k is

$$v_{spj,k} = (2\pi R_{chnl}/360)\Delta\theta_{j,k}/t_{j,k} \tag{5.3}$$

The spoke velocity for the correlation method is the mean spoke velocity calculated between N_{bins} compared

$$v_{sp} = \frac{1}{N_{bins}} \sum_j \sum_k v_{spj,k} \tag{5.4}$$

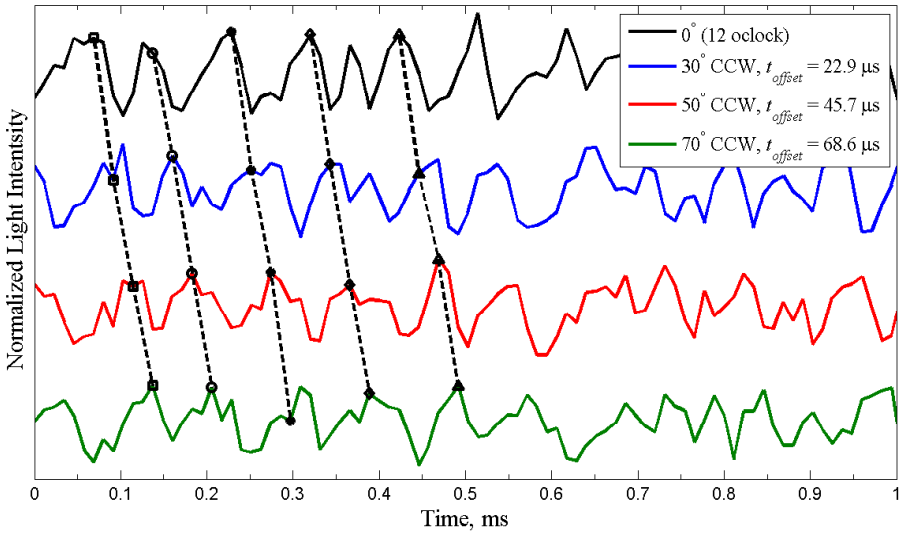

Figure 5.4: Light intensity traces for 4 azimuthal locations from the normalized spoke surface in Figure 5.2. Selected locations are thruster 12 o'clock as the reference and 30°, 50° and 70° CCW from 12 o'clock. The offset times are calculated via linear cross-correlation from 12 o'clock to the other locations. Five peaks have been selected to demonstrate how spokes propagate CCW around the thruster using the calculated offset times.

In principle, the spoke velocity can be calculated from the average time delay using every

combination of the 180 bins, which would be over 32,000. However, practical considerations limit the range of bins that can be compared. The camera frame rate is 87,500 fps so each frame represents 11.4 μs. A spoke traveling at 2000 m/s will travel 16° or 8 bins in the time span of one frame. Therefore, a practical lower limit is $\Delta\theta_{j,k} \geq 20°$ or 10 bins. A single spoke typically propagates one-quarter of the discharge channel circumference for most B-field settings. In strong spoke regimes, a single spoke will propagate one-half to even the entire channel circumference. A reliable upper limit for automated processing is to only compare bins where $\Delta\theta_{j,k} \leq 70°$ or 35 bins. In Figure 5.4, 6 cycles can be identified in ~0.55 ms, which corresponds to ~11 kHz or a spoke period of $\tau_{sp} \sim 90\ \mu$s. Due to signal noise, the cross-correlation peak occasionally matches to a spoke ahead or behind the correct spoke so the calculated offset time is in error by one or two τ_{sp}. Although this occurs more often when $\Delta\theta_{j,k} > 90°$, it occasionally occurs for $\Delta\theta_{j,k} < 70°$. These points are easy to identify via manual inspection, but reject criteria are set for automated data processing so any spoke velocity outside of 500 to 3500 m/s is rejected. In order to reduce computational time, only 90 bins (every other bin) are used for reference start points. All bins from bin 10 to 35 CCW from the reference bin are used for comparison. Therefore, j is 1, 3, 5, ... to 180 and k is 10 to 35 in Equation 5.4 which yields a maximum of N_{bins} = 2430 possible points. The spoke velocities for smaller $\Delta\theta_{j,k}$ will have larger uncertainty because half of the camera frame period (5.7 μs) represents a large fraction of the spoke travel time (~ 14 μs to travel 20°). The standard deviation can be reduced by choosing a larger value for the lower limit of $\Delta\theta_{j,k}$ instead of 20°, but the number of points used in the calculation, N_{bins}, will also be reduced, so a balance must be reached.

Using the correlation method on the spoke surface in Figure 5.2 yields a spoke velocity of v_{sp} = 1470 ± 270 m/s where the uncertainty is the standard deviation of the velocities used in Equation 5.4. This is within 4% of the manual technique described above. For this data point N_{bins} = 2266 of the possible 2430 points are used for $20° \leq \Delta\theta_{j,k} \leq 70°$. The manual method and correlation method produce very similar results as shown later in Figs. 5.7 and 5.9. Representative uncertainties for the correlation method are the mean uncertainties in Fig. 5.9 of 280 m/s and 260 m/s for 300 V and 400 V, respectively. The correlation method is important since it is an automated and reliable procedure of providing the same results as the laborious manual method.

5.5.3 Dispersion Relation Method

Dispersion relations are common place in plasma physics to describe the relationship between oscillation frequency and wave number. This method determines the spoke velocity from the phase velocity of an empirically determined dispersion relation. The 2-D PSD identifies a peak frequency for each spoke order, which is equivalent to wave number, and thus yields a dispersion

plot from high-speed imaging results. An assumed functional form is fit to the data in order to calculate the numerical values for the dispersion relation.

The HIA method developed by McDonald [6] and described in detail in Section 3.5 generates PSD from the 2-dimensional spoke surface. Figure 5.5. shows examples for the 300 V, 19.5 mg/s test case where peaks are clearly visible for each spoke order, m. As described by McDonald in his original derivation [78], m is analogous to number of wave lengths per channel circumference. Hence $m = 0$ or m_0 is no wave in the channel (the entire channel is dark or bright), $m = 1$ means one wave in the channel (one half bright, the other dark), $m = 2$ is two waves per channel (two bright regions, two dark regions), $m = 3$ is three waves per channel (three bright regions, three dark regions), etc. In the literature m is often called the wave mode, but we call it spoke order to avoid nomenclature confusion with the HET operational modes discussed in Chapter 4. The azimuthal wave number, k_θ, is calculated from the spoke order by $k_\theta = m/r$. Figure 5.5 shows each spoke order has a unique peak frequency that is typically 3-5 kHz higher than the previous m. Therefore, the HIA PSDs can be used to generate dispersion plots of peak frequency ω versus wave number k_θ.

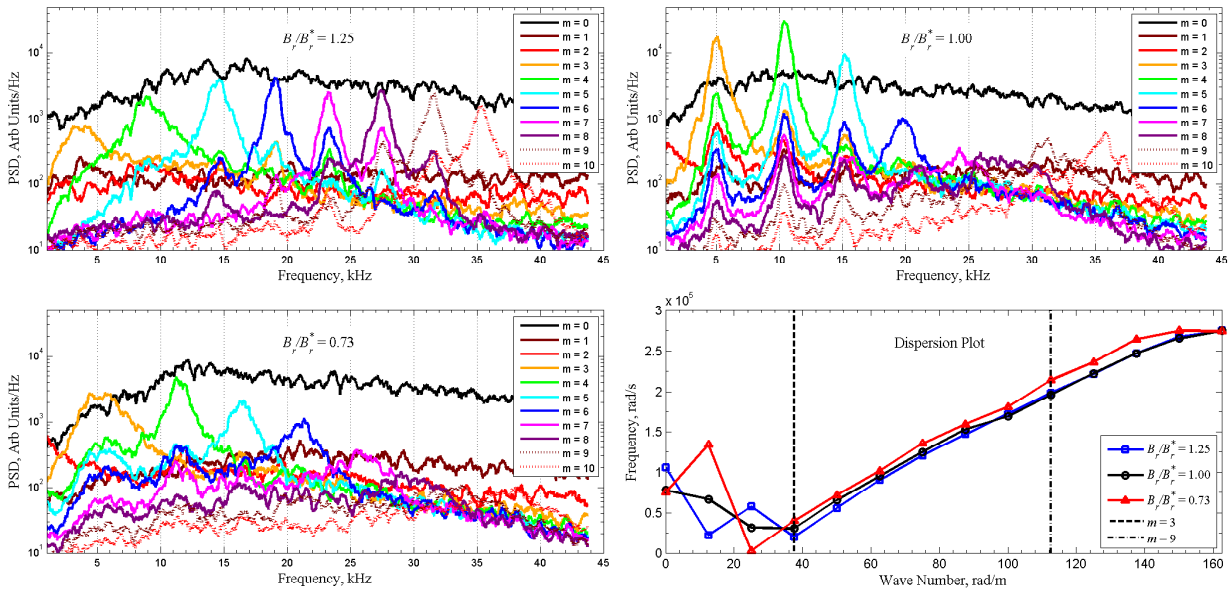

Figure 5.5: HIA PSDs for $B_r/B_r^* = 1.25$, 1.00 and 0.73 for 300 V and 19.5 mg/s with $m = 0 - 10$ shown. A 500 Hz moving average window has been applied to each PSD trace to reduce noise. Bottom right: the peak frequencies are identified and plotted versus wave number for corresponding dispersion relations.

The HIA PSDs are a powerful tool for understanding the plasma oscillations associated with HET operation. Figures 4.10 and 4.11 showed that ion saturation reference probes identified the same peak frequencies as the HIA PSDs indicating that spoke related oscillations extended out

into the plume. The same spoke surface that generated the normalized spoke surface in Figure 5.2 was used to generate the HIA PSD for $B_r/B_r^* = 1.00$ in Figure 5.5. Note the most dominant peak for $B_r/B_r^* = 1.00$ is $m = 4$ at 10.4 kHz, which is close to the crudely estimated frequency from Figure 5.4 of ~11 kHz.

In order to automatically identify the peak frequencies for each spoke order, the PSDs are first smoothed with a 250 Hz moving average filter and the maximum value identified. Due to noise from the DFT the maximum value is not always the frequency at the center of the peaks seen in Figure 5.5 so a Lorentzian [100] of the form

$$PSD(f) = \frac{A_0}{\pi} \frac{\frac{1}{2}\Gamma}{(f - f_0)^2 + \left(\frac{1}{2}\Gamma\right)^2} \tag{5.5}$$

is fitted to a segment of the PSD around the maximum value. The fit variables in Equation 5.5 are the full-width at half maximum Γ, amplitude A_0, and center frequency f_0. This identifies the frequency f_0 or ω_0 at the center of the primary peak for each m. Example dispersion plots using this technique for the three HIA PSDs are also shown in Figure 5.5.

For high magnetic field strength, $B_r/B_r^* = 1.25$, the higher spoke orders are most prominent with $m = 10$ showing a peak near the same height as $m = 5$. At the reference setting, $B_r/B_r^* = 1.00$, the spoke orders $m = 3-5$ are an order of magnitude higher than $m \geq 6$, although peaks are visible up to $m = 10$. At the lowest magnetic field setting, $B_r/B_r^* = 0.73$, spoke orders $m = 3-5$ are still dominant but lower in magnitude than $B_r/B_r^* = 1.00$. Although very weak, peaks are still visible for $m = 6-9$. As magnetic field is increased, the frequency of each spoke order decreases as shown in the PSDs and dispersion plot in Figure 5.5.

Dispersion relations can be of any functional form and can be quite complicated as will be discussed extensively in Section 5.6. It is important to remember that the dispersion relations analyzed in Section 5.6 are derived from linearized, first-principles based plasma physics equations and represent a physical process for a given oscillation. Unfortunately, the empirical relationship between ω and k_θ shown in Figure 5.5 does not offer any physical explanation for the cause of the azimuthal oscillations. In order to gain insight into the physical mechanisms behind azimuthal spokes, we will choose a functional form to fit the data and compare the coefficients calculated in the least-squared fit with the coefficients from physics based dispersion relations. The chosen empirical dispersion relation functional form most likely will not exactly replicate a first-principles derived dispersion relation, but similarities between them may be insightful. This comparison may show which physical properties are important or which region of the discharge channel or near-field plume is the likely origin for spokes. A first-principles derived dispersion relation that explains spokes should reduce to a form similar to the empirical relation using a set of assumptions

or approximations. With the above discussion in mind, we list several functional forms that can represent the data shown in Figure 5.5

$$\omega^{\alpha} = c_1 k_{\theta}^{\alpha} + c_2 \tag{5.6}$$

$$\omega = c_3 k_{\theta}^2 + c_4 k_{\theta} + c_5 \tag{5.7}$$

$$\omega^2 = c_6 k_{\theta} + c_7 \tag{5.8}$$

where Equation 5.6 is a power law relation and $\alpha = 1$ recovers a simple linear relationship, Equation 5.7 is a second order polynomial, and Equation 5.8 is a parabola. These functional forms do not constitute an exhaustive list of all possible functional forms, but they all share an important characteristic that ω is monotonically increasing with k_{θ}, which is required to fit the empirical results in Figure 5.5. The coefficients $c_1 - c_7$ are linear fit coefficients from a least-squares curve fit to the dispersion plots for each functional form. In the spirit of the many elementary plasma waves found in homogenous plasmas, Equations 5.6-5.8 can be written as dispersion relations of the form

$$\omega^{\alpha} = \mathrm{v}_{ch}^{\alpha} k_{\theta}^{\alpha} - \omega_{ch}^{\alpha} \tag{5.9}$$

$$\omega = -\mathrm{v}_{ch2}^2 k_{\theta}^2 + \mathrm{v}_{ch1} k_{\theta} - \omega_{ch} \tag{5.10}$$

$$\omega = \sqrt{\omega_{ch}(\mathrm{v}_{ch} k_{\theta} - \omega_{ch})} \tag{5.11}$$

where v_{ch} is a characteristic velocity such as ion acoustic speed or Alfvén speed and ω_{ch} is a characteristic frequency such as the ion cyclotron frequency or plasma frequency. The negative signs in Equations 5.9-5.11 are the result of least-squares fits and will be discussed in more detail later for the power law.

Figure 5.6 shows the results fitting Equations 5.6-5.8 to the empirical dispersion results at the reference magnetic field setting of $B_r/B_r^* = 1$ with $\alpha = 1$, 2 and 3 in the power law. The numerical values for the characteristic velocities and frequencies are shown in Equations 5.12-5.16.

$$\omega = (2170) k_{\theta} - (4.40 \times 10^4) \tag{5.12}$$

$$\omega^2 = (1820)^2 k_{\theta}^2 - (6.05 \times 10^4)^2 \tag{5.13}$$

$$\omega^3 = (1760)^3 k_{\theta}^3 - (7.11 \times 10^4)^3 \tag{5.14}$$

$$\omega = -(2.87)^2 k_{\theta}^2 + (3410) k_{\theta} - (8.52 \times 10^4) \tag{5.15}$$

$$\omega = \sqrt{(1.43 \times 10^5)((3500) k_{\theta} - 1.43 \times 10^5)} \tag{5.16}$$

Only data for $m = 3 - 9$ are used in the fits shown in Figure 5.6. The power law relation of Equation 5.9 displays the smallest deviations for all values including those outside the range of $m = 3 - 9$.

The parabolic relation from Equation 5.11 has the largest deviations from the data. Except for the second order coefficient of Equation 5.15 at 2.87 m/s, the characteristic velocities for each functional form were the same order of magnitude in the range of 1760-3500 m/s. It is interesting to note this velocity range corresponds to ion acoustic speeds with 4-17 eV electrons (commonly observed in HET discharge channels and plumes), as will be discussed in more detail in Section 5.6. The characteristic frequencies showed excellent similarities with a range of $4.40 - 14.3 \times 10^4$ rad/s. The power law relation in Equation 5.9 with $\alpha = 1$ and 2 will be used for further analysis due to its simplicity and because it provides the best fit for the largest range of k_θ and ω.

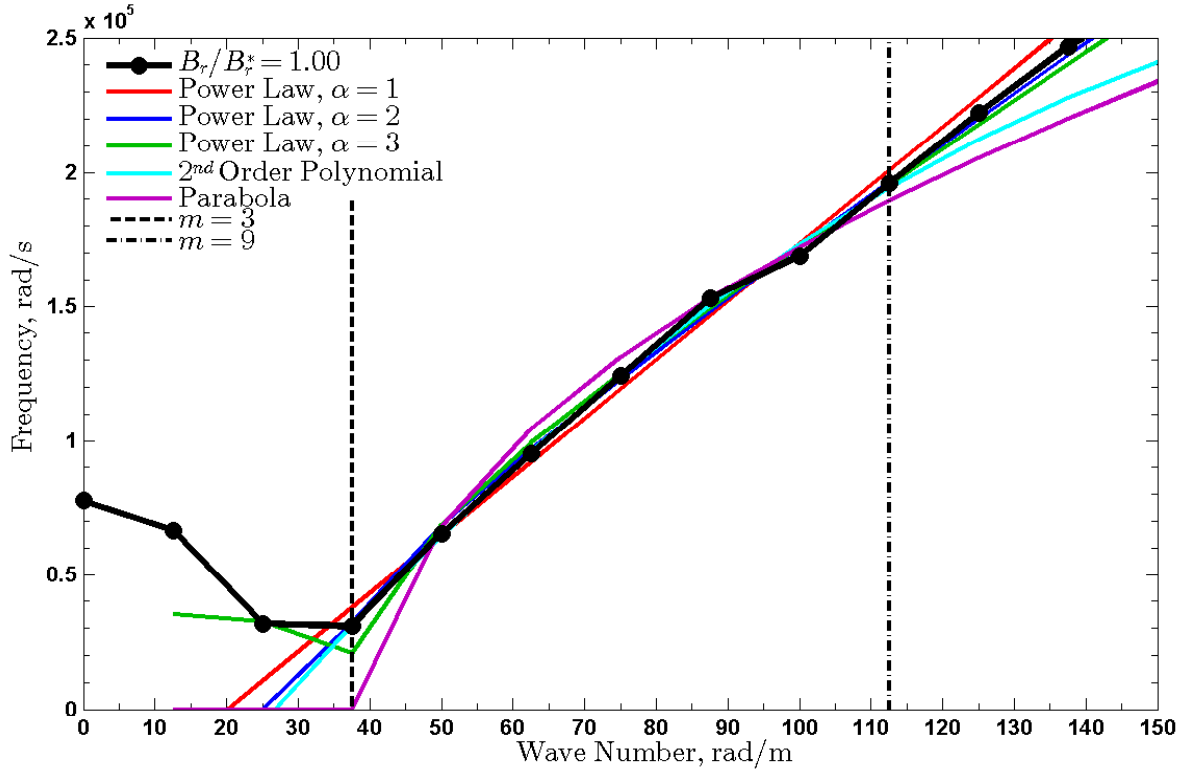

Figure 5.6: Empirical dispersion data for B_r/B_r^* = 1.00 at 300 V and 19.5 mg/s with the least-squares fit for Equations 5.6-5.8 used to represent the dispersion relation. Data in the range of $m = 3 - 9$ are used in the fits.

The characteristic quantities for the power law form in Equation 5.9 are $v_{ch} = c_1^{1/\alpha}$ and $\omega_{ch} = |c_2|^{1/\alpha}$, with the unexpected minus sign resulting from the fact that c_2 in Equation 5.6 is always less than zero for all fits. This can be seen from the example dispersion plots in Figures 5.5 and 5.6 where the ordinate intercept is $\omega < 0$ when extrapolating backwards for $m < 2$ using the points from $3 \le m \le 12$. The physical implications of $c_2 < 0$ is a limit of $v_{ch}^\alpha k_\theta^\alpha > \omega_{ch}^\alpha$ for ω to be real,

otherwise it will have a growing imaginary component and thus be unstable. This implies the only spoke orders that can exist are

$$m > R_{chnl}\frac{\omega_{ch}}{\mathrm{v}_{ch}} = m_{min} \tag{5.17}$$

In practice, m_{min} is typically 3 or 4. The phase velocity, v_{ph}, and group velocity, v_{gr}, from the dispersion relation in Equation 5.9 are

$$\mathrm{v}_{ph} = \frac{\omega}{k_\theta} = \left[\mathrm{v}_{ch}^{\alpha} - \left(\frac{\omega_{ch}}{k_\theta}\right)^{\alpha}\right]^{1/\alpha} \tag{5.18}$$

$$\mathrm{v}_{gr} = \frac{\partial\omega}{\partial k_\theta} = \mathrm{v}_{ph}\left(\frac{\mathrm{v}_{ch}}{\mathrm{v}_{ph}}\right)^{\alpha} \tag{5.19}$$

Equation 5.18 shows that the phase velocity will always be less than the characteristic velocity and Equation 5.19 shows the group velocity will always be greater than the phase velocity. In the limit of $(\omega_{ch}/(k_\theta \mathrm{v}_{ch}))^{\alpha} \ll 1$ that follows from Equation 5.17, a binomial expansion of Equation 5.18 yields a simplified phase velocity

$$\mathrm{v}_{ph} \simeq \mathrm{v}_{ch}\left[1 - \frac{1}{\alpha}\left(\frac{\omega_{ch}}{k_\theta \mathrm{v}_{ch}}\right)^{\alpha}\right] = \mathrm{v}_{ch}\left[1 - \frac{1}{\alpha}\left(\frac{m_{min}}{m}\right)^{\alpha}\right] \tag{5.20}$$

With the FastCam frame rate at 87,500 fps the Nyquist limit is 43.8 kHz (2.75×10^5 rad/s) which is the asymptotic peak value for $m \geq 12$ observed in the dispersion plots of Figure 5.5. In fitting the simple dispersion relation of Equation 5.9 to the data in Figure 5.5, a parametric study was done to determine the limits on m. Three different ranges were selected for spoke orders: $3 \leq m \leq 8, 9, 10$. In general the results were not sensitive to the upper limit of m used, but the $m = 8$ case had more variation in characteristic velocity. For all future comparison plots the range of m used for curve fitting will be $m = 3 - 9$ and $\alpha = 1, 2$ in Equation 5.6.

The manual and correlation methods described above both identify a single, dominant spoke velocity for a given magnetic field setting and operating condition. However, the phase velocity from Equation 5.18, which is assumed to be the spoke velocity, is a function of wave number. Figure 5.7 shows v_{ph} as a function of spoke order m as a proxy for k_θ for 300 V and 400 V and $\alpha = 1, 2$ ($\alpha = 3$ is very similar to $\alpha = 2$ and is not shown). A single, representative spoke velocity can

be calculated from a weighted average spoke velocity using the PSD value at the peak frequency f_m as the weighting factor w_m for each m. The spoke velocity and weighting factors are

$$v_{sp} = \sum_{m=5}^{9} w_m v_{ph} \tag{5.21}$$

$$w_m = \frac{\mathrm{PSD}(f_m)}{\sum_{m=5}^{9} \mathrm{PSD}(f_m)} \tag{5.22}$$

The HIA PSDs shown in Figure 5.5 show that certain spoke orders are dominant at different magnetic field settings, with spoke orders $m = 4$ and 5 are dominant for $B_r/B_r^* < 1.0$. Figure 5.7 shows for 300 V the phase velocities for m = 3 are far too low and for 400 V the the phase velocities for m = 3 and 4 are too low. The higher spoke orders are either dominant or the same magnitude as $m = 4, 5$ for the higher magnetic field settings. The weighting method of Equation 5.22 accounts for the higher spoke order dominance at higher B_r/B_r^* values and causes the upward shift above ~ 1, which tracks very well with the spoke velocities calculated via the manual and correlation method and builds confidence in the dispersion method. The minimum spoke order $m = 5$ was chosen in Equations (5.21) and (5.22) such that Equation 5.17 is satisfied for all conditions. Figure 5.7 shows the velocity from the correlation method typically follows the phase velocity for $m = 5$ or 6 closely for $B_r/B_r^*|_{trans} \leq B_r/B_r^* \lesssim 1.0$ and for $B_r/B_r^* \gtrsim 1.0$ the correlation velocity follows $m \geq 6$. Therefore using the phase velocities for $5 \leq m \leq 9$ to calculate a representative spoke velocity is reasonable. Figure 4.23 from Chapter 4 shows the dominant spoke order is 5 for lower B_r/B_r^* and 6 for higher B_r/B_r^*, which justifies the use of $m \geq 5$ in Equation 5.21. Using $4 \leq m \leq 12$ yields the same shape, but shifted lower by 100-200 m/s. Figure 5.7 shows for 300 V both $\alpha = 1$ and 2 yield spoke velocities from the dispersion method that match the manual and correlation methods, but $\alpha = 2$ is better correlated for 400 V.

The standard error σ_{c_1} and σ_{c_2} for fit coefficients c_1 and c_2 in a linear, least-squared fit are easily calculated according to Ref. 139. Using the error propagation equation [130], the uncertainty in phase velocity from Equation 5.18 for wave number k_θ is

$$\sigma_{v_{ph}} = \frac{v_{ph}}{\alpha}\left[\left(\frac{\sigma_{c_1}}{c_1}\right)^2\left(\frac{v_{ch}}{v_{ph}}\right)^{2\alpha} + \left(\frac{\sigma_{c_2}}{c_2}\right)^2\left(\frac{w_{ch}/k_\theta}{v_{ph}}\right)^{2\alpha}\right]^{1/2} \tag{5.23}$$

The coefficients c_1 and c_2 are correlated so using the error propagation equation so Equation 5.23 will conservatively over estimate the error in the phase velocity. The total uncertainty in spoke velocity is calculated using the weighted average technique of Equations (5.21) and (5.22). For the same example used in Figure 5.2 of $B_r/B_r^* = 1.00$, 300 V and 19.5 mg/s, the spoke velocity is

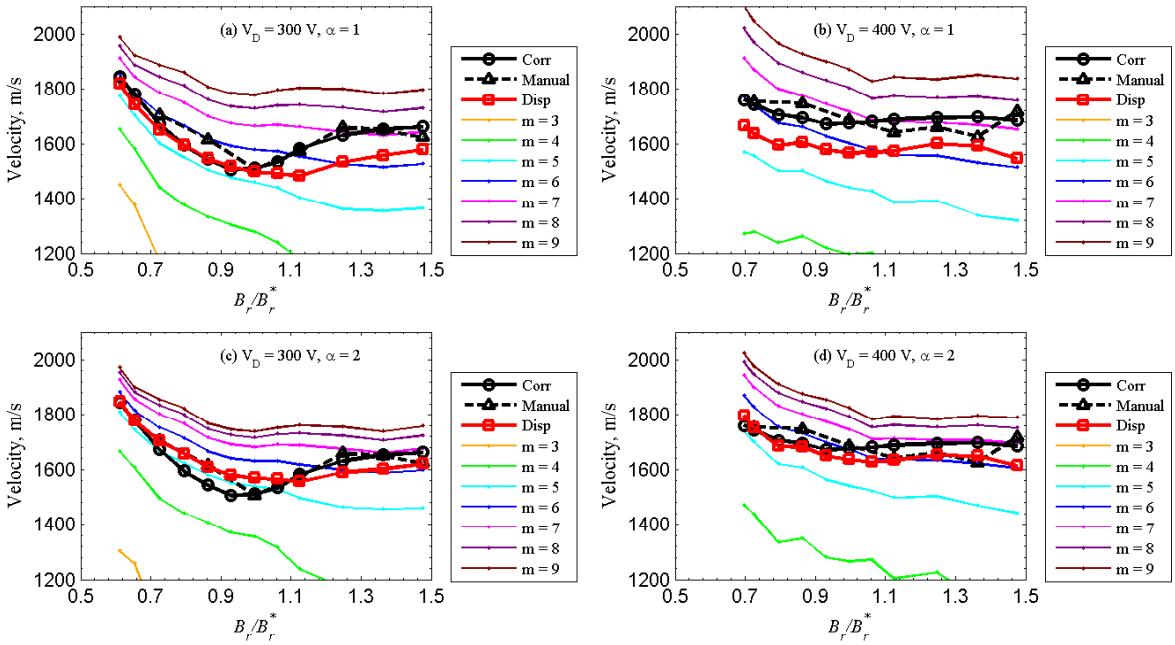

Figure 5.7: Comparison of phase velocities and spoke velocities for (a,c) 300 V and (b,d) 400 V, 19.5 mg/s for α = 1 (a,b) and 2 (c,d). Colored lines represent the phase velocity for each spoke order m calculated with Equation 5.18. Red lines with squares are spoke velocities calculated with the dispersion method and Equation 5.21. Solid black lines with circles are spoke velocities calculated using the correlation method. Dashed black lines with triangles are spoke velocities calculated using the manual method.

1510 $\pm$ 140 m/s for α = 1 and 1570 $\pm$ 60 m/s for α = 2. This is within 4% of the spoke velocity calculated with the manual method. Representative uncertainties for the dispersion relation method are the mean uncertainties in Figure 5.9 of 120 and 47 m/s for α = 1 and 2 at 300 V, and 157 and 41 m/s for α = 1 and 2 at 400 V.

5.5.4 Probe Delay Method

A final method to calculate spoke velocity is to calculate the time delay with linear cross-correlation of a signal passing from one azimuthally spaced probe to another. The downstream probes are azimuthally separated on channel centerline and observe the same plasma oscillations with a time delay. This time offset is converted to linear velocity based on the probe azimuthal spacing. ISR probes are used to measure plasma oscillations in the plume that correlate to light intensity oscillations in the discharge channel. As discussed at length in Section 4.5, both ISR probes observed the same plasma oscillations, but in local mode the signal was delayed whereas in global mode the oscillations occurred nearly simultaneously at each probe. The time delay, t_d,

was determined from a linear cross-correlation and Figure 4.13 shows the time delay in local mode was between 10 and 15 μs.

The spoke velocity can be calculated from the linear, azimuthal distance between each probe, $L_{pr} = (2\pi R_{chnl}/360)\Delta\theta_{1,2}$, divided by the time delay

$$v_{sp} = L_{pr}/t_d \tag{5.24}$$

The uncertainty in L_{pr} is calculated from the probe spacing uncertainty of 1.7° and the uncertainty of t_d is assumed to be 10% of the value [128]. These uncertainties are used to calculate the maximum and minimum values for spoke velocity at a given setting $v_{sp}|_{min}^{max} = \left(L_{pr} \pm \sigma_{Lpr}\right)/(t_d \mp \sigma_{td})$. For the sample data point used in the previous methods of $B_r/B_r^* = 1.00$, 300 V and 19.5 mg/s the spoke velocity is 2090 $\pm$ 380 m/s, which is 38% higher than the spoke velocity calculated via the manual method. Representative uncertainties for the probe delay method are the mean uncertainties in Figure 5.9 of 390 m/s and 420 m/s for 300 V and 400 V, respectively.

5.5.5 Probe Dispersion Plot Comparison

This section compares dispersion plots calculated from azimuthally spaced probes with dispersion plots described in the previous section. Azimuthally spaced probes can be used to determine the azimuthal wave number at a given frequency based on the phase delay between probe signals calculated from frequency domain transfer functions. The purpose of this calculation is to build confidence in the dispersion method by demonstrating a similarity in dispersion plots from two completely separate diagnostics measuring different locations: HIA observes the discharge channel and ISR probes observe the plume.

Lobbia initially showed that light intensity oscillations in the discharge channel were linearly related to electron density oscillations from 3 to 11 discharge channel radii downstream in a BHT-600 [128]. McDonald conducted research on a segmented anode H6 where frequency oscillations in discharge current to the segmented anode correlated to oscillations observed with high-speed imaging [78]. Chapter 4 showed that downstream probes observe the same frequencies in plasma oscillations as the FastCam observes with light intensity oscillations in the channel. Therefore, plasma oscillations in the channel are related to oscillations observed downstream. In order to justify using a dispersion relation for the HIA results, a dispersion plot for downstream probes should be related to HIA dispersion plots.

Lobbia developed a frequency domain transfer function technique in order to calculate aggregate maps of electron density oscillations [5]. The same technique is used to calculate a frequency domain transfer function between the ISR probes that yields gain and phase lag as a function of frequency. Note that we have employed set averaging as discussed by Lobbia [97], which increases

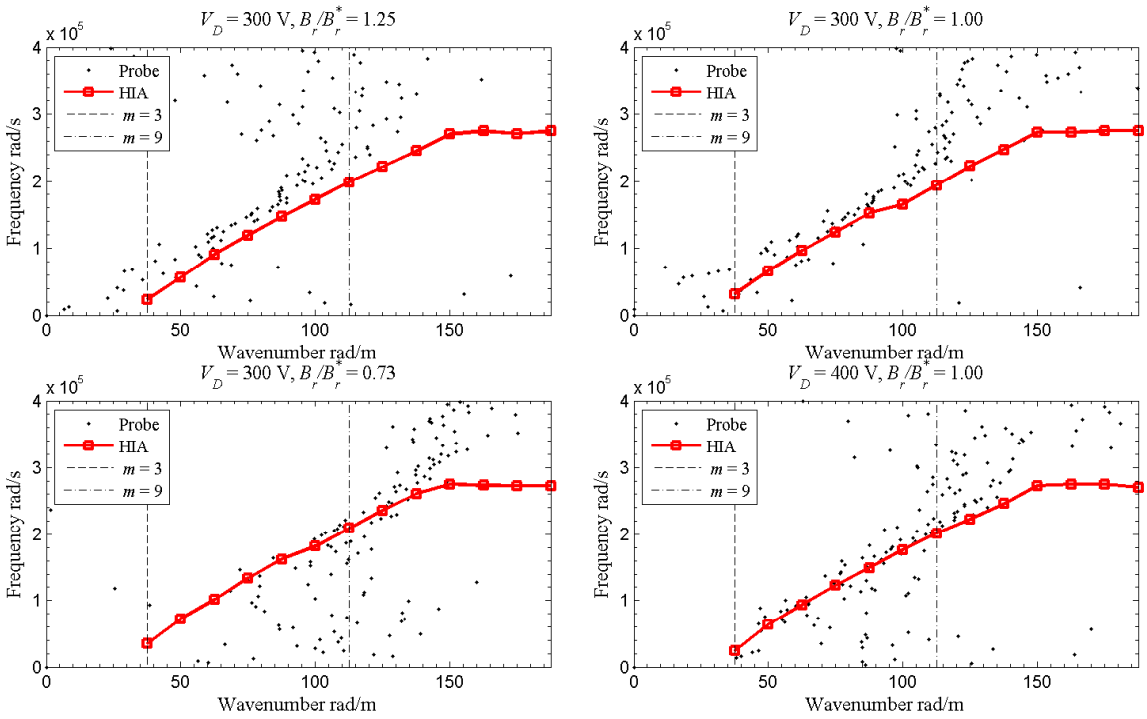

Figure 5.8: Probe dispersion plots for $B_r/B_r^* = 1.25$, 1.00 and 0.73 at 300 V, 19.5 mg/s and $B_r/B_r^* = 1.00$ for 400 V, 19.5 mg/s. The points are the dispersion plots from the phase lag between probes positioned 1.5 R_{chnl} downstream as a function of frequency and the red lines are the dispersion plots from HIA described in Section 5.5.3 and shown in Figure 5.5.

the signal-to-noise ratio and helps smooth out turbulent uncertainties. Unfortunately, this reduces the number of points for the Fourier transform by the number of sets averaged, which ultimately decreases the frequency resolution. For this analysis, the number of sets averaged is 75. The local azimuthal wave number at the probes is calculated from the phase lag, ϕ_{pr}, using the probe gap L_{pr}, by $k_\theta = \phi_{pr}/L_{pr}$ [140]. Figure 5.8 plots frequency versus azimuthal wave number for three conditions at 300 V (same conditions shown in Figure 5.5) and one condition at 400 V for a 19.5 mg/s anode flow rate. Remarkably, the dispersion plots from probes 1.5 R_{chnl} downstream show striking similarities to the dispersion plots calculated from HIA analysis described in Section 5.5.3; the correlation appears strongest for $B_r/B_r^* = 1.25$ and 1.00. Note there appears to be an small offset where the probe dispersion plots are a slightly higher frequency by $\sim 2\times10^4$ rad/s or ~ 3 kHz. This indicates similar oscillations observed in the discharge channel with high-speed imaging are also detected in the plume as shown by PSD analysis in Figures 4.10 and 4.11. This qualitatively builds confidence in the use of a dispersion relation to represent plasma oscillations from HIA.

5.5.6 Comparison and Discussion of Spoke Velocities

Figure 5.9 shows the spoke velocity calculated via all four methods discussed above with error bars for 300 V and 400 V at 19.5 mg/s flow rate. The manual, correlation and dispersion methods are all very well correlated. The spoke velocity from probe delay is consistently higher by $\sim 30\%$ for both conditions with the 400 V condition showing an unusual rise for $B_r/B_r^* > 0.9$. The reason for this divergence is unknown. The spoke velocity is initially inversely dependent on B_r/B_r^* until $B_r/B_r^* \sim 1$ then levels out for higher magnetic field strength. The inverse dependence of v_{sp} on B_r/B_r^* is stronger for the 300 V condition than 400 V.

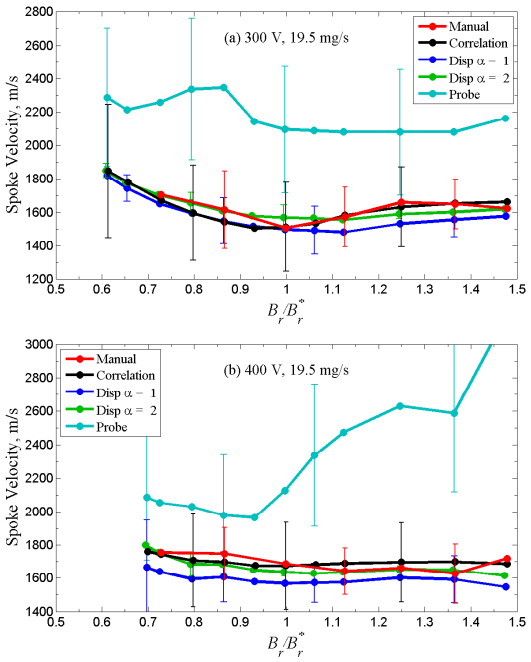

Figure 5.9: Comparison of spoke velocity calculation methods: manual, correlation, dispersion relation with $\alpha = 1, 2$ and probe delay method for (a) 300 V and (b) 400 V. Not all error bars are shown for clarity. For the dispersion relations, $m \geq 5$ has been used in Equations (5.21) and (5.22).

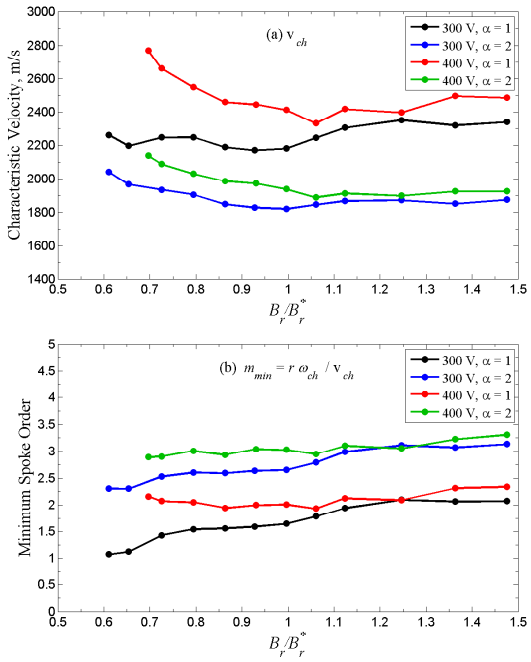

Figure 5.10: Comparison of the (a) characteristic velocity v_{ch} and (b) minimum spoke order from Equation 5.17 for 300 V and 400 V, 19.5 mg/s. Power dependence α = 1 and 2 are considered.

Figure 5.10 shows the characteristic velocity v_{ch} and m_{min} for the dispersion method for 300 V, 400 V and α = 1 and 2. The characteristic velocity for the 300 V and 400 V cases with α = 2 in Figure 5.10(a) are between 1800 and 2200 m/s. The characteristic velocities are higher for the α = 1 and for α = 2 they show the same inverse dependence on B_r/B_r^* until ~ 1, after which they become level at the same value. The minimum spoke order in Figure 5.10(b) appears to be linearly dependent on B_r/B_r^* with α = 2 higher. Although not shown in Figure 5.10, the characteristic

frequency, ω_{ch}, for all conditions at $\alpha = 2$ is in the range of $5-8\times10^4$ rad/s at the low magnetic field strength near mode transition and in the range of $7-8\times10^4$ rad/s at the highest magnetic field strengths.

Figure 5.11 shows a comparison of spoke velocities calculated from the correlation method for all five conditions tested. The 300 V, 19.5 mg/s condition is the average of four sweeps and the 400 V, 19.5 mg/s condition is the average of two sweeps. All conditions show the same trend of spoke velocity inversely dependent on B_r/B_r^* until $B_r/B_r^* \sim 1$. Power dependencies of $v_{sp} \propto (B_r/B_r^*)^{-0.5}$ and $v_{sp} \propto (B_r/B_r^*)^{-0.25}$ are shown in Figure 5.11 for reference purposes only and were not generated from curve fits. The 300 V, 19.5 mg/s and 14.7 mg/s conditions show the strongest inverse dependence closer to the -0.5 reference, all others are closer to the -0.25 reference. For $B_r/B_r^* \gtrsim 1$, the 300 V, 14.7 mg/s condition still decreases, but not as steeply and 300 V, 19.5 mg/s actually increases velocity before stabilizing. All other conditions are essentially constant for the higher magnetic field settings. With the exception of 300 V, 14.7 mg/s, all conditions asymptote between 1600 and 1700 m/s for the maximum magnetic field settings. The trend of decreasing spoke velocity with increasing B_r/B_r^* for $B_r/B_r^* \lesssim 1$ is clear, but the velocity change is small, typically less than 25%. The variation in spoke velocity during a magnetic field sweep is on the order of the uncertainty, reinforcing that the dependence on magnetic field magnitude is not strong.

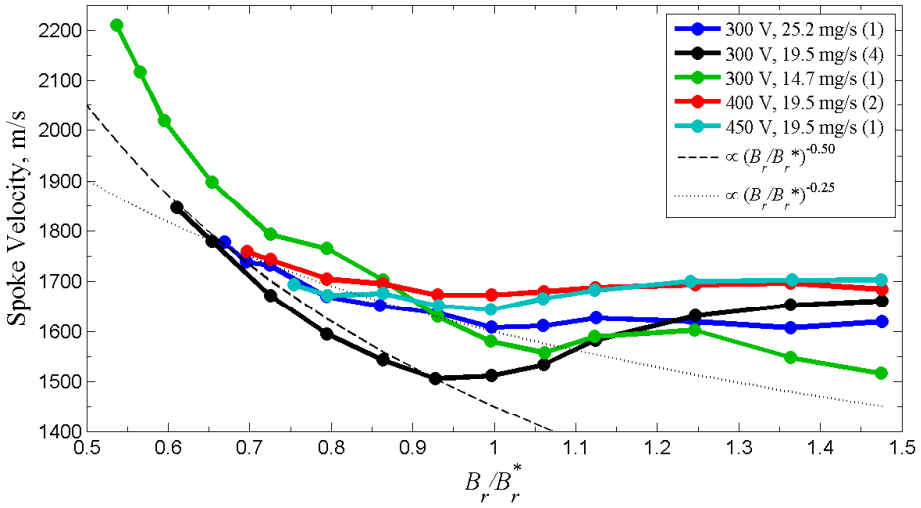

Figure 5.11: Spoke velocity calculated with the correlation method for all conditions tested. Parenthetical numbers are the number of B-field sweeps averaged together. Reference lines for possible functional forms of v_{sp} dependence on B_r/B_r^* are shown for discussion purposes only.

The manual method, correlation method and dispersion method all yield very similar results for the spoke velocity, building confidence in all three techniques. The manual and correlation methods do not require a selection of which spoke orders to consider, so they are more objective

at determining a single, representative spoke velocity. The correlation method is preferred over the manual method due to ease of automation. In the future, spoke velocities from the correlation method will be reported routinely as an additional metric with high-speed imaging data.

The inverse relation of spoke velocity to magnetic field is an interesting trend that should help identify the spoke mechanism even though the spoke velocity is only weakly dependent on magnetic field ($v_{sp} \propto B^{-\beta}$ where $0.25 \lesssim \beta \lesssim 0.5$). A previous study [67] showed similar results, but the spoke velocity for each spoke order m was calculated from ω_m/k_θ (which effectively gives the characteristic velocity) instead of the more rigorous techniques used here. The results in Figure 5.7(a) can be compared with Figure 5 from Ref. 67, which shows the same trend of decreasing spoke velocity up to point. However, the same H6 thruster was used and lower spoke orders were seen to dominate in that study for unexplained reasons. In contrast, the early work of Lomas [99] found that spoke velocity increased with magnetic field, which is contrary to what was observed by McDonald [67] and in this investigation.

The $E \times B$ drift velocity also appears to have a simple 1/B dependence at first glance. However, noting that E is related to B from $E = \eta\left(1 + \Omega_e^2\right) j$ where η is the plasma resistivity, j is the discharge current density and Ω_e is the Hall parameter. According to the discussion in Section 2.3.6, the $E \times B$ drift velocity scales as $v_{E\times B} \propto B$. Spokes propagate in the $E \times B$ direction, so they may be related to electron or possibly even ion $E \times B$ drift. The Larmor radius for electrons is less than $0.05\ L_{chnl}$ using their thermal velocity so they are magnetized as expected. The ion Larmor radius for +1 ions using the ion velocity calculated from plasma potential and energy conservation is greater than $10\ L_{chnl}$ for most of the discharge channel except for the ionization region before they are accelerated by the large electric field. Note the Larmor radius for ions decreases for higher charge states, which are known to exist. If the ionization region is sufficiently offset upstream from the acceleration region, then a region of large ion density with relatively low ion velocity may exist ($< 5 \times 10^3$ m/s which is same order as spoke velocity). In this region, the ions may be able to undergo some azimuthal motion before being accelerated downstream, although unlikely completing a full cyclotron orbit. This motion could contribute to azimuthal spokes.

If the spokes are related to the $E \times B$ drift, then the results of Figure 5.11 could provide insight into the electric field variations with magnetic field. For $B_r/B_r^* \lesssim 1$, the electric field may be approximately constant and the increase in magnetic field causes the spoke velocity to decrease. For $B_r/B_r^* \gtrsim 1$, the ratio of E/B may be approximately constant causing the spoke velocities to asymptote indicating the electric field is increasing with magnetic field.

For $B_r/B_r^* = 0.86$, the spoke velocity is 1540 m/s from Figure 5.11 and the characteristic velocities are 2190 and 1850 m/s for $\alpha = 1$ and 2 from Figure 5.10(a). Figure 5.12 shows a comparison of those velocities with the channel centerline ion acoustic velocity from Figure 5.13(h) and the critical ionization velocity. Janes and Lowder suggested that the spokes may be related to the crit-

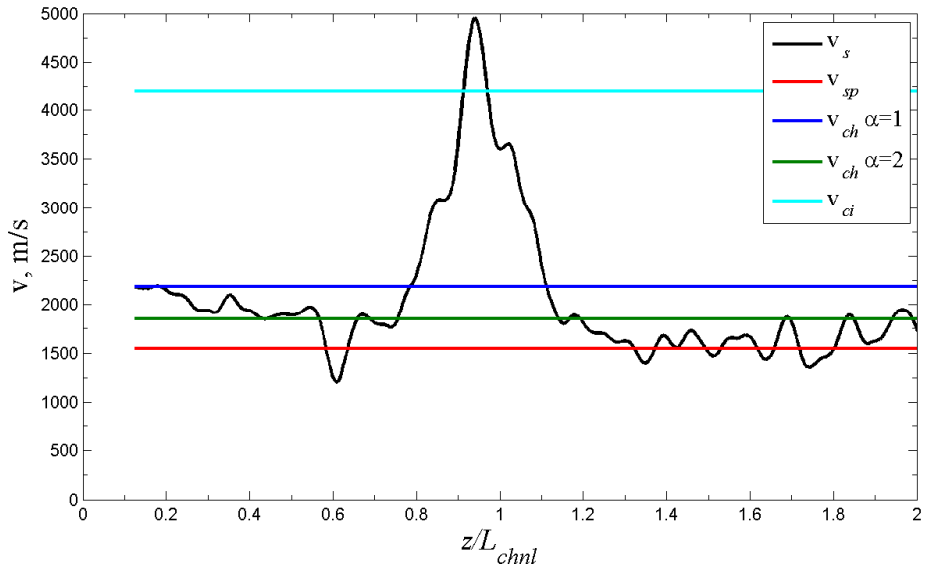

Figure 5.12: Ion acoustic speed on channel center line for $B_r/B_r^* = 0.86$ from Figure 5.13(h) smoothed by a 0.038 z/L_{chnl} moving average filter. The critical ionization velocity, spoke velocity and characteristic velocities for $\alpha = 1, 2$ are shown for comparison.

ical ionization velocity [47] first proposed by Alfvén, and Ref. 67 contains a good discussion of the phenomenon and the implication to HETs. The critical ionization velocity for xenon shown in Figure 5.12 is 4200 m/s, which is the same order of magnitude as the spoke velocity, but is still over twice the value. The ion acoustic speed matches the characteristic speed for $\alpha = 2$ better than $\alpha = 1$, particularly for $z/L_{chnl} < 0.7$. The observation that ion acoustic speed matches the characteristic speed from the dispersion method is encouraging because v_s commonly appears in waves such as the electrostatic ion cyclotron wave and arises prominently in drift waves. In Escobar's simplified model that includes ionization, [98] the wave speed was found to be of order the ion acoustic speed and Cavalier recently found modes that resemble ion acoustic waves. [49] The spoke velocity is lower than the ion acoustic speed in the near-anode region, but is similar for the near field plume region. The similarity between ion acoustic speed and spoke velocity or characteristic velocity will be further investigated with the more detailed dispersion relations discussed in Section 5.6.

5.5.7 Spoke Criteria

Combining the above discussion, we can state the following observations regarding spoke velocities; any theory on spoke mechanisms and propagation should account for these results.

1. Propagation is in the $E \times B$ direction. Reversal of the magnet field direction will cause the spokes to propagate in the opposite direction. [1]

2. Spoke velocity is 1500-2200 m/s in the H6; spoke velocity dependence on thruster radius or channel width are unknown although likely weak as noted by McDonald [67]. Spoke velocities are not dependent on discharge voltage or mass flow rate to within experimental error.

3. The dispersion relation can be approximated by a functional form where ω monotonically increases with k_θ such as a power law dependence $\omega^\alpha \approx \mathrm{v}_{ch}^\alpha k_\theta^\alpha - \omega_{ch}^\alpha$ where $\alpha \geq 1$. The characteristic velocity is the same order of magnitude as the spoke velocity and can be represented by the ion acoustic speed for 4-17 eV electrons commonly measured in HETs. The spoke velocity v_{sp} is less than the characteristic velocity v_{ch} and is dependent on the dominant spoke orders, typically $m > 4$. In general, the dominant spoke order increase with increasing magnetic field strength.

4. Spoke velocity is weakly, inversely dependent on magnetic field for $B_r/B_r^*|_{trans} < B_r/B_r^* \lesssim 1$. An example dependence of $\mathrm{v}_{sp} \propto B^{-\beta}$ where $0.25 \lesssim \beta \lesssim 0.5$ is shown in Figure 5.11, but other functional forms are possible. For $B_r/B_r^* \gtrsim 1$ the spoke velocity nearly asymptotes to a constant value.

5. Spokes are not observed in magnetically shielded thrusters except for very high magnetic field strengths as discussed in Appendix C.

5.6 Plasma Wave Dispersion Analysis

5.6.1 H6 Internal Data

Internal measurements were made by Reid [44] on the H6 at 300 V with 20 mg/s anode flow rate after less than 300 hours of total thruster operation. The magnet settings used were I_{IM} = 3.00 A and I_{OM} = 2.68 A, which corresponds to $B_r/B_r^* = 0.86$. Table 5.1 shows the source of internal data used for calculations in the following sections. These figures have been reproduced in Figure 5.13(a)-(e) for reference. Fig. 5.14 shows the centerline plasma properties normalized by the maximum values. The electric field and electron temperature are nearly constant until $z/L_{chnl} \sim 0.8$, while the plasma density begins a significant increase at $z/L_{chnl} \sim 0.5$ and the region

[1] Personal correspondence with M. McDonald. During a test in July 2009, he reversed the polarity of the H6 magnets while the thruster was running at V_D = 300 V, I_D = 10 A and $B_r/B_r^* = 0.70$, and observed the spokes change directions using the FastCam. Videos of 1/4 of the discharge channel were acquired at 54,000 fps.

of peaked electron temperature is $z/L_{chnl} = 0.8 - 1.0$. The region of peaked electric field is $z/L_{chnl} = 1.0 - 1.2$, which constitutes the approximate acceleration zone.

The data in Figure 5.13 corresponds to $B_r/B_r^* = 0.86$ and referring to Figure 5.5 for $B_r/B_r^* = 0.73$ and 1.00, the peak spoke order is $m = 4$ at $f \approx 11$ kHz. Referring to Figure 5.11, the corresponding spoke velocity for $B_r/B_r^* = 0.86$ is 1550 m/s. These will be used as the comparison frequency and velocity for the dispersion wave analysis.

Variable	Source	Notes
n_i	Reid [44] Figure 7-10, 20 mg/s	Blended solution from OML and thin sheath Langmuir probe measurements
T_e	Reid [44] Figure 7-5, 20 mg/s	Langmuir Probe, compare with Figure 15 from Hofer [37]
V_p	Reid [44] Figure 7-18, 20 mg/s	Emissive probe corrected with T_e from Langmuir probe, compare with Figure 15 from Hofer [37], referenced to cathode
E_z	Reid [44] Figure 7-21, 20 mg/s	Computed from derivative of plasma potential
n_n	Reid [44] Figure 8-9, 20 mg/s	Computed from 1-D heavy particle continuity analysis

Table 5.1: Reference and notes for plasma measurements of H6 discharge channel (internal). Data are shown in Figure 5.13(a)-(e).

5.6.2 Frequencies

The frequencies of interest for this investigation are 5-15 kHz for breathing mode and 5-35 kHz for spokes. For comparison, the cyclotron frequency is $\omega_{ci,e} = |q|B/m_{i,e}$ and the plasma frequency is $\omega_{pi,e} = \sqrt{nq^2/(\epsilon_0 m_{i,e})}$, where subscript i is for ions and e is for electrons. Variables include q for the elementary charge, B for the magnitude of the magnetic field, $m_{i,e}$ are the ion and electron mass, n for the plasma density where quasi-neutrality has been assumed such that $n_i \simeq n_e \simeq n$, and ϵ_0 is the permittivity of free space. The lower hybrid frequency [43] is $\omega_{lh} \simeq \sqrt{\omega_{ci}\omega_{ce}}$ for $\omega_{pi} \gg \omega_{ci}$. Table 5.2 shows these characteristic frequencies at three different locations in the discharge channel $z = 0.25$, 1.00 and 1.5 L_{chnl} based on the data in Figure 5.13, but can be summarized as: $\omega_{ci} \lesssim \omega < \omega_{lh} < \omega_{pi} < \omega_{ce} < \omega_{pe}$.

Now consider the empirically identified, approximate dispersion relation of Equation 5.9. The characteristic velocity, v_{ch} is shown in Figure 5.10 to be between 2200 and 2800 m/s for $\alpha = 1$ and between 1800 and 2200 for $\alpha = 2$. In addition, Figure 5.11 shows the spoke velocity or phase velocity is between 1500 and 2200 m/s for all tested operating conditions. The characteristic

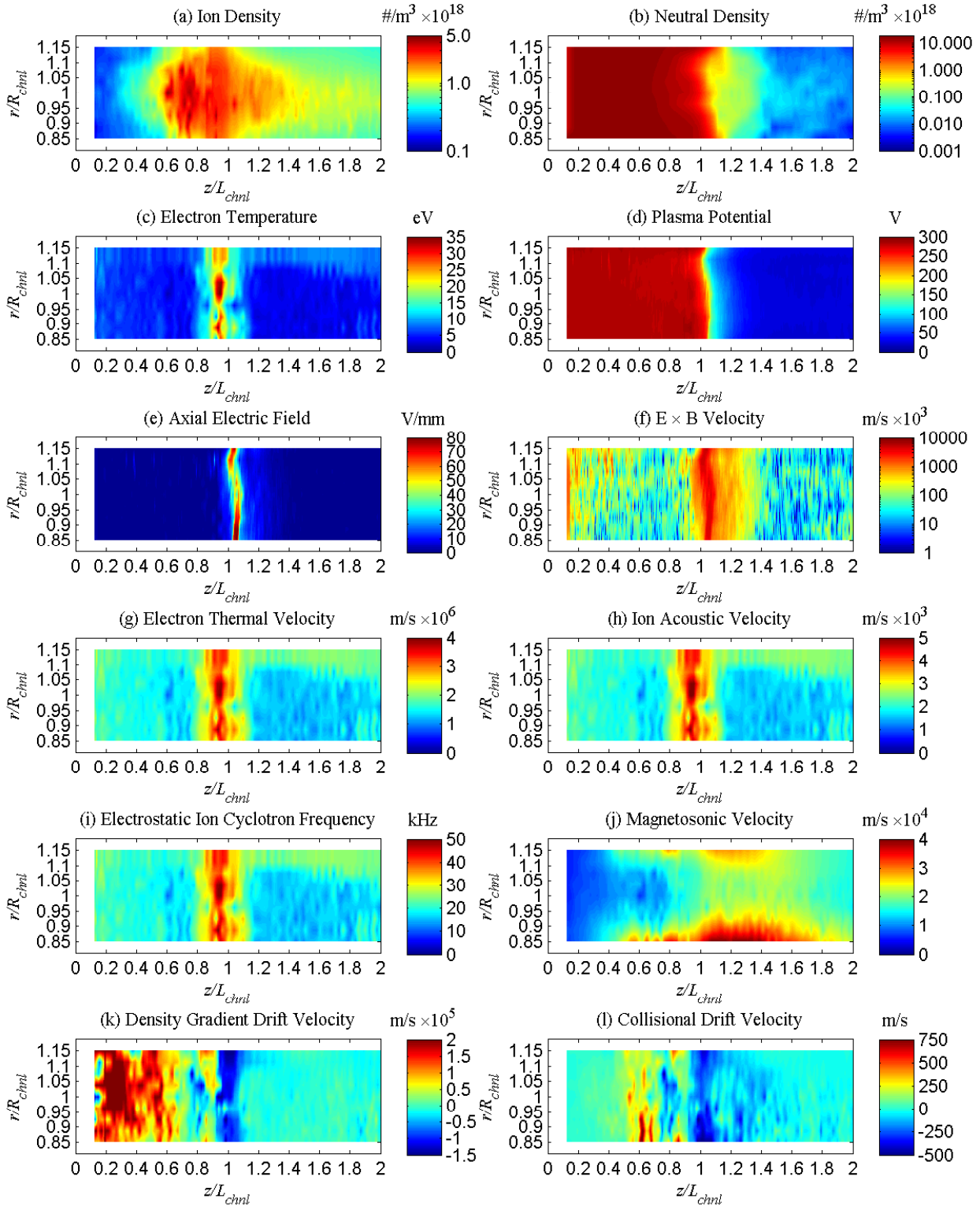

Figure 5.13: Internal measurements of the H6 discharge channel from Reid [44] as discussed in Table 5.1 for (a) ion density, (b) neutral density, (c) electron temperature (d) plasma potential, and (e) axial electric field. Calculated velocities include (f) $E \times B$ drift velocity, (g) electron thermal velocity, (h) ion acoustic velocity and (j) magnetosonic velocity, (k) density gradient drift velocity and (l) collisional drift velocity. (i) is electrostatic ion cyclotron frequency.

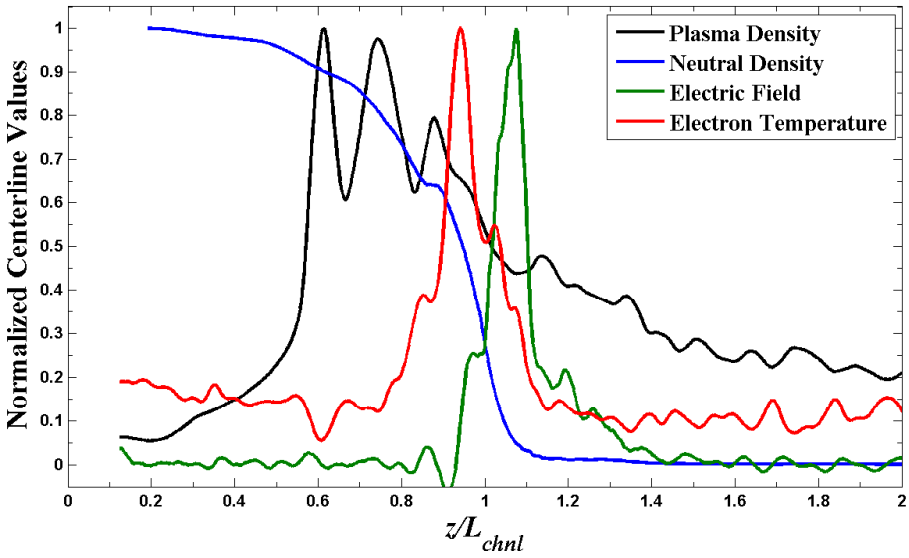

Figure 5.14: Measured discharge channel centerline plasma properties of the H6 showing plasma density, neutral density, electric field and electron temperature based on the data in Figure 5.13 from Reid [44]. All values have been normalized to the maximum value. A 0.025 L_{chnl} moving average window is applied to E_z and T_e, and 0.050 L_{chnl} window applied to n_i for smoothing. The multi-peaked structure of plasma density is likely experimental error and the values for neutral density are calculated.

frequency, ω_{ch}, is typically a few times larger than the peak ion cyclotron frequency, ω_{ci}, but is within the same order of magnitude. We can now attempt to identify any frequencies in the 10's of kHz range and characteristic velocities or phase velocities that are in the range of ~ 2000 m/s. The following analysis and discussion assumes +1 ions, but multiply charged ions are known to exist in HETs. $E \times B$ probe measurements in the plume of the H6 showed probe currents for Xe^{2+} of 20% and Xe^{3+} of 10%, respectively, normalized to the maximum Xe^{1+} current. [37]

Oscillation	Units	$0.25L_{chnl}$	$1.00L_{chnl}$	$1.50L_{chnl}$
Ion cyclotron	kHz	0.25	1.7	1.3
Lower hybrid	kHz	120	810	650
Ion plasma	MHz	9.4	27	20
Electron cyclotron	MHz	61	400	320
Electron plasma	GHz	4.6	13	9.6

Table 5.2: Representative frequencies on channel centerline for Region I, II and III at 0.25, 1.00 and 1.50 L_{chnl}, respectively. Ion cyclotron and ion plasma frequencies are for Xe^{1+}.

5.6.3 (Nearly) Homogeneous Waves

Here we consider some simple drifts and homogeneous plasma waves that propagate perpendicular to magnetic fields such as $E \times B$ drift, electrostatic ion cyclotron waves and magnetosonic waves. Other waves summarized by the Clemmow-Mullaly-Allis diagram [141] that can propagate perpendicular to magnetic fields such as ordinary waves (O wave), extra ordinary waves (X waves) and upper-hybrid resonance are of higher frequency than the 10's kHz spoke oscillations.

5.6.3.1 E x B Drift

The $E \times B$ drift velocity and the $\hat{\theta}$ component are given by [135]

$$\vec{\mathrm{v}}_{E\times B} = \frac{\vec{E} \times \vec{B}}{|B|^2} \tag{5.25}$$

$$\mathrm{v}_{E\times B}\hat{\theta} = \frac{E_z B_r - E_r B_z}{B_r^2 + B_z^2} \tag{5.26}$$

Spokes are observed to propagate in the $E \times B$ direction and one could reasonably assume they are related to the azimuthal Hall current, $j_\theta = q n_e \mathrm{v}_{E\times B}$. However, it will be shown that spokes are not the azimuthal Hall current for the following reasons:

1. The typical $E \times B$ drift velocity is two to three times the typical spoke velocity.

2. The $E \times B$ drift velocity should scale as B as shown in Equation 2.44 of Section 2.3.6 (contrary to the expected 1/B scaling) whereas the spoke velocity scales as $\mathrm{v}_{sp} \propto 1/B^{0.25}$ to $\mathrm{v}_{sp} \propto 1/B^{0.5}$ for $B_r/B_r^* < 1$.

A more complete theory will be needed that accounts for the observation that spokes propagate in the $E \times B$ direction, yet do not have the same characteristics as the Hall current.

The calculated $E \times B$ drift velocity distribution in the discharge channel is shown in Figure 5.13(f) where the maximum value is over 4×10^6 m/s at the peak electric field and of order 10^5 m/s within $\pm 0.2 L_{chnl}$. These velocities are two to three orders of magnitude higher than the typical spoke velocity of 1500 to 2200 m/s. Figure 5.15 shows the channel centerline values for $\mathrm{v}_{E\times B}$ and v_{th_e} where the electron thermal velocity is the average of an assumed Maxwellian distribution [43] $\mathrm{v}_{th_e} = \sqrt{8qT_e/(\pi m_e)}$ with T_e in eV. The region from $0.16 < z/L_{chnl} < 0.94$ is upstream from the ionization and acceleration zones with a mean value of 1.9×10^4 m/s and standard deviation of 8.4×10^4 m/s. Although the mean value is an order of magnitude larger than the spoke velocity, the large standard deviation (over 4 times the mean) is indicative of the experimental error and the $E \times B$ drift velocity could be of the same order as the spoke velocity in this region. Figure 5.18 uses representative values for the electric field to calculate the $E \times B$ drift velocity along

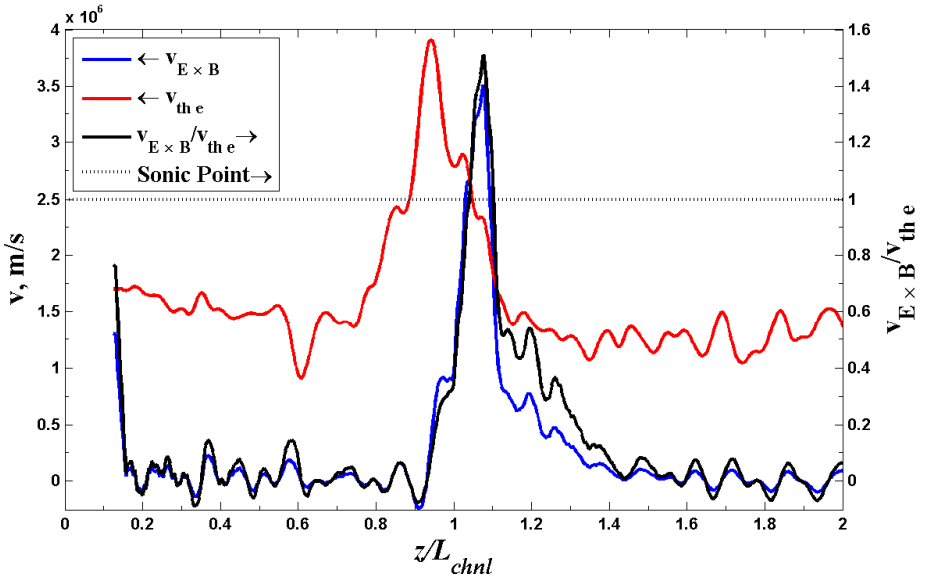

Figure 5.15: Left axis: Comparison of $E \times B$ drift velocity to electron thermal velocity on channel centerline from Figure 5.13(f) and (g). A moving average window of 0.025 L_{chnl} has been applied to smooth the data. Right axis: The ratio is shown to indicate the $E \times B$ drift velocity is faster than the thermal velocity in the acceleration region ($z/L_{chnl} \sim 1.08$). The sonic point is $v_{E\times B} = v_{the}$.

channel centerline and everywhere it is orders of magnitude higher than the spoke velocity. The electric field would have to be small, $E_z \sim$ 0.01 V/mm, for $v_{E\times B} \sim v_{sp}$ and is considered unlikely. Assuming the electrons follow a circular path on channel centerline, they would circle the thruster in 0.13 μs (8 MHz) at the peak $v_{E\times B}$ and 26 μs (38 kHz) upstream from the ionization region.

The electron thermal velocity shown in Figures 5.13(g) and 5.15 is the same order of magnitude as the $E \times B$ drift velocity near the channel exit. The $E \times B$ drift velocity is greater than the thermal velocity for $1.0 < z/L_{chnl} < 1.1$ which is within the acceleration region. Outside of $0.9 < z/L_{chnl} < 1.4$, $v_{E\times B}/v_{the} < 0.1$ so the electron thermal velocity is an order of magnitude or larger than the $E \times B$ drift velocity throughout most of the channel and plume.

5.6.3.2 Electrostatic Ion Cyclotron Waves

Similar to sound waves in air, ion acoustic waves follow a simple dispersion relation

$$\omega = k v_s \tag{5.27}$$

where v_s is the ion acoustic speed with electrons of temperature T_e in eV

$$v_s = \sqrt{\frac{qT_e}{m_i}} \tag{5.28}$$

As shown in Figure 5.13(c) the electron temperature in most of the channel and the near field plume is ~ 5 eV, except for near the exit plane $0.7 < L_{chnl} < 1.1$ where the electron temperature peaks at ~ 35 eV. The ion acoustic speed for $T_e = 5$ eV is 2000 m/s and for $T_e = 35$ eV is 5000 m/s. Figure 5.13(h) shows the acoustic speed, which is close the characteristic speed of ~ 2000 m/s for most of the discharge channel. Unfortunately, ion acoustic waves propagate parallel to the magnetic field while spokes propagate perpendicularly.

An electrostatic ion cyclotron wave [141] is similar to an ion acoustic oscillation except the Lorentz force provides a restoring force [43] which yields a modification to Equation 5.27

$$\omega^2 = k^2 \mathrm{v}_s^2 + \omega_{ci}^2 \tag{5.29}$$

Electrostatic ion cyclotron waves can propagate nearly perpendicular to B and have a phase velocity of

$$\mathrm{v}_{ph} = \sqrt{\mathrm{v}_s^2 + \omega_{ci}^2/k^2} \tag{5.30}$$

Except for the difference in sign inside the radical, note the similarity to Equation 5.18 with $\alpha = 2$, the ion acoustic speed as the characteristic velocity and the ion cyclotron frequency as the characteristic frequency. Since the spoke location is unknown, spokes could be related to electrostatic ion cyclotron waves in the channel near the anode or in the near field plume region where $T_e \sim 5$ eV. A map of the electrostatic ion cyclotron frequencies is shown in Figure 5.13(i) for k_θ corresponding to $m = 5$ where the frequencies are within the expected range for spokes. Unfortunately, this mechanism only implies that waves are perpendicular to the magnetic field (axial, CW azimuthal or CCW azimuthal) and does not force spokes to propagate in the $E \times B$ direction (CCW azimuthal for the H6). Figure 5.16 shows the frequencies are within the expected 5-25 kHz range for spokes upstream ($z/L_{chnl} < 0.7$) and downstream ($z/L_{chnl} > 1.0$) from the ionization region. Figure 5.18 shows the velocity is within the 1500-2000 m/s range expected for spokes for $z/L_{chnl} < 0.5$.

5.6.3.3 Collisional Ion Acoustic Wave with Sheaths

Smolyakov [105] recently derived a dispersion relation for an unstable ion acoustic wave that develops a positive feedback loop between the sheaths formed on parallel walls. Considering a plasma within a crossed electric and magnetic field with the magnetic field directed between the walls (i.e. an annular HET), the long wavelength limit of the dispersion relation is

$$\omega^2(\omega + i\nu_{sh}) = \frac{|k_\theta| \mathrm{v}_s \omega_{pi}^2}{\nu_{sh}}(\omega - \omega_0 + i\nu_{sh}) \tag{5.31}$$

where $\nu_{sh} = \mathrm{v}_s/(2W)$ and $\omega_0 = k_\theta \mathrm{v}_{E\times B}$. Figure 5.16 shows that the two roots for the dispersion relation in Equation 5.31 have frequencies that are $10^6 - 10^7$ Hz, which are several orders of mag-

nitude too large for spokes. Figure 5.17 shows unstable modes throughout the entire channel with $10^4 - 10^7$ Hz growth rates. Not surprisingly, the velocities in Figure 5.18 for one root are close to the $E \times B$ from $10^5 - 10^6$ m/s. The velocities for the other root are exactly $v_{E\times B}$, so they are not shown.

5.6.3.4 Magnetosonic Waves

Magnetosonic waves are low frequency, electromagnetic waves propagating across the magnetic field. They are similar to acoustic waves, but the oscillations are produced by $E \times B$ drifts across E. [43] The phase velocity is

$$v_{ph} = c\sqrt{\frac{v_s^2 + v_A^2}{c^2 + v_A^2}} \tag{5.32}$$

where $v_A = B/\sqrt{\mu_0 m_i n}$ is the Alfvén speed and μ_0 is the permeability of free space. Figure 5.13(j) shows the magnetosonic phase velocity (which is very close to the Alfvén speed so it is not shown in Figure 5.13), both of which are an order of magnitude too large to be azimuthal spokes. Figure 5.16 and Figure 5.18 shows the frequencies and velocities, respectively, are too high to be spokes.

5.6.4 Gradient Drift Waves

Drift waves are common when spatial gradients exist in plasma properties because they provide free energy from which an instability can grow and a wave can propagate. Figures 5.13(a)-(e) clearly shows the plasma in the discharge channel and near-field plume are not uniform therefore spatial gradients exist, predominantly near the channel exit. There are many forms of drift waves that have been studied from fusion research. Here we start with the most common form of the drift wave that arises from a gradient in plasma density and proceed with increasing complexity. Also important is the definition of gradient length scale for parameter ϱ

$$L_{\nabla\varrho} = \left(\frac{1}{\varrho}\frac{d\varrho}{dz}\right)^{-1} \tag{5.33}$$

5.6.4.1 Density Gradient Drift Waves

The most fundamental gradient driven wave is the density gradient which assumes no steady state electric field and constant magnetic field, neither of which are fundamentally true in a HET dis-

charge channel. The dispersion relation for density gradient drift waves and the diamagnetic drift velocity are [141]

$$\omega = k_\theta \mathrm{v}_{Drift} \tag{5.34}$$

$$\mathrm{v}_{Drift} = \frac{T_e}{B}\frac{1}{n_e}\frac{\mathrm{d}n_e}{\mathrm{d}z} = \frac{T_e}{BL_{\nabla n_e}} \tag{5.35}$$

Drift waves are caused by density perturbations from ion $E \times B$ drift where ions "slosh" back and forth in the gradient (axial) direction, with the phase velocity in the $\nabla n_e \times B$ direction. [135] Therefore, no particles or energy are moving in the θ direction. In the H6, ∇n_e is in the $+z$ direction from the anode to $L < 0.8L_{chnl}$ and is in the $-z$ direction for $L > L_{chnl}$ from Figure 5.13(a). Drift waves would be in the $E \times B$ for $L < 0.8L_{chnl}$ and in the $-E \times B$ for $L > L_{chnl}$. Spokes always propagate in the $E \times B$ direction, so we focus on the density gradient upstream from the ionization zone for density gradient waves to be the source of spoke motion.

The measured temperature in the discharge channel varies from 5 to 35 eV as shown in Figure 5.13(c). Although the magnetic field magnitude and profile cannot be shown, it is of order 100's of G similar to the SPT-100. Therefore, the T_e/B term in Equation 5.35 is of order 10^3, which is the same as the spoke velocity. The density length scale term $L_{\nabla n_e}$ must be of order unity for v_{Drift} to be in the spoke velocity range of 1500-2200 m/s. The experimental data from Reid in Figure 5.13(a) for ion density on channel centerline shows an unexpected multi-peaked feature that is likely experimental error so the axial derivative of density is smoothed with a $0.06L_{chnl}$ moving average filter. The density gradient length scale is of order $L_{\nabla n_e} \sim 10^{-2}$ causing the drift velocity to be approximately two orders of magnitude too large. Discounting the unusual multi-peaked ion density yields a similar result where the density increases from 1×10^{18} to 4×10^{18} m^{-3} in $0.2L_{chnl}$ which corresponds to $\mathrm{d}n/\mathrm{d}z = 3.6 \times 10^{20}$ m^{-3}/m and $\mathrm{v}_{Drift} \sim 10^5$ m/s. The drift velocity is shown in Figure 5.13(k) for the entire discharge channel and is larger than the spoke or characteristic velocities we are seeking. It is interesting to note that this velocity is of the same order or lower than $E \times B$ drift velocity. Figure 5.16 and Figure 5.18 show that the frequencies and velocities, respectively, are too high to be spokes. Note for $z/L_{chnl} > 0.6$ the density gradient reverses sign so the waves propagate in the other direction and are not shown.

5.6.4.2 Collisional Density Gradient Drift Waves

The next step is to include collisional drift waves assuming long wavelengths along the magnetic field (small $k_{||}$) for a simple slab (cartesian coordinates) is [135]

$$\omega = \frac{k_\theta \mathrm{v}_{Drift}}{1 + k_\theta^2 \mathrm{v}_s^2/\omega_{ci}^2} \tag{5.36}$$

The phase velocity for Equation 5.36 is shown in Figure 5.13(l) for k_θ corresponding to $m = 5$, which yields results lower than the expected spoke velocity by as little as 50% to as much as an order of magnitude. Noting that $k_\theta^2 v_s^2/\omega_{ci}^2 \gg 1$, Equation 5.36 reduces to $\omega \sim \omega_{ci}/(k_\theta L_{\nabla n_e})$, which is not the same functional form as Equation 5.9. Therefore, the spokes are unlikely caused by density gradient drift waves or collisional drift waves. Figure 5.16 and Figure 5.18 shows the frequencies and velocities, respectively, are too low to be spokes. Note for $z/L_{chnl} > 0.6$ the density gradient reverses sign so the waves propagate in the other direction and are not shown.

5.6.4.3 Density and Magnetic Field Gradient Drift Waves

Esipchuk and Tilnin [91] derived a dispersion relation for small amplitude planar waves using an ideal, two-fluid, collisionless formulation of an unbounded plasma [73] without an energy equation. However, the formulation is not truly collisionless because the Hall parameter is used in the mobility and diffusion coefficients in order to calculate axial electron motion. It accounts for gradients in the magnetic field, but assumes the length scale gradient defined by Equation 5.35 is less than the channel length, which is not always true near the ionization and acceleration region. Furthermore, it assumes that $\omega_{lh} \ll \omega_{pi}$, which is justified from Table 5.2. Choueiri [73], used the dispersion relation to identify ~ 55 kHz azimuthal oscillations immediately downstream from the exit plane of an SPT-100. The dispersion relation is

$$\omega = k_z v_i - \frac{k_\perp^2 v_i^2}{2k_\theta(v_{e\perp} - v_B)} \pm \frac{k_\perp v_i^2}{2(v_{e\perp} - v_B)} \sqrt{1 + \left(\frac{k_z}{k_\theta}\right)^2 - \frac{4k_z(v_{e\perp} - v_B)}{k_\theta v_i} + \frac{4v_{e\perp}(v_{e\perp} - v_B)}{v_i^2}} \tag{5.37}$$

where $k_\perp = \sqrt{k_\theta^2 + k_z^2}$ is wave number perpendicular to the magnetic field (k_θ and k_z are azimuthal and axial components, respectively), v_i is the ion velocity, $v_{e\perp}$ is defined by Equation 2.34 and the magnetic drift velocity is

$$v_B = \frac{v_i^2}{\omega_{ci} L_{\nabla B}} \tag{5.38}$$

Figure 5.16($\nabla n_e, \nabla B$) shows the frequencies are within the expected range for spokes (5-25 kHz) for $z/L_{chnl} < 0.7$, which is upstream of the ionization and acceleration regions. Figure 5.18 shows the velocity is close to that expected for spokes as well. However, Figure 5.17 shows there is no imaginary component upstream of the ionization and acceleration zones, so this mode is not unstable in this region. At the exit plane there is a growth rate of 10^5 Hz and the frequency is within the rage expected for spokes. This is similar to what Choueiri [73] observed for the SPT-100, that the only region this instability was excited was near the exit plane. Further outside the discharge channel the frequency becomes too low. In the ionization and acceleration regions the frequencies and velocities are too large to be spokes.

Frias [102, 103] derived a similar dispersion relation to Equation 5.37 which also accounts for electron flow incompressibility and does not neglect incompressibility of the electron diamagnetic flow. The dispersion relation is

$$\omega = k_z \mathrm{v}_i - \frac{k_\perp^2 \mathrm{v}_s^2}{2(\omega_* - \omega_D)} \pm \frac{k_\perp^2 \mathrm{v}_s^2}{2(\omega_* - \omega_D)} \sqrt{1 + 4\frac{k_z \mathrm{v}_i}{k_\perp^2 \mathrm{v}_s^2}(\omega_* - \omega_D) - 4\frac{k_\theta^2}{k_\perp^2}\rho_s^2 \Delta} \tag{5.39}$$

where v_s is the ion acoustic speed from Equation 5.28 and $\omega_* = -k_\theta \mathrm{v}_{Drift}$. The remaining variables in Equation 5.39 are

$$\omega_D = \frac{-2k_\theta T_e}{BL_{\nabla B}} \tag{5.40}$$

$$\rho_s^2 = \frac{T_e m_i}{qB^2} \tag{5.41}$$

$$\Delta = \left(\frac{2}{L_{\nabla B}} + \frac{E_z}{T_e}\right)\left(\frac{1}{L_{\nabla n}} - \frac{2}{L_{\nabla B}}\right) \tag{5.42}$$

Figures 5.16 and 5.18($\nabla n_e, \nabla B$ (Frias)) show that this is similar to the dispersion relation from Esipchuk and Tilinin for $z/L_{chnl} < 0.7$, but the frequencies and velocities, although the correct order of magnitude, are slightly higher than those of spokes. Figure 5.17 shows some points in the ionization/acceleration zone and downstream have growth rates $10^4 - 10^5$ Hz, in these regions the frequencies are typically an order of magnitude higher than spoke frequencies, with a notable exception at $z/L_{chnl} = 0.9$ where the frequency is within the range for spokes.

5.6.4.4 Density, Magnetic Field, and Temperature Gradient Drift Waves

Frias [102, 103] expanded on the dispersion relation in Equation 5.39 by including the electron energy equation and considered gradients in the electron temperature, which yielded the cubic dispersion relation

$$a\omega_3 + b\omega^2 + c\omega + d = 0 \tag{5.43}$$

$$\begin{aligned} a &= \omega_* - \omega_D \\ b &= -k_\theta^2 \mathrm{v}_s^2 - \omega_* \omega_0 - \frac{7}{3}\omega_* \omega_D + \omega_0 \omega_D + \frac{5}{3}\omega_D^2 + \omega_{*T}\omega_D \\ c &= 2k_\theta^2 \mathrm{v}_s^2 \omega_0 + \frac{10}{3}k_\theta^2 \mathrm{v}_s^2 \omega_D \\ d &= -k_\theta^2 \mathrm{v}_s^2 \omega_0^2 - \frac{10}{3}k_\theta^2 \mathrm{v}_s^2 \omega_D \omega_0 - \frac{5}{3}k_\theta^2 \mathrm{v}_s^2 \omega_D^2 \end{aligned}$$

where $\omega_{*T} = -k_\theta T_e/(BL_{\nabla T_e})$ and $\omega_0 = -k_\theta v_{E\times B}$. Two of the three roots for Equation 5.43 are shown in Figure 5.16($\nabla n_e, \nabla B, \nabla T_e$) with one closely tracking the dispersion relation from Equation 5.39 and the other much higher at $10^6 - 10^7$ MHz. Figure 5.18 shows the phase velocity for the high frequency oscillation tracks the $E\times B$ drift velocity. Figure 5.17 shows this oscillation has a growth rate of 10^5 Hz near the exit plane and immediately downstream. Everywhere else in the discharge channel the growth rate is zero.

5.6.5 Summary and Comparison

In order to compare the dispersion relations detailed in this section, channel centerline plasma properties were used from the measurements in Figure 5.13 at 9 different axial locations. The real part of the frequency in Hertz (not rad/s) is shown in Figure 5.16, the growth rate for instabilities (i.e. the imaginary part of the frequency) in Hertz is shown in Figure 5.17, and the phase velocity $v_{ph} = \omega/k_\theta$ is shown in Figure 5.18. Negative frequencies are not shown as they are in the $-E\times B$ direction, e.g. the drift waves change direction at $z/L_{chnl} = 0.6$. Spoke order $m = 4$ has been used so $k_\theta = 50$ rad/m and largely azimuthal propagation is desired so $k_z = 0.1k_\theta$ similar to Ref. 73. The reference spoke order is $m = 4$ with a solid black line shown at 11 kHz in Figure 5.16 for the frequency peak and a line at 1550 m/s in Figure 5.18 for the spoke velocity. The empirical dispersion relation from Equation 5.9 with $\alpha = 2$ is plotted as a dashed black line in Figure 5.16. The characteristic velocity is assumed to be the ion acoustic speed, $v_{ch} = v_s$, and the characteristic frequency is approximated as $\omega_{ch} \approx 2\pi\omega_{ci}$. Note that by the coordinate system convention used in the derivation, $-k_\theta$ in Equations 5.37, 5.39, 5.43 and 5.31 correspond to the $E\times B$ direction and has been accounted for when comparing the dispersion relations.

Figure 5.17 shows the electrostatic ion cyclotron frequency is a close match for the empirical dispersion relation, which is not surprising given the similarities between Equation 5.9 and Equation 5.29. Electrostatic ion cyclotron oscillations are also similar to different gradient driven oscillations outside of the ionization and acceleration zone. The density gradient drift wave and collisional drift wave cannot be responsible for spokes because their directions are not tied to the $E\times B$ direction. The ion acoustic and sheath driven oscillation theoretically showed significant promise because it is the only dispersion relation to consider walls and sheaths, but the frequencies are too high to be responsible for spokes. However, this does not mean they are not present in HETs. Figure 5.17 shows that the gradient driven oscillations are only excited near the exit of the discharge channel or in the very near field plume, which agrees with previous work. [73] Figure 5.18 shows how much larger the $E\times B$ velocity and electron thermal velocity are than the spoke velocities. The gradient driven waves that account for spatial variations in density, magnetic

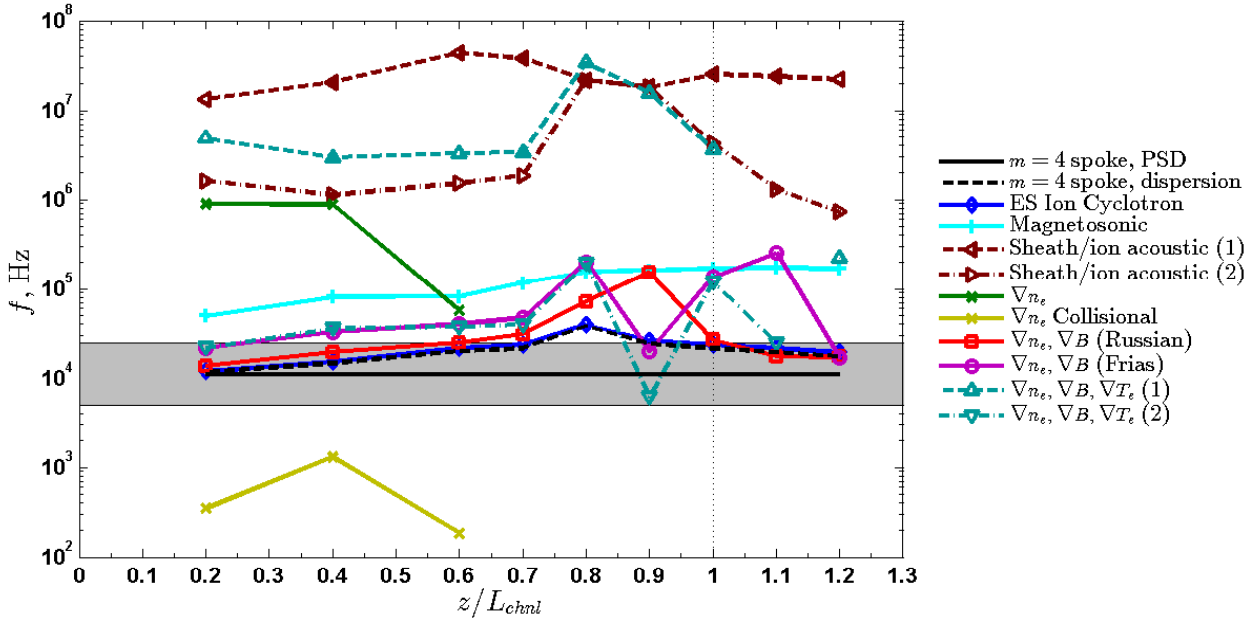

Figure 5.16: Real component of the frequency for the dispersion relations discussed in Section 5.6. Shaded area is the typical spoke frequency range from 5-25 kHz. Solid black line is the 11 kHz peak frequency for an $m = 4$ spoke. The empirical dispersion relation in Equation 5.9 is the dashed black line that coincides with electrostatic ion cyclotron blue line. Parenthetical numbers indicates different roots of a cubic dispersion relation.

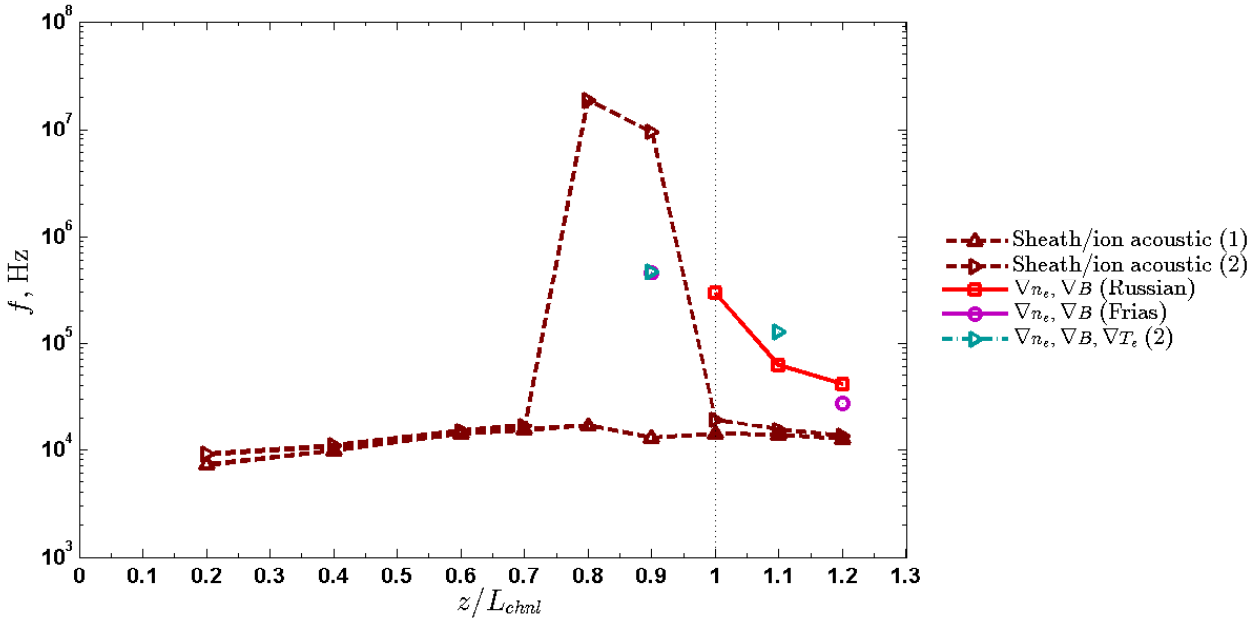

Figure 5.17: Imaginary component of the frequency for the dispersion relations discussed in Section 5.6 showing growth rates. Parenthetical numbers indicates different roots of a cubic dispersion relation.

field, and/or electron temperature have phase velocities that most closely match the observed spoke velocities.

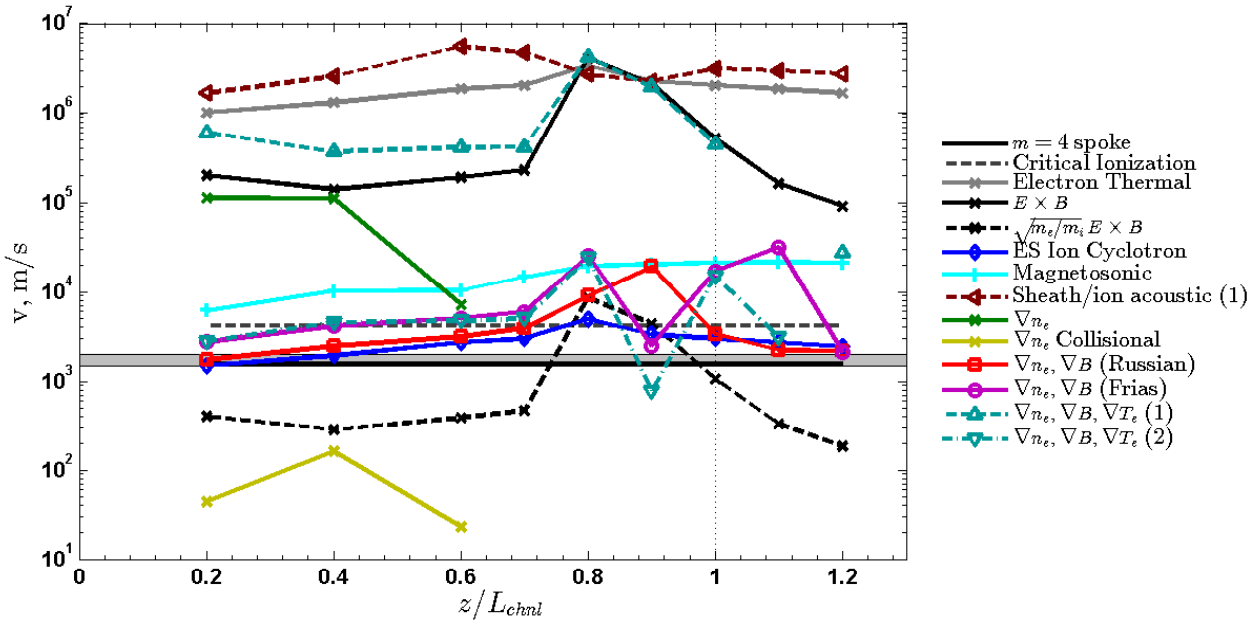

Figure 5.18: Phase velocities for the dispersion relations discussed in Section 5.6. Shaded area is the typical spoke velocity range from 1500-2000 m/s. Parenthetical numbers indicates different roots of a cubic dispersion relation.

It is very important to emphasize that this analysis is not complete without considering the other dispersion relations discussed in Section 7.2.5. Of particular interest are ionization wave or other collisional dispersion relations which have not been considered in this work.

5.7 Sequential Breathing Mode

Bellan [135] provides an excellent overview of the general linearization process to calculate dispersion relations such as those found in Section 5.6. The process of linearizing a system of partial differential equations begins with assuming a perturbation of ϵf_1 to the dependent variable f such that it becomes $f = f_0 + \epsilon f_1$ and $\epsilon \ll 1$. If there is a variable g that is dependent on f through the system of equations such that $g = g(f) = g(f_0 + \epsilon f_1)$, then a Taylor expansion yields $g = g_0 + \epsilon g_1 + \epsilon^2 g_2 + \epsilon^3 g_3 + ...$ Assuming $\epsilon \ll 1$ justifies discarding all terms of order ϵ^2 and higher to linearize the equations to first order perturbations. Even if we relax our initial assumption of $f_1/f_0 \ll 1$, we must still have the oscillation amplitude be less than the steady-state value, $f_1/f_0 < 1$, to justify using linearized wave theory. However, as discussed in Sections 2.5.2 and 6.5 and shown in Figures 2.21, 6.5, 6.6, and 6.12 for breathing mode oscillations, the oscillation amplitudes are

in the range $n_1/n_0 \approx 2-10$, so the underlying premise of linear analysis is invalid. In addition, Adam [50] points out from 2-D fully kinetic simulations that plasma density varies by a factor of 5-10 during a breathing mode cycle. Therefore we treat this mechanism separately with a mostly qualitative argument, but that does not preclude the possibility of a dispersion relation description. Detailed, time-resolved, internal plasma measurements of an HET discharge channel do not exist to verify the simulations. We can postulate that the same fundamental mechanism may exist between the spokes and breathing mode, where the breathing mode (global mode in Chapter 4) exhibits a uniform channel discharge and replenishment process while the spoke mode (local mode in Chapter 4) exhibits an azimuthally local discharge and replenishment process.

As shown by several numerical simulations [33, 76, 77] and in Figure 6.6, the breathing mode is a slow progression of the neutral front down the channel leading up to a rapid ionization event that Barral [95] calls avalanche ionization. During the neutral replenishment period within the discharge channel, slight perturbations or azimuthal non-uniformities in electron density, electron temperature and/or neutral density (all related to ionization rate), cause a local region in the discharge channel to reach the avalanche ionization point before adjacent regions, thus causing a localized increase in plasma density. The localized electron density enhancement travels azimuthally in the $E \times B$ direction initiating avalanche ionization in an adjacent region thus propagating the perturbation in a cascade like event. Extensive numerical and experimental characterization of the neutral flow and plasma within the discharge channel was performed on the H6 [44] where a primary ionization region of ~25% of the discharge channel length and neutral flow velocity of 250 m/s can be reasonably inferred. These assumptions yield a neutral refill time of the ionization region of ~40-50 μs, corresponding to a 20-25 kHz oscillation, which is in line with the oscillation frequencies observed. Breathing mode is typically lower frequency than spokes, so in breathing mode the neutral front could be receding deeper into the channel. Neutral velocity is constant so the rate of progression for the ionization front (which recedes upstream after avalanche ionization) to move down the discharge channel towards the exit plane is constant. Therefore, a lower frequency indicates a longer refill time for neutrals so the ionization has receded deeper into the channel.

Consider the discharge channel region upstream of the acceleration zone where the electric field is small and the ions are essentially stationary with respect to the electron velocity. The ion velocity after the acceleration zone is $\sim 10^4$ m/s, but before the acceleration zone it is close to the neutral thermal velocity of $\sim 10^2$ m/s. The azimuthal electron velocity is $\sim 10^4 - 10^6$ m/s from $E \times B$ drift. The kinetic energy per unit volume for electrons in a quasineutral plasma of density n propagating around the discharge channel through nearly stationary ions at $\mathrm{v}_{E\times B}$ is $\varepsilon = \frac{1}{2} n m_e \mathrm{v}_{E\times B}^2$. A local perturbation in the plasma density caused by a local avalanche ionization event will create a perturbation in the ionization front in the $z-\theta$ plane as shown in Figure 5.19. As discussed

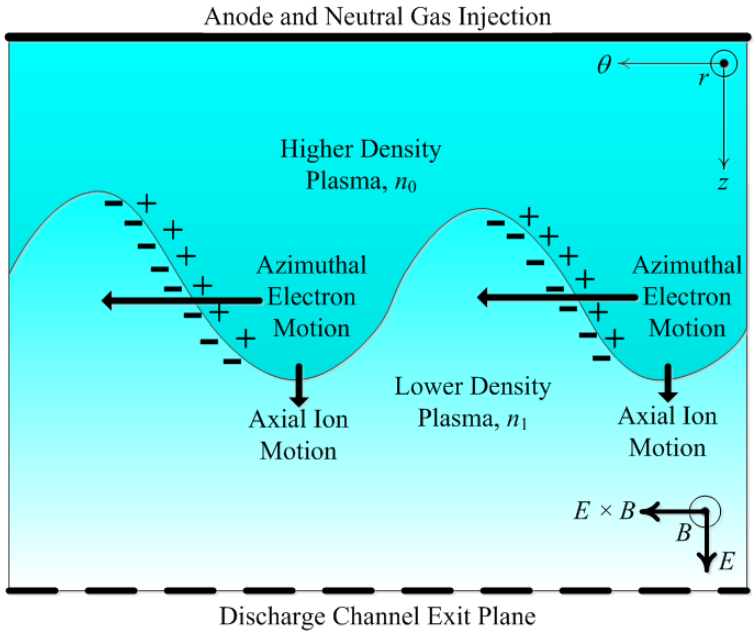

Figure 5.19: Diagram of $z-\theta$ plane of discharge channel showing exaggerated ionization front deformation due to localized avalanche ionizations. Electrons propagating in $E \times B$ direction through quasi neutral plasma of density n_0 will encounter region of lower plasma density n_1 and be slowed by ambipolar forces.

in Section 6.2, the ionization front recession rate from simulations is $\sim 10^3$ m/s after avalanche ionization. The ions are moving axially in the $\hat{z}$ direction, but the electrons are moving azimuthally in the $\hat{\theta}$ direction. When the electrons of density n_0 try to enter the region with lower density n_1, ambipolar forces will retard their motion because of the charge imbalance and the electric field formed from Gauss' Law. As a result of this electric field, the electrons will try to drag sufficient ions ($\Delta n = n_0 - n_1$) to create a quasineutral plasma in a form of ambipolar diffusion. An energy balance will require this new system of electrons and some ions to move at a slower azimuthal velocity v_θ

$$\varepsilon = \frac{1}{2} n m_e v_{E\times B}^2 = \frac{1}{2}(\Delta n m_i + n m_e) v_\theta^2 \tag{5.44}$$

As shown by the breathing mode simulations, $\Delta n \sim n/2$, so it can be assumed that $\Delta n m_i \gg n m_e$. Solving Equation 5.44 for the new azimuthal velocity yields

$$v_\theta \approx \sqrt{\frac{n}{\Delta n}\frac{m_e}{m_i}} v_{E\times B} \tag{5.45}$$

Noting that $\sqrt{n/\Delta n}$ is $\mathcal{O}(1)$, then $v_\theta \sim \sqrt{m_e/m_i} v_{E\times B} \approx 0.002 v_{E\times B}$, so the ambipolar velocity is three orders of magnitude lower than the $E \times B$ velocity. As discussed in Section 5.6.3.1 and shown in

Figure 5.18, the $E \times B$ drift velocity in the ionization zone can be $\sim 10^6$, so $v_\theta \sim 10^3$ is the correct order of magnitude for spokes.

It is interesting to note that if $v_{E\times B}$ is replaced in Equation 5.45 with the electron thermal velocity and the plasma expands into vacuum ($n/\Delta n \approx 1$), the resulting velocity is the ion acoustic speed $v_s = \sqrt{qT_e/m_i}$. This is the approximate net velocity of a plasma expanding into vacuum from ambipolar diffusion. As discussed in Section 5.6.3.2, the spoke velocity is close to the ion acoustic speed for ~ 5 eV electrons and in Figure 5.15 of Section 5.6.3.1 the $E \times B$ drift velocity is the same order of magnitude as the electron thermal velocity for part of the channel. Unfortunately, the electron thermal velocity is not a directed velocity like the $E \times B$ drift velocity in the azimuthal direction, so it alone cannot explain spoke propagation.

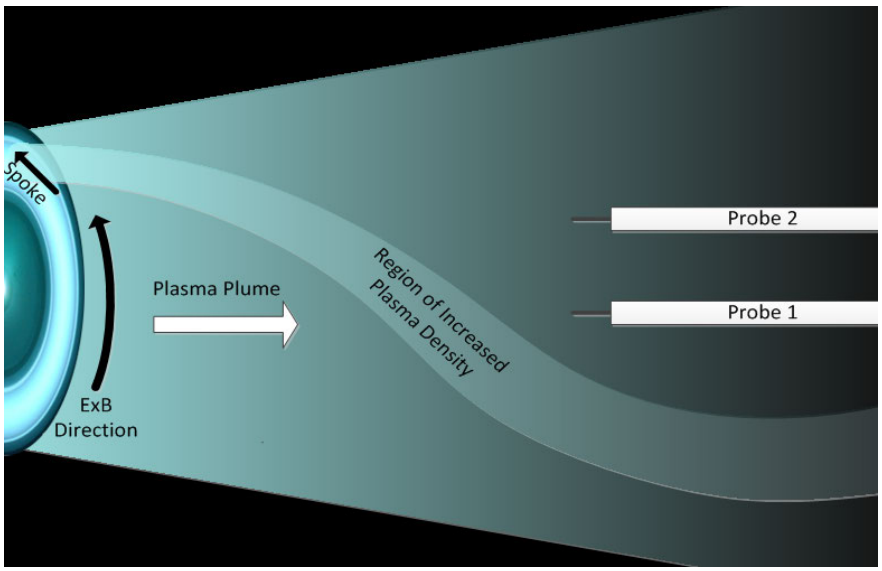

Figure 5.20: Illustration of spokes as regions of increased ion density producing helical structures of increased plasma density within the plume and how that would be measured by vertically spaced probes.

The results from azimuthally spaced probes supports the idea that rotating azimuthal non-uniformities (spokes) are azimuthally propagating regions of increased ionization producing a helical structure within the plasma. The regions of increased ionization propagating in the $E \times B$ direction would cause a delay between probe signals as illustrated in Figure 5.20. As the spoke rotates, this ion production zone moves azimuthally but the ions produced always move axially once created thereby creating a helical structure within the plume of increased ion density. Note there are always ions being produced in the discharge channel, regardless of spoke location, so there is a constant axial stream of plasma emanating from everywhere in the discharge channel. This possible helical structure would exist in addition to the plume generated globally in the discharge

channel. With a spoke velocity of 1800 m/s and an approximate axial ion velocity of 18,000 m/s, the helix angle or pitch angle would be approximately 6° from a line normal to the thruster face.

5.8 Wall Effects

This section presents and discusses observations that wall-effects or wall sheaths must play a role in spoke propagation. The evidence includes spoke direction with the Hall current and azimuthal electron propagation, the absence of spokes in magnetically shielded thrusters, wall material studies, and wall temperature.

5.8.1 Azimuthal Electron Propagation

Spokes are observed to propagate in the $E \times B$ direction and reversing the magnetic field direction reverses the spoke direction. When the magnetic field direction is reversed, plasma properties in the channel and their respective gradients are not changed. Therefore, spokes must be related to the azimuthal Hall current and cannot be the result of gradient-driven waves alone. Note this does not prohibit gradient-driven instabilities from playing a role in spoke mechanics.

A HET does not naturally have a radial restoring force like a magnetron so the electrons likely interact with the wall in some way (magnetic mirror or radial electric field) to propagate their motion to make HETs "closed-drift" devices. Section 2.3.7 discussed in detail the different ideas for how electrons propagate azimuthally around the channel, whether the path is circular or they "bounce" between the channel walls. Regardless, a mechanism is required to reflect electrons back into the channel or to keep electrons in a circular motion around the discharge channel. If this field cannot be established or becomes perturbed, then the electron motion around the discharge channel could be disrupted, which could disrupt spoke propagation assuming they are related. From this discussion we can conclude that spokes must be related to azimuthal electron motion, which are reliant on plasma-wall interactions, B-field topology, and/or sheaths to propagate.

5.8.2 Magnetically Shielded Thrusters

Spokes in unshielded thrusters are observed to propagate in the $E \times B$ direction, so they are likely linked to azimuthal electron motion. Net azimuthal electron motion in the $E \times B$ direction forming the Hall current in HETs will be different in magnetically shielded thrusters as discussed qualitatively in Section 2.3.8. This difference results from the reduced plasma interaction with the walls where radial electric fields will be different. A mode transition study was conducted in magnetically shielded thrusters similar to Chapter 4 where the magnetic field magnitude was varied to induce mode transitions with the results and detailed discussion provided in Appendix C. This study

showed a global to local mode transition similar to those detailed in Chapter 4 at low magnetic field magnitudes, except that spokes are not observed in the local mode. A second mode transition is observed in magnetically shielded thrusters at higher magnetic field magnitudes where spokes are observed simultaneously with cathode oscillations and breathing mode type oscillations. Additionally, Jorns [60] did not observe spokes while investigating a single operating point of the magnetically shielded H6, which showed similar performance to the unshielded H6 [37]. All of this suggests that spokes are only prominent in non-magnetically shielded thrusters, which have increased plasma-wall interactions. Therefore, it can be inferred that spokes are caused by or related to sheaths at the walls.

5.8.3 Wall Material

While investigating different wall materials in the SPT-100, Gascon [65] observed mode transitions similar to those observed in Chapter 4. Gascon did not have the ability to observe spokes in that investigation so we cannot confirm that spokes were present in the low discharge current mode. The accompanying theory provided by Barral [66] suggested Space Charge Saturation, when the wall secondary electron emission coefficient approaches unity, was responsible for the mode transition. If this is correct, it implies a wall related phenomenon for mode transition and hence the onset or disappearance of spokes.

5.8.4 Wall Temperature

The mode transition investigation of Chapter 4 revealed that the transition point varied if the thruster was not run long enough to be at thermal equilibrium or to complete out-gassing. Thruster operation is also known to be highly oscillatory during start-up or after the thruster has been exposed to atmosphere (i.e. the discharge channel absorbs moisture) for an extended period of time. In addition, the transition between modes was noted to be affected by time at the given operating condition, which could be related to wall heating and thermal equilibrium, although wall temperatures were not measured in this investigation. These observations are only qualitative in nature and circumstantially link wall conditions to mode transitions, but combined with the above arguments reinforce the idea that wall effects play a role in mode transition and spoke propagation.

5.9 Conclusions

The investigation of mode transitions showed the presence of spokes is associated with improved thruster performance without determining causality, which motivates this investigation into the underlying fundamental physics. Plasma oscillations in the channel and plume have been extensively

characterized in local mode with azimuthal spokes present using time-resolved diagnostics. The spoke velocity is determined using three methods with similar results: manual fitting of diagonal lines on the spoke surface, linear cross-correlation between azimuthal locations, and an approximated dispersion relation. The spoke velocity for three discharge voltages (300, 400 and 450 V) and three anode mass flow rates (14.7, 19.5 and 25.2 mg/s) yields spoke velocities between 1500 and 2200 m/s across a range of normalized magnetic field settings. These detailed observations are distilled into a list of five criteria any theory for spoke mechanics must explain: 1. Propagate in the $E \times B$ direction, 2. The spoke velocity is 1500-2200 m/s in the H6, 3. The dispersion relation has a functional form where ω monotonically increases with k_θ similar to $\omega^\alpha \approx \mathrm{v}_{ch}^\alpha k_\theta^\alpha - \omega_{ch}^\alpha$, 4. Spoke velocity is weakly, inversely dependent on magnetic field for $B_r/B_r^*|_{trans} < B_r/B_r^* \lesssim 1$, and 5. Spokes are typically not observed in magnetically shielded thrusters.

A coherent theory with supporting experimental evidence for spoke propagation has yet to emerge, but the first inclusive list of possible mechanisms is presented including: 1. Linearized plasma waves (homogeneous, gradient driven and ionization related), 2. Localized breathing mode, and 3. Wall effects. It is unknown whether spokes originate in the near-anode, ionization/acceleration region or the near-field plume, so the plasma properties along channel centerline from previous internal measurements at $B_r/B_r^* = 0.86$ are used to investigate various dispersion relations for linearized plasma waves. The 10's of kHz oscillations associated with spokes are compared to standard plasma oscillations showing $\omega_{ci} \lesssim \omega < \omega_{lh} < \omega_{pi} < \omega_{ce} < \omega_{pe}$. The homogeneous plasma waves investigated are $E \times B$ drift, electrostatic ion cyclotron waves, collisional ion acoustic waves with sheaths, and magnetosonic waves. The gradient driven dispersion relations investigated consider spatial variations in plasma density, magnetic field and electron temperature. Ionization related waves have been reserved for future work.

The $E \times B$ drift is two to three orders of magnitude larger than the spoke velocity and is of the same magnitude as the electron thermal velocity, in agreement with previous results. Electrostatic ion cyclotron waves are of the same frequency as spokes and the dispersion relation has a similar functional form to the empirically approximated dispersion relation of $\omega^\alpha = \mathrm{v}_{ch}^\alpha k_\theta^\alpha - \omega_{ch}^\alpha$ with $\alpha = 2$. The ion acoustic speed is the characteristic velocity in the electrostatic ion cyclotron dispersion relation while the characteristic velocity in the empirical dispersion relation approximation matches the ion acoustic speed for ~ 5 eV electrons that exist in the near-anode and near-field plume regions of the discharge channel. The other homogeneous plasma waves do not have frequencies or velocities that coincide with spokes, but dispersion relations that account for gradients in density, magnetic field and electron temperature do near the anode and exit plane. The sequential breathing mode mechanism may produce an ambipolar type drift due to azimuthal variations in plasma density with a velocity that scales as $\mathrm{v}_{E\times B}\sqrt{m_e/m_i}$ and can be within the range expected for spokes. Results with magnetically shielded thrusters where spokes are only observed at high

magnetic field settings suggest that plasma contact with the discharge channel walls plays a role in spoke formation. Both of these ideas require further investigation.

No definitive mechanism for spoke formation and propagation can be determined until all possible mechanisms have been analyzed and compared. The work presented here does not include ionization instabilities, shearing instabilities or a more detailed theory with wall sheaths, so concluding a spoke mechanism is premature. However, the electrostatic ion cyclotron wave and gradient driven waves (∇n_e,∇B and ∇n_e,∇B,∇T_e) fall within the expected range for spoke frequencies and velocities at some locations along discharge channel centerline and should be considered further.

CHAPTER 6

Global Mode and Breathing Mode Oscillations

"Research is to see what everybody else has seen, and to think what nobody else has thought."

– Albert Szent-Györgi

6.1 Introduction

This chapter characterizes the oscillations observed in global oscillation mode and proposes they are the ubiquitous breathing mode oscillation that has been well studied in literature and discussed in Section 2.5.2. The mode transitions investigated in Chapter 4 showed the oscillations associated with global mode decreased thruster performance, which motivates an investigation to understand their mechanisms so they can be avoided. Section 6.3 characterizes the global mode frequency as a function of operating parameters and compares it to the classic breathing mode frequency model developed by Fife. [77] Section 6.4 discusses triggers for breathing mode oscillations. Section 6.5 investigates global mode oscillations as breathing mode oscillations using two different numerical models. The fluid model developed by Barral [33] for breathing mode oscillations in an SPT-100 is used to re-create mode transitions by varying magnetic field strength. Further hybrid direct kinetic simulations by Hara [34] also re-create mode transitions. Both of these simulations support the postulate that mode transition to global mode indicates de-stabilization of the ionization zone location in the discharge channel akin to breathing mode oscillations.

6.2 Breathing Mode Oscillations and Global Mode

A postulate is proposed here that the global oscillation mode is the well-studied breathing mode and the transition to local oscillation mode represents a damping or cessation of the breathing mode mechanism allowing the azimuthal spokes to propagate. This implies the transition from global

mode to local mode indicates the ionization region has been stabilized axially in the discharge channel. The breathing mode has been numerically modeled by Fife [77], Boeuf [76], Barral [33], Hara [86], and Szabo [51]. However, Choueri [73] pointed out in 2001 that stability criteria have yet to be theoretically developed. Barral [142] recently published the first known stability analysis for the breathing mode using linear and non-linear techniques, but further validation is necessary to confirm the criteria.

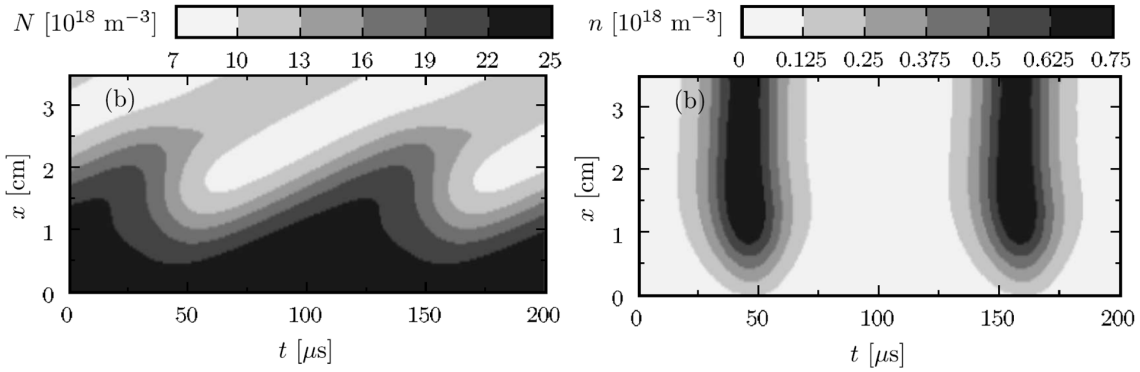

Figure 6.1: Neutral density (left) and plasma density (right) from 1-D fluid simulation of an SPT-100 on channel centerline with V_D = 220 V. x direction is axial distance on channel centerline (labeled z in the present investigation) with the anode at $x = 0$. Reproduced from Figure 3(b) and 4(b) of Ref. 33.

The analysis in Section 5.6 on spoke propagation and dispersion relations assumes the plasma properties are constant in time within the discharge channel allowing spokes to propagate and Figure 5.11 shows the spoke velocities are 1500-2000 m/s. In the H6, a typical spoke will require $\sim 300\ \mu s$ to travel around the entire discharge channel. However, a single spoke typically does not propagate around the entire channel, but will fade out and a new spoke will form as shown in Figure 4.9. At the reference magnetic field setting they can propagate for over half of the channel circumference, but at high magnetic field settings the spoke duration is shorter so they may propagate for less than a quarter of the channel. Therefore, the typical spoke lifetime is $\sim 75-150\ \mu$s, which is the same timescale as ~ 10 kHz breathing mode oscillations. The 1-D fluid simulation of an SPT-100 developed by Barral [33] with results reproduced in Figure 6.1 shows that during a $\sim 100\ \mu s$ breathing mode cycle the plasma properties can change significantly. For the plasma properties on discharge channel centerline Figure 6.1 shows that neutral density can change by a factor of 2-3, plasma density can change up to an order of magnitude, and electron temperature can change by a factor of 2 (from Figure 5 of Ref. 33, not reproduced here). The simulation calculated a slow progression of the neutral front down the discharge channel building up to avalanche ionization. Figure 6.1 shows that once avalanche ionization occurs at $\sim 50\ \mu$s and again at $\sim 150\ \mu s$, the plasma density peaks and the neutral front recedes with a velocity in

the range of $0.5-5\times10^3$ m/s. Assuming global mode oscillations are breathing mode oscillations, spokes may not be able to propagate since the breathing mode period is of the same order or smaller than the time required for spoke propagation and the recession rate can be greater than the spoke velocity of $\sim$ 1700 m/s.

The assumption is made that global mode oscillations observed in Chapter 4 are the same mechanism as breathing mode oscillations occurring everywhere in the channel simultaneously. Therefore, the term breathing mode and global mode will be used interchangeably throughout this chapter. Significant evidence exists to support this assumption as will be shown in this chapter, but experimental validation is still required and is discussed in Section 7.2.1.

Section 4.4.3 discusses highly oscillatory behavior versus unstable operation for a HET. Global mode is highly oscillatory with large amplitude fluctuations in discharge current, but the mean discharge current and oscillation amplitude remain constant so the thruster is stable. Unstable thruster operation is defined by discharge current "run-away" as shown in Figure 4.7. This use of "stable" and "unstable" contrasts the nomenclature used in plasma oscillation literature where the term "unstable" indicates oscillations are present and "stable" indicates they are absent. In this chapter, when we refer to excitation of the breathing mode as unstable to follow the convention used in literature, this indicates the highly oscillatory behavior in global mode and not a "run-away" discharge current.

6.3 Global/Breathing Mode Frequency

6.3.1 Empirical Characterization

This section seeks to characterize the global mode oscillation frequency as a function of operating conditions and compare it with the breathing mode frequencies observed by other investigations. Here the global mode frequency is determined by the peak in the I_D (same as peak in m_0 PSD) which is clearly visible in Figures 4.12. The peak is identified using the Lorentzian fit method described in Chapter 5.5.3. The peak I_D frequencies for all of the conditions shown in Table 4.1 are shown in Figure 6.2 versus B_r/B_r^* for global mode, $B_r/B_r^* \leq B_r/B_r^*|_{trans}^{lower}$.

The data from Figure 6.2 can be used to plot f versus V_D and $\dot{m}_a$ at constant B_r/B_r^* as shown in Figure 6.3(a) and (b), respectively. Figure 6.2 can be used to infer $f \propto (B_r/B_r^*)^{\alpha}$ where $\alpha \gtrsim 0.5$. Figure 6.3(a) can be used to infer $f \propto V_D^{-\beta}$ where $1 \lesssim \beta \lesssim 1.5$ and Figure 6.3(b) implies $f \propto \dot{m}_a^{-\gamma}$ where $0.5 \lesssim \gamma \lesssim 1$. Therefore the frequency can be written as

$$f = C\frac{(B_r/B_r^*)^{\alpha}}{V_D^{\beta}\dot{m}_a^{\gamma}} \tag{6.1}$$

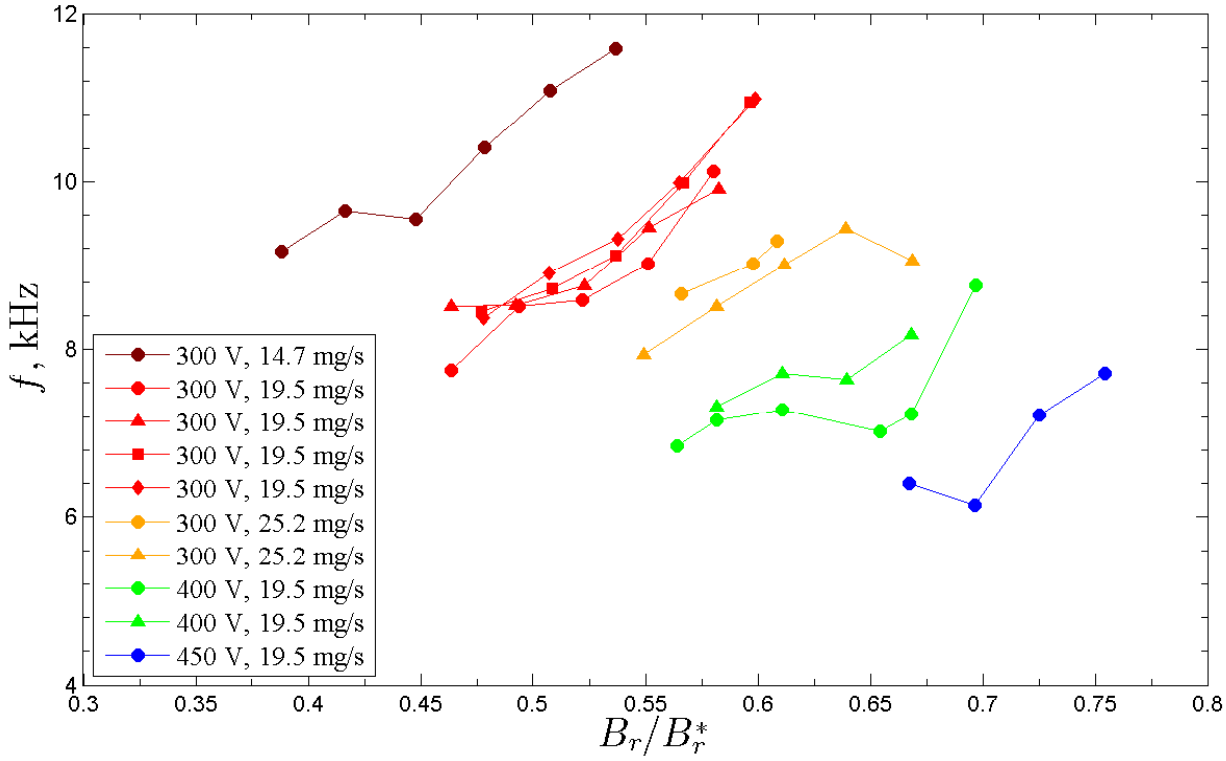

Figure 6.2: Peak global mode frequency variation with B_r/B_r^* for all conditions. Note there are 4 sweeps for 300 V, 19.5 mg/s, two for 300 V, 25.2 mg/s and 400 V, 19.5 mg/s. The values shown are up to $B_r/B_r^*|_{trans}^{lower}$.

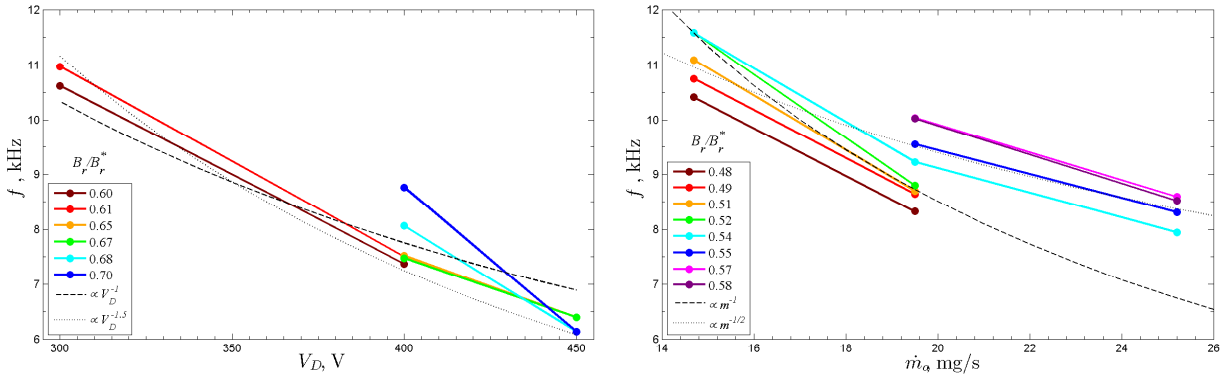

(a) $\dot{m}_a$ = 19.5 mg/s

(b) V_D = 300 V

Figure 6.3: Global mode frequency variation with (a) discharge voltage at constant flow rate and (b) anode flow rate at constant discharge voltage. For conditions with multiple sweeps, the frequency is the average of all sweeps. Lines for $f \propto V_D^{-1}$ and $f \propto V_D^{-1.5}$ are shown in (a) and $f \propto \dot{m}_a^{-1}$ and $f \propto \dot{m}_a^{-0.5}$ are shown in (b) for reference only and are not calculated from least-squares fit.

where C is an unknown constant coefficient to ensure correct units. Equation 6.1 can be written in matrix form with the discharge voltage and anode mass flow rate normalized by the nominal values, $V_D^* = 300$ V and $\dot{m}_a^* = 19.5$ mg/s

$$\log(f) = \begin{bmatrix} \log(C) \\ \alpha \\ -\beta \\ -\gamma \end{bmatrix} \begin{bmatrix} 1 & \log\left(\frac{B_r}{B_r^*}\right) & \log\left(\frac{V_D}{V_D^*}\right) & \log\left(\frac{\dot{m}_a}{\dot{m}_a^*}\right) \end{bmatrix} \tag{6.2}$$

The unknowns in Equation 6.2 can be solved by inverting the matrix

$$\begin{bmatrix} \log(C) \\ \alpha \\ -\beta \\ -\gamma \end{bmatrix} = \log(f) \begin{bmatrix} 1 & \log\left(\frac{B_r}{B_r^*}\right) & \log\left(\frac{V_D}{V_D^*}\right) & \log\left(\frac{\dot{m}_a}{\dot{m}_a^*}\right) \end{bmatrix}^{-1} \tag{6.3}$$

Equation 6.3 can be solved using the data shown in Figure 6.2 and yields many more equations than unknowns. The Moore-Penrose pseudoinverse matrix is used to solve Equation 6.3 which is the least-squares solution to the over-determined problem. The resulting power law relation shown in Figure 6.4 is

$$f[\text{kHz}] = 16.29 \frac{(B_r/B_r^*)^{0.88}}{(V_D/V_D^*)^{1.32}(\dot{m}_a/\dot{m}_a^*)^{0.70}} \tag{6.4}$$

6.3.2 Frequency Comparison with Theory

The frequency variation must be related to other plasma properties such as ion velocity and neutral density in order to compare with existing theories. The ion velocity can be related to the discharge potential using conservation of energy

$$V_D = \frac{m_i \mathrm{v}_i^2}{2q\eta_V} \tag{6.5}$$

where the voltage utilization efficiency, η_V, is the fraction of the discharge potential the average ion is accelerated through (Equation 2.12). The mass flux of particles through a the discharge channel of area A_{chnl} is

$$\dot{m} = A_{chnl} n_N m_N \mathrm{v}_{th_N} \tag{6.6}$$

where n_N is the neutral particle density and $\mathrm{v}_{th_N} = \sqrt{8k_B T_N/(\pi m_N)}$ is the thermal velocity for neutrals of temperature T_N and mass m_N. A flow rate of $\dot{m}_a = 20$ mg/s and $\mathrm{v}_{th_N} = 220$ m/s for 300 K Xe atoms in Equation 6.6 yields a density of 2.7×10^{19} m^{-3}, which is in approximate agreement

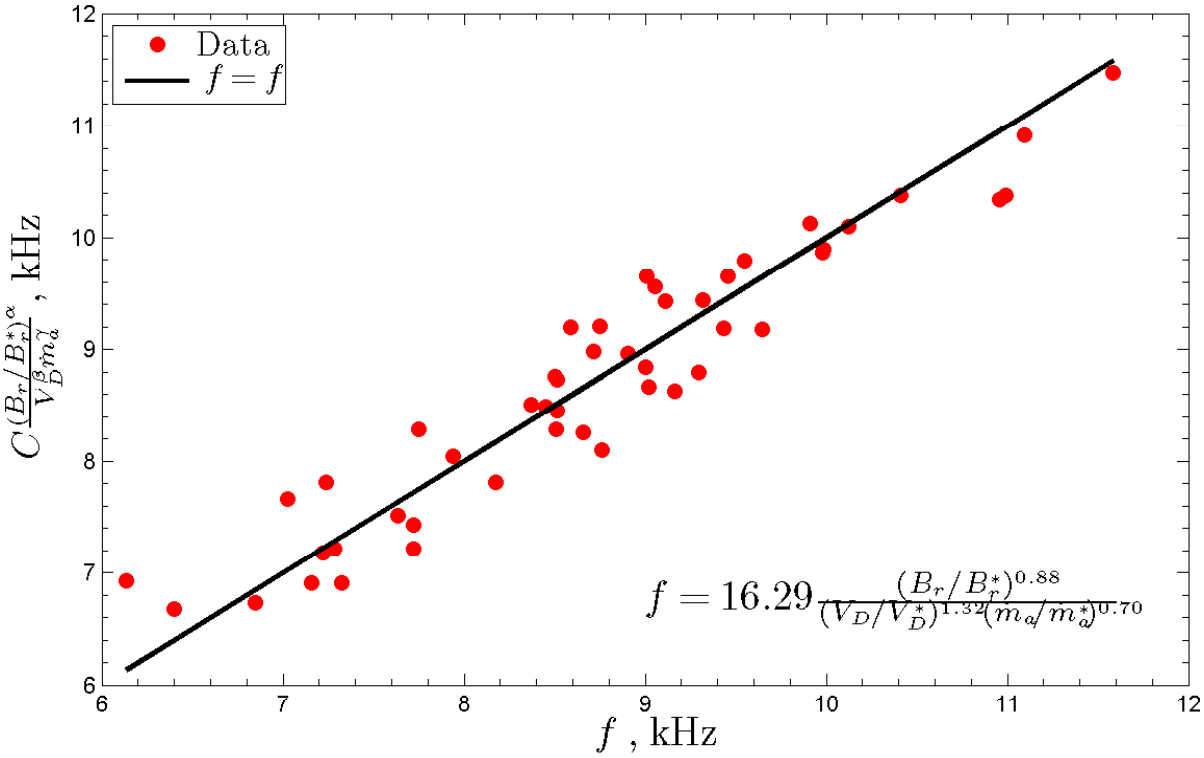

Figure 6.4: Power law fit for global mode frequency oscillations in kHz for all data shown in Figure 6.2 using Equation 6.4. A line with slope of 1 is shown for reference.

with Figure 5.13(b) for most of the discharge channel. Writing the frequency in Equation 6.4 as a function of magnetic field, discharge potential, and anode mass flow rate

$$f = C\frac{B_r^{\alpha}}{V_D^{\beta}\dot{m}_a^{\gamma}} \tag{6.7}$$

and then using the definition of electron cyclotron frequency, Equation 6.5, and Equation 6.6, the frequency from Equation 6.7 can be written as

$$f = \frac{C\left(\omega_{ce}\frac{m_e}{q}\right)^{\alpha}}{\left(\frac{m_i v_i^2}{2q\eta}\right)^{\beta}(An_N m_N v_{th_N})^{\gamma}} = \frac{\omega_{ce}^{\alpha}}{n_N^{\gamma}}\frac{1}{v_i^{2\beta}v_{th_N}^{\gamma}}\left[C\left(\frac{m_e}{q}\right)^{\alpha}\left(2\eta\frac{q}{m_i}\right)^{\beta}\left(\frac{1}{A_{ch}m_N}\right)^{\gamma}\right] \tag{6.8}$$

Using Equation 6.4, the fit coefficient in Equation 6.7 is $C = 5.65 \times 10^5$ with the correct units to yield frequency in Hz for Equation 6.4. Assume $\alpha \sim \gamma$ (justified from Equation 6.4), noting $m_N = m_i$, and using the ionization rate, $\nu_i = k_i(T_e)n_N$, Equation 6.8 can be written as

$$f = \frac{\Upsilon}{\mathrm{v}_i^{2\beta}} \left(\frac{\Omega_i}{\mathrm{v}_{th_N}} \right)^{\alpha} \tag{6.9}$$

where $\Omega_i = \omega_{ce}/\nu_i$ is the ionization rate Hall parameter and the coefficient Υ is

$$\Upsilon = \left[C \left(\frac{k_i m_e}{A_{ch} m_i q} \right)^{\alpha} \left(2\eta \frac{q}{m_i} \right)^{\beta} \right] \tag{6.10}$$

Note the coefficient Υ defined in Equation 6.10 is a function of T_e because of the ionization rate, k_i. From the empirical fit in Figure 6.4 and Equation 6.4, $\alpha \sim 3/4$ and $\beta \sim 4/3$.

The simple model for breathing mode frequency first proposed by Fife [77] and given in Equation 2.51 of Section 2.5.2 is

$$f = \frac{\sqrt{\mathrm{v}_{th_N} \mathrm{v}_i}}{2\pi L_i} \tag{6.11}$$

where v_i is the velocity of ions leaving the ionization zone of length L_i. However, Fife admits that L_i is a function of ionization rate, which is dependent on neutral velocity and thermal velocity so Equation 6.11 is more complicated than it initially appears. For frequency to increase as B-field increases, the ionization length would have to decrease, assuming the ion velocity and neutral velocity are unaffected by the change in B-field. This would mean neutral ionization is more confined to a region closer to the channel exit and less ionization occurs upstream towards the anode. therefore, the ionization region decreases with increasing B until it eventually reaches a constant value when the breathing mode is no longer excited.

The form of Equation 6.9 and 6.11 are significantly different, albeit the explicit dependence of L_i on B_r, v_{th_N}, and v_i is unknown and could account for the discrepancies. For the models to match, the ionization length would have to scale as $L_i \sim \mathrm{v}_{th_N}^{\alpha+1/2} \mathrm{v}_i^{2\beta+1/2} \Omega_i^{-\alpha}$. More rigorously, equating Equations 6.8 and 6.11 yields the ionization length

$$L_i = \frac{1}{C_1} \frac{\mathrm{v}_i^{2\beta+1/2} \mathrm{v}_{th_N}^{\gamma+1/2} n_N^{\gamma}}{w_{ce}^{\alpha}} \approx 24.5 m_i \frac{\mathrm{v}_i^{3.14} \mathrm{v}_{th_N}^{1.2} n_N^{0.7}}{\omega_{ce}^{0.88}} \tag{6.12}$$

$$C_1 = 2\pi C \left(\frac{m_e}{q} \right)^{\alpha} \left(2\eta \frac{q}{m_i} \right)^{\beta} \left(\frac{1}{A_{ch} m_i} \right)^{\gamma} \tag{6.13}$$

Assuming v_i and v_{th_N} are not functions of B, then Equation 6.12 shows that $L_i \sim 1/B^{\alpha}$, which supports the idea that ionization length decreases with increasing B-field. Several simplifying

assumptions have been made to derive Equation 6.9 from empirical results and Equation 6.11 from first principles, but they both generally support the same qualitative argument. Increasing L_i means that more ionization is occurring deeper in the discharge channel closer to the anode. Once the ionization length is larger than a critical value, too much ionization occurs deep in the discharge channel and the neutral supply is depleted before reaching the exit plane. The depleted neutral supply forces oscillations to maintain continuity and current conduction in the plasma to sustain the discharge.

6.3.3 Excitation Criterion from Frequency Measurements

A properly designed HET will ionize most of the propellant gas injected from the anode, [11] so an approximate ionization length, L_i, can be determined assuming full ionization

$$n_n n_e \langle \sigma_i \mathrm{v}_e \rangle A_{chnl} L_i \approx n_n \mathrm{v}_{th_N} A_{chnl} \tag{6.14}$$

where $\langle \sigma_i \mathrm{v}_e \rangle$ is the ionization rate coefficient for Maxwellian electrons. Therefore, the ionization length is approximately

$$L_i \approx \frac{\mathrm{v}_{th_N}}{n_e \langle \sigma_i \mathrm{v}_e \rangle} \tag{6.15}$$

Figure 5.14 shows that the plasma density begins a sharp increase at $z/L_{chnl} \sim 1/2$ and Figure 5.13(a) shows that $n_e \sim 10^{18}$ m^{-3} from $0.5 \lesssim z/L_{chnl} \lesssim 1$. The significantly higher plasma density for the outer half of the discharge channel indicates the ionization region length should be $L_i/L_{chnl} \sim 1/2$. Although the electron temperature in the discharge channel peaks over 30 eV, Figure 5.13(c) shows that the electron temperature is $5-10$ eV in most of the channel except near the exit. Using these value ranges with the ionization rate coefficients from Appendix E of Ref. 11 in Equation 6.15, the ionization length is $L_i/L_{chnl} \sim 0.1-0.6$. This is admittedly a large range, but corroborates our previous observation of expected ionization length.

Armed with this idea of the approximate ionization region length as half of the discharge channel, the empirical transition criterion can be combined with the empirical and theoretical breathing mode frequency relations to determine the ionization length criterion. Equations 4.9 and 4.10 in Section 4.4.2 relate the transition magnetic field strength ($B_r/B_r^*|_{trans}^{lower}$) to ion velocity, neutral velocity and neutral density from empirical observations (the 'transition surface'). This provides a criterion to remain in local mode $B_r/B_r^*|_{local} > B_r/B_r^*|_{trans}^{lower}$ where the breathing mode is not excited. In Section 6.3.2, Equation 6.8 relates global mode oscillation frequency to magnetic field strength, ion velocity, neutral velocity and neutral density from empirical observations. Equation 6.11 relates breathing mode oscillation frequency, ion velocity and ionization length from

a simple, first-principles model. Combining these equations to eliminate the magnetic field and oscillation frequency yields the ionization length criterion to stabilize breathing mode oscillations

$$L_i < 9.06 \times 10^{-19}\ \mathrm{v}_i^{2\beta-\alpha+1/2}\ \mathrm{v}_{th_N}^{\gamma-\alpha/2+1/2}\ n_n^{\gamma-\alpha/2} \tag{6.16}$$

where α, β and γ are the empirically determined power dependencies in Equation 6.1. From Equation 6.4, $\alpha = 0.88$, $\beta = 1.32$, and $\gamma = 0.70$, so Equation 6.16 can be written as

$$L_i \lesssim \frac{17}{3} q\ \mathrm{v}_i^{2.26}\ \mathrm{v}_{th_N}^{0.76}\ n_n^{0.26} \tag{6.17}$$

Using $\mathrm{v}_i = 2 \times 10^4$ m/s from a 300 V discharge with 90% voltage utilization efficiency, $\mathrm{v}_{th_N} =$ 220 m/s from 300 K neutrals, and $n_n = 2 \times 10^{19}$ m^{-3} from Table 3.1, the stability criterion for the ionization length in Equation 6.17 is $L_i/L_{chnl} \lesssim 0.75$. This means that if the ionization region becomes larger than $\sim 3/4$ the discharge channel, then the breathing mode instability will be triggered. A significant number of approximations were used to distill the ionization length criterion in Equation 6.17, but the qualitative idea is valid that if the ionization rate is too high deep in the channel close to the anode, such that the neutrals are consumed too quickly after exiting the anode, then the breathing mode oscillation will occur.

Close inspection of the magnetic field lines inside the discharge channel of the H6 in Figure 3.2 reveals that the first magnetic field lines to intersect the anode originate from $z/L_{chnl} \sim 1/2$ on the discharge channel walls. Therefore, electrons approximately half way down the discharge channel colliding with the wall can have a guiding center about a field line that will take them directly to the anode. This magnetic field topology may play a role in mode transitions if the ionization length extends too far upstream where it is easier for electrons to become trapped on field lines intersecting the anode.

Barral [94] pointed out Equation 6.11 is fundamentally flawed in that the influx of neutrals is dependent on a priori knowledge of neutrals inside the chamber, however more detailed analysis by Barral [142] with a modified Lotka-Volterra model determined that Fife's model [77] is still relevant. The only stability analysis for the breathing mode was by Barral [142] where he conducted a linearized analysis of the modified predator-prey model. An excitation threshold was found from the time-delay incurred by neutral transit time through what he called the 'pre-ionization region.' In principle this agrees with the above discussion, where the critical time is $t_i = L_i/\mathrm{v}_{th_N} = 135$ μs from the above example for a neutral to transit L_i. This would corresponds with a frequency of $f = 1/t_i = 7.4$ kHz, which is in line with the frequencies observed in Figure 6.2.

6.4 Breathing Mode Stability Criterion

6.4.1 Mode Transition as Neutral Deficiency

In this section we discuss a simple criterion to identify the onset of breathing mode oscillations using a simple 0-D model. The continuity equations for ion, electrons and neutrals in the axial direction, z, are

$$\frac{\partial n_i}{\partial t} + \frac{\partial}{\partial z}(n_i \mathrm{v}_i) = k_i n_n n_e - \nu_{iw} n_i \tag{6.18}$$

$$\frac{\partial n_e}{\partial t} + \frac{\partial}{\partial z}(n_e \mathrm{v}_{ez}) = k_i n_n n_e - \nu_{ew} n_e \tag{6.19}$$

$$\frac{\partial n_n}{\partial t} + \frac{\partial}{\partial z}(n_n \mathrm{v}_n) = -k_i n_n n_e + \nu_{iw} n_i \tag{6.20}$$

where ν_{iw} and ν_{ew} are the ion and electron collision frequencies with the wall, respectively. Assume quasi-neutrality so $n_i \sim n_e \sim n$ where n is the plasma density. Focus on the heavy species and neglect ion to wall collisions and assume a constant neutral velocity to reduce Equations 6.18-6.20 to

$$\frac{\partial n}{\partial t} + \mathrm{v}_i \frac{\partial n}{\partial z} + n \frac{\partial \mathrm{v}_i}{\partial z} = k_i n_n n \tag{6.21}$$

$$\frac{\partial n_n}{\partial t} + \mathrm{v}_n \frac{\partial n_n}{\partial z} = -k_i n_n n \tag{6.22}$$

Introduce the definition of gradient length scale for parameter ϱ

$$L_{\nabla \varrho} = \left(\frac{1}{\varrho} \frac{\mathrm{d}\varrho}{\mathrm{d}z} \right)^{-1} \tag{6.23}$$

so Equations 6.21 and 6.22 can be written as

$$\frac{\partial n}{\partial t} + \frac{\mathrm{v}_i n}{L_{\nabla n}} + \frac{\mathrm{v}_i n}{L_{\nabla \mathrm{v}_i}} = k_i n_n n \tag{6.24}$$

$$\frac{\partial n_n}{\partial t} + \frac{\mathrm{v}_n n_n}{L_{\nabla n_n}} = -k_i n_n n \tag{6.25}$$

If the breathing mode is not excited, then the plasma properties are not varying in time along the discharge channel length so $\partial/\partial t = 0$. However, the breathing mode is triggered when an imbalance exists. More sophisticated numerical simulations show that the breathing mode is characterized by

a depletion of neutrals due to rapid, intense ionization. Therefore, the criterion for stabilization of the breathing mode is $\partial n_n/\partial t \geq 0$ and Equation 6.25 is

$$k_i n_n n \leq \frac{\mathrm{v}_N n_n}{-L_{\nabla n_n}} \tag{6.26}$$

Equation 6.26 shows the criterion for stability is that the loss of neutrals to ionization in a given volume must be less than or equal to the flux of neutrals through the volume. Note the neutral density is typically decreasing along the length of the channel so generally $L_{\nabla n_n} < 0$ and ion velocity is always increasing so $L_{\nabla \mathrm{v}_i} > 0$. However, the plasma density increases in the ionization region and decreases in the acceleration region so $L_{\nabla n}$ can be positive or negative. The stability criterion in Equation 6.26 can be re-written using Equation 6.24 with $\partial n/\partial t \approx 0$

$$\frac{\mathrm{v}_n}{\mathrm{v}_i} \geq \frac{n}{n_n}\left(\frac{-L_{\nabla n_n}}{L_{\nabla n}} + \frac{-L_{\nabla n_n}}{L_{\nabla \mathrm{v}_i}}\right) \tag{6.27}$$

Rewrite Equation 6.27 as particle fluxes, $\Gamma = n\mathrm{v}$ in #/s/m^2, of ions and neutrals with a coefficient α

$$\Gamma_n \geq \alpha \Gamma_i \tag{6.28}$$

$$\alpha = \frac{-L_{\nabla n_n}}{L_{\nabla n}} + \frac{-L_{\nabla n_n}}{L_{\nabla \mathrm{v}_i}} \tag{6.29}$$

The criterion shown in Equations 6.27 and 6.28 must be satisfied throughout the entire length of the discharge channel, particularly the ionization zone, or breathing mode oscillations will occur. Because all the length scales should be similar, the coefficient α should be $\mathcal{O}(1)$ and the breathing mode stability criterion in Equation 6.28 for conditions in the ionization region of the channel can be approximated as

$$\frac{\Gamma_i}{\Gamma_n} < 1 \tag{6.30}$$

The ionization region is defined here as the region between the peak plasma density and the peak electric field.

6.4.2 Mode Transition as Electron Deficiency

The traditional predator-prey model for breathing mode oscillations treats neutrals as the prey and electrons as the predators. The breathing mode is excited when neutrals are depleted, which is supported by the fluid simulations shown later in Figure 6.9. This model inherently assumes that a sufficient supply of electrons exists to continue ionization since neutral density is the limiting factor. However, the mode transitions discussed in Section 2.4 hint that the electron supply to the discharge channel or electron retention in the discharge channel may affect mode transitions. The

wall material discussion and space-charge saturation [65, 66] directly relate to electron retention in the channel from near-wall conductivity and supply in the channel from secondary electron emission. A change in CFF [41, 67] causes a change in the near field plume plasma, which could indicate the electron supply to the channel is disrupted from changes in electron mobility. This prompts a different perspective on the initiation of breathing mode where insufficient electron density causes a loss of continuity in the plasma, interrupts ionization, and excites oscillations.

Consider the same 0-D model used in Section 6.4.1 with a control volume as the primary ionization region and the electron flow into and out of the volume. The ionization region is assumed to start in the discharge channel ($1/4 \lesssim z/L_{chnl} \lesssim 3/4$) in a region where the B-field is increasing with axial distance $\partial B/\partial dz > 0$. The ionization region may end upstream or downstream from the B-field peak, which occurs near the exit plane ($\partial B/\partial dz = 0$ near $z/L_{chnl} = 1$). Electron source mechanisms for the ionization region include: cross-field diffusion from the plume, cold secondary electron emission from the walls, azimuthal motion in the channel (into the volume), and electrons produced from ionization processes. Electron loss mechanisms for the ionization region include: cross-field diffusion to the anode, hot electrons lost to the wall, azimuthal motion in the channel (out of the volume), and electrons lost to recombination. Initiation of the breathing mode from a depleted electron population can be broadly described as insufficient supply or insufficient retention/excessive loss:

1. Insufficient Supply

    (a) If changes in the plume cause the near-field mobility to significantly decrease, then the electron supply from the cathode will be "choked-off" and could trigger breathing mode oscillations.

    (b) Insufficient ionization from cold electrons (reducing ionization rate coefficient) or lack of neutral population means that not enough electrons are produced in the volume of the channel.

2. Insufficient Retention/Excessive Loss

    (a) Changes in the wall sheath could cause significant electron flux to the walls that could trigger breathing mode oscillations (space charge saturation). Similarly, the wall sheath changes could prevent electrons from being reflected into the channel to continue azimuthal propagation and they are "shunted" to the anode along the wall (near-wall conductivity).

    (b) If the magnetic field is too low, then too many electrons will flow across magnetic field lines to the anode because the cross-field mobility in the ionization region is too large.

A rigorous treatment is not provided here and is recommended for future work. This will require a 0-D model or 1-D model which includes continuity, momentum and energy equations.

6.5 Transition as Breathing Mode Damping

This section will use two different numerical simulations to investigate mode transitions by varying magnetic field strength similar to the experimental investigation of Chapter 4. The first model is a fully fluid description of the plasma developed by Barral [33] to simulate the discharge channel of an SPT-100. The second model is a hybrid-direct kinetic simulation of the SPT-100 discharge channel by Hara [86] where ions, neutrals and one excited neutral state are treated with kinetic descriptions and the electrons are treated as a fluid. Both models are 1-D axial, time-resolved simulations that have successfully reproduced breathing mode oscillations. Motivated by the work discussed in Chapter 4, Hara used the hybrid direct kinetic model to conduct an investigation of varying magnetic field strength to induce mode transition. [34] The use of Barral's fluid mode to investigate mode transitions is presented here. Both investigations reproduced mode transitions similar to those observed experimentally where the global mode corresponds to excitation of the breathing mode oscillation and local mode corresponds to damping of the breathing mode.

6.5.1 Fluid Model Description

A 1-D, time-resolved, numerical, fluid model of an HET discharge has been developed by Barral and used to analyze a SPT-100 discharge. The model is derived and detailed in Ref. 33 and only summarized here. It uses axial continuity equations for neutrals, electrons and +1 ions. Axial momentum equations are included for electrons and ions, and the azimuthal momentum equation and energy equation for electrons only. The radial magnetic field is approximated by a Gaussian curve

$$B(z) = B_{max} \exp\left[-\left(\frac{z - L_{ch}}{L_B}\right)^2\right] \tag{6.31}$$

where L_{ch} is the channel length, L_B is the characteristic width of the magnetic field and a peak value of B_{max} = 220 G was used in Ref. 33. The SPT-100 channel length is 2.5 cm and the simulated domain is 3.5 cm, at which there is a virtual cathode providing 5 eV electrons. Electron and ion losses at the walls are accounted for using a simplified theory for radial sheath and pre-sheath. The neutral velocity is assumed to be 200 m/s and a constant 1/160 coefficient is used for Bohm-type electron diffusion so α = 0.1 in Equation 2.7. The total electron energy is

$$\epsilon = \frac{3}{2}T_e + \frac{1}{2}m_e\left(\mathrm{v}_{ez}^2 + \mathrm{v}_{e\theta}^2\right) \tag{6.32}$$

where T_e is the thermal temperature, v_{ez} is the axial electron velocity, and $v_{e\theta}$ is the azimuthal electron velocity.

The model was used to numerically investigate the breathing mode oscillation of an SPT-100 operated at 220 V, anode mass flow rate of 5 mg/s Xe in Ref. 33. Figure 6.1 shows the time-resolved ion and neutral density during two breathing mode oscillation cycles. The computer code for the work in Ref. 33 was provided by the author and recompiled. The results from Figure 6.1 have been recalculated in Figure 6.5.

Axial profiles were extracted from the results in Figure 6.5 at times 50, 80, 125, 145, 150, and 158 μs and shown in Figure 6.6. At the beginning of the cycle, t = 50 μs, the neutral density front is recessed deep into the channel near the anode, the electron temperature has a 15 eV peak at 1.5 cm, and the plasma density is $0.5 - 1.0 \times 10^{18}$ m^{-3} in the channel. Neutral replenishment of the discharge channel continues at t = 80 μs with the neutral front propagating downstream with a peak at 0.5 cm[1], the electron temperature peak has moved to 2.0 cm, the plasma density is $\sim 10^{15} - 10^{16}$ m^{-3}, and the peak axial electric field has shifted downstream by 0.2 cm. The final profile of neutral replenishment is t = 125 μs where the neutral density peak is located at 1.5 cm, the electron temperature peak is much broader with a lower 10 eV peak at the channel exit, the electric field peak value is also lower, and plasma density is still below 10^{17} m^{-3}. Avalanche ionization begins at t = 145 μs with the neutral density peak located at 2 cm, the electron temperature peak is outside the channel with a second peak forming at 1.5 cm, and the plasma density is beginning to increase. The avalanche ionization process continues at t = 150 μs with the neutral density rapidly decreasing, the plasma density rapidly increasing, the electron temperature peak at 1.5 cm is now dominant, and the peak electric field has moved back to 2.0 cm. In the final step of the avalanche ionization at t = 158 μs, the neutral density is approximately half of the initial value, the plasma density is nearly 2×10^{18} m^{-3}, the electron temperature peaks at 1.5 cm, and the electric field peak has recessed into the channel at less than 2 cm. After t = 158 μs the breathing mode cycle repeats itself and the next frame is similar to t = 50 μs. The refill time is $\sim$ 100 μs and the depletion time is $\sim$ 10 μs so the total cycle time is $\sim$ 110 μs, which corresponds to a breathing mode frequency of 9 kHz.

In Chapter 4, Figure 4.9 shows the H6 discharge current density in global mode varies from $\sim$ 50 mA/cm^2 at the minimum of a cycle to $\sim$ 300 mA/cm^2 at the peak with the mean value of $\sim$ 150 mA/cm^2 calculated from the mean discharge current. Assuming the plasma density is linearly related to the current density (which was assumed in the HIA), the peak plasma density in a breathing mode cycle is $\sim 6\times$ the minimum plasma density. The simulation results in Figures 6.5 and 6.6 for the SPT-100 show the plasma density in most of the discharge channel varying from 10^{15} to 10^{18} m^{-3}. It is unlikely the plasma density is varying by 3 orders of magnitude during a

[1]The cause for the neutral density peak is unknown, but it is likely an artifact of the simulation and not physical.

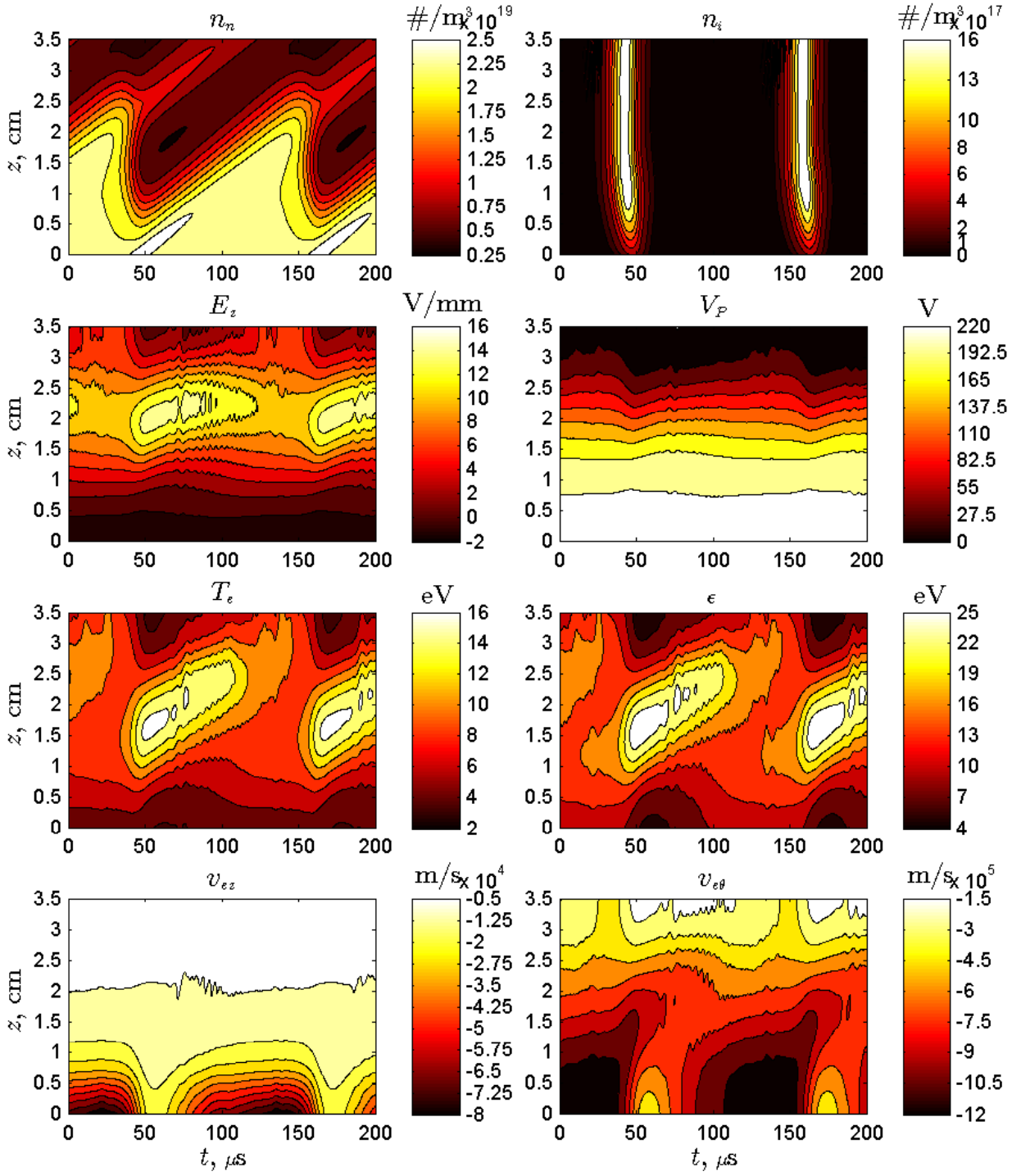

Figure 6.5: Plasma properties for the SPT-100 with V_D = 220 V and B_{max} = 220 G from fluid simulation showing breathing mode oscillations based on the analysis by Barral [33]. Properties shown are neutral density n_n, plasma density (ion and electron) n_i, axial electric field E_z, plasma potential V_P, electron temperature T_e, total electron energy ϵ, axial electron velocity v_{ez}, and azimuthal electron velocity $v_{e\theta}$. All properties except the densities have been smoothed by a 15 point, radial smoothing algorithm with a cosine weighting in order to remove higher frequency oscillations not associated with the breathing mode.

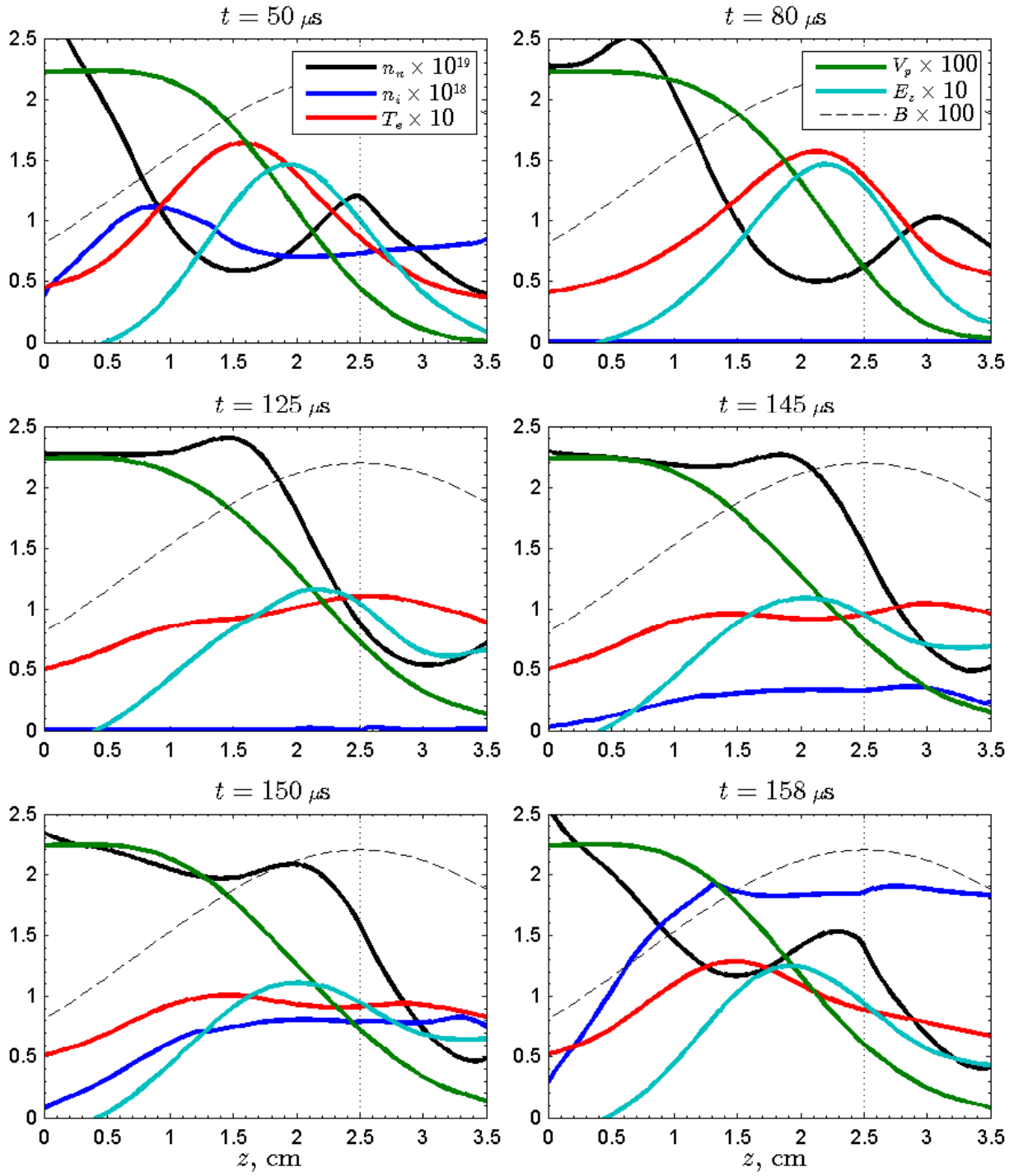

Figure 6.6: Plasma property profiles extracted from Figure 6.5 for selected times showing the evolution of a breathing mode cycle. Units are: m^{-3} for n_n and n_i, V/mm for E_z, V for V_P, eV for T_e and ϵ, m/s for v_{ez} and $v_{e\theta}$, and G for B. The magnetic field is shown for reference, which does not change throughout the cycle. The channel exit is shown as a vertical, dotted black line at $z = 2.5$ cm.

cycle, so this extreme is likely an artifact of the fluid simulation and the many simplifying assumptions made in its implementation. However, the qualitative description it provides of the plasma during a breathing mode cycle is still valuable.

6.5.2 Mode Transition with Fluid Model

A numerical investigation is conducted similar to the experimental mode transition investigation where the magnetic field magnitude is varied with all other parameters constant in order to induce mode transitions. The same computational code and parameters that produced the breathing mode simulations in Figures 6.5 and 6.6 was run with B_{max} in Equation 6.31 varied. This was completed for discharge voltages of 200, 220, 240 and 255 V as shown in Figure 6.7. The simulation time was 5 ms to ensure steady-state equilibrium conditions or oscillations are reached. The discharge current is the mean of the time-resolved I_D trace from 2.5 to 5.0 ms and the discharge current oscillation amplitude is the RMS of the same time-history segment. Transition is defined as the magnetic field magnitude where sustained (non-damped) oscillations are first observed when decreasing the magnetic field magnitude.

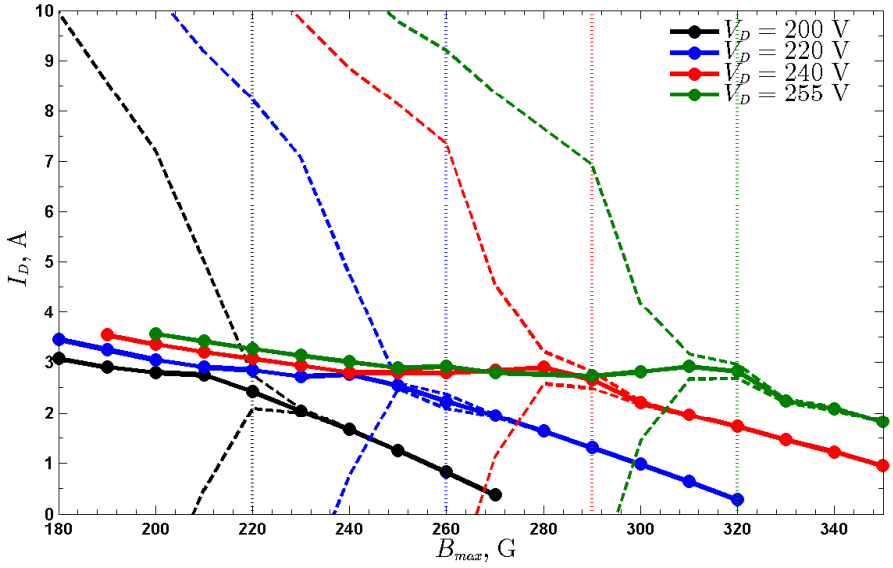

Figure 6.7: Mode transition investigation using numerical fluid model for different discharge voltages V_D = 200, 220, 240 and 255 V. Solid lines are $\bar{I}_D$, dashed lines are $\bar{I}_D \pm \widetilde{I}_D$, and vertical dotted lines are the transition point. The trend of increasing transition point with increasing discharge voltage is observed qualitatively similar to the experimental investigation shown in Figure 4.2.

The B-field sweeps in the numerical investigation in Figure 6.7 followed the same trend as the experimental investigation in Figure 4.2 where the mode transition occurred at higher magnetic

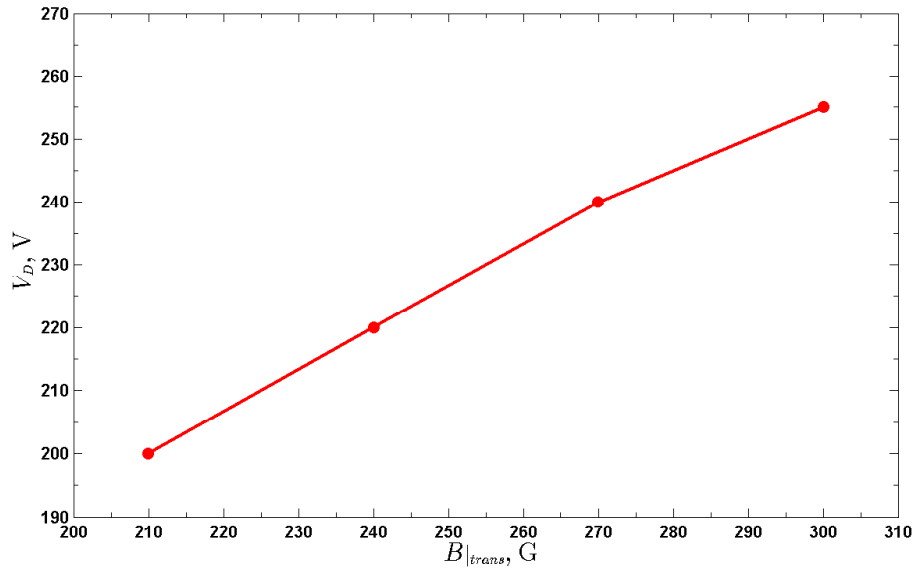

Figure 6.8: Mode transition investigation using numerical fluid model to identify the transition point for different discharge voltages V_D = 200, 220, 240 and 255 V. The trend of increasing transition point with increasing discharge voltage is observed qualitatively similar to the experimental investigation shown in Figure 4.4.

field strengths for higher discharge voltages. In contrast to the experimental observations, no discharge current oscillations are observed for the higher magnetic field settings, which is not surprising given the simple 1-D nature of the model. As the magnetic field is decreased, sustained low-amplitude oscillations are initially observed that eventually transition to full breathing-mode oscillations. Below this transition point, the discharge current oscillation amplitude continues to increase with only a slight increase in mean discharge current. The transition points have been extracted in Figure 6.8 to compare B_{trans} versus V_D, which shows remarkable qualitative similarity to Figure 4.4. These results are only meant to give qualitative insight into mode transitions and are not expected to replicate the empirical results shown in Figure 4.4 for two reasons: (1) the diffusion coefficients were constant throughout this investigation and no attempt was made to fit the coefficients to experimental performance data for the SPT-100 and (2) despite some similarities, the SPT-100 and H6 are different thrusters.

The criterion for breathing mode stabilization developed in Equations 6.28 and 6.30 are analyzed in Figure 6.9 for each discharge voltage setting. The lowest B_{max} shown for each V_D is the transition point where oscillations are first observed. Breathing mode oscillations begin for the 200 and 220-V discharge cases when $\Gamma_i/\Gamma_n > 1$ or $\alpha < 1$ near the discharge channel exit plane. For the 240 and 255-V cases, breathing mode oscillations begin when $\Gamma_i/\Gamma_n > 1$ or $\alpha < 1$ within 1 cm of the exit plane inside the discharge channel. Note that the Γ_i/Γ_n and α are closely related

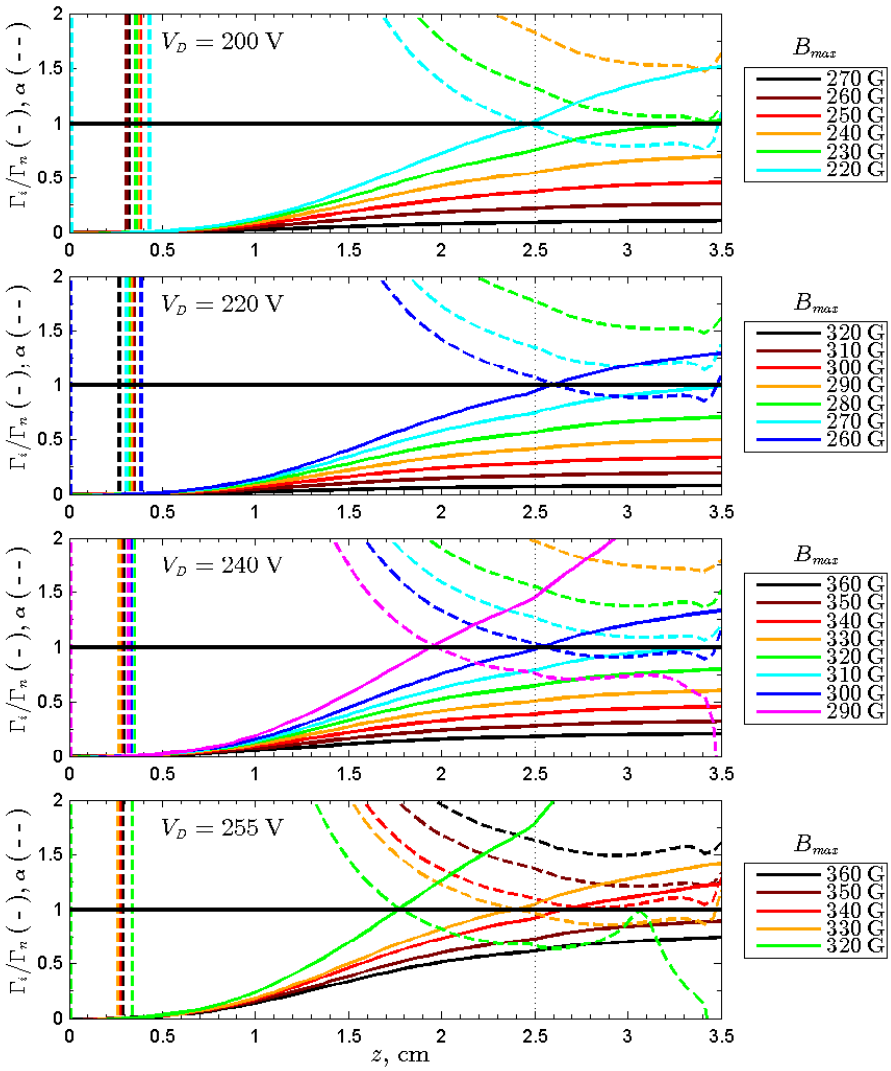

Figure 6.9: Ion to neutral flux comparison and α for stable magnetic field conditions throughout the discharge channel for different discharge voltages V_D = 200, 220, 240 and 255 V. Solid lines are Γ_i/Γ_n, dashed lines are α defined by Equation 6.29, and vertical dotted lines are the channel exit. The lowest B_{max} shown is the transition point where oscillations are first observed. Breathing mode oscillations begin when $\Gamma_i/\Gamma_n > 1$ or $\alpha < 1$ inside the discharge channel for all voltages.

because they are derived from the continuity equation, which is by definition satisfied in the fluid analysis. Numerical artifacts are observed in the simulation results of Figure 6.9 which should be disregarded such as the vertical lines from $z = 0.3 - 0.5$ cm and the perturbed α lines outside the discharge channel. The condition for breathing mode excitation is when neutrals are depleted in the ionization zone of the discharge channel ($1.5 \lesssim z \lesssim 2.5$ cm). This technique can be used to determine the margin of stability against exciting breathing mode oscillations (i.e. global mode) by how far outside of the discharge channel exit $\Gamma_i/\Gamma_n > 1$ or $\alpha < 1$. A trade likely occurs, however, between stabilizing breathing mode oscillations and system performance. When $\Gamma_i/\Gamma_n \ll 1$, not all neutrals are ionized and accelerated in the primary acceleration zone and represents a system inefficiency. A balance must be maintained between increasing system performance with sufficient margin against exciting breathing mode oscillations and transitioning to global mode.

6.5.3 Variation of Axial Plasma Parameters for Stable Conditions

Figure 6.10 shows axial profiles of plasma properties for magnetic field conditions where the breathing mode is stabilized in Figure 6.9 for discharge voltages V_D = 200, 220, 240 and 255 V from fluid simulations. The lowest B_{max} shown is the transition point where oscillations are first observed. The properties shown are neutral density n_n, plasma density n_i, radial magnetic field B, axial electric field E_z, azimuthal electron velocity $v_{e\theta}$, electron temperature T_e, total electron energy ϵ, and ionization rate ν_i. Profiles for axial ion velocity and axial electron velocity are not shown because they do not vary significantly with magnetic field strength, which supports the observation of constant thrust through mode transition.

As the magnetic field decreases, the plasma density increases and the neutral density decreases. The electric field changes in magnitude are less than 10%, but the peak shifts towards the channel exit by $\sim 0.1 L_{ch}$ closer to mode transition. The azimuthal electron velocity magnitude increases (becomes more negative, which is the $E \times B$ direction) in the discharge channel with decreasing B. The electron temperature and the total energy defined by Equation 6.32 increase closer to mode transition with decreasing magnetic field strength. This causes an increase in the ionization rate, ν_i and ionization rate constant [33], k_i, defined by

$$\nu_i = k_i(\epsilon) n_n \tag{6.33}$$

$$k_i(\epsilon) = k_{i0} \left(\frac{\epsilon}{\epsilon_i} \right)^{1/4} \exp\left(-\frac{2\epsilon_i}{\epsilon} \right) \tag{6.34}$$

where $k_{i0} = 1.8 \times 10^{-13}$ m^3/s.

Based on the results of this simple fluid model analysis, the trigger for breathing mode oscillations is changes in the plasma and neutral density profiles. The neutral velocity is considered

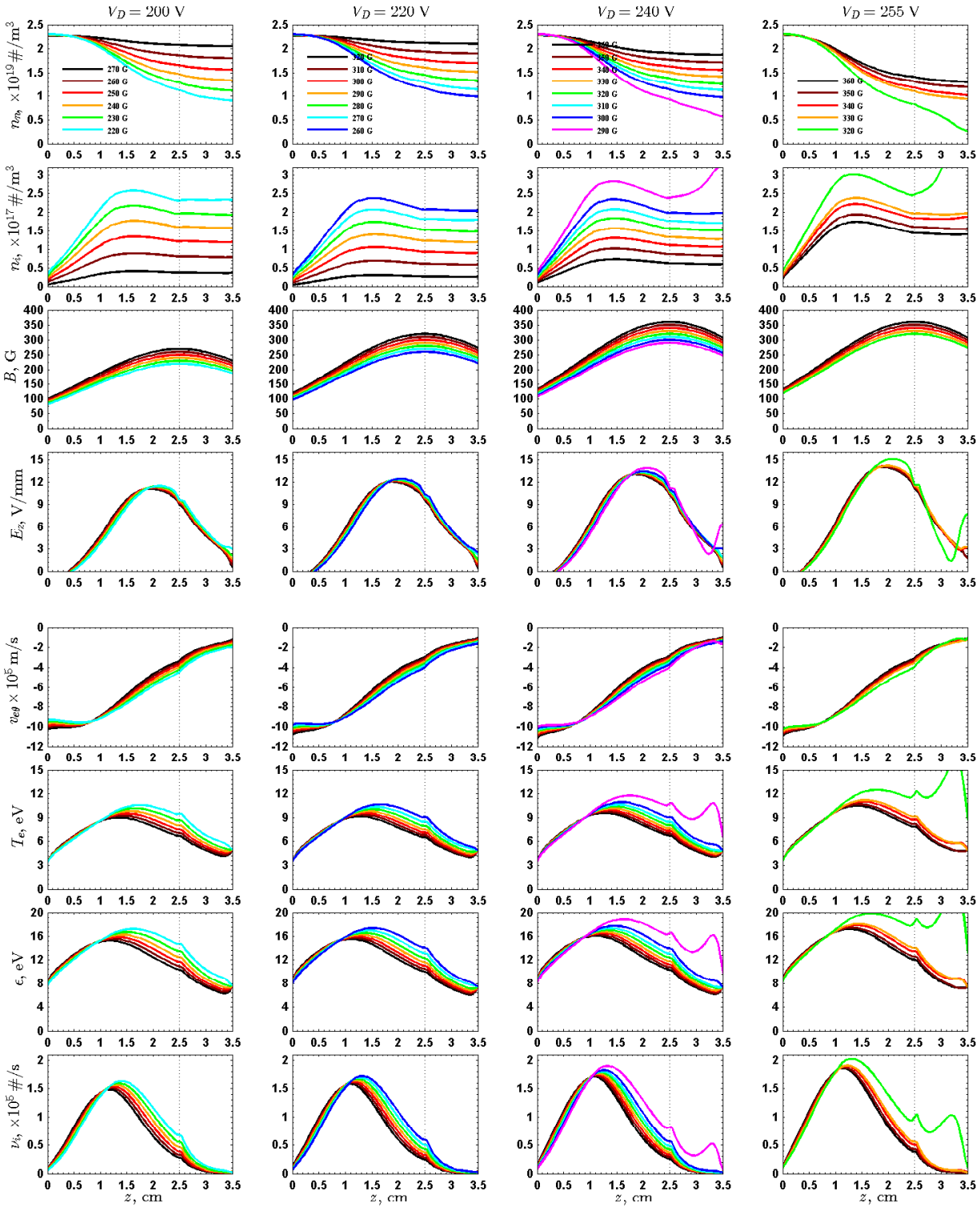

Figure 6.10: Axial profiles of plasma properties for stable magnetic field conditions for different discharge voltages V_D = 200, 220, 240 and 255 V from fluid simulations. The lowest B_{max} shown is the transition point where oscillations are first observed. The properties shown are neutral density n_n, plasma density n_i, radial magnetic field B, axial electric field E_z, azimuthal electron velocity $v_{e\theta}$, electron temperature T_e, total electron energy ϵ, and ionization rate ν_i. The discharge channel exit is marked by a dashed vertical black line.

constant throughout the discharge channel length and the ion velocity profile in the discharge channel does not change significantly with magnetic field variations ($v_i(z) \ncong v_i(B_{max})$). Therefore, the breathing mode is excited when the criterion in Equation 6.30 is violated by the change in $n_n(z)$ and $n_i(z)$ with magnetic field magnitude. A combination of increased cross-field mobility from the decreased magnetic field and increased ionization from the increased electron temperature causes the change in neutral and plasma density along the discharge channel length that leads to the onset of breathing mode.

6.5.4 Breathing Mode Stability Criterion Discussion

The method presented here can be used to check more sophisticated, time-averaged, numerical codes for stability against breathing mode oscillations (i.e. global mode) by analyzing Γ_i/Γ_n or α in the discharge channel. Margins of stability can also be estimated by determining how far outside of the ionization and acceleration zones the stability criterion exist. It must be cautioned that this is not predictive of new thruster designs, but just a check. The simplistic criterion derived in Equations 6.28 through 6.30 and shown in Figure 6.9 indicates that a depletion of neutrals leads to the onset of breathing mode oscillations. The supply of neutrals in this simulation is primarily from the upstream anode, although some neutrals come from recombination at the discharge channel walls. However, in real HETs neutrals can also be provided by the ground facility where more neutrals will diffuse into the channel for higher background pressures. Therefore, the thruster could be *less* susceptible to breathing mode oscillations at *higher* background pressures seen in ground test facilities because there is a neutral supply from the facility that would not occur in flight conditions.

If these observations are correct, they would also have implications for magnetically shielded HETs where much more of the ionization and acceleration zones are outside of the discharge channel walls. The plasma-to-wall interactions are greatly reduced in magnetically shielded thrusters by design, and this is visible as a dark gap between the plasma and the discharge channel walls in photographs. The detachment of the plasma from the wall significantly reduces channel erosion, but also provides a path for neutrals to escape. Additionally, ions that would diffuse to the walls and re-enter the ionization zone as neutrals are lost. In ground testing, however, this is offset by more neutrals diffusing into the ionization region from the ambient background pressure. In flight conditions with significantly lower background pressures, it is expected that the *magnetically shielded thrusters would be more susceptible to mode transitions* and breathing mode oscillations.

6.5.5 Mode Transition with Hybrid Direct-Kinetic Model

Motivated by the results in Chapter 4, a recent investigation by Hara [34] used a hybrid-direct kinetic simulation developed in Ref. 86 to vary magnetic field and induce a mode transition in an SPT-100 type thruster. The model uses a direct kinetic simulation for ions, neutrals and one excited neutral state and treats the electrons as a fluid. Incorporating metastable xenon atoms allows for excitation collisions and stepwise ionization to more accurately determine velocity distributions, ionization rates and plasma density. In addition, light intensity is calculated from spontaneous emission during de-excitation. It has been used to recover the breathing mode for the SPT-100 of approximately 20 kHz. The simulation is 1-D axial on thruster centerline similar to Barral's fluid simulation. [33] Figure 6.11 shows the mean discharge current and oscillation amplitude, which qualitatively compare well with the H6 experimental data in Figures 4.2 and 4.3. The breathing mode is damped in a region of optimal performance similar to the local mode in the H6.

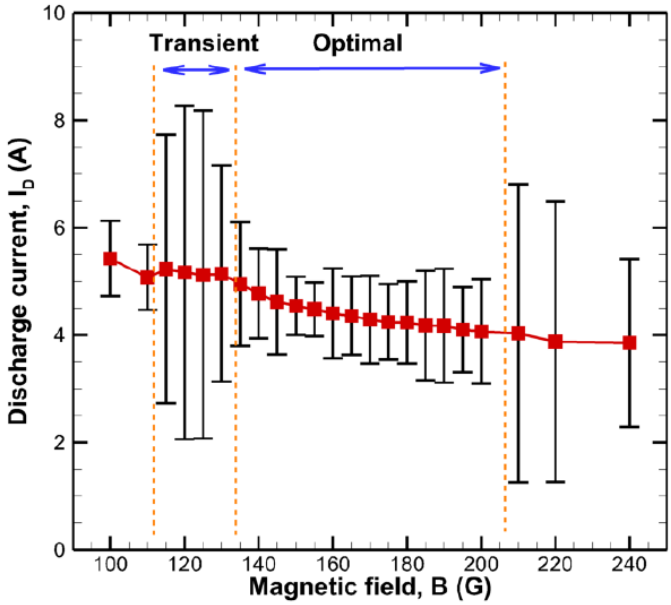

Figure 6.11: Discharge current mean (red squares) and oscillation amplitude or standard deviation (error bars) during a B-field sweep in an SPT-100 with a hybrid-direct kinetic simulation. Mode transitions are identified similar to the experimental results with the H6. The "Transient" regime corresponds with global mode oscillations and the "Optimal" regime with local mode. Reproduced from Figure 5 of Ref. 34.

The time resolved plasma properties are shown in Figure 6.12 where the two modes are labeled breathing mode and quiescent mode,[2] which are the equivalent of global mode and local mode,

[2]Ref. 34 uses the term "stable mode" to describe the condition where the breathing mode has been damped. The term "quiescent" is used here to avoid confusing nomenclature. The term "local mode" cannot be used appropriately because the 1-D simulation cannot resolve azimuthal perturbations such as spokes.

respectively. The neutral density in Figure 6.12(a) and ion density Figure 6.12(b) in breathing mode display the same features as the previous numerical simulations shown in Figure 6.5. The neutral density varies by a factor of ~ 2 and the ion density varies by up to an order of magnitude between cycles. Increasing the magnetic field strength induces a mode transition to quiescent mode, which is the equivalent of local mode in the H6 investigation. The neutral density in Figure 6.12(c) and ion density Figure 6.12(d) for quiescent mode show that the ionization front has been stabilized axially in the discharge channel. Lower amplitude oscillations are still observed in the ion density, but the variation is within a factor of ~ 2 instead of an order of magnitude.

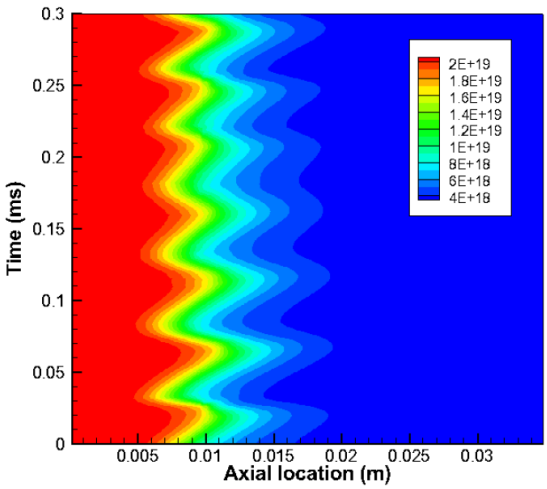

(a) Ground state neutral density in breathing mode. Reproduced from Figure 6(a) of Ref. 34.

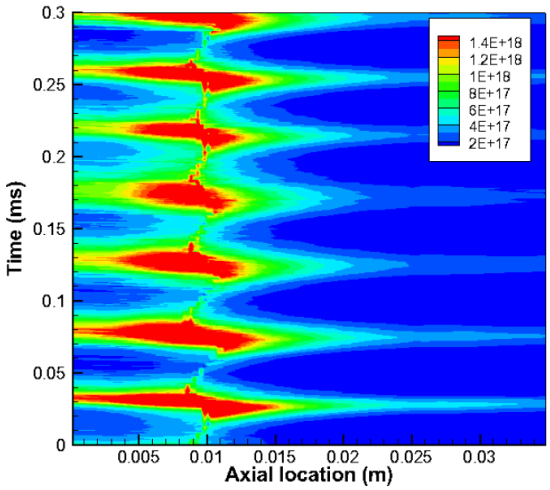

(b) Ion density in breathing mode. Reproduced from Figure 6(c) of Ref. 34.

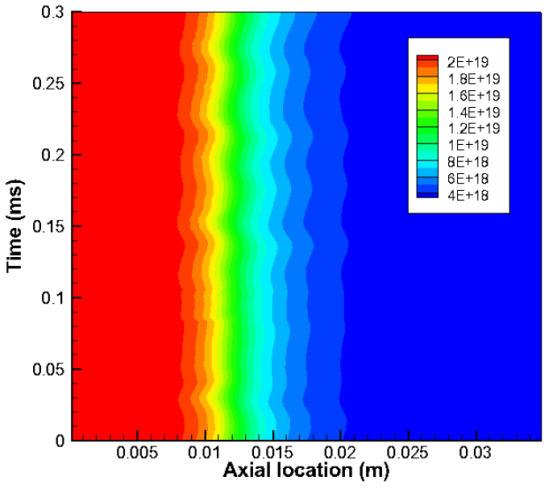

(c) Ground state neutral density in quiescent mode. Reproduced from Figure 7(a) of Ref. 34.

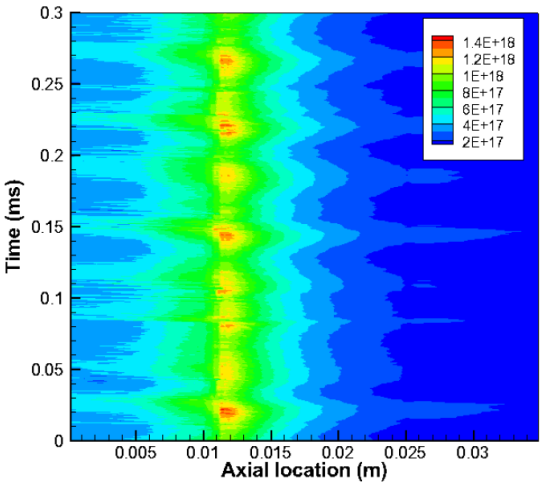

(d) Ion density in quiescent mode. Reproduced from Figure 7(c) of Ref. 34.

Figure 6.12: Time-resolved neutral ground state density and ion density from hybrid-direct kinetic simulations of an SPT-100. Breathing mode is shown in (a) and (b), quiescent mode is shown in (c) and (d). All units are m^{-3}.

The total electron energy is approximately the same between quiescent and breathing mode, but the distribution is different. The directed kinetic energy is larger in breathing mode than quiescent mode, and the thermal energy is larger in stable mode. This could be related to the formation of a space charge limited sheath on the channel wall as suggested by Barral [66], but Hara's code cannot capture this effect. Regardless of the detailed mechanism, the hybrid-direct kinetic simulations of Hara support the idea that mode transitions are evidence of damped breathing mode in quiescent or local oscillation mode.

6.6 Conclusions

Mode transition investigations have showed the oscillations associated with global mode decreased thruster performance, which motivates an investigation to understand their mechanisms so they can be avoided. Global oscillations have been characterized and it is proposed they are the well-studied breathing mode oscillation. This implies that mode transitions from local to global mode represent de-stabilization of the ionization front similar to excitation of the breathing mode.

The global mode oscillation frequency is characterized as a function of operating parameters from empirical results and is compared to the classic breathing mode frequency model developed by Fife [77]. The frequency characterizations are noted to have different functional forms. Combining the frequency models with the transition criterion empirically determined in Chapter 4, a stability criterion for the maximum ionization length is derived. This shows the breathing mode is excited if the ionization region extends too deep into the channel, which agrees in principle with the only other known stability analysis. [142]

Based on results from the fluid model presented here and the hybrid-direct kinetic results presented by Hara [34], it is concluded that the global mode is the breathing mode occurring simultaneously around the discharge channel. The transition to local mode is evidence of breathing mode damping where the ionization front is stabilized, which presumably then allows azimuthal spokes to propagate via other mechanisms discussed in Chapter 5. These ideas cannot be conclusively proven until time-resolved internal measurements of the discharge channel are acquired in global and local oscillation mode. These results provide important characterization for the initiation of oscillations, but a more complete theory for breathing mode stability is needed.

CHAPTER 7

Summary

"*Judge a man by his questions rather than his answers.*"

– Voltaire

7.1 Conclusions

The primary objectives of the research presented here were to study mode transitions in HETs using time-resolved diagnostics in order to develop new system characterization techniques and improve the understanding of the causes for mode transition. The secondary objective was to improve time-resolved diagnostics capabilities and analysis techniques to facilitate the study of plasma oscillations. All of these objectives were accomplished.

New system characterization techniques were utilized, including discharge current, discharge voltage and magnetic field ($I_D - V_D - B$) maps to identify modes of operation within a three variable parameter space ($V_D, \dot{m}, B$). These results are used to calculate a transition surface for use by operators to maintain thruster operation in an optimal mode. This leads to the conclusion that new thruster designs should have magnetic circuits with more capability and not be designed near saturation. These techniques are extendable to comparing ground-test operation with on-orbit operation.

The transition criterion and plasma oscillation characteristics in each mode are investigated and described to provide unambiguous determination of operational mode. Two primary modes of oscillation are identified as global oscillation mode and local oscillation mode. In global mode the entire discharge channel is oscillating in unison and spokes are either absent or negligible with discharge current oscillation amplitude (RMS) greater than 10% of the mean value and can even be as high as 100%. Downstream azimuthally spaced probes show no signal delay between each other and are very well correlated to the discharge current signal. In local oscillation mode perturbations in the discharge current density are observed to propagate in the $E \times B$ direction with

clear spokes shown in a HIA PSD. Spokes are localized oscillations that are typically 10-20% of the mean discharge current density value. The discharge current oscillation amplitude and mean values are significantly lower than global mode. Downstream azimuthally spaced probes show a clear signal delay between each other indicating the passage of spokes, but are not well correlated to the discharge current indicating localized plasma oscillations within the discharge channel. The mode transitions were consistent across different tests and showed no hysteresis, but did change at different operating conditions. The transition between global mode and local mode occurred at higher relative B-field strengths for higher mass flow rate or higher discharge voltage. The thrust was approximately constant through the mode transition, but the thrust-to-power ratio and anode efficiency decreased significantly in global mode. The peaks in thrust-to-power and anode efficiency typically occurs near the transition point. This important result demonstrates that if the magnetic field is optimized for peak anode efficiency or thrust-to-power in local mode, then the thruster will be operated near a transition point where changes or degradation over thruster lifetime could induce a mode transition to global mode.

Plasma oscillations in the channel and plume have been extensively characterized in each mode with time-resolved diagnostics. For the azimuthal spokes observed in local mode, spoke velocities are calculated and an empirical dispersion relation is found. A detailed list of observations are presented that any theory for the mechanism of spoke formation and propagation must explain: 1. Propagate in the $E \times B$ direction, 2. The spoke velocity is 1500-2200 m/s in the H6, 3. The dispersion relation has a functional form where ω monotonically increases with k_θ similar to $\omega^\alpha \approx \mathrm{v}_{ch}^\alpha k_\theta^\alpha - \omega_{ch}^\alpha$, 4. Spoke velocity is weakly, inversely dependent on magnetic field for $B_r/B_r^*|_{trans} < B_r/B_r^* \lesssim 1$, and 5. Spokes are typically not observed in magnetically shielded thrusters. A definitive mechanism for spokes is not determined from existing theories that fit the aforementioned list of observations, but plasma waves, sequential breathing mode and wall effects are considered. The homogeneous plasma waves investigated are $E \times B$ drift, electrostatic ion cyclotron waves, collisional ion acoustic waves with sheaths, and magnetosonic waves. The gradient driven plasma waves investigated consider spatial variations in plasma density, magnetic field and electron temperature. Electrostatic ion cyclotron waves are of the same frequency as spokes throughout the discharge channel and the dispersion relation has a similar functional form to the empirically approximated dispersion relation. Dispersion relations that account for gradients in density, magnetic field and electron temperature are within the expected frequency for spokes near the anode and exit plane. The new methodology developed in this work can be extended to investigate many other possible mechanisms for spoke formation and determine the causal relationship between spokes and optimal thruster performance.

For the breathing mode oscillations in global mode, the frequency is characterized as a function of the operating parameters that differ from previous theories. A postulate is put forward that mode

transitions from local to global mode represent de-stabilization of the ionization front similar to excitation of the breathing mode. This postulate is supported by time-resolved fluid simulations and hybrid direct kinetic simulations of the discharge channel plasma. If validated by future experiments, ionization front stabilization will become a critical performance metric for future thruster designs.

Finally, this investigation improved upon the ground breaking time-resolved techniques the HDLP and HIA. An ISR probe was added to the HDLP for ion density measurements and to monitor plasma oscillations. Simultaneous time-resolved ion and electron density measurements provides valuable insight into plasma oscillations. A new technique was developed to calculate ion density in a flowing plasma from a probe aligned with the flow that agreed with the electron density measurements. New methods were developed to calculate discharge current density from HIA. This non-intrusive technique was critical to characterizing the change in plasma oscillations through mode transition. Finally, new techniques for reliably calculating spoke velocity were developed and rigorously compared, which has provided a new tool for investigations into the physics of HETs.

Mode transitions provide valuable insight to thruster operation and suggest improved methods for thruster performance characterization. Time-resolved diagnostics are critical to measuring the plasma oscillations to identify HET operational mode. Future HETs should include plasma oscillation measurements and mode transition characterization throughout the their developmental and operational life-cycles.

7.2 Future Work

7.2.1 Internal Measurements

The most important follow-on work that is suggested from the results presented here is time-resolved measurements of the plasma in the discharge channel. Measurements are needed to determine how plasma properties fluctuate in the different modes from the anode to the near field plume at least 1 channel width downstream. A comparison with the fluid and hybrid direct kinetic simulations presented here can then be performed to assess whether the global mode is the breathing mode and whether mode transition to local mode represents damping of the breathing mode. It could also answer whether breathing mode oscillations are a deficiency of neutrals through ionization avalanche or depletion of electrons through loss mechanisms. Finally, it could determine where in the discharge channel spokes originate. Such an investigation could compile empirical results for what triggers mode transitions and what properties or parameters become “critical” right before transition. This research could be accomplished with HDLP, time-resolved emissive probes

and/or time-resolved LIF. [143, 144] Use of time-resolved LIF would enable measurement of the change in time-averaged and time-resolved ion velocity distribution between operational modes. Additionally, this will allow time resolved ion velocity distributions to observe changes after passage of a spoke in local mode. All of these difference should also be measured on magnetically shielded thrusters in different operational modes.

7.2.2 Time Resolved Near-Field Plume Measurements

Another useful investigation suggested by this work is time-resolved near field plume measurements in global and local oscillation mode. This could determine how plasma properties fluctuate in the different modes in a planar region of the near field plume from the font pole to 1 channel diameter downstream and from cathode centerline to the outer pole diameter. Such measurements would enable calculation of how electron transport in the near field plume evolves during an oscillation cycle and how that changes between modes. It would also potentially add critical measurements to address the role plasma oscillations play in electron transport. Repeating these tests with external versus internal cathode as well as different background pressures will provide a more complete picture for the fundamentals of electron transport within the plume of an HET. These difference should also be measured on magnetically shielded thrusters in different operational modes.

7.2.3 Parameter Variation

The characterizations presented here vary discharge voltage, V_D, and mass flow rate, $\dot{m}_a$, but one will notice in many of the equations that the mean discharge channel radius, R_{chnl}, and ion mass, m_i, frequently appear as variables. Using the two-channel NHT called the X2 or the newly developed three-channel NHT called the X3, [27] where each channel design cross-section is the same with a different mean radius, would allow R_{chnl} to be varied while holding all other parameters constant. In addition, using krypton or another gas will allow for variation of m_i. Repeating a subset of the experiments presented here will provide a more complete validation of the plasma oscillation characterizations by changing these two variables held constant here.

7.2.4 Segmented Anode

An assumption is made in the HIA techniques in Section 3.5 that local light intensity is linearly related to local discharge current. This assumption is validated with the hybrid direct kinetic simulations, [34] but should also be validated by experimental results. The segmented anode developed by McDonald [78] experienced electrical and thermal difficulties during testing. However, correcting these issues and operating the segmented anode in local and global mode will experimentally

validate the assumption needed to calculate local discharge current density from ultra-fast imaging and thus provide a valuable tool for non-intrusively measuring critical discharge channel properties in an HET.

7.2.5 Dispersion Analysis

The body of literature on dispersion relations for various drift waves is voluminous and many other appropriate relations should be considered using the techniques described in Chapter 5. Future work will investigate the collisional drift instability in cylindrical coordinates as developed by Ellis [145], which was successfully used by Jorns [60] to identify drift waves related to cathode oscillations in magnetically shielded thrusters. Additionally, a drift relation shown by Esipchuk [91] that accounts for density and magnetic field gradients has been used to reproduce azimuthal oscillations in the 10's kHz in the near-field plume of an SPT-100. [73] Kapulkin [101] developed a similar dispersion relation analysis for the near-anode region of an SPT-100, which is also very applicable to the H6 conditions tested here. Frias recently developed two new dispersion relations; one accounts for electron flow compressibility and the other includes temperature oscillations and gradients. [102, 103] The linearized 2-D axial-azimuthal models by Chesta [104] and Escobar [98] that account for ionization and neutral density should be investigated. A dispersion relation developed by Ducrocq [48] to investigate high-frequency azimuthal oscillations has been used by Cavalier [49] to numerically investigate azimuthal waves, uncovering modes that resemble ion acoustic waves. Figures 5.13(f), 5.15 and 5.18 all show large gradients in the $E \times B$ drift velocity throughout the axial and radial extent of the discharge channel. The differences in velocities could result in shear driven instabilities that drive spokes, similar to the shearing instabilities that have been cited as a possible source of anomalous electron transport. [45] Finally, a dispersion relation that takes into account sheaths at the walls was developed by Smoldevy that merits very close inspection. [105] Applying all of these dispersion relations to the plasma parameters described above and comparing to the empirical dispersion analysis of Section 5.6 could yield valuable insight into the origin and nature of azimuthal spokes.

7.2.6 Magnetically Shielded Thruster B-field Verification

Appendix C showed three different oscillatory modes for magnetically shielded thrusters, with the highest magnetic field mode exhibiting azimuthal spokes. However, simulations or measurements of the magnetic field were not performed and it is suspected that the magnetic circuit was saturated at the highest coil currents. If the magnetic circuit was saturated and the B-field streamlines were not shaped properly like Figure 2.11, then the streamlines may have intersected the channel walls. This would increase the plasma-wall interactions like unshielded thrusters and may be evi-

dence that spokes are associated with or caused by plasma conditions at the walls. Although any plasma-wall contact in Appendix C is unintentional, the ability to intentionally increase or decrease plasma-wall interactions during thruster operation may provide researchers the ability to study the role of plasma-wall interactions in HETs by intentionally forcing the plasma to contact the wall (unshielded) or have reduced plasma-wall contact (shielded) by changing the B-field during a test.

APPENDIX A

Ion Density Calculation in Flowing Plasma

A.1 Introduction

The first technique for measuring plasma properties was the electrostatic probe developed by Irving Langmuir circa 1924 [116] and remains one of the most fundamental diagnostics for plasma measurements today. Despite the ubiquitous use of Langmuir proobes, there exists a void of analysis for calculating ion density with the following conditions:

1. Low aspect ratio ($L/D < 10$) cylindrical Langmuir probe
2. Negatively biased in ion saturation
3. Collisionless thin sheath limit
4. Immersed in a flowing plasma where the directed ion velocity is greater than the Bohm velocity, $v_i > v_B$

Yet this is the often the case for Langmuir probes measuring ion density in the plume of an HET. The L/D requirement is driven from the necessity for a large enough diameter probe to survive in an HET plume where erosion will destroy probes and short enough probe length to increase spatial resolution. These probes operate in the collisionless thin sheath limit due to the density of the plasma in an HET plume. Finally, the ions in an HET plume have been accelerated by $\eta_V V_D$ potential so they typically have a velocity of $\sim 2\times10^4$ m/s, which is higher than the typical Bohm velocity of $\sim 2\times10^3$ m/s for 5 eV electrons.

The objective is to calculate ion density, n_i, independent of electron density, n_e, but with knowledge of electron temperature, T_e, and plasma potential, V_p, with respect to probe bias potential, ϕ_p. This section proposes and utilizes a method for approximating sheath size without a priori knowledge of Debye length (noting that $\lambda_D \sim \sqrt{1/n_e}$) and subtracting the estimated ion ram current to extract the ion sheath current in order to calculate ion density using existing collisionless

thin sheath theory. Section A.2 provides a brief background on the significant volume of literature for Langmuir probe measurements. Section A.3 discusses ion density calculations in quiescent plasmas and flowing plasmas. Section A.4 details methods of calculating sheath size in order to subtract the ion ram current. Section A.5 discusses the criteria for a "long probe" when considering the techniques describe here. Section A.6 describes how these techniques are implemented to calculate ion density in Appendix B where good agreement is seen between ion and electron density measurements indicating a quasineutral plasma in an HET plume as expected.

A.2 Background

Probe orientation has been known to affect ion current collection since the Explorer 17 mission [146] where a narrow peak more than twice the normal ion current resulted when the probe was roughly aligned with the velocity vector of the spacecraft. Since that observation, theoretical, computational and experimental studies [146–149] have been conducted to investigate the so called "end effect" of increased ion current when the axis of a cylindrical probe is aligned to within a few degrees of the bulk flow direction in a flowing plasma. This is caused by ions that are not originally on a trajectory to impact the probe entering the sheath and being deflected to the probe surface as shown schematically in Figure A.1.

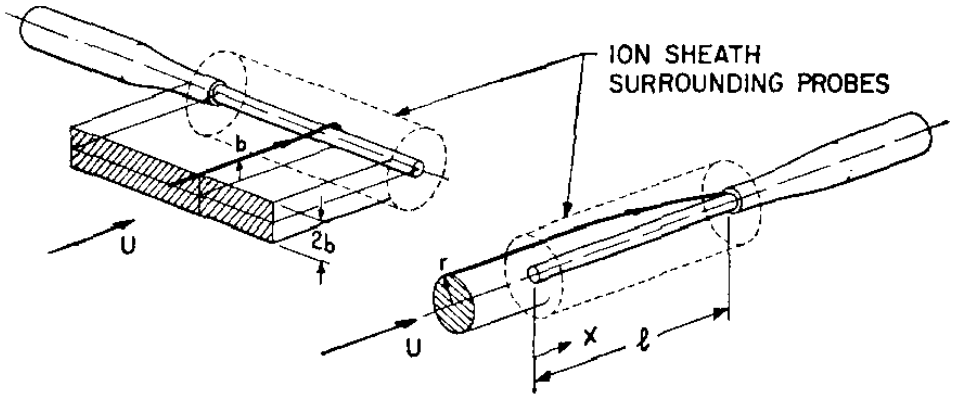

Figure A.1: Ion collection by sheaths of cylindrical Langmuir probes oriented transverse (left) and aligned (right) with the plasma flow. Reproduced from Figure 3 of Ref. 147

The original probe theory by Langmuir and Mott-Smith predicted the relation between ion current collection and probe orientation for an infinitely long probe which does not exhibit the end effect. [148] Consider a cylindrical probe of radius R_p with sheath radius R_s and length L_p with the longitudinal axis aligned with the plasma flow as shown in the right schematic of Figure A.1. The collection area of the probe is $A_p = 2\pi R_s L_p + \pi R_s^2 \approx 2\pi R_s L_p$ for a long probe. The projected area

of the sheath is $A_{proj} = \pi R_s^2$. As $L \to \infty$ then $A_p \gg A_{proj}$, so whether in the thick sheath regime, i.e. Orbit Motion Limited (OML), or thin sheath regime, if the probe is long enough then extra ions collected by sheath expansion on the end will be negligible compared to the ions collected by the majority of the probe surface area.

As the sheath expands and the additional current collected by the sheath and deflected towards the probe can be a significant fraction of the total current collected. The end effect studies have focused on the OML regime where the sheath expansion draws in significant extra current as shown in Figure A.1. References to probes aligned with a flowing plasma for thin sheath have concluded that sheath expansion does not effect the results and traditional quiescent plasma thin sheath Langmuir probe analysis applies. [127] However, these results are for sufficiently long probes as to be considered infinite probes with length to diameter ratios of 80 or higher.

The conflicting constraint of a short probe for improved spatial resolution and larger diameter for survivability in the flowing plasma of an HET plume leads to cylindrical probes with length to diameter of less than 10. The area ratio of side to end is still $\gg 1$, but the shorter length than previous studies means that even a slight sheath expansion will draw in extra current that causes an error in density calculations. Previous authors [5, 146, 148, 150] have suggested that a probe in flowing plasma requires subtraction of the so-called ion "ram" current

$$I_{ram} = A_{proj} q n_i v_i \tag{A.1}$$

where A_{proj} is the projected area of the probe to the flow, n_i is the ion density, v_i is the ion velocity (assuming mono-energetic flowing plasma) and q is the elementary charge (assuming +1 ions).

A.3 Ion Density Calculation

A.3.1 Quiescent Plasma

In traditional collisionless thin sheath theory the ion saturation current to a negatively biased probe in a quiescent plasma is related to the ion density by [116–118, 151]

$$I_i = 0.605 A_p q n_i v_B \tag{A.2}$$

$$v_B = \sqrt{q T_e / m_i} \tag{A.3}$$

where v_B is the Bohm velocity, A_p is the probe area, and the electron temperature T_e is in eV.

Note that Equation A.2 does not account for probe bias, which has been shown to affection ion collection. Laframboise [152] conducted numerical calculations to quantify the effects of probe bias on current collection as the sheath surrounding the probe grows with larger negative biases.

Peterson and Talbot [153] approximated the thin sheath regime $R_p/\lambda_D \geq 5$ results of Laframboise with an algebraic expression which requires knowledge of R_p/λ_D obtained by other means and assumes ion collection only, $T_i \ll T_e$ and +1 ions. Therefore, collected ion current is a function of probe bias, which is not accounted for in Equation A.2. Incorporation of Peterson and Talbot's approximation into the present analysis method is reserved for future work.

A.3.2 Flowing Plasma

Returning to the unexpected ion current spike when a negatively biased probe on Explorer 17 was aligned with the spacecraft velocity vector. Bettinger and Chen [146] explained this as the "end effect" with a finite probe length. They postulated that an infinitely long probe aligned with plasma flow would behave the same as a probe in quiescent plasma, but a finite probe would collect extra current through the sheath end that would artificially increase the saturation ion current. They separated the collected ion current into current from the sheath side where traditional Langmuir probe theory applies and current from the sheath end. This current from the projected area of the sheath end is the so called "ram" current because the ions are flowing faster than the Bohm velocity and are pushed through the sheath.

For very long (large aspect ratio) probes, there will be ram current entering through the sheath end, but that will be negligible compared to the current entering through the side of the sheath. Bettinger and Chen's work [146] focused on OML as have others who have investigated probe alignment in flowing plasma. For Hester and Sonin [147], the probe aspect ratio for their OML analysis was between 76 and 225 and for Bettinger and Chen [146] the aspect ratio was 411. Previous researchers have found that in the thin sheath regime for large aspect ratio probes, traditional thin sheath theory can be applied without correction. [127] However, for aspect ratios less than 10, it will be shown that a correction factor is necessary.

The current collected by an ISR probe can be written as the sum of the traditional Langmuir probe current from Equation A.2 and the ram current of Equation A.1

$$I_{ISR} = I_i + I_{ram} \tag{A.4}$$

The projected area in Equation A.1 can be approximated as $A_{proj} = \pi R_s^2$ with a sheath radius, R_s, for a cylindrical probe aligned with the plasma flow as shown in Figure A.1(right). Using the non-dimensional sheath radius, $\gamma_s = R_s/R_p$, Equation A.4 can be solved for ion density

$$n_i = \frac{I_{ISR}}{0.605 A_p q v_B + \pi\left(\gamma_s R_p\right)^2 q v_i} \tag{A.5}$$

In order to use this technique, the sheath radius, must be calculated using probe bias, plasma potential, and electron temperature. The calculation of γ_s must be independent of the value of n_e to ensure the density calculations are not coupled, i.e. $\gamma_s = \gamma_s(\phi_p, V_p, T_e) \neq \gamma_s(n_e)$.

A.4 Sheath Size Estimate

A.4.1 Approximate Sheath Radius from Space Charge Limited Current in Cylindrical Coordinates

The sheath surrounding a negatively biased probe can be approximated by a cylindrical space charge limited diode with the sheath edge acting as the cathode of radius R_c and the probe surface acting as the anode of radius R_a assuming the probe is of sufficient length that a majority of the current enters from the side. The boundary conditions are zero electric field and potential at the sheath edge and probe bias at the probe surface. Chen [154] derived an approximate analytical solution for the space charge limited current density at the cathode, J_c, between a cylindrical outer cathode and concentric inner anode that does not involve a power series expansion like the well-known Langmuir-Blodgett law [155]

$$J_c = \frac{4\varepsilon_0}{9}\sqrt{\frac{2e}{m_i}}\frac{\phi_p^{3/2}}{R_c^2\beta^2} \approx \frac{4\varepsilon_0}{9}\sqrt{\frac{2e}{m_i}}\frac{\phi_p^{3/2}}{(R_c - R_a)^{1/2}R_c^{3/2}}\left(\frac{1}{\ln(R_c/R_a)}\right)^{3/2} \tag{A.6}$$

The first part of Equation A.6 is the Langmuir-Blodgett law where β is a geometry correction factor that is a function of cathode and anode radii that cannot be explicitly solved for R_c. Used the non-dimensional radius is $\gamma = r/R_p$ so the non-dimensional sheath radius is $\gamma_s = R_s/R_p$. Solving the second part of Equation A.6 using a 4$^{\text{th}}$ order Taylor series expansion about 1 yields a sheath radius of

$$\gamma_s = \left(\frac{8\pi}{9}\frac{\varepsilon_0 L_p}{I_{ion}R_p}\right)^{1/2}\phi_p^{3/4} + 1 \tag{A.7}$$

where L_p is the length of the probe, I_{ion} is the current collected by the probe, and ϕ_p is the probe bias. Equation A.6 has less than 10% error from the Langmuir-Blodgett solution for $\gamma_s < 10$, but the expansion in Equation A.7 limits the validity to $\gamma_s < 2$ for 50% error. Despite the seemingly large error, Equation A.7 is a reasonable analytical approximation to the numerically integrated Poisson's equation that does not have electron density as a variable.

The validity of Equation A.7 can be further checked by comparison with other expressions for sheath thickness that are a function of electron density outside the sheath. Using Equations A.2

and A.7, approximating the probe area, A_p, by the cylindrical sheath area $2\pi R_s L_p$, and using the non-dimensional potential $\chi_p = \phi_p / T_e$, the non-dimensional sheath radius can be written as

$$\gamma_s \approx \frac{\lambda_D}{R_p}\chi_p^{3/4} + 1 \approx \frac{1}{\sqrt{\alpha}}\chi^{3/4} + 1 \tag{A.8}$$

after neglecting a 1.02 constant coefficient. The Debye length is $\lambda_D = (\varepsilon_0 T_e / e n_e)^{1/2}$ in SI units and $\alpha = (R_p/\lambda_D)^2$. This matches well to previous analytical estimates for sheath thickness [156] calculated from equating charge on a body to charge in the sheath

$$\gamma_s = 1.66\frac{\lambda_D}{R_p}\chi_p^{3/4} + 1 \tag{A.9}$$

or calculated from ignoring electron density in the 1-D Cartesian approximation solution to Poisson's equation [120]

$$\gamma_s = 1.02\left(\lambda_D / R_p\right)\left(\sqrt{\chi_p} - 1/\sqrt{2}\right)^{1/2}\left(\sqrt{\chi_p} + \sqrt{2}\right) + 1 \approx \frac{\lambda_D}{R_p}\chi_p^{3/4} + 1 \tag{A.10}$$

A.4.2 Sheath Radius from Numerical Integration

The sheath radius can be solved numerically from Poisson's equation and thin sheath probe theory with several assumptions:

1. Quasi-neutral electron and singly charged ion plasma of density n_0 outside the sheath with steady-state plasma conditions
2. Axi-symmetry and uniform conditions along probe length in cylindrical coordinates so $\partial/\partial\theta = \partial/\partial z = 0$
3. Electrons are much higher temperature than electrons, $T_e \gg T_i$
4. T_e follows a Boltzmann distribution
5. Large negative probe bias so $\left|\phi_p\right| \gg T_e$

Poisson's equation is then

$$\nabla \cdot \vec{E} = -\nabla^2 \phi = \frac{q}{\varepsilon_0}(n_i - n_e) \tag{A.11}$$

where $\vec{E}$ is the electric field represented by the gradient of the scalar potential ϕ and n_i and n_e are the ion and electron density, respectively. The boundary conditions are $\phi(R_s) = 0$, $\phi\left(R_p\right) = \phi_p$, and

$\partial\phi/\partial r|_{R_s} = 0$ where ϕ_p is the probe bias and the plasma potential is set to zero. Using the reduced potential, $\chi = \phi/T_e$, the electron distribution as a function of non-dimensional radius becomes

$$n_e(\gamma) = n_0 \exp[\chi(\gamma)] \tag{A.12}$$

Assume continuity at the sheath edge where all ions entering the side of the sheath reach the probe surface with most of the ion current entering from the side. Also assume conservation of energy with ions entering the sheath at the Bohm velocity in the radial direction. The ion density becomes

$$n_i(\gamma) = n_0 \frac{\gamma_s}{\gamma}[1 - 2\chi(\gamma)]^{-1/2} \tag{A.13}$$

Using Equations A.2, A.12, and A.13, Equation A.11 can be written in cylindrical coordinates as

$$\frac{d^2\chi}{d\gamma^2} + \frac{1}{\gamma}\frac{d\chi}{d\gamma} = \frac{\alpha}{\gamma_s}\left[\exp(\chi) - \frac{\gamma_s}{\gamma}(1-2\chi)^{-1/2}\right] \tag{A.14}$$

$$\alpha = \left(\frac{R_p}{\lambda_D}\right)^2 \cong \frac{I_i R_p}{0.605 T_e \varepsilon_0 2\pi L_p v_B} \tag{A.15}$$

subject to the boundary conditions

$$\begin{aligned} &\chi(1) = \chi_p \\ &\chi(\gamma_s) = 0 \\ &\partial\chi/\partial\gamma|_{\gamma_s} = 0 \end{aligned} \tag{A.16}$$

The second order ODE in Equation A.14 subject to the conditions in Equation A.16 represents a problem of three variables and three unknowns since γ_s is also unknown. Iteratively numerically solving the boundary value problem ODE using a built in MatLab solver until all boundary conditions are met generated a solution set within the limits of $1 \le \alpha \le 3000$ and $-65 \le \chi \le -1$ as shown in Figure A.2(a). For small probe bias, such as $\chi > -5$, the assumption of $|\phi_p| \gg T_e$ has questionable validity and for $\alpha < 4$ the thin sheath assumption of $R_p \gg \lambda_D$ also is questionable. Therefore, the limits were selected based on the range seen during experimentation and limitations of assumptions. Numerically solving Equations A.14 yielded potential profiles $\phi(\gamma)$ for $1 \le \gamma \le \gamma_s$ which were found to fit very well to a power law assumption

$$\phi(\gamma) = -|\phi_p|\left[\frac{\gamma_s - \gamma}{\gamma_s - 1}\right]^{\xi} \tag{A.17}$$

using a least squared curve fit to the numerical results. This is similar to Bettinger and Chen [146] but the assumption that $\xi < 2$ is not imposed with the non-convergent integral dealt with by a limit analysis. Figure A.2(a) shows that over the majority of α and χ values $\gamma_s < 2$ which supports thin

sheath and the use of Equation A.7. Figure A.2(c) shows the difference is less than 25% for $\alpha > 200$ so the space charge limited result of Equation A.7 is a good approximation to the numerically integrated Poisson's equation. The power law fit for potential profiles in Figure A.2(d) shows that ξ only varies from $\sim$ 2.8 – 3.6 over a vast majority of the trade space.

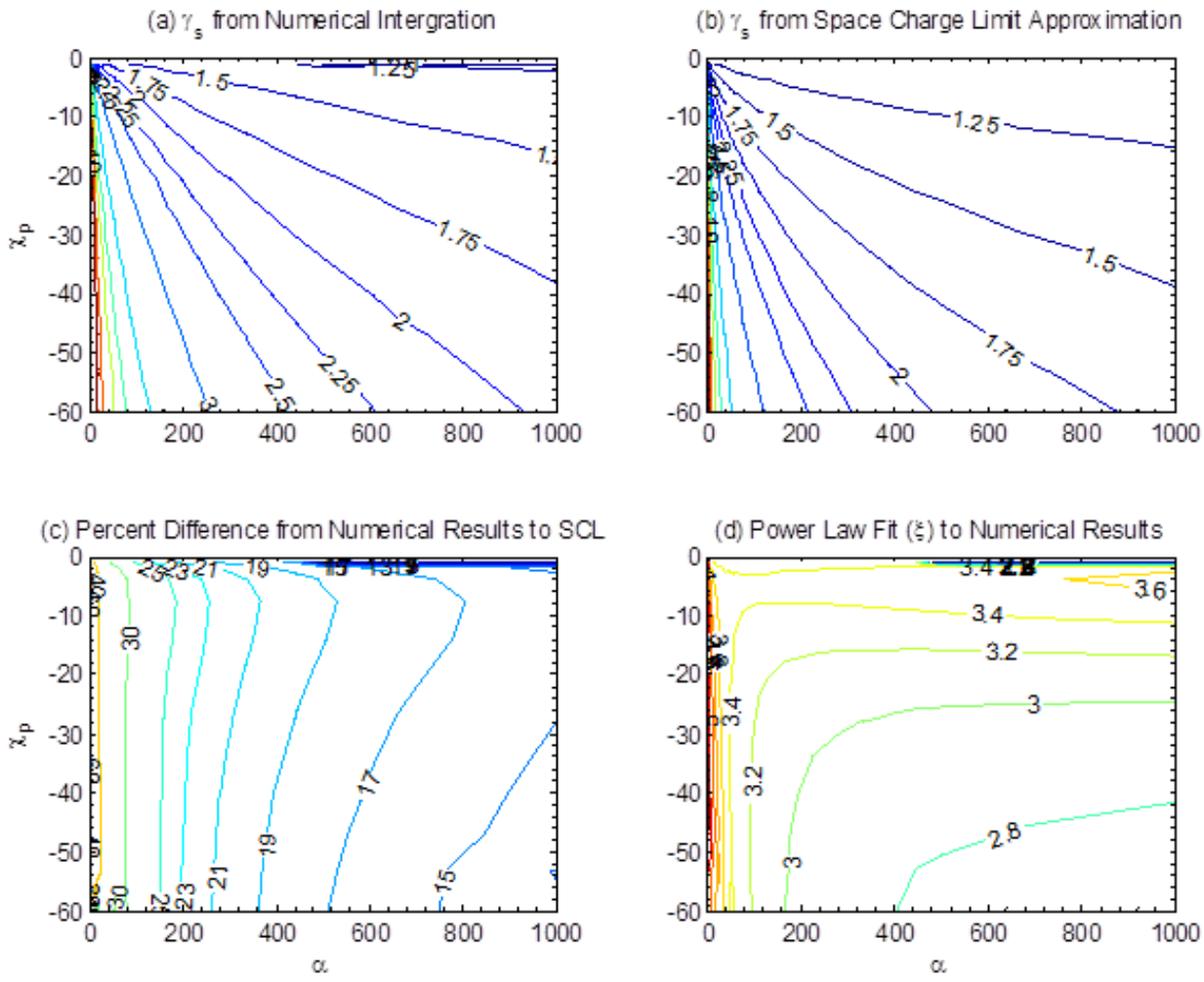

Figure A.2: Contour plots showing non-dimensional sheath edge γ_s for a range of α and χ from (a) numerical integration of Equation A.14, and (b) the space charge limit approximation of Equation A.8. The percent difference between (a) and (b) is shown in (c) and the power law fit from Equation A.17 is shown in (d).

A.5 Long Probe Criteria

Up to this point in the derivation a quiescent plasma has been assumed for simplicity and to avoid an all-out computational Computational Fluid Dynamics (CFD) or PIC assault. However, now

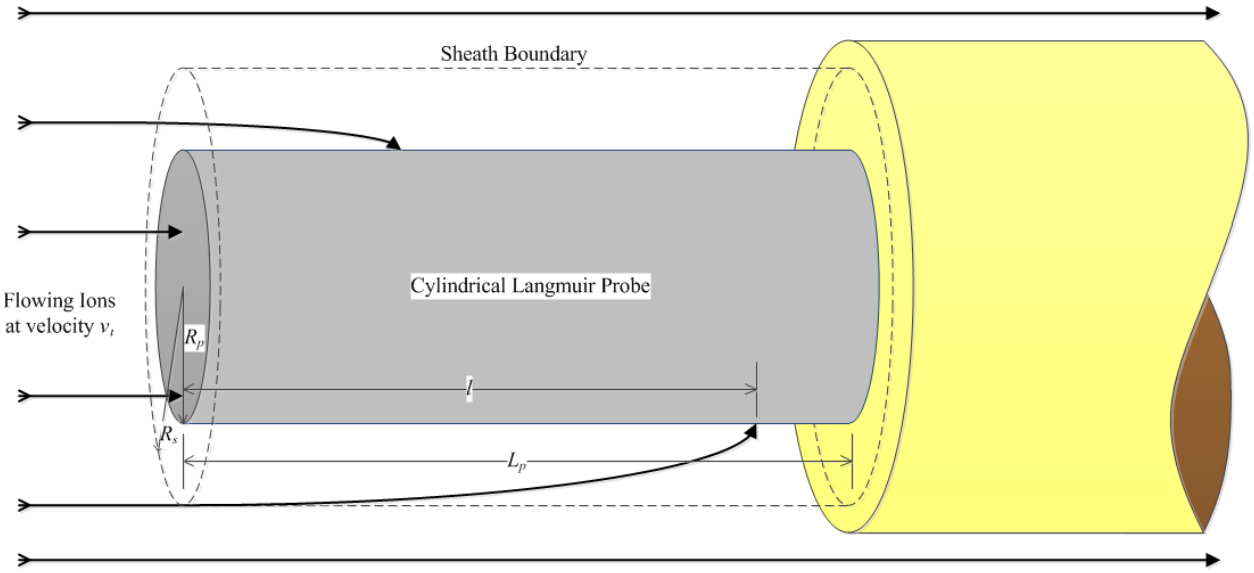

Figure A.3: Cylindrical Langmuir probe with length L_p and radius R_p in thin sheath regime with sheath radius R_s axially aligned with flowing plasma of velocity v_i. Ions entering the sheath are shown to be collected by the probe a distance l from the end.

consider a flowing plasma end on to the probe superimposed onto the previous model of a simple cylindrical sheath as shown in Figure A.3. An ion flowing parallel to the longitudinal axis of the probe enters the sheath near the edge. The velocity vector initially is only in the $\hat{z}$ direction, but it bends towards the probe as it converts potential energy from the electrical field into kinetic energy in the $\hat{r}$ direction. Conservation of energy and the power law assumption for potential profile from Equation A.17 are used to create a differential equation

$$\frac{1}{2}m_i v_r^2 = e\phi(r) \Rightarrow \frac{d\gamma}{dt} = \frac{1}{R_p}\sqrt{\frac{2e}{mi}\left|\phi_p\right|\left[\frac{\gamma_s - \gamma}{\gamma_s - 1}\right]^{\xi}} \tag{A.18}$$

There are no electric fields in the $\hat{z}$ direction so the velocity along the length of the probe will be constant at v_i. Assuming an ion enters the cylindrical sheath at γ_a, which is less than γ_s, then the ion will travel a length l down the probe in time l/v_i before it impacts the probe to be collected. Integrating Equation A.18 for γ from γ_a to 1 and t from 0 to l/v_i yields

$$\gamma_s - 1 - (\gamma_s - \gamma_a)^{\frac{2-\xi}{2}}(\gamma_s - 1)^{\frac{\xi}{2}} = \frac{\xi - 2}{2}\sqrt{\frac{2e}{m_i}\left|\phi_p\right|}\frac{l}{R_p}\frac{1}{v_\infty} \tag{A.19}$$

Taking the limit as $\gamma_a \rightarrow \gamma_s$ and using the space charge limited approximation for γ_s from Equation A.8, equation Equation A.19 can be rewritten as

$$\frac{l}{\lambda_D} = \frac{\sqrt{2}}{\xi - 2}\frac{v_\infty}{v_B}\chi_p^{1/4} \tag{A.20}$$

If the length of the probe L_p is much greater than l, $L_p \gg l$, then most of the probe surface area will be collecting current that entered from the side of the sheath instead of the end and the above assumptions for traditional thin sheath quiescent plasma theory with subtraction of the end-effect ram current is valid. Define the parameter τ as

$$\tau = \frac{L_p}{\lambda_D}\frac{v_B}{v_\infty}\frac{\xi - 2}{\sqrt{2}}\chi_p^{-1/4} \tag{A.21}$$

which is very similar to a previous definition [147] in the OML regime

$$\tau_l = \frac{L_p}{\lambda_D}\frac{v_B}{v_\infty} \tag{A.22}$$

Hester and Sonin stated that $\tau_l > 3$ was a sufficiently long probe where all current entering the sheath end was collected by the probe and for $\tau_l \gg 1$ the current from the end effect was negligible [148]. Here we will consider three separate regimes of probe operation

- $\tau \leq 1$ The end effect current dominates the current from the side sheath and the entire probe area will be collecting ions entering from the end as well as the side so the above assumptions are invalid.
- $\tau \sim R_p/\lambda_D$ The end effect current contributes to the total ion collected current and must be subtracted out, but the simple assumptions made above are valid for most of the probe surface area. For $\tau \cong R_p/\lambda_D$ the end effect current is 50% of the total ion current.
- $\tau \gg R_p/\lambda_D$ The end effect current is a negligible component of the total collected ion current and the use of simple collisionless thin sheath theory applies.

This work focuses on the second regime where $\tau \sim R_p/\lambda_D$ and the end effect current is present but not dominant and therefore must be subtracted out.

A.6 Implementation in Analysis

The analysis presented here has been implemented in the automated Langmuir probe processing scripts using Matlab. The three steps are

1. The plasma potential V_p and electron temperature T_e are determined from HDLP measurements and the probe bias ϕ_p is known. This allows α to be calculated from Equation A.15 and χ_p to be calculated from

$$\chi_p = \frac{\phi_p - V_p}{T_e} \tag{A.23}$$

2. The ODE in Equation A.14 is pre-solved so the sheath radius, γ_s, is determined from a look-up table given α and χ_p.

3. Using γ_s and an assumed value for ion velocity, v_i, the ion density is calculated from Equation A.5. For Figure B.5(b) an ion velocity of 16.7 km/s was assumed based on I_{sp} = 1700 s. However, in the future it will be determined from the time delay calculated by linear cross-correlation from the ISR signal to I_D.

The ion density results shown in Figure B.5(b) calculated using the method described here match very well the electron density results shown in Figure B.5(a). Without correcting for the ion ram current, the ion density would be larger than the electron density by at least 50% or up to an order of magnitude.

APPENDIX B

Plume Maps

B.1 Introduction

Maps of plasma properties in the plume of an HET are valuable to understanding thruster operation. This appendix describes a technique where plasma plume maps are created from a series of axial probe injections at different radial locations. Section B.2 describes the analysis techniques to take multiple axial probe injections and create 2-D contour maps of plasma properties. Each injection of the probe into the plasma plume is analyzed individually to generate time-averaged and time-resolved quantities. The time-averaged quantities are stitched together to create 2-D contour maps of the plasma plume properties. The difference between time-resolved and time-averaged plasma property calculation is discussed and the results are compared with previous investigations in the literature. Section B.3 shows the contour maps of plasma plume properties including electron density, ion density, plasma potential and electron temperature. Section B.4 uses PSD analysis from time-resolved plume measurements to identify dominant oscillations in different regions of the plume.

All of the plume maps and measurements in this Appendix are for the H6 operated with Xe at nominal magnet settings. The anode mass flow rate was 18.81 mg/s and the cathode mass flow rate was 1.32 mg/s (7% CFF), which resulted in a discharge current of 20.1 $\pm$ 0.1 A. The discharge voltage was maintained at 300.0 $\pm$ 0.1 V. The cathode to ground voltage was -11.3 V and the cathode keeper to ground voltage was -6.7 V.

B.2 Plume Map Generation

B.2.1 Single HDLP-ISR Shot

The HDLP-ISR was swept using a 200 kHz sine wave with each cycle completing two I-V sweeps (one up-sweep and one down-sweep). Each HARP injection lasted approximately 420 ms, which

yielded approximately 168,000 I-V sweeps per radial location. Given the sinusoidal velocity profile of the HARP, the "dwell time" at each axial location was not constant. For the time averaged results, all sweeps within 1 mm of travel were averaged together to give one I-V trace to represent that point in the $R-Z$ plane. This represented 100's to 1000's of I-V traces for each 1 mm of axial travel. Each I-V trace was processed using the automated algorithms and manual auditing described in Chapter 3.4 to generate time-averaged plasma properties as a function of axial distance for each radial location measured.

B.2.2 Time-Averaged Plasma Property Contour Maps

The probes were injected 61 times at varying radial locations as shown in Figure B.1 to measure plasma properties in a 2-D plane. Figure B.4 shows examples of the time-averaged axial plasma properties during probe injections at four different radial locations. Combining each individual probe injection yielded 2-dimensional contour maps of time-averaged plasma properties in the $R-Z$ plane shown in Figure B.5. The spatial domain extended from cathode centerline radially out to over 3 channel radii and from the channel exit plane downstream to over 5 channel radii. Smoothing was done for each individual probe injection using a $1/8\,R_{chnl}$ moving average window. All 2-D contour plots have also been smoothed by a two-index radius, cosine weighted, moving average window to reduce noise. Despite the smoothing some noise still remained in Figure B.5 which can be seen as jagged edges of contour lines or small "islands" of increased or decreased plasma properties seen in the contour plots. A quadrant of the H6 is shown to scale at the contour plot top in order to show cathode, inner-pole and discharge channel locations for reference. All locations and lengths are non-dimensionalized by the discharge channel centerline radius, R_{chnl}.

As shown in Figure 3.1, the ISR probe was mounted above the HDLP for the results presented here. Later experiments used two HDLP-ISRs mounted similar to Figure 3.1 for measurements on of the X2, which was significantly better. Because the ISR probe was mounted 25 mm above the HDLP, the radial location of the ISR differed from the HDLP, which varied as function of r as shown in Figure B.2. The difference is most pronounced over the cathode at $r/R_{chnl} = 0$ and decreases at larger radial positions.

Details of the H6 are discussed in Section 3.3 and Figure 3.2 shows the magnetic field stream lines generated from simulations. The 2-D plume maps shown in this section all have the magnetic field streams lines overlaid to identify which plasma properties are tied to the magnetic field lines.

B.2.3 Time Resolved Plasma Properties

Every two traces were averaged together to yield time-resolved plasma properties during each injection. This technique reduced the rate of I-V traces (hence plasma properties) to 200 kHz but

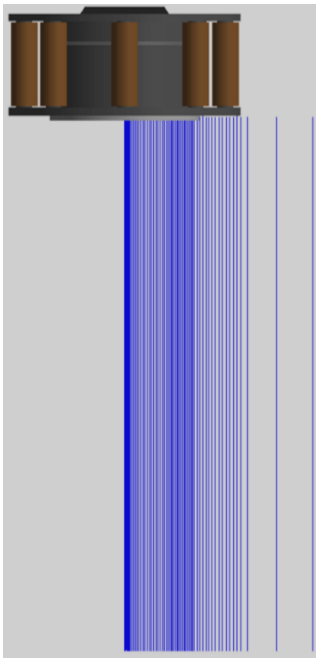

Figure B.1: Top view of H6 (discharge channel not visible) with blue lines representing radial locations of probe injections with the HARP. Note the increased resolution (more injections per radial length) over the cathode on thruster centerline and over the discharge channel.

averaged out slight differences between up-sweeps and down-sweeps. With approximately 168,000 total I-V traces per injection this resulted in 84,000 I-V traces to calculate plasma properties every 5 μs. The same technique used for time-averaged plasma property calculations of automated I-V analysis with manual audits was employed as described in Chapter 3.4.

A common sense check was performed whereby the time-resolved properties (n_e, T_e, V_p) were averaged together for each millimeter of HARP travel and compared to the time-averaged results obtained by averaging the I-V traces together before calculating plasma properties. Figure B.3 shows an example of this comparison for the radial location of 1.25 R_{chnl} and the time selected of 227 ms corresponding to an axial location of 2.13 R_{chnl} during injection. As expected, the results are very similar indicating that the time-resolved plasma properties are indeed oscillating about the calculated time-averaged values. The time-averaged plasma properties for the time segment shown in Figure B.3 was calculated from over 250 individual I-V sweeps averaged together to create one I-V trace. The time resolved points in Figure B.3 are at 200 kHz because every other trace was averaged together.

The comparison of time-averaged to the average of time-resolved did not correlate well within $\sim 3/4\ R_{chnl}$ of the cathode or channel exit where the I-V traces became very distorted due to noise. In those situations, the time-averaged values maintained better integrity since over 500 sweeps were averaged together to calculate the plasma properties which was able to average out the noise

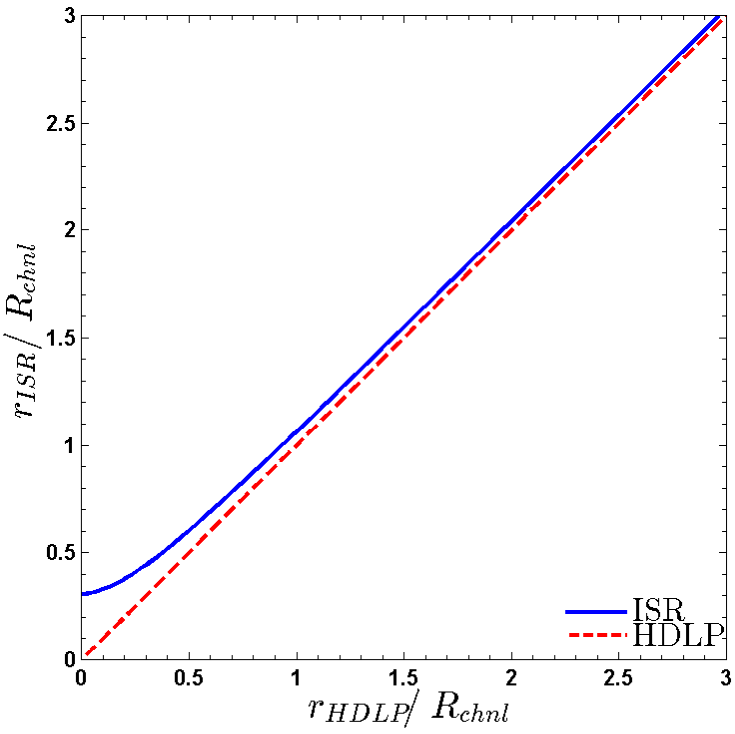

Figure B.2: Radial location of ISR probe with radial location of HDLP. The difference is due to the 25 mm vertical offset of the ISR probe and becomes less significant with increasing radial distance.

to generate a clean I-V trace. Therefore, the time-resolved data near the cathode and channel exit were less reliable.

Simply counting the number of cycles over the 0.3 ms shown in Figure B.3 yields estimated 20-30 kHz plasma property oscillations. This also confirms that measuring plasma properties at 200 kHz is well above the Nyquist criteria for the 10's kHz oscillations present and meaningful time resolved plasma property data is present.

B.2.4 Comparison With Previous Results

The next check is to compare the time-averaged values with previous results for the thruster operating at or near this condition. The experimental thesis of Jameson [114] characterized the sensitivity of H6 efficiency which included plume maps at the 300 V, 20 A operating condition (Section 6.2.1). Time-averaged measurements were made of plasma potential and electron temperature using emissive probes and Langmuir probes. The electron temperature and plasma potential in Figure B.3 can be compared with Figure 6.44 and 6.40 in Ref. 114, respectively. For the same location within the plume, the electron temperature is 4 eV in Figure 6.44 of Ref. 114 and the time-averaged

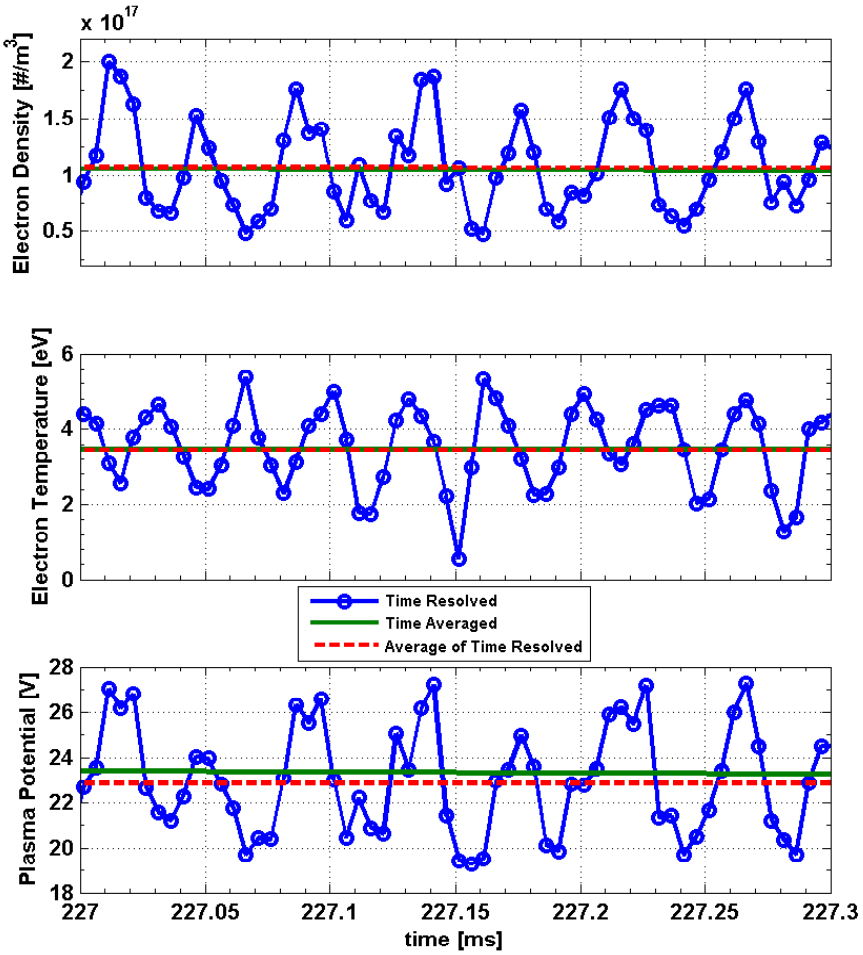

Figure B.3: Comparison of time-resolved and time-averaged plasma electron density, electron temperature and plasma potential (with respect to ground) for $r/R_{chnl} = 1.25$ and time 227.0 to 227.3 ms which corresponds to an axial position of $z/R_{chnl} = 2.13$ during probe injection.

quantity in shows 3.5 eV. Similarly, the plasma potential is 22-23 V in Figure 6.40 of Ref. 114 and the time-averaged quantity in Figure B.3 shows 23 V. However, the time-resolved quantities in Figure B.3 show the electron temperature and plasma potential are oscillating a few eV and several volts, respectively, about those average values.

The electron temperature in Figure B.4(c) on cathode and channel centerline can be compared with Figure 6.45 and 6.46 of Jameson [114], respectively. Figure 6.46 for channel centerline electron temperatures shows a distinct hump in T_e around $z/R_{chnl} = 1$. Figure B.4(c) also shows a temperature increase 1 to 1.5 z/R_{chnl} before settling out to the far field temperature of ~ 2.5 eV. The near field temperature of just over 12 eV at $z/R_{chnl} = 0.1$ is within 1 eV of the value reported by Jameson. Figure 6.45 shows cathode centerline electron temperature with a peak near 8.5 eV inside

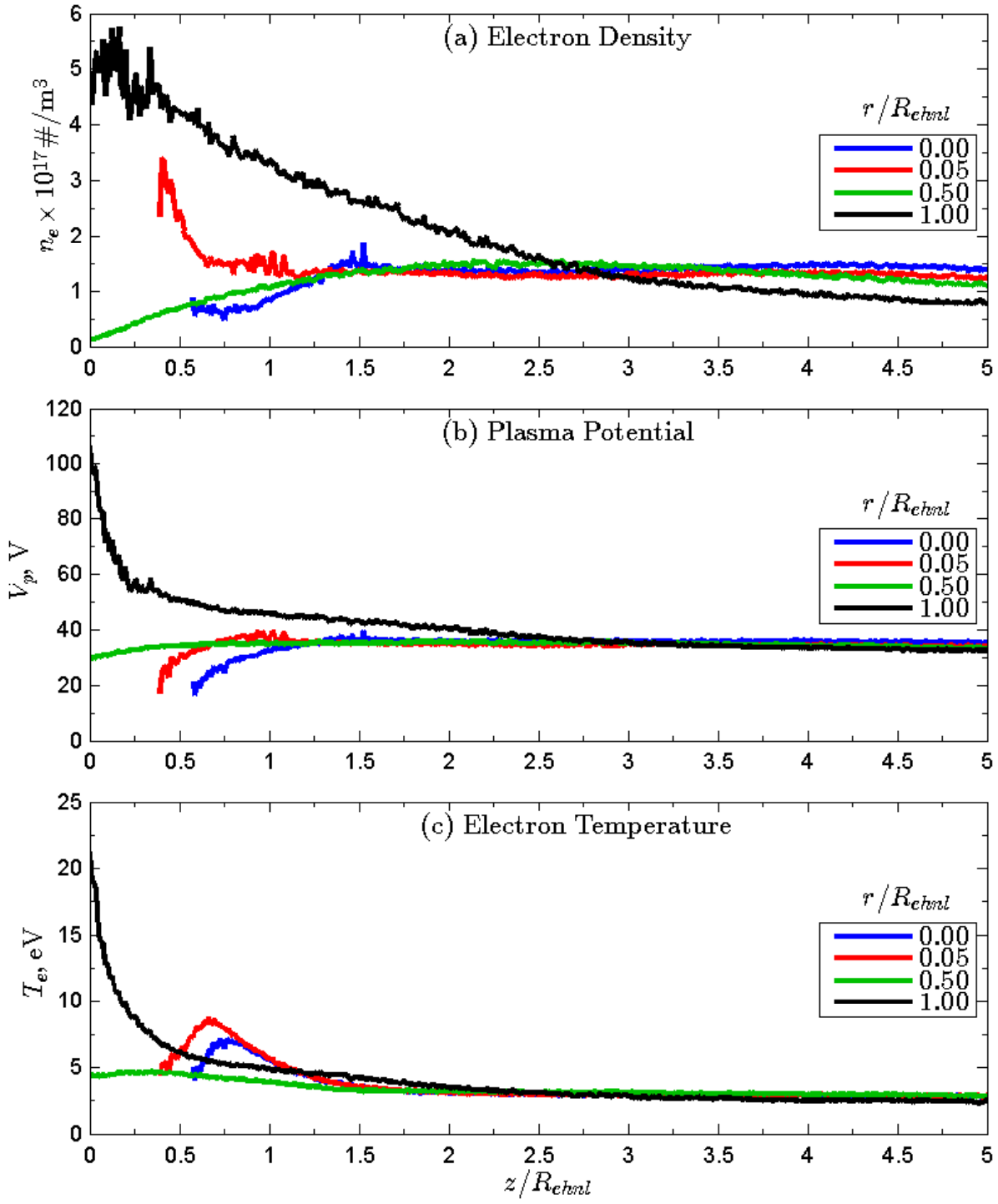

Figure B.4: Axial profiles at four radial locations of (a) electron density, (b) plasma potential (referenced to cathode potential), and (c) electron temperature. Radial locations (r/R_{chnl}) include: 1) on thruster centerline and cathode orifice (0.00), 2) near thruster centerline over cathode keeper (0.05), 3) inner-pole (0.50), and 4) discharge channel centerline (1.00). All plots have been smoothed by a $1/8R_{chnl}$ moving average window.

$z/R_{chnl} = 1$ before decreasing while Figure B.4(c) shows the peak of 7 eV just inside $z/R_{chnl} = 1$. The far field of Figure 6.46 and 6.45 are 4 eV while in Figure B.4 for the same location the electron temperature is 3.2 eV. Therefore, the same trends are observed between Jameson's research and this investigation with slight differences in magnitudes that are within 1 eV.

Figure 8.18 of of Jameson [114] shows the plasma potential with respect to cathode potential for cathode centerline. Comparing with Figure B.4(b), they both show 27 V at $z/R_{chnl} = 0.75$. Jameson Figure 8.18 shows $\sim$ 33 V at $z/R_{chnl} = 1.9$ which is within 10% of the 36 V shown in Figure B.4(b). The plasma potential in Figure B.4(b) on channel centerline can be compared with Figure 6.42 of Jameson [114]. The results from Jameson are with respect to ground and a cathode to ground voltage of -11 V is shown in Figure 7.4 of Jameson for a 7% CFF, which will be used for direct comparison. Jameson shows 48, 38 and 35 V at $z/R_{chnl} = 0.13$, 1.0 and 2.0, respectively. Figure B.4(b) shows 72, 46 and 41 V at $z/R_{chnl} = 0.13$, 1.0 and 2.0, respectively. The values reported here are higher than Jameson, but both have a significant change in slope at $z/R_{chnl} = 0.5$. Reid [44] also measured plasma potential and electron temperature using emissive and Langmuir probes, but at 300 V and 20 mg/s flow which is not exactly the test case here. Assuming the values Reid [44] reported in Figure 7-20 are with respect to ground and the cathode to ground potential is -11 V, then the plasma potential at $z/R_{chnl} = 0.4$ is $\sim$ 50 V. This agrees with Figure B.4(b) that shows 52 V at $z/R_{chnl} = 0.4$. The near field values agree with Reid and the far field values show the same trend but are higher than Jameson. In conclusion, the results presented here agree with previous investigations.

B.3 Plasma Plume Property Maps

Figure B.5 shows the time-averaged, spatial distribution of plasma properties in the plasma plume of the H6 operating at nominal conditions. The result for electron density, ion density, plasma potential referenced to ground and electron temperature are shown in Figure B.5(a)-(d), respectively.

The scales of the plots in Figure B.5 were selected in order to maximize the observable detail in the downstream plume. However, this often saturated the plasma properties within one channel width downstream of the exit plane on discharge channel centerline. The ion density peaks at 7.5×10^{17} m^{-3} on channel centerline, but the upper limit is set to 5.0×10^{17} m^{-3} for direct comparison with electron density. The uncertainty in ion density is significantly higher than electron density due the subtraction of ion ram current described in Appendix A. The plasma potential peaks at 95 V in the near-field plume in front of the discharge channel, but within one channel width downstream of the exit plane decreases to less than 50 V. The electron temperature peaks at 25 eV, but within 0.2 channel widths decreases to 15 eV.

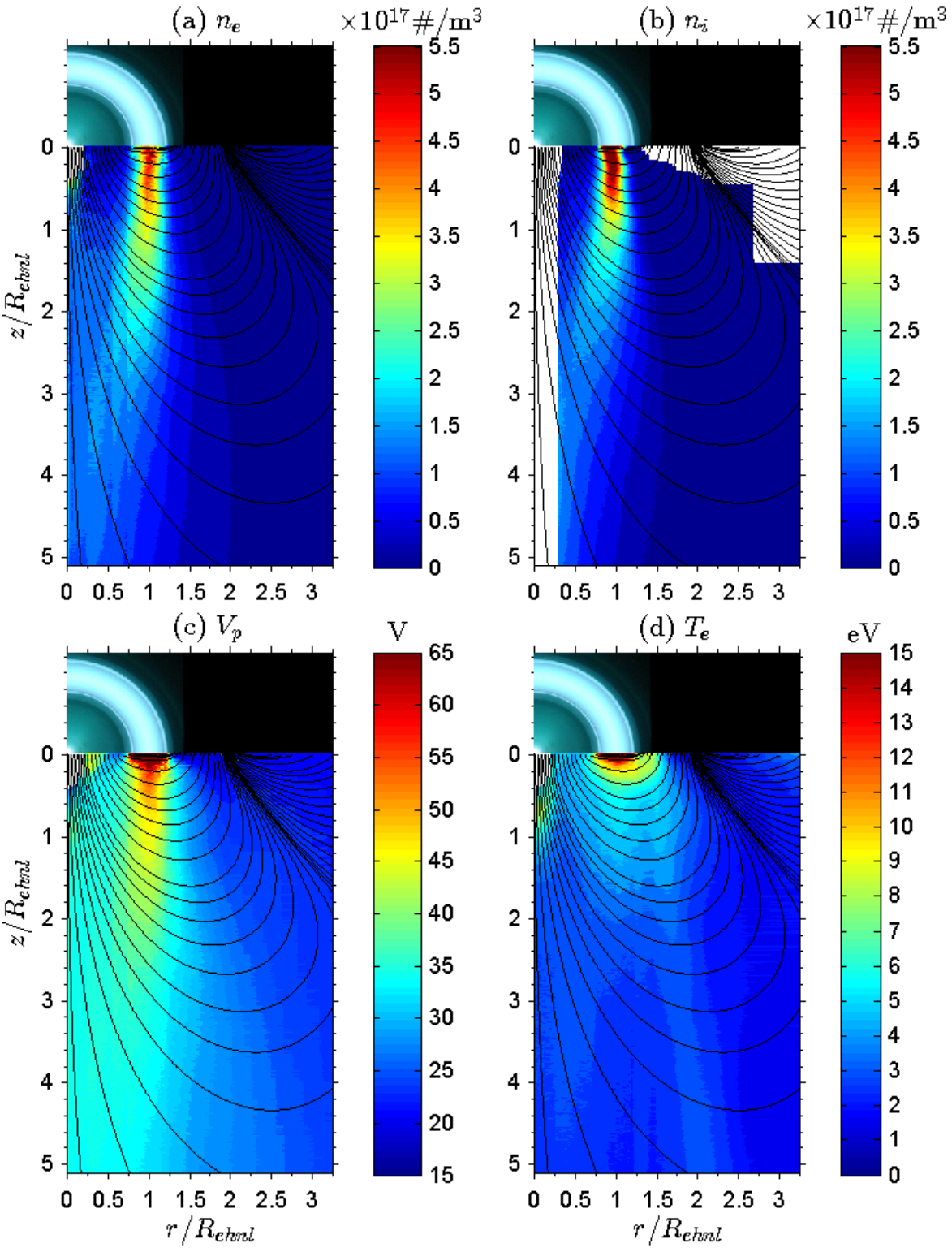

Figure B.5: Plasma plume maps for (a) electron density, (b) ion density, (c) plasma potential (referenced to cathode potential), and (d) electron temperature. Contour intervals for density in (a) and (b) are 2.5×10^{16} m^{-3}, for plasma potential in (c) is 1 V, and for electron temperature in (d) is 0.5 eV. All plots have been smoothed by a two-index radius, cosine weighted, moving average window. Magnetic field direction lines are shown in black.

B.3.1 Electron Density

Figure B.4(a) shows axial profiles of electron density on cathode and thruster centerline (r/R_{chnl} = 0.00), over the cathode keeper near thruster centerline (r/R_{chnl} = 0.05), over the inner-pole (r/R_{chnl} = 0.50), and discharge channel centerline (r/R_{chnl} = 1.00). The axial profiles for all radial locations have been combined into a 2-D contour map of electron density in Figure B.5(a). Results near the cathode that are clearly erroneous from the quality control steps in Section 3.4.6.5 have been removed. Figures B.4 and B.5(a) shows the electron density is peaked over the discharge channel, is very low near the inner pole and is low outside of the channel radius. The general shape of the contours show that as plasma emanates from the entire discharge channel the plasma streams converge towards and merge onto thruster centerline without crossing it.

The density in Figure B.5(a) shows a peaked region above 3×10^{17} m^{-3} on discharge channel centerline (r/R_{chnl} = 1) that extends directly downstream until $z/R_{chnl} \sim 1$. Figure B.4(a) shows that the peak value is over 5×10^{17} m^{-3} and then decays to below 1×10^{17} m^{-3} at z/R_{chnl} = 5. The plume appears to merge onto thruster centerline in the range of $z/R_{chnl} = 2-3$. The plasma on thruster centerline for axial distances $z/R_{chnl} > 3$ would have emanated from all locations of the discharge channel, which will be important in the discussion of oscillations within the plasma plume in Section B.4.

Figure B.5(a) and (b) show a slight wave in the radial direction making the properties appear to "flicker" back and forth slightly like a flame. This is likely due to probe movement side-to-side during injection on the HARP of approximately ±2 mm. As seen in Figure 3.1 the probes have a very long aspect ratio and likely did not shoot into the thruster without latitudinal swaying. During injection, a significant torque was applied to the probe array from the HARP while accelerating them towards the thruster. Close inspection of the time-averaged spatial plasma properties data where the radial shots over the discharge channel were spaced 2 mm apart indicated that the probes did not completely sway more than one radial increment, therefore a conservative estimate of 2 mm is assume for the probe location uncertainty both horizontally and vertically.

The density over the inner-pole (r/R_{chnl} = 0.50) is less than 1×10^{17} m^{-3} for $z/R_{chnl} < 1$ and increases to match the density on thruster centerline for $z/R_{chnl} > 1.25$. The densities for all four locations in Figure B.4 converge at 1.5×10^{17} m^{-3} at z/R_{chnl} = 2.75. One can speculate that the "bridge" for electrons emitted from the cathode to the plasma emanating from the discharge channel begins before this axial distance. So electrons would on average travel at least $\sim z/R_{chnl} = 2$ downstream before entering the discharge channel plume for neutralization and electron supply for the discharge channel.

On thruster and cathode centerline (r/R_{chnl} = 0.00), the electron density is below 1×10^{17} m^{-3} and then increases to $\sim 1.5\times10^{17}$ m^{-3} at z/R_{chnl} = 1.5. Since the cathode is an electron source, the density is expected to peak near thruster and cathode centerline close to the cathode exit at

$z/R_{chnl} = 0$. Therefore, a dip in electron density over the cathode orifice is unexpected and requires further investigation as this may be an erroneous result. This could be due to the magnetic field perturbing the assumption of unmagnetized plasma for traditional, thin sheath Langmuir probe analysis. The cause for this result is systematic since the same trend was observed for all injections that were directly over the cathode orifice where B-field lines directly connected plasma inside the cathode, through the orifice opening and out into the plume with the probe. Over the cathode keeper, which is just off thruster and cathode centerline at $r/R_{chnl} = 0.05$, the density is initially peaked near 3×10^{17} m^{-3} at $z/R_{chnl} \sim 0.5$ and then decreases to match the centerline at $z/R_{chnl} \sim 1.5$. Although only a few millimeters from the injections over the cathode orifice, these profiles to follow the expected results.

In general the density contours in Figures B.5(a) and (b) are not parallel or perpendicular to the magnetic field directions shown. This indicates that the plasma is generally unmagnetized as assumed. However, an exception may be seen in Figure B.5(a) for electron density from $z/R_{chnl} = 1.5 - 2.5$ close to thruster centerline ($r/R_{chnl} < 0.25$) where the electrons appear to emanate from the near-cathode region along B-field lines.

B.3.2 Ion Density

Figure B.5(b) show ion density calculated from the ISR probe mounted above the HDLP, which is why the map does not extend to thruster centerline. Areas where the density is so low that the Debye length is greater than the probe radius have been masked. The techniques described in Appendix A were used to calculate the ion density. Using these techniques, excellent agreement is seen with electron density in Figure B.5(a), which are shown on the same scale for reference. This is not surprising as the plasma is expected to be quasi-neutral.

The ion density contours show a similar "flicker" to the electron density showing the uncertainty in probe radial position due to probe lateral movements. The HDLP-ISR was aligned with the HDLP on discharge channel centerline so the ISR had larger error, estimated to be ±4 mm. This accounts for the observation of the peak ion density not perfectly aligned with discharge channel centerline in Figure B.5(b) as seen with electron density in Figure B.5(a).

Table B.1 quantifies the difference between ion and electron density for various axial locations along discharge channel centerline. In general, the peak of near-field n_i density is higher than n_e, and n_e is larger at all other plume locations. The ion density shows a peak on discharge channel centerline that propagates downstream. The plume seems to merge towards centerline for $z/R_{chnl} > 2$. The ion density outside of the discharge channel radius ($r/R_{chnl} > 1$) is below 0.5×10^{17} m^{-3}.

z/R_{chnl}	r/R_{chnl}	n_e	n_i
0.5	1	4.20	4.89
1	1	3.41	2.96
2	1	2.18	1.53
3	1	1.29	0.95
4	1	1.02	0.67

Table B.1: Comparison between n_e and n_i at axial locations on discharge channel centerline. Units for n_e and n_i are $\times 10^{17}$ m^{-3}.

B.3.3 Plasma Potential

Plasma potentials in shown in Figures B.4 and B.5 are with respect to cathode potential. The plasma potential was first calculated with respect to ground and then shifted to account for the cathode potential 11.3 V below ground. Displaying the plasma potential with respect to cathode potential has more physical meaning since the discharge voltage is applied between cathode and ground.

The plasma potential contours in Figure B.5(c) show the expected increase in plasma potential near the channel exit. The plasma potential is higher for $r/R_{chnl} < 1$ (the plume region within the discharge channel diameter) and decreases significantly outside the channel diameter. Figure B.4(b) has the same shape and similar magnitude as Figure 6.43 of Jameson [114] and Figure 5-12 (top) of Reid. [44].

Figure B.4(b) shows the peak plasma potential on discharge channel centerline is over 100 V and quickly decays to less than 55 V by $z/R_{chnl} \sim 0.25$. The sharp transition in potential profile at $z/R_{chnl} \sim 0.25$ likely indicates the end of the ion acceleration region. For $z/R_{chnl} > 0.25$ the plasma potential gradually decreases to far field value between 30-35 V. The plasma potential for all axial profiles in Figure B.4(b) equilibrate at $\sim 30-35$ V for $z/R_{chnl} > 3$, which supports the postulate of the plasma connection between cathode and discharge channel plasma in this region.

The entire axial profile for the plasma potential on the inner-pole is between 30 and 35 V. Although the data was unreliable for plasma potential for $z/R_{chnl} < 0.25$, Figure B.4(b) shows the two profiles near thruster centerline are decreasing towards cathode potential with decreasing z/R_{chnl}.

B.3.4 Electron Temperature

Figure B.5(d) shows the electron temperature contours with a peak near the channel exit as expected. The axial profile in Figure B.4(c) shows the peak at the discharge channel exit ($z/R_{chnl} = 0$) is 20 eV, which decreases to below 5 eV for $z/R_{chnl} > 1$. Unlike the density and plasma potential,

the electron temperature contours do approximately follow the magnetic field contours downstream from the discharge channel up to $z/R_{chnl} \sim 2$. This follows the assumption of isothermality where electrons are approximately the same temperature along magnetic field lines. Isothermal lines do not hold near the cathode where a downstream temperature peak is seen close to thruster centerline in the map of Figure B.5(d) and the axial profiles of Figure B.4(c). Cold electrons are emitted from the cathode and some collisional process causes a temperature peak downstream at $z/R_{chnl} \sim 0.75$. The electron temperature is ~ 5 eV at $z/R_{chnl} \sim 0.5$ and then peaks to over 7 eV at $z/R_{chnl} \sim 0.75$ before decreasing below 5 eV for $z/R_{chnl} > 1$.

The electron temperatures for all axial profiles in Figure B.4(c) equilibrate at $\sim 2.5 - 3$ eV for $z/R_{chnl} > 2.5$, which also supports the postulate of the plasma connection between cathode and discharge channel plasma in this region. The electron temperature along the inner-pole axial profile does not change by more than 1 eV.

An interesting observation is the stream of higher temperature electrons ($T_e > 3$) emanating from the outer pole (regions on the thruster face outside the channel) extending out at approximately 5° from the thruster axis as seen in Figure B.5(d). The rest of the plasma for the far-field plume is $T_e < 3$ eV. Figures B.9 and B.10 in Section B.4.2 show the plume regions where the spoke oscillations dominate. This stream of relatively hotter electrons corresponds with the plume regions where spoke oscillations dominate. This could indicate that spoke oscillations propagating into the plume from the discharge channel provide a lower resistance path for higher temperature electrons to escape the hotter discharge channel region.

B.4 Spatial Dominance of Oscillations

The purpose of this section is to identify, quantify and discuss how different types of oscillations are dominant within different spatial regions of the plume. This will be accomplished by discretizing the probe injection at each radial location into axial steps to calculate the PSD at each axial increment. Then the PSDs at each axial and radial position can be compared to identify peak frequencies and signal strengths. Figure 4.10 shows distinct peaks in the HDLP-ISR PSD that match the peaks from HIA, which are azimuthal spokes. Of particular interest is identifying where these azimuthal spokes are dominant or absent.

Each HDLP-ISR injection yielded time-resolved data on electron density, ion density, plasma potential and electron temperature. Figure 11 of Ref. 157 shows an example of position versus time for probe injection using the HARP. The position profile very closely resembles half of a cosine wave, where there is longer residence time at the extrema (far field plume and near the truster). The frequency resolution of a DFT depends on the number of points and sample rate for a given signal. To facilitate a direct comparison, all PSDs will be calculated from the same number

of data points. The axial extent of each probe injection will be divided into ten equal number of points and not equal length increments. Therefore, a PSD from the center of a probe injection will be calculated from the same number of points as one close to the thruster, but it will cover more axial distance in the plume.

B.4.1 Plume PSD

Calculating a PSD from Equation 3.40 yields the signal power as a function of frequency. All PSDs have been normalized according to Equation 3.3 where the AC component is isolated by subtracting the mean value and dividing by the RMS value normalizes the amplitude. The result is that all PSDs are scaled the same as shown in Figure B.6.

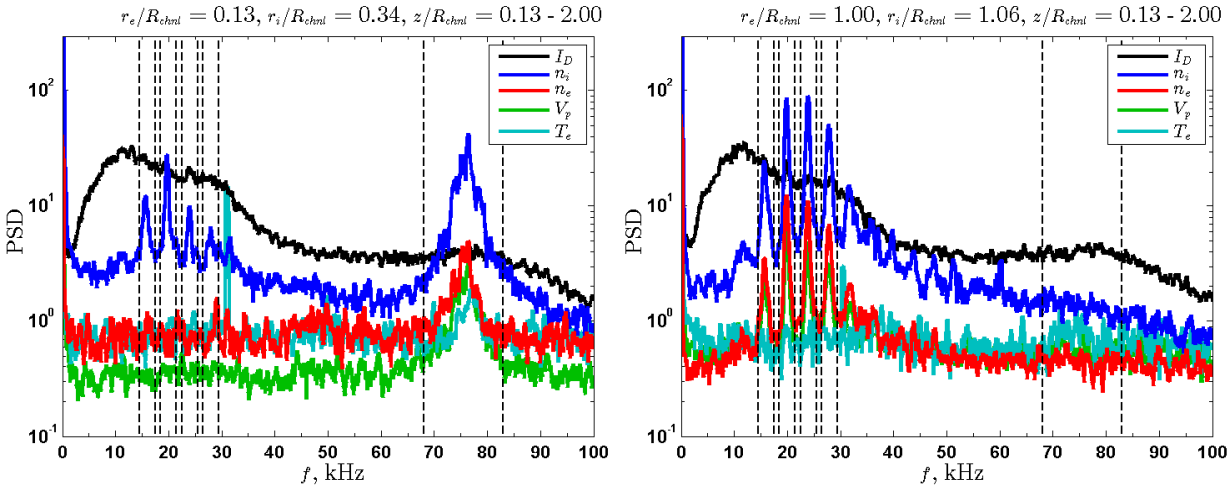

Figure B.6: PSDs for probe injections over the inner-pole near the cathode (left) and on channel centerline (right). The PSDs for discharge current, ion density, electron density, plasma potential, and electron temperature are shown for an axial range of z/R_{chnl} = 0.13 to 2.00. Black dashed vertical lines are the frequency bands used for relative signal power plots. Distinct cathode oscillations are observed near the cathode and inner-pole (left). Azimuthal spoke oscillations are dominant on channel centerline (right).

Example PSDs from probe injections over the inner-pole near the cathode and on channel centerline are shown in Figure B.6 where all points from $0.13 \leq z/R_{chnl} \leq 2.00$ are used. Cathode oscillations as discussed by Jorns [60] are present in Figure B.6(left) between 68 and 83 kHz. The peaks for spoke oscillations are clearly present in Figure B.6(right) for n_i, n_e, V_p and T_e similar to Figure 4.10. The discharge current does not display any of these characteristic oscillations. The spoke orders for $m = 5-8$ can be neatly divided into 3 kHz wide bands as shown in Table B.2 and in Figure B.6. Note that other spoke orders are clearly present in Figure 4.10 such as $m = 3$ and 4, but are not as well defined as $m = 5-8$.

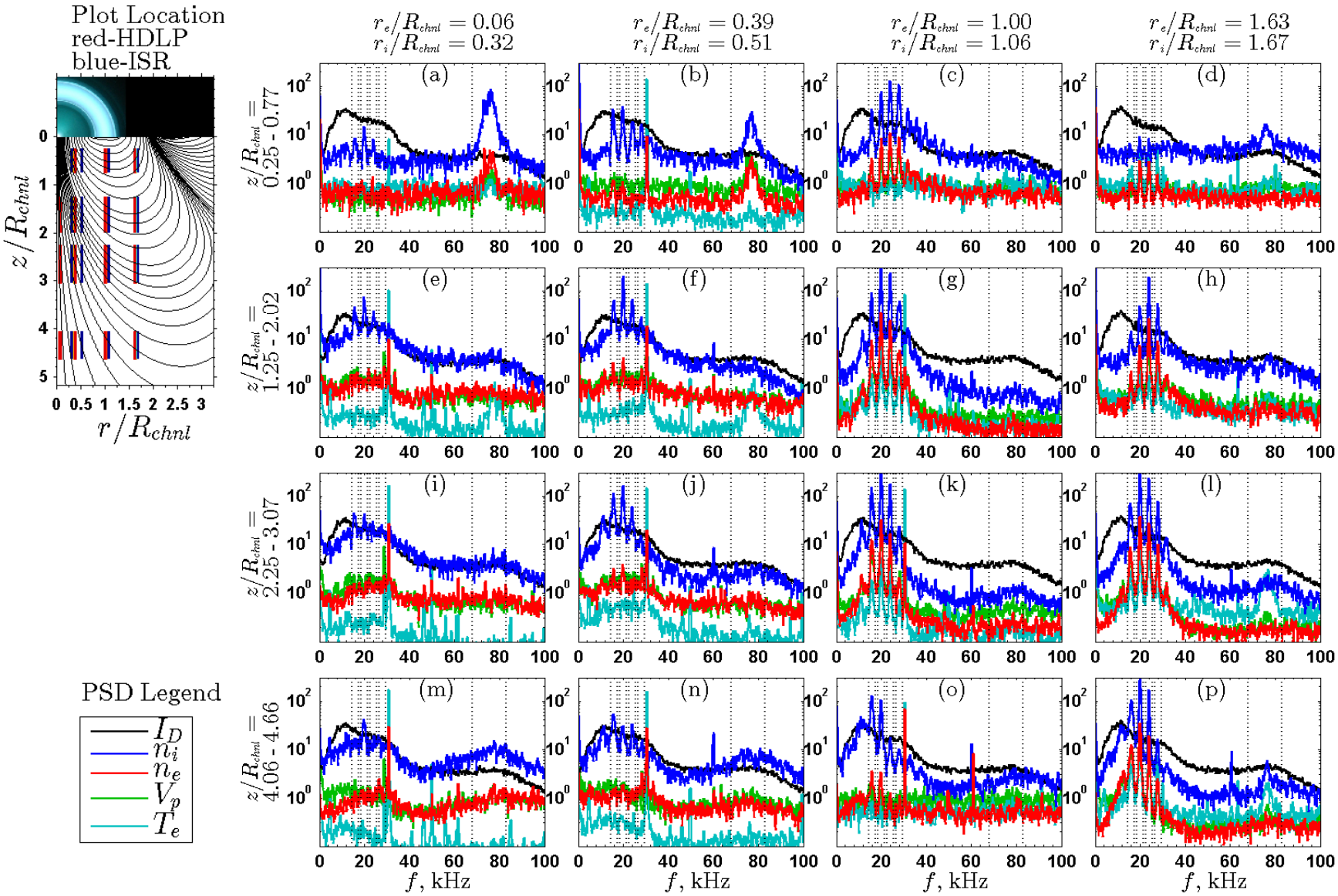

Figure B.7: PSDs of I_D, n_i, n_e, V_p and T_e at various locations in the plume. A plume map shows the location and axial extent for the points included in PSD calculation where red if for HDLP location (n_e, V_p, T_e) and blue is ISR location (n_i). A 500 Hz moving average filter has been used to smooth all traces. Vertical lines are the frequency ranges used for relative signal strength calculations.

Feature	f_1 (kHz)	f_2 (kHz)
$m = 5$	14.5	17.5
$m = 6$	18.5	21.5
$m = 7$	22.5	25.5
$m = 8$	26.5	29.5
Cathode	68.0	83.0

Table B.2: Frequency bands for spoke orders $m = 5-8$ and the cathode oscillation used to calculate relative signal power in the plume from HDLP-ISR measurements.

The thruster was operated at nominal conditions, which is local oscillation mode. The plume can be roughly divided into three regions of primary oscillations as shown in Table B.3. The oscillations in each region exhibit different characteristics which are manifestations of azimuthal spokes and cathode related oscillations. As shown repeatedly throughout this work, the azimuthal spokes are localized oscillations that originate in the discharge channel or in the very near-field plume outside the channel. These are localized density perturbations that: 1) propagate down stream into the plume, 2) cause an increase in local discharge current (electrons crossing B-field lines to reach the anode), and 3) increase optical light emission. The cathode oscillations are dominant close to thruster centerline and are characterized as high-frequency, density gradient-driven drift waves. [60]

Figure B.7 shows PSDs from various locations within the plasma plume that are graphically identified in the figure, where the red lines represent the radial location and axial extent for n_e, V_p and T_e and blue lines represent n_i. As discussed previously, because the probe is moving during injection, the PSD is calculated from data within a certain axial extent. The same number of points are used for each PSD so the plots from the center of the plume cover a large axial range as seen in Figure B.7 because of the probe time-position profile. Due to the vertical offset of the ISR probe, the n_i calculations are always at a larger radial distance than the n_e calculations. Note this causes the largest discrepancy for smallest radial location (left most column of plots in Figure B.7) where $r_e/R_{chnl} = 0.06$ and $r_i/Rchnl = 0.32$ are shown together.

Region 1 in Figure B.7 is near the cathode and is dominated by cathode oscillations from 68 - 83 kHz as described by Jorns [60] and faint spokes are only observed as closer to the discharge channel. Using similar high-speed image analysis techniques to those described in Section 3.5, Jorns investigated oscillations in a magnetically shielded H6. [60] The magnetically shielded H6 at NASA JPL is the same design as the H6 described in Section 3.3 with a centerline mounted cathode, but the magnetic circuit and and discharge channel walls have been modified to employ the magnetic shielding techniques described in Section 2.3.8. [22]. Global oscillations in the entire discharge channel were observed in the frequency range of 7-12 kHz that resemble the global modes

Region	Description	r/R_{chnl}	z/R_{chnl}	Plots in Fig. B.7	Dominant Oscillations
1	Cathode and inner-pole	0 - 0.5	0 - 0.75	(a) (b)	Dominated by cathode oscillations with weak spoke oscillations
2	Discharge channel centerline	0.5 - 1.5	0.5+	(c) (f) (g) (h) (j) (k) (l) (o) (p)	Dominated by azimuthal spoke oscillations
3	Thruster centerline	0 - 0.5	1.0+	(e) (i) (m) (n)	Broad PSD peak similar to discharge current with weak spoke oscillations

Table B.3: Identification and description of plume oscillations. The approximate radial and axial extents are shown for the three different oscillation regions identified. The subplots of Figure B.7 are assigned to the oscillation regions.

oscillations in Chapter 4 for the unshielded H6 and Appendix C for the magnetically shielded NASA-300MS. Additional oscillations were detected over the inner pole between the cathode and the discharge channel in the frequency range of 75-90 kHz that were identified as cathode oscillations. Using linearized two-fluid equations in cylindrical coordinates, the cause for the oscillations was determined to be density gradients near the cathode. They are not related to the azimuthal Hall current as spokes are suspected to be and these cathode related oscillations propagate CW opposite to the $E \times B$ direction. The presence of these oscillations in the discharge current PSD of magnetically shielded thrusters and absence in unshielded thrusters leads to the conclusion that pushing the ionization zone outside of the discharge channel causes a strong coupling between the near cathode plasma and discharge plasma not observed in unshielded thrusters.

Region 2 in Figure B.7 is immediately in front of the discharge channel, downstream from the discharge channel, and outside the discharge channel displays very strong spoke oscillations as evidenced by the PSD peaks that match the HIA peaks from 15 - 30 kHz. This is can be explained from the following argument. Consider a local section of the discharge channel that is generating plasma and as the plasma propagates downstream it also diverges radially. Assuming the ions do not have an azimuthal velocity component, which is the premise for assuming ions are unmagnetized in HETs, the plasma at $r/R_{chnl} > 1$ will be predominantly generated from a local segment of the discharge channel at the same azimuthal location due to the cylindrical geometry of an HET. Therefore, we expect these regions to be dominated by spoke oscillations, which are localized oscillations. We also expect the plasma immediately downstream from the discharge channel to exhibit spoke oscillations since the plasma is focused to propagate directly downstream by design of a high-performing thruster. These characteristics are observed in Region 2.

Region 3 in Figure B.7 is downstream close to thruster centerline is dominated by oscillations from 5 - 20 kHz that match the discharge current oscillations and the closer to thruster centerline, the weaker the azimuthal spoke peaks. This is also expected from the following argument. Consider a point in the plasma plume close to thruster centerline (nearly in front of the cathode for the internal cathode configuration) that is $4R_{chnl}$ downstream. This point would have an equal view factor to every location of the discharge channel and will therefore be populated by plasma that originates from everywhere around the discharge channel effectively "summing" the localized oscillations. Since azimuthal spokes are localized oscillations, when they are "summed" around the discharge channel, they will constructively and destructively interfere to wash out any individual spokes. Plume convergence is supported by the ion current density measurements from Figure 5-8 of Reid [44] that show that the plume from the discharge channels converge before $\sim 4R_{chnl}$ downstream on thruster centerline. The downstream probes in front of the discharge channel are strongly correlated to spoke oscillations, but they are also weakly correlated to the discharge current with ρ typically less than 0.3. This indicates the discharge current is either a weak global oscillation or is the "summation" of the localized discharge current oscillations due to the spokes. Regardless, we expect the plasma oscillations downstream near thruster centerline would be similar to the discharge current oscillations since the discharge current is a global measurement of the entire discharge channel, which is observed in Region 3.

B.4.2 Signal Strength in the Plume

The different regions can be visualized by examining the relative signal strength of n_i, n_e, and V_p. The probe injections at each radial location are divided into 10 equi-point (but not equi-distance) axial regions. The relative signal power for a particular frequency band from Table B.2 is calculated according to Equation B.1 at each axial step and each radial location. The resulting plume maps in Figures B.9-B.8 show the spatial domain where various frequencies listed in Table B.2 dominate.

The total signal power in a frequency band can be calculated by integrating the PSD over the frequency band. The relative signal power, S, is the signal power of a given frequency band from f_1 to f_2 divided by the signal power over the entire frequency range of consideration (0-100 kHz here) according to

$$S_{f_1-f_2} = 10 \log_{10}\left[\frac{\int_{f_1}^{f_2} PSD\, df}{\int_0^{100} PSD\, df}\right] \tag{B.1}$$

where S is in decibel, dB. Reviewing dB notation, 100% of the signal power is 0 dB, 50% of the signal power is -3 dB, and 25% of the signal power is -6 dB. The HDLP sample rate was 200 kHz so only signals below the Nyquist frequency of 100 kHz will be considered, which are shown as the integral limits in the denominator of Equation B.1. If the PSD is constant, $PSD \neq PSD\,(f)$, then

a 3 kHz band of the PSD would be 3% of the signal power from 0-100 kHz and in Equation B.1 $S = -15$ dB. A 15 kHz band of the same "flat" PSD would be 15% of the signal power from 0-100 kHz and in Equation B.1 $S = -8$ dB.

Figures B.8-B.9 shows oscillations in ion density, electron density and plasma potential. As shown in Section 4.5.4 for a stationary HDLP-ISR, oscillations in n_e and V_p are well correlated. The correlation coefficient was calculated between n_e and V_p for the entire plume with $\rho > 0.5$ for all areas except near the cathode. For the domains associated with Region 1 in Table B.3, the correlation coefficient decreased to $\rho \sim 0.2$. This could indicate that density and potential oscillations are out of phase near the cathode.

Figures B.8 shows how cathode oscillations dominate in Region 1 and Figure B.7(a) and (b) shows the clear peak in 68-83 kHz. This region extends to from the cathode keeper $r/R_{chnl} \sim 0.05$ out to $r/R_{chnl} \sim 0.75$. Interestingly, it does not appear directly on cathode centerline. The cathode oscillation is dominant from the inner-pole downstream to $z/R_{chnl} \sim 1$. Figure B.7(d) also shows a slight peak in this band for areas far outside of the discharge channel radius where large radial density gradients will occur. This can also be seen in Figures B.8 for n_i at $r/R_{chnl} \sim 2.5$ and $z/R_{chnl} \sim 1.75$. This could be related to the cathode oscillations where the electrons are bouncing along B-field lines from inner to outer pole.

Figures B.9 and B.10 shows Region 2 where the $m = 5-8$ spoke order oscillations dominate. They are clearly seen to dominate in an area downstream from discharge channel centerline extending inward to $r/R_{chnl} \sim 0.5$ and outward to $r/R_{chnl} \sim 2.5$ For the ellipsoidal area (angled out from thruster centerline) with major axis extending from $1.5 \lesssim z/R_{chnl} \lesssim 4.0$ and minor axis from $1.0 \lesssim r/R_{chnl} \lesssim 2.0$, over 70% of the signal power is in the 4 azimuthal spoke oscillation bands that comprise only 12% of the bandwidth from 0-100 kHz. Figures B.9 and B.10 for n_e and V_p show that spoke oscillations are not dominant on thruster/cathode centerline for $r/R_{chnl} < 0.5$. In fact, Figure B.7(a),(e),(i) and (m) show that spokes are scarcely detectable on thruster centerline over the cathode. The plasma in this region is populated by the cathode and cathode oscillations for $z/R_{chnl} < 2$ and by plasma produced equally around the discharge channel for $z/R_{chnl} > 2$.

Region 3 is shown by an absence of any one dominant oscillation in the triangular region from $0 < r/R_{chnl} < 1$ and $3 < z/R_{chnl} < 5$ in Figures B.9-B.8. The discharge current PSDs in Figure B.7(a)-(p) has a peak between 11 and 12 kHz, but the spectrum is broad with significant signal strength from 4-40 kHz. The plasma density PSDs follow this shape with spokes or cathode oscillations either absent or negligible.

Plots of relative signal strength are very helpful in identifying regions where a particular oscillation is dominant; however, caution is warranted in concluding that an oscillation is not present if the relative signal strength is low. For example, one should not view Figures B.9 and B.10 as evidence that spokes originate near $z/R_{chnl} \sim 3$ and $r/R_{chnl} \sim 1.2$ and propagate upstream into

the channel. Figures B.9 and B.10 show that the relative signal strength for spoke oscillations on discharge channel centerline $r/R_{chnl} = 1$ near the exit plane $z/R_{chnl} < 1$ appears low. However, Figure B.7(c) shows the absolute strength of spoke oscillations are just as strong as further down stream, but the strength of oscillations in the entire 0-100 kHz band is higher by the discharge channel exit than farther downstream so the relative strength of spokes is weaker. Therefore, plots like Figures B.9-B.8 should always be used in conjunction with Figure B.7.

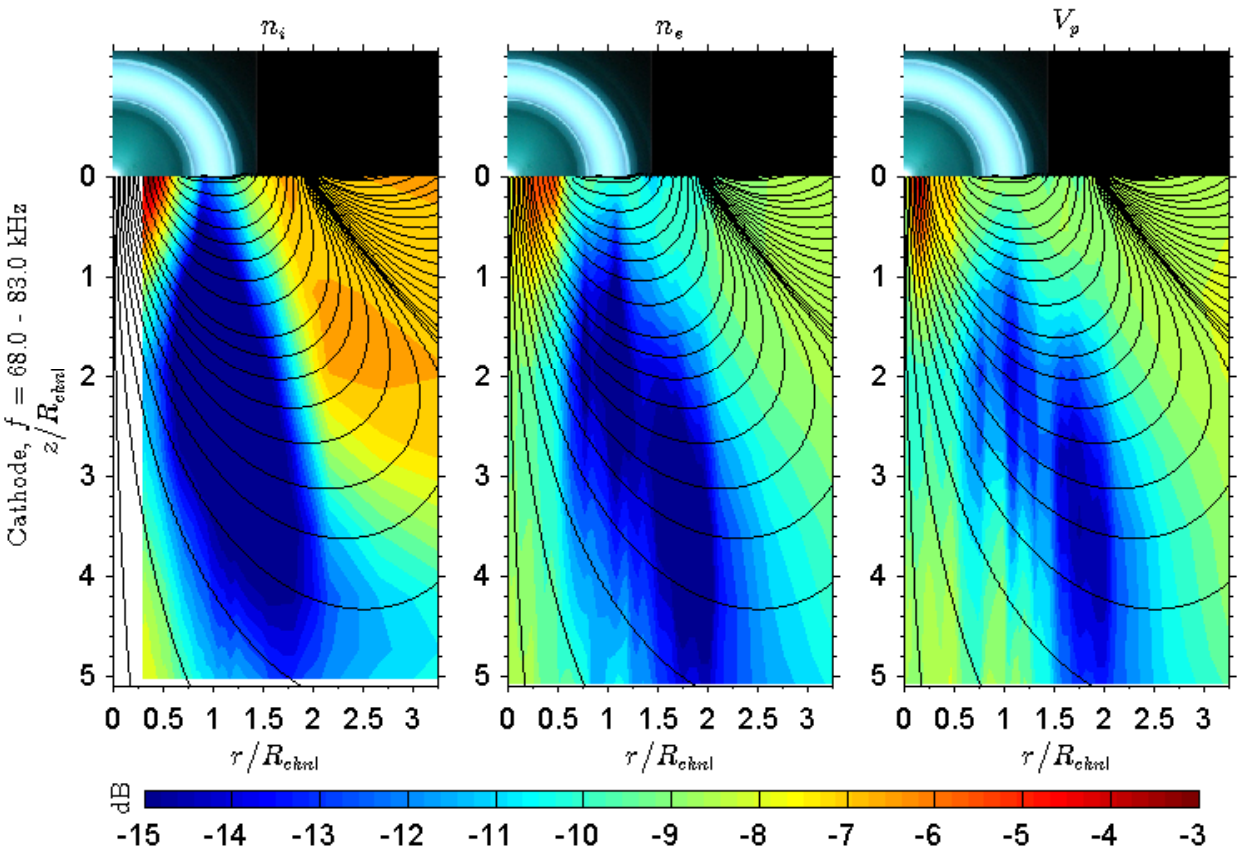

Figure B.8: Relative signal strength for oscillations in n_i, n_e, and V_p throughout the plume that correspond to cathode oscillations in the frequency band shown in Table B.2. Magnetic field directions are shown overlaid. Maps have been smoothed by a two-index radius, cosine weighted, moving average window to reduce noise.

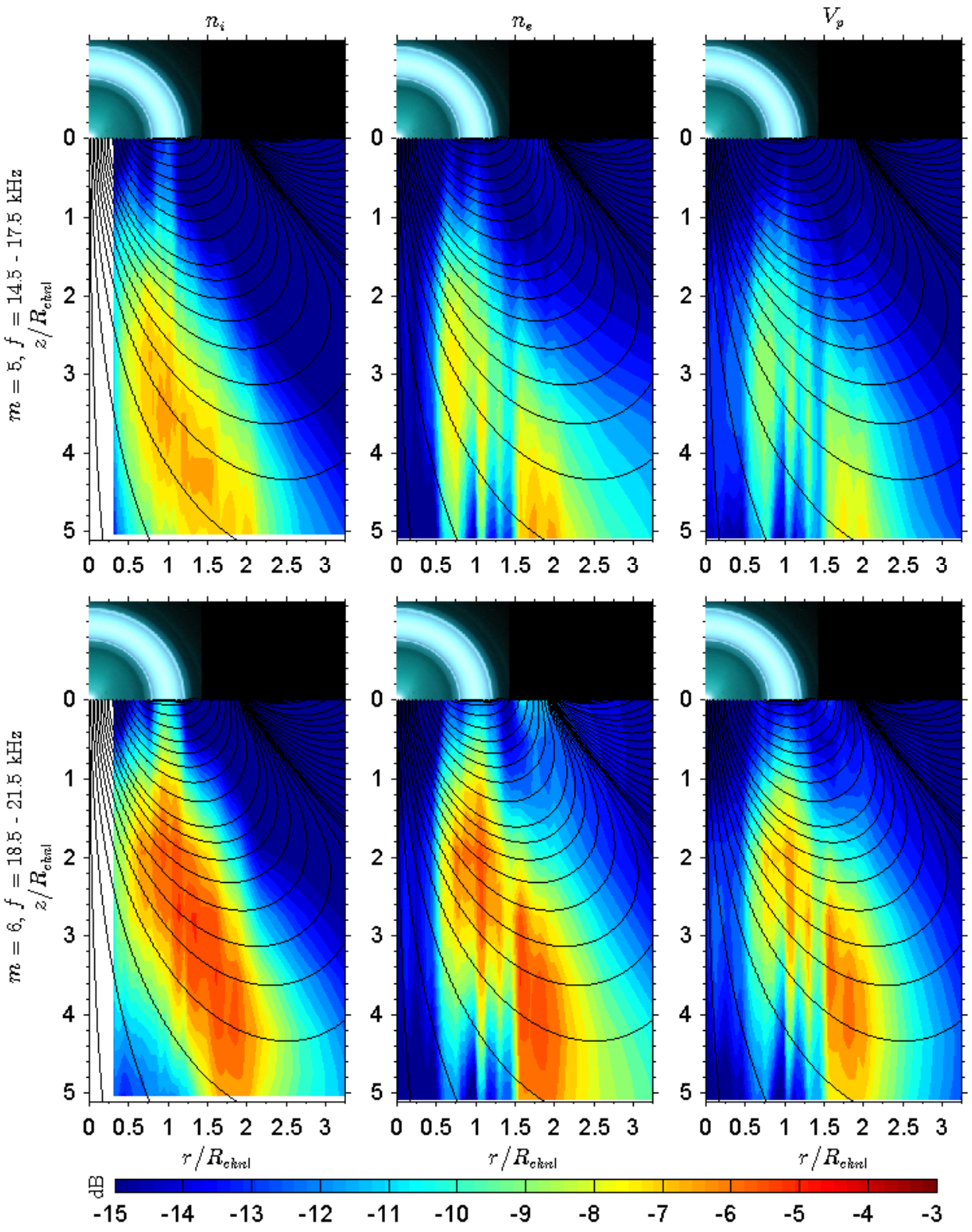

Figure B.9: Relative signal strength for oscillations in n_i, n_e, and V_p throughout the plume that correspond to spoke orders m = 5, 6 in the frequency bands shown in Table B.2. Magnetic field directions are shown overlaid. Maps have been smoothed by a two-index radius, cosine weighted, moving average window to reduce noise.

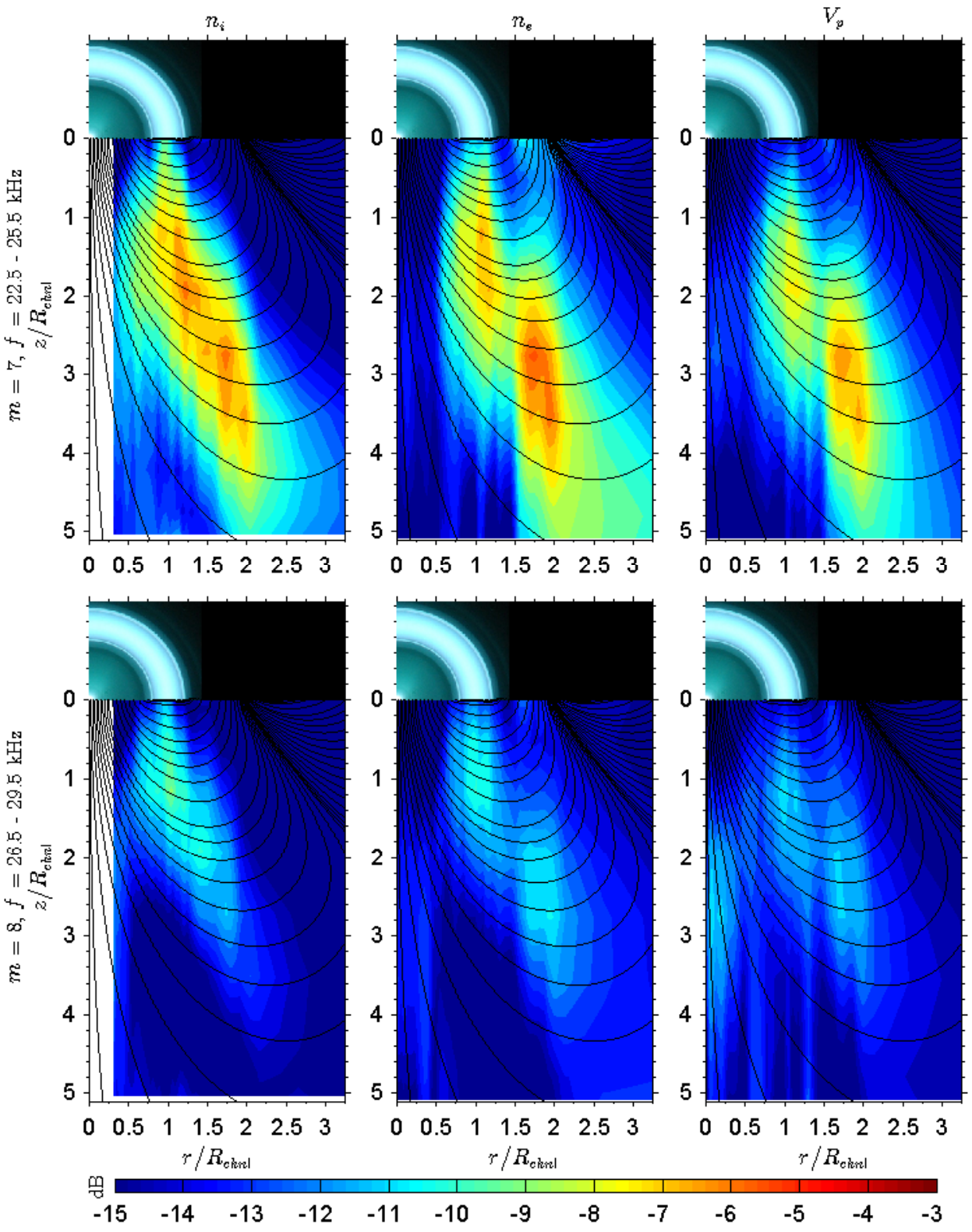

Figure B.10: Relative signal strength for oscillations in n_i, n_e, and V_p throughout the plume that correspond to spoke orders m = 7, 8 in the frequency bands shown in Table B.2. Magnetic field directions are shown overlaid. Maps have been smoothed by a two-index radius, cosine weighted, moving average window to reduce noise.

APPENDIX C

Magnetically Shielded HETs

C.1 Introduction

Mode transitions in two magnetically shielded thrusters are investigated using the same techniques described in Chapter 3 for the investigation of the unshielded H6 in Chapter 4. Section C.2 describes the NASA-300MS at NASA GRC and Section C.3 describes the H6MS at NASA JPL. Both magnetically shielded thrusters exhibit two transition points with three different oscillatory modes.

C.2 Magnetically Shielded 300M (NASA-300MS)

C.2.1 NASA-300MS Information

NASA is developing a 10-15 kW HET for a Solar Electric Propulsion Technology Demonstration Mission. As part of this effort, the NASA-300M thruster was modified with magnetic shielding and called the NASA-300MS shown in Figure C.1. Ref. 158 details an extensive characterization effort at NASA GRC to characterize the NASA-300MS with far field diagnostics including Faraday probes, $E \times B$ probes, retarding potential analyzer, Langmuir probe, and thrust data. HIA was also performed on the NASA-300MS and is presented here. For brevity, the NASA indicator in front of the thruster name will be dropped.

The 300MS in Figure C.1 is the based on the 300M, which is a magnetic layer HET with a magnetic lens topology designed for high specific impulse missions [159] and a centrally mounted cathode. The magnetic circuit and the discharge channel walls of the 300M were modified to accommodate the magnetic shielding, but rest of the thruster including the mean channel diameter remains unchanged. A second configuration of the 300MS was used with a shortened discharge channel length. The anode was moved down stream reducing the discharge channel length by 20% and is denoted as the 300MS-2. [158] All results presented here for high-speeding imaging were

performed on the 300MS-2. The magnetic field was radially out so the $E \times B$ direction was CCW like the H6. The thruster was operated on xenon with an anode mass flow rate of 40 mg/s and cathode mass flow rate of 3.2 mg/s for an 8% CFF. Two operating conditions were tested:

1. V_D = 300 V, I_D = 50 A, P = 15 kW
2. V_D = 400 V, I_D = 50 A, P = 20 kW

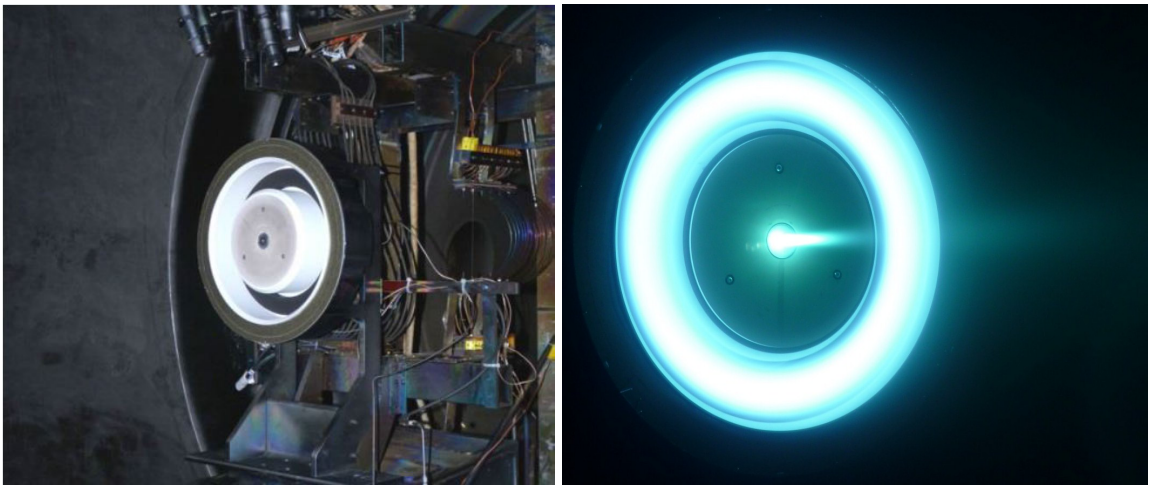

(a) On the thrust stand at NASA GRC. Reproduced from Figure 2 of Ref. 158

(b) Operating in VF-5 at 15 kW.

Figure C.1: The NASA-300MS at NASA GRC.

The investigation in Ref. 158 concluded that "the 300MS data shows ~ 2% higher voltage utilization efficiency, ~ 2.5% lower divergence efficiency, and ~ 1.5% higher current utilization efficiency than the 300M data. The two thrusters have roughly the same values in charge and mass utilization efficiencies. The general conclusion is that the 300M and 300MS have very similar performance as measured by the anode efficiency." The 300MS and the 300MS-2 had the same performance within measurement uncertainty.

The same techniques of varying magnetic field strength without varying shape used in the H6 investigation were employed here by maintaining a constant magnetic coil current ratio of $I_{IM}/I_{OM} = 1.05 \pm 0.01$. Note that no magnet field simulations or measurements were conducted at the different I_M settings to verify the magnetic field shape was unaltered. This short coming is significant as the magnetic circuit was likely saturated at the highest magnet currents. If the magnetic field topology shown schematically in Figure 2.11 is not maintained because the magnetic circuit was saturated, then the plasma may unintentionally interact with the walls similar to unshielded thrusters. If this is the case, then it may provide researchers the ability to study the role of plasma-

wall interactions in HETs by intentionally forcing the plasma to contact the wall (unshielded) or have reduced plasma-wall contact (shielded) by changing the B-field during operation.

C.2.2 Experimental Setup

The tests were conducted in Vacuum Facility 5 (VF-5) at NASA GRC and described in Ref. 158, with key metrics summarized here. VF-5 is a cylindrical vacuum chamber 4.6 m in diameter and 18.3 m long equipped with cryo-panels and 20 oil diffusion pumps. The pressure as measured by an ion gauge mounted near the thrust stand was 2.6×10^{-5} Torr, corrected for xenon. The commercial gas feed system includes a 1000-sccm mass flow controller for the anode and 200-sccm controller for the cathode with an uncertainty of measurement of ±1.0% of reading. The commercial discharge power supply can provide up to 2000 V and 100 A with a 5.5 mF output filter capacitance, and a 15.3 mF capacitor bank was connected in parallel. Separate commercial power supplies were used to power the cathode heater, cathode keeper, and electromagnets. The thrust stand is an inverted pendulum thrust stand designed by Haag [109] and is actively cooled during operation. The nominal accuracy is ±2% [159] and thermal drift is corrected by measuring thrust signal periodically without gas flow, where the maximum was ~ 10 mN. The thrust to power is calculated from Equation 2.23 and the anode efficiency is calculated from Equation 2.24.

VF-5 does not have a view port on or close to thruster centerline like LVTF. Therefore, the thruster was imaged from a side view port using a mirror 4.4 m downstream as shown in Figure C.2. This caused the thruster image captured by the FastCam to be inverted, which was corrected in post-processing. Vibration was noticed in the mirror, but the frequency was lower than the plasma oscillations and did not perturb the data analysis.

The same equipment and analysis techniques described in Section 3.5 were used to acquire and process the HIA results presented here. An Agilent DSOX3024A digital oscilloscope with built in function generator was used to trigger the FastCam and the oscilloscope to acquire discharge current data. The discharge current was measured with a Tektronix A6303 current probe connected after the capacitor bank and a Tektronix TM502A amplifier set to AC-coupled mode.

C.2.3 Results and Discussion

Magnetic field sweeps were completed for the magnetically shielded 300M and two mode transitions were identified. During magnetic field sweeps, the magnet current increments were typically 0.5 A, which is more coarse than the 0.1 A increments used for the H6 investigation near the transition points. As a result, transition regions could not be defined like the H6 investigation. A transition similar to the local-to-global mode transition in the unshielded H6 was observed at I_{IM} = 3.5 A where the discharge current and low frequency oscillations dominated for $I_{IM} < 3.5$ A;

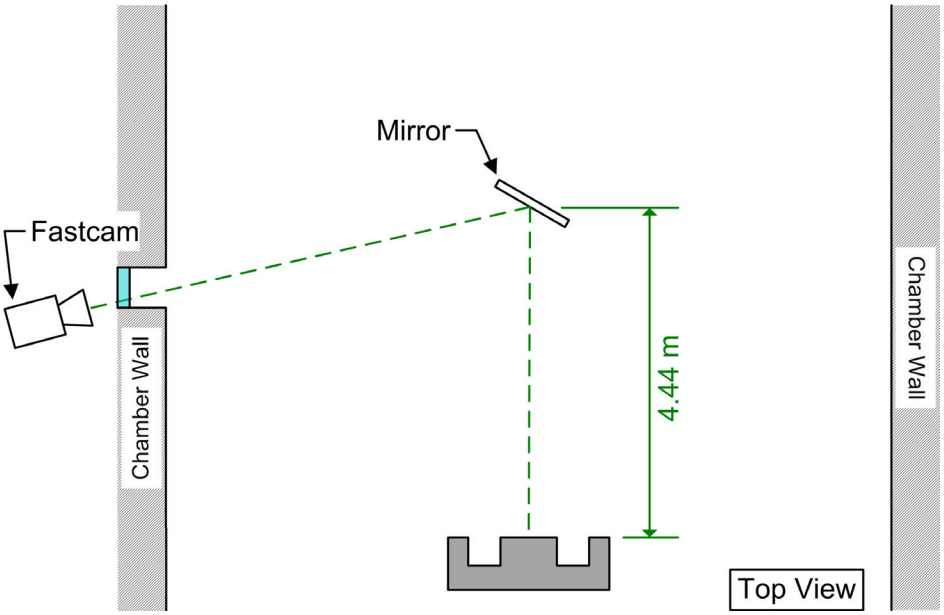

(a) Schematic showing FastCam, view port, mirror and thruster.

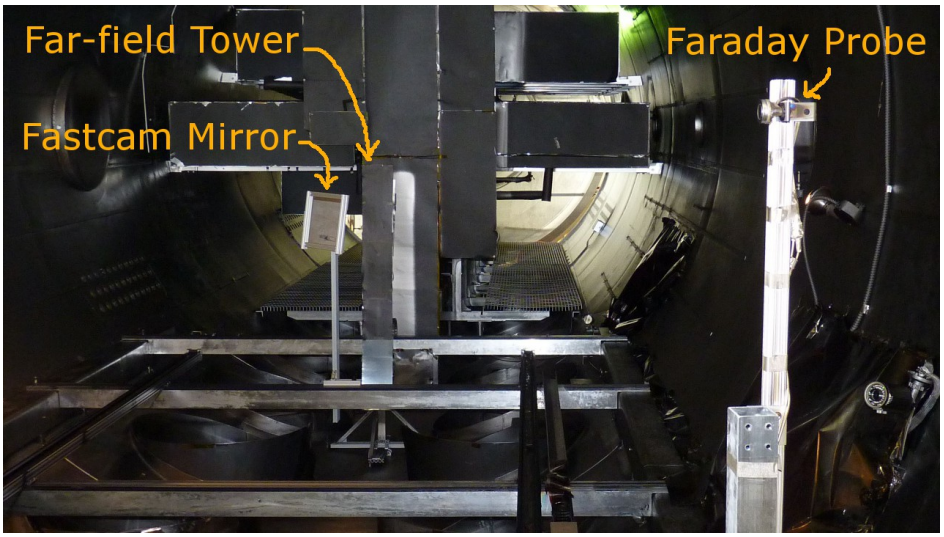

(b) Downstream mirror and probes.

Figure C.2: Experimental setup of 300MS in VF-5 at NASA GRC showing thruster, mirror, and view port for high-speed imaging.

however, no spokes were observed for $I_{IM} > 3.5$ A. A new transition was observed between $I_{IM} = 5.5 - 6.0$ A where there was no noticeable change in discharge current, but spokes were observed for $I_{IM} \geq 6.0$ A. For the discussion here, Mode 1 is $I_{IM} < 3.5$ A, Mode 2 is $3.5 \leq I_{IM} \leq 5.75$ A and Mode 3 is $I_{IM} > 5.75$ A. The modes are summarized in Table C.1 and their characteristics are detailed below.

Figure C.3 shows the discharge current, thrust, thrust-to-power, and anode efficiency for the 300 and 400 V condition. Except for thrust, the same trends are observed as the unshielded H6 in Figure 4.30. The 300M-MS shows a general decrease in thrust with decreasing magnetic field magnitude, which is different than the H6 that was nearly constant. The sharp increase in discharge current and oscillation amplitude in Mode 1 is very similar to the local to global transition observed in the unshielded H6 in Figure 4.3. Mode 1 shows the highest discharge current, lowest thrust, lowest thrust-to-power and lowest anode efficiency. The performance values peak in Mode 2 where the discharge current is minimum, the thrust-to-power peaks, and the anode efficiency peaks. The 400 V condition shows high-amplitude oscillations near the spoke transition point that will be discussed later. The thrust peaks in Mode 3, but the discharge current is higher than Mode 2 so the thrust-to-power is less than Mode 2. In general, thrust peaks near the spoke mode transition, but the discharge current is unaffected by the spoke mode transition. The observation that the presence or absence of spokes does not affect the discharge current between Modes 2 and 3 and could be an important clue in understanding the nature of spokes in magnetically shielded thrusters.

The B-field sweeps for the 300 V and 400 V condition are shown in Figures C.4 and C.5, respectively. The top row shows the mean discharge current with the RMS values as dashed lines around the mean to visualize oscillation amplitude. The selected magnet settings shown are $I_{IM} =$ 3.0 or 3.1, 4.5 and 6.5 A which correspond to oscillation Mode 1, 2 and 3, respectively, as described in Table C.1. The second row is the PSD for the discharge current and HIA. The I_D PSD corresponds to the left axis while m_0 and spoke orders $m = 2 - 9$ correspond to the right axis. The different scaling is due to different units of the original signals (current in A versus current density in mA/cm^2). The traces overlay each other when scaled as shown in Figure C.4 and C.5, which reinforces the correlation between I_D and m_0 that has been shown previously. The HIA upper frequency limit is 43.75 kHz due to the camera frame rate of 87.5 kHz, but the discharge current sampling rate allowed the upper limit on I_D PSD to be over 80 kHz. This is important because the cathode oscillations between 50-60 kHz cannot be resolved by HIA (with the Photron SA5 at 256×256 resolution), but they can be seen in the discharge current. The third row plots in Figures C.4 and C.5 are discharge current density, j, calculated using the HIA techniques discussed in Section 3.5. The fourth row is a normalized spoke surface that is calculated by normalizing each

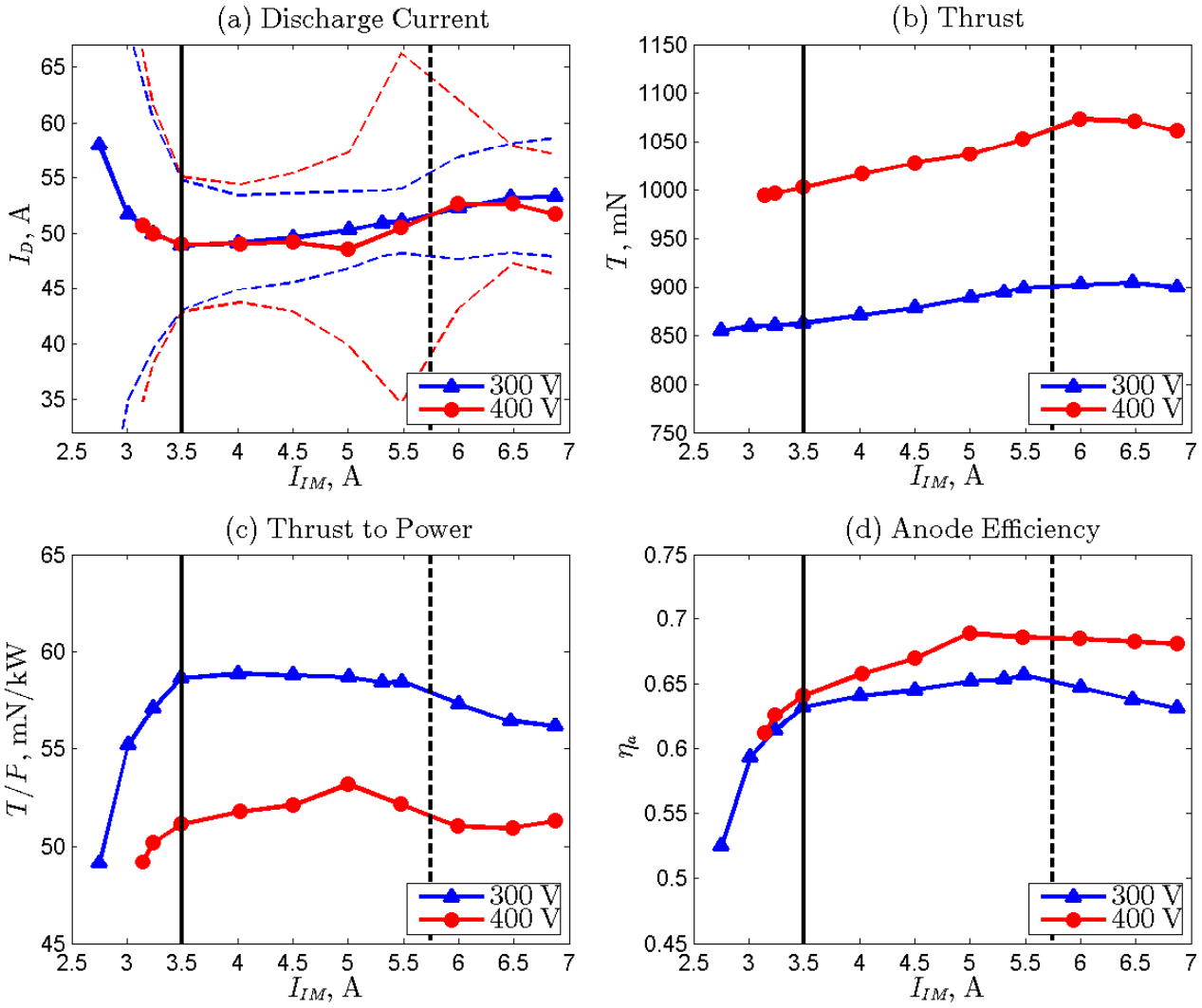

Figure C.3: 300MS (a) discharge current, (b) thrust, (c) thrust-to-power, and (d) anode efficiency for the 300 V (blue) and 400 V (red) during B-field sweeps. The dashed lines around I_D are the discharge current oscillation amplitude or RMS values. The two mode transition lines are shown.

frame (vertical column of points or $\theta = 0 \rightarrow 360^{\circ}$ at a given time, t_i) from the discharge current density according to

$$\hat{j}_i(\theta, t_i) = \frac{j(\theta, t_i) - \bar{j}(\theta, t_i)}{\widetilde{j}(\theta, t_i)} \tag{C.1}$$

This technique isolates and intensifies any azimuthal spokes that may be present by eliminating entire channel oscillations. When spokes are not present, the normalized spoke surfaces appear as nearly random noise.

In Figure C.4, the lowest magnetic field setting of $I_{IM} = 3.0$ A corresponds to Mode 1 in Table C.1 and shows the breathing mode similar to the unshielded thruster. There is a strong peak at 3 kHz, a lower peak at 24 kHz and another broad peak from 56-60 kHz. No spokes are present in the PSD. The discharge current shows large amplitude global oscillations from 50 to 250 mA/cm^2. The indeterminate, noisy nature of the normalized spoke surface reinforces that no spokes are present. The discharge current oscillation amplitude is the largest in this mode and is > 20% of the mean as shown in Figure C.6, which increases with decreasing magnetic field strength starting at the mode transition line.

The magnetic field setting of $I_{IM} = 4.5$ A in Figure C.4 corresponds to Mode 2 in Table C.1 and shows that cathode oscillations are dominant. The peak at ~ 60 kHz is larger than the breathing mode peak at ~ 5 kHz. Again, no spokes are present in the PSD, which is reinforced with the noisy normalized spoke surface. Oscillations in j are smaller than Mode 1 vary between 115 and 140 mA/cm^2; however, the cathode oscillations are higher frequency than the Nyquist limit of the FastCam so the oscillations are not fully resolved. The discharge current oscillation amplitude is the least of all modes at less than 10% in Mode 2 for 300 V in Figure C.6 with the minimum at $I_{IM} = 5.5$ A close to the spoke transition line.

The highest magnetic field setting of $I_{IM} = 6.5$ A in Figure C.4 corresponds to Mode 3 in Table C.1 and simultaneously shows the breathing mode, spokes, and cathode oscillations. The I_D PSD shows a peak at ~ 3 kHz that corresponds to the breathing mode and a broad peak at ~ 60 kHz that corresponds to cathode oscillations. Spokes are clearly present by the strong peaks in $m = 2-9$ of the HIA PSD. The strongest peak is $m = 3$, which is over an order of magnitude higher than all other spokes orders. The normalized spoke surface shows that only 3 spokes are present at one time. Angular striations can be seen in j intermixed with vertical lines showing a mixture of whole-channel oscillations and azimuthal spokes that are between 110 and 160 mA/cm^2. The normalized spoke surface isolates the spokes very clearly with a spoke velocity of $v_{sp} = 1000 \pm 100$ m/s. The discharge current oscillation amplitude in Figure C.6 is $\sim 10\%$ in this Mode 3 for 300 V. Section 2.3.8 discussed how the electron reflection is likely different between magnetically shielded and unshielded thrusters. It identified that electrons would be reflected back into the plasma by either the magnetic mirror effect near the poles or the ambipolar effect, but further theoretical,

computational and experimental investigations are required to determine the exact mechanism. In trying to understand why spokes only propagate for strong magnetic field settings, one could speculate that the electron reflection mechanism changes from ambipolar reflection to magnetic mirror reflection, which allows spokes to propagate through an unknown mechanism.

Figure C.5 for the 400 V condition shows many of the same trends as the 300 V condition. In Mode 1 a strong breathing mode peak is observed at 5.5 kHz that is evidenced by strong vertical lines in j with oscillations between 50 and 250 mA/cm^2. The normalized spoke surface and the HIA do not show any evidence of spokes. In Mode 2 the cathode oscillations dominate at 57 kHz with breathing mode oscillations at 6 kHz of lower magnitude. The discharge current density oscillation amplitudes are smaller between 115 and 140 mA/cm^2. As with Mode 1, the normalized spoke surface and the HIA do not show any evidence of spokes. In Mode 3 a combination of breathing mode, cathode and spokes are present. Spoke are clearly visible in the HIA PSD with the dominant spoke order of $m = 3$ and three spokes observed in the normalized spoke surface. The breathing mode peak is $\sim$ 2 kHz and is the same strength as the broad cathode oscillations from 50-60 kHz.

The PSDs for different magnet settings for 300 V and 400 V are shown in Figure C.7. The 300 V condition in Figure C.7(a) shows the 3-5 kHz breathing mode oscillation is present for Modes 1-3. There is always a 50-60 kHz peak for cathode oscillations that is only higher in magnitude than the breathing mode for Mode 2. The 400 V condition in Figure C.7(b) shows the 2-6 kHz breathing mode oscillation is present for Modes 1-3. There is also always a 50-60 kHz peak for cathode oscillations that is higher in magnitude than the breathing mode for Mode 2.

The most significant difference between the 300 V and 400 V conditions is the very sharp peak in discharge current oscillation amplitude for 400 V at I_{IM} = 5.5 A, which corresponds to a minimum in oscillation amplitude for 300 V as shown in Figure C.6. This trend of large discharge current oscillation amplitude crosses the spoke mode transition boundary and suggests the spokes are unrelated this phenomenon. Surprisingly, Figure C.3(a) shows that mean discharge current is unaffected by these increased oscillations. This indicates it is not a global or breathing mode oscillation since those have increased mean discharge current and oscillation amplitude. The high amplitude oscillations observed in Mode 2 at I_{IM} = 5.5 A are cathode oscillations strongly peaked at 59 kHz. The oscillation amplitude (Figure C.6) and oscillation strength (Figure C.7(b)) are nearly the same as the breathing mode in Mode 1. However, these oscillations do not affect thruster performance as shown in Figure C.3. The 300M-MS appears to be more susceptible to cathode oscillations at 400 V that do not impact performance. The magnetic field setting of I_{IM} = 5.5 A appears to be a resonance with cathode oscillations and merits further investigation.

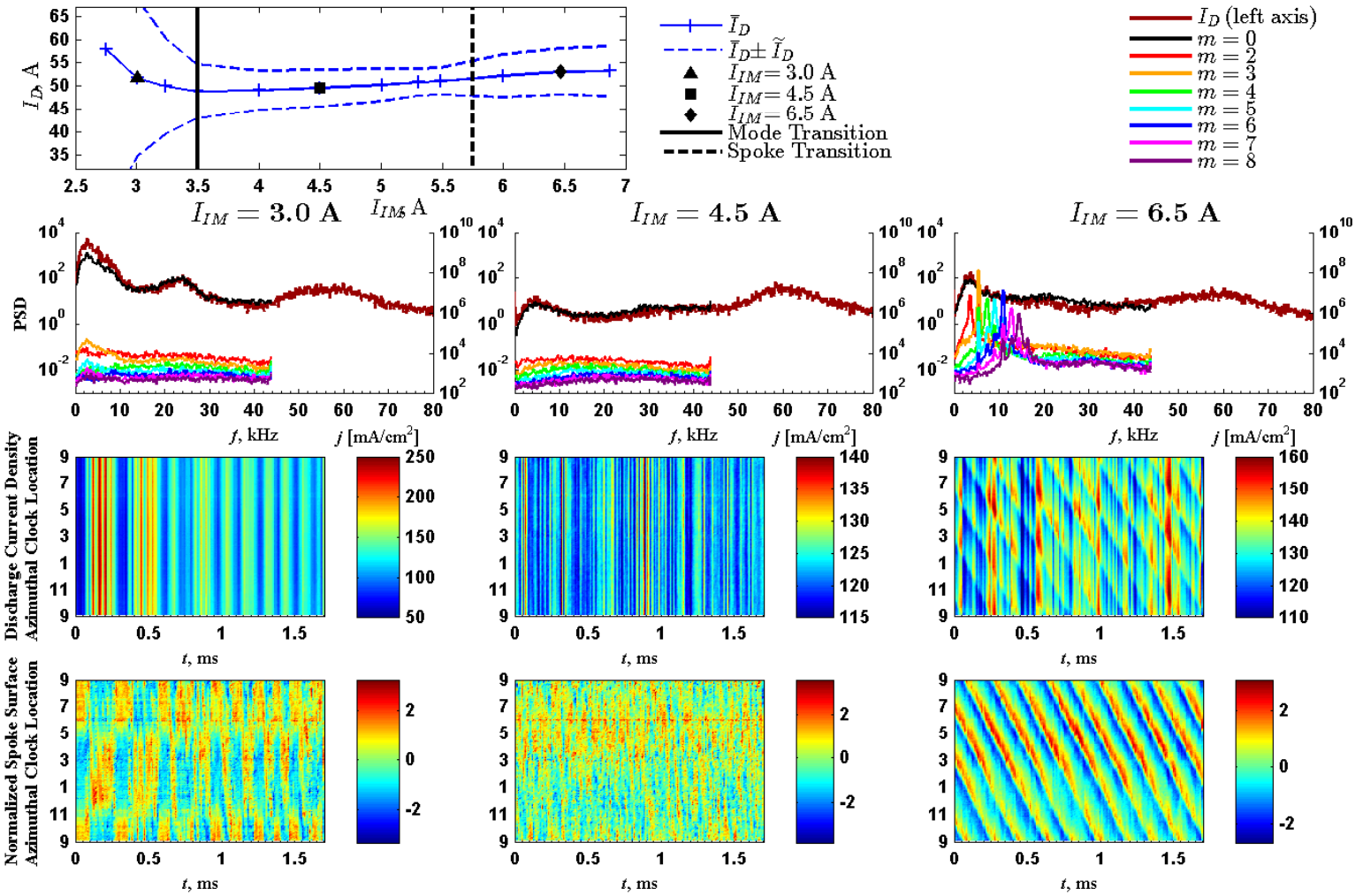

Figure C.4: 300MS B-field sweep for 300 V with three magnetic field strengths chosen for detailed analysis. Row 1: Discharge current mean and oscillation amplitude with mode transitions. Row 2: Discharge current PSD (left axis) from $f = 0 - 80$ kHz and HIA PSDs (right axis) from $f = 0 - 43.8$ kHz; a 200 Hz moving average filter has been applied. Row 3: Discharge current density. Row 4: Normalized spoke surface.

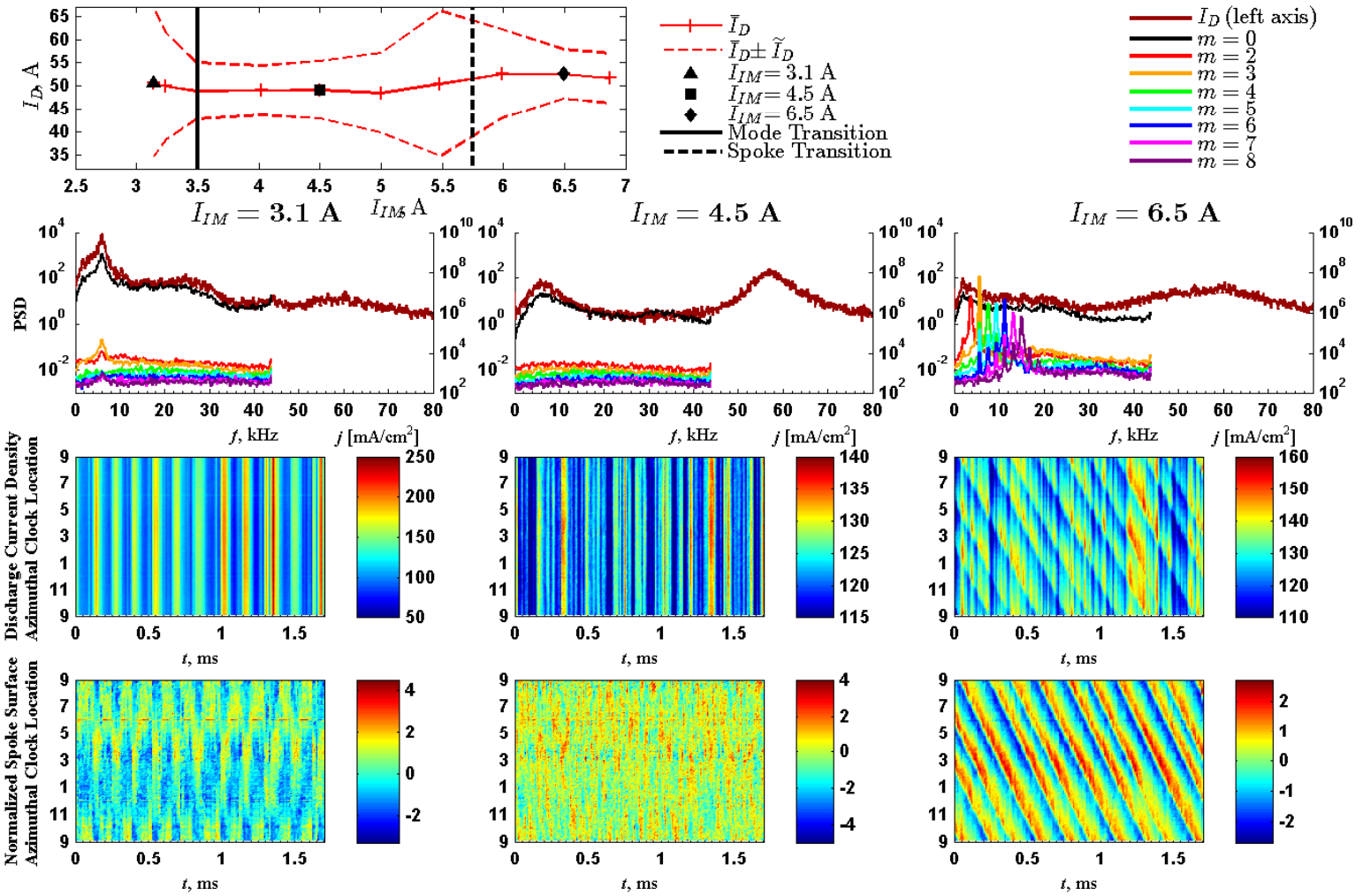

Figure C.5: 300MS B-field sweep for 400 V with three magnetic field strengths chosen for detailed analysis. Row 1: Discharge current mean and oscillation amplitude with mode transitions. Row 2: Discharge current PSD (left axis) from $f = 0 - 80$ kHz and HIA PSDs (right axis) from $f = 0 - 43.8$ kHz; a 200 Hz moving average filter has been applied. Row 3: Discharge current density. Row 4: Normalized spoke surface.

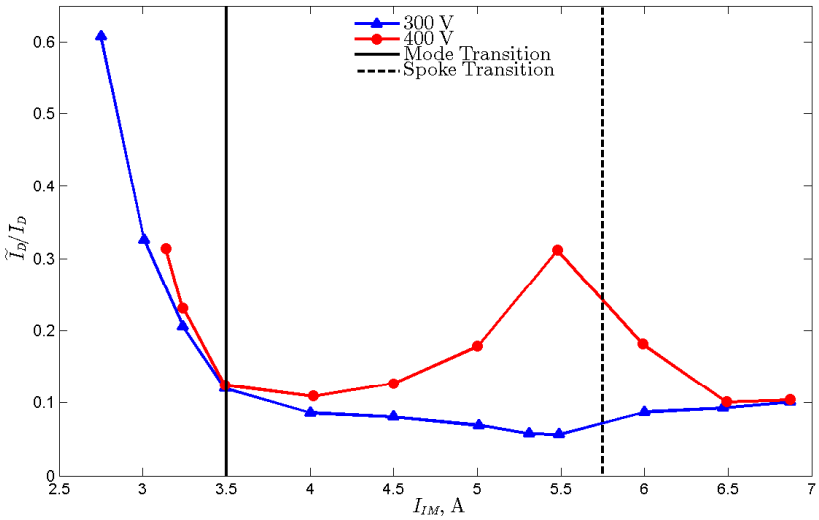

Figure C.6: Discharge current oscillation amplitude for 300M-MS during magnetic field sweeps for 300 V (blue) and 400 V (red). Oscillation amplitude is the RMS value divided by the mean value. Mode transition lines are shown.

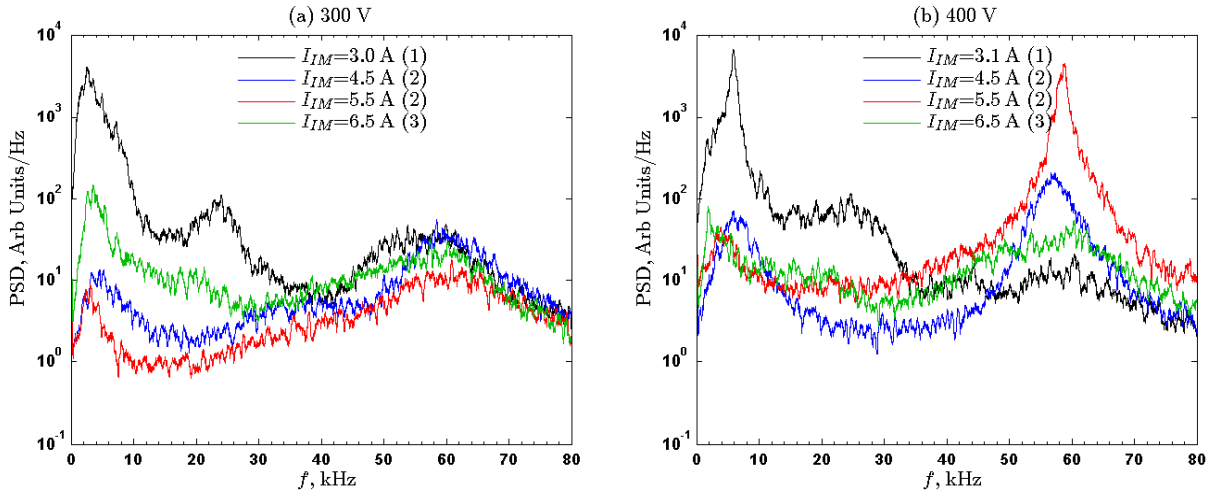

Figure C.7: Discharge current PSD for (a) 300 V and (b) 400 V for selected magnet settings. Mode numbers are shown in parentheses. All PSDs have been smoothed by a 400 Hz moving average filter.

	Mode 1	Mode 2	Mode 3
Limits	$I_{IM} < 3.5$ A	$3.5 < I_{IM} < 5.75$ A	$I_{IM} > 5.75$ A
Description	Global oscillation (breathing mode)	Cathode oscillation	Combined cathode, spoke and breathing mode
Low Frequency $f < 20$ kHz	**Dominant** 1-5 kHz (300 V) 5-10 kHz (400 V)	~ 5 – 10 kHz oscillations present but not dominant	~ 5 – 10 kHz oscillations present, can be large than cathode oscillations
High Frequency $f = 20 - 100$ kHz	Weak or not present	**Dominant** 60 kHz (300 V) 50-60 kHz (400 V)	Cathode related oscillations at 60 kHz
Spokes	Not present	Not present	Strong spokes; v_{sp} = 1000 ± 100 m/s
Discharge Current RMS/Mean	> 15%	< 10% (300 V) 10 – 30% (400 V)	~ 10% (300 V) 10 – 20% (400 V)
I_D	High	Low	Middle
T	Low	Middle	High
T/P	Low	High	Middle
η_a	Low	High	Middle

Table C.1: Summary table of modes and oscillations for the 300M-MS. The bottom four rows show a qualitative ranking for I_D, T, T/P and η_a

C.3 Magnetically Shielded H6 (H6MS)

C.3.1 H6MS Information

The H6MS shown in Figure C.8 is based on the H6 described in Section 3.3. The inner and outer front pole pieces and the inner and outer screens were modified to implement magnetic shielding in the H6. Changes were also made to the discharge chamber with new rings modified as described and shown in Figure 3 of Ref. 37. The design, detailed numerical modeling, and extensive testing of the H6MS has been well documented in a series of publications. [4, 22, 36, 37, 160] During the initial test campaign to compare the H6MS to the H6, [37] "practically erosion-free operation has been achieved for the first time in a high performance Hall thruster." It was noted that the specific impulse increased by 2.9%, the total efficiency decreased by 1.7% and the insulator ring temperature decreased reduced by 12-16%. The discharge current oscillations increased by 25%, but did not affect the thruster stability. The investigation presented in Ref. 37 used an anode mass flow rate of 18.35 mg/s with a cathode flow rate of 1.28 mg/s. The present investigation had an anode flow rate of 18.23 mg/s (< 1% lower) with a cathode flow rate of 1.28 mg/s. As shown in Figure C.9(a), the discharge currents are the same to within 1% so this difference is negligible.

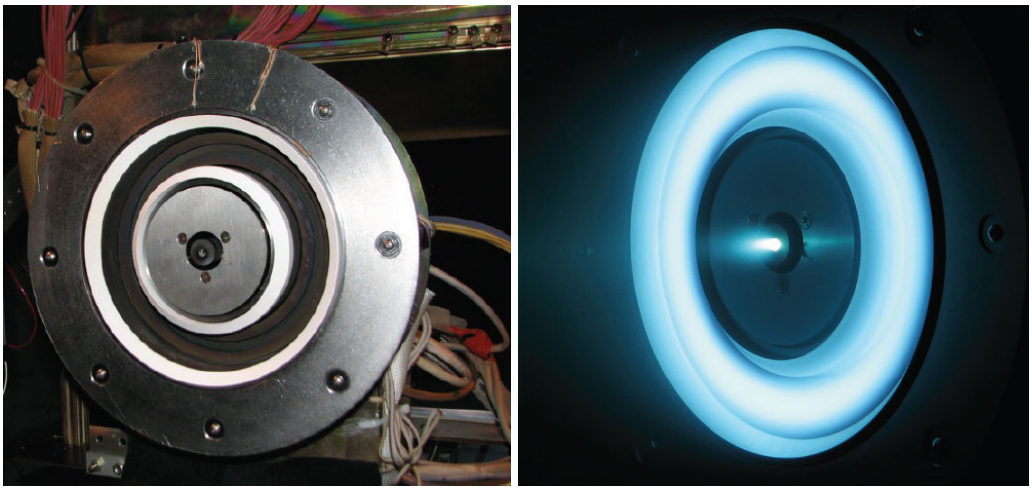

(a) On the thrust stand at NASA JPL. Reproduced from Figure 9 of Ref. 37.

(b) Operating in the Owens Chamber at 6 kW. Reproduced from Figure 7 of Ref. 37.

Figure C.8: The H6MS at NASA JPL.

The same techniques of varying magnetic field strength without varying shape used in the H6 investigation were employed here by maintaining a constant magnetic coil current ratio of $I_{IM}/I_{OM} = 1.21$. The magnetic field shape variations over magnet current settings were not verified with simulations like the H6. The magnetic field was known to become skewed due to saturation

for $I_{IM} \geq 5$ A[1], so ratio of $I_{IM}/I_{OM} = 1.00$ was investigated for the higher magnetic field settings. Although not shown here, the results are indistinguishable from the nominal coil current ratio, so $I_{IM}/I_{OM} = 1.21$ is used for this investigation in order to provide a direct comparison with previous work.

The first study on oscillations in the H6MS was conducted by Jorns [60] where classic breathing mode oscillations were observed from 7-12 kHz and cathode related observations were observed from 75-90 kHz as discussed in Section B.4.1. The cathode oscillations are dominant close to thruster centerline and are characterized as high-frequency, density gradient-driven drift waves. The results presented here agree with that work so the lower frequencies observed here are labeled as breathing mode and the higher frequencies are identified as cathode oscillations.

C.3.2 Experimental Setup

This experiment was conducted in the Owens Chamber at NASA JPL, which is a 3 m diameter by 10 m long cryogenically pumped vacuum chamber. The pressure during testing was 1.2×10^{-5} Torr corrected for xenon as measured by an ion gauge mounted near the thrust stand. Similar to Figure 3 of Ref. 60, the FastCam described in Section 3.5.1 is in a viewport of the Owens Chamber ~ 7.5 m downstream and off thruster centerline by $\sim 5°$. The FastCam acquisition and discharge current acquisition were triggered by a Wavetek 178 function generator sending a TTL pulse. A Tektronix DPO-3054 digital oscilloscope recorded the AC component of the discharge current at 500 kHz. Section IV of Ref. 37 contains additional details about the facility, the thruster and measurement diagnostics. Processing of the high-speed images was done according to the techniques described in Section 3.5.

C.3.3 Results and Discussion

The discharge current with oscillation amplitude (RMS) is shown in Figure C.9(a) for a 300 V discharge. Only discharge current was measured in the present work, but matched well from the initial investigation by Hofer [37] so the thrust data shown in Figure 10 of that work is applicable here and shown in Figure C.9(b). Similar to the NASA-300MS, three modes are observed with two transition points at approximately $I_{IM} \approx 2.75$ A and $I_{IM} \approx 5.25$ A. The performance data for the H6MS Figure C.9 shows the same trends as the NASA-300MS in Figure C.3.

The discharge current in Figure C.9(a) is minimized in mode 2 and shows a minimum value at $I_{IM} = 3.5$ A, which is a lower setting than the nominal setting of $I_{IM} = 4.0$ A. The thrust in Figure C.9(b) continually decreases throughout the B-field sweep with a 5% decrease from the peak in mode 3. The thrust to power in Figure C.9(c) shows a peak in mode 2 at a lower B-field

[1]Personal correspondence with R. Hofer, February 2014.

setting than the nominal setting. The total efficiency is presented in Figure 10 of Ref. 37, but the anode efficiency shown in Figure C.9(d) was calculated from the discharge current in Figure C.9(a), thrust in Figure C.9(b), an anode mass flow rate of 18.35 mg/s, and Equation 2.24. Similar to the 300MS, the anode efficiency peaks in mode 2.

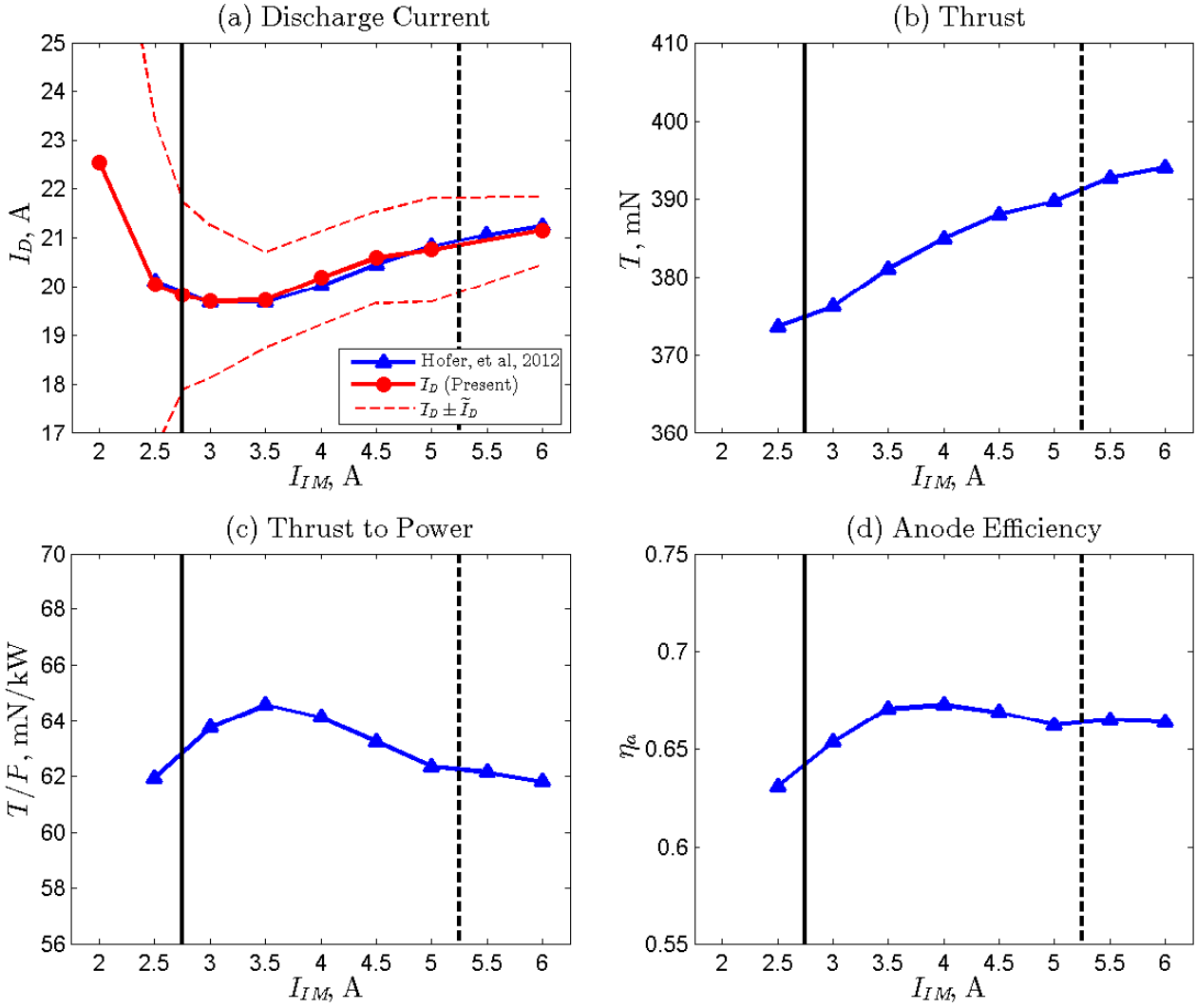

Figure C.9: H6MS (a) discharge current, (b) thrust, (c) thrust-to-power, and (d) anode efficiency for the 300 V (blue) reproduced from Figure 10 of Ref. 37 the present work (red) during B-field sweeps. Only discharge current was measured in the present work, but matched well from the previous investigation so the performance data is valid. The dashed lines around I_D are the discharge current oscillation amplitude or RMS values. The two mode transition lines are shown.

Figure C.10 shows the H6MS magnetic field sweep at 300 V. Similar to the NASA-300MS in Figure C.4, three modes are observed with two transition points. Select magnetic field strengths

have been chosen for further analysis in each of the modes. Figure C.10 can be compared to the unshielded H6 300 V sweep in Figure 4.9 of Section 4.5.1.

In mode 1 at I_{IM} = 2.5 A, the breathing mode at 10 kHz is an order of magnitude higher than the cathode oscillations at 69 kHz with no detectable spokes in the normalized spoke surface. Although not shown, the cathode oscillations nearly disappear at I_{IM} = 2.0 A, which is deep into breathing mode. The discharge current density oscillates globally around the discharge channel with fluctuations between 100 and 150 mA/cm^2 with some spikes up to 180 mA/cm^2.

The nominal conditions at I_{IM} = 4.0 A is in mode 2 and also does not exhibit any detectable spokes in the normalized spoke surface. The breathing mode frequency remains at 10 kHz and is approximately the same strength as the cathode oscillations. The cathode oscillations peak at 78 kHz, but the peak width is broader than in mode 1 before they disappear. The discharge current density oscillates globally around the discharge channel with fluctuations between 120 and 140 mA/cm^2 with some spikes up to 150 mA/cm^2. However, the cathode oscillations are above the Nyquist frequency of the FastCam so these oscillations are not adequately captures in the HIA PSD or spoke surfaces.

Mode 3 at I_{IM} = 6.0 A shows a strong $m = 3$ spoke order in the HIA PSD, which can be observed as three bright regions on any vertical line of the normalized spoke surface. The $m = 3$ peak is over an order of magnitude higher than the next highest $m = 6$, which is a harmonic, and 2 orders of magnitude higher than other spoke orders. Using the correlation method described in Section 5.5.2, the spoke velocity is 1450 ± 170 m/s. The cathode oscillation peak is even broader in mode 3 and the approximate peak is at 68 kHz. The discharge current PSD has a broader peak between 7 and 10 kHz and is the same strength as the cathode oscillations. The discharge current density displays spokes (diagonal striations) and global oscillations (vertical lines) with the fluctuations between 130 and 150 mA/cm^2.

Figure C.11 shows the same B-field sweep as Figure C.10, but the selected magnetic field settings for further analysis are within mode 2, I_{IM} =3.0, 4.0 and 5.0 A. These represent the limits before the upper and lower transition as well as the nominal setting of I_{IM} = 4.0 A. The discharge current increases with increasing magnetic field strength, $\bar{I}_D$=19.7, 20.2 and 20.8 A, respectively. The breathing mode frequency remains the same strength, but the frequency decreases with increasing magnetic field strength, f =10.3, 9.1, and 6.8 kHz, respectively. The cathode oscillations show a significant change in response to the magnetic field strength. The cathode oscillation strength decreases from nearly the same strength as the breathing mode near the lower transition point to barely detectable near the upper transition point. The frequency peaks are 75, 77 and a barely perceptible peak near 70 kHz. No spokes are observed in the normalize spoke surface.

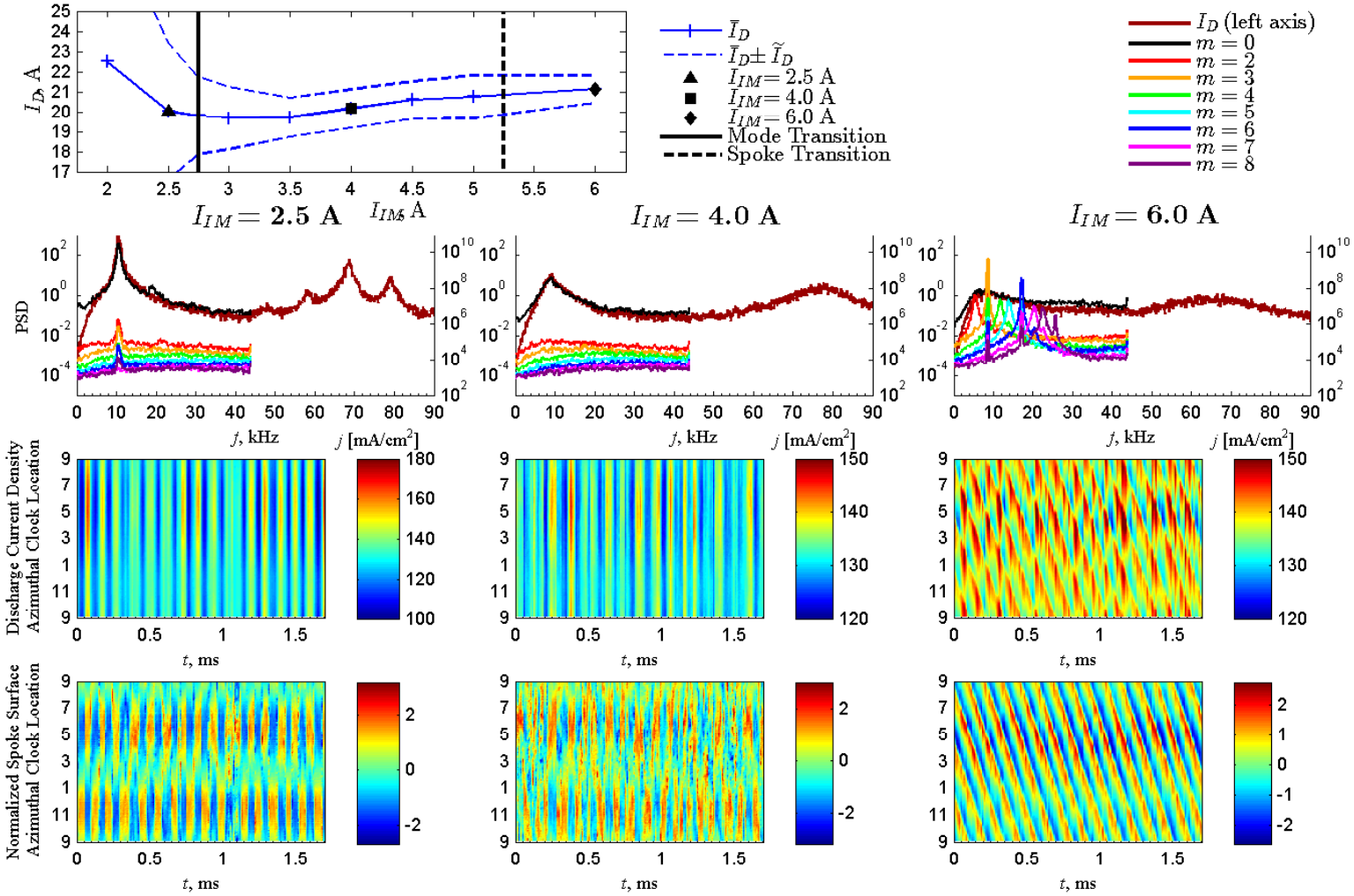

Figure C.10: H6MS B-field sweep for 300 V with three magnetic field strengths in each oscillatory mode chosen for detailed analysis. Row 1: Discharge current mean and oscillation amplitude with mode transitions. Row 2: Discharge current PSD (left axis) from $f = 0 - 90$ kHz and HIA PSDs (right axis) from $f = 0 - 43.8$ kHz; a 200 Hz moving average filter has been applied. Row 3: Discharge current density. Row 4: Normalized spoke surface.

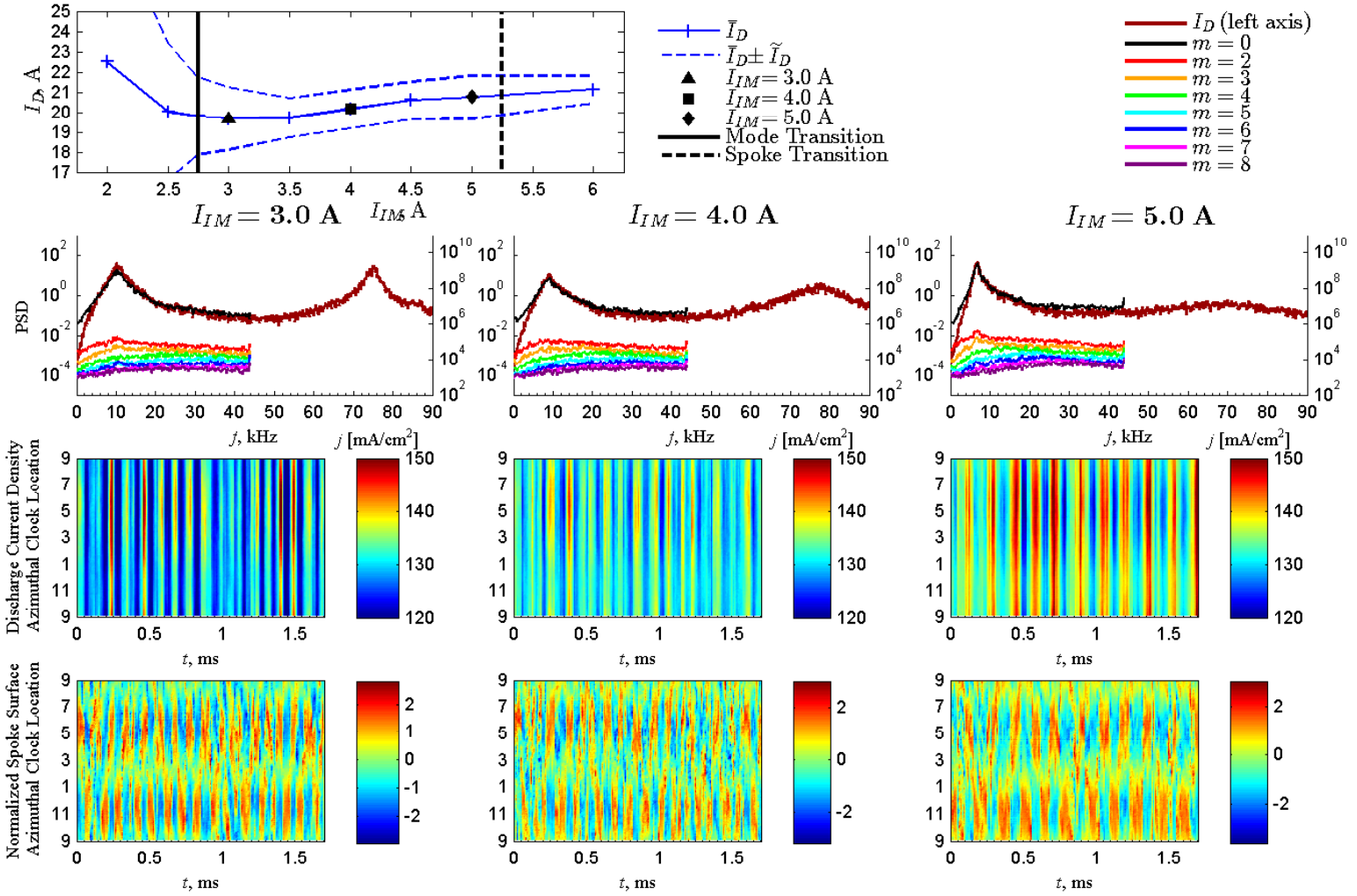

Figure C.11: H6MS B-field sweep for 300 V with three magnetic field strengths chosen in mode 2 for detailed analysis. Row 1: Discharge current mean and oscillation amplitude with mode transitions. Row 2: Discharge current PSD (left axis) from $f = 0 - 90$ kHz and HIA PSDs (right axis) from $f = 0 - 43.8$ kHz; a 200 Hz moving average filter has been applied. Row 3: Discharge current density. Row 4: Normalized spoke surface.

C.3.4 Comparison between H6 and H6MS

The mean discharge current and oscillation amplitude (RMS) for the H6 and H6MS at 300 V are compared in Figure C.12. The flow rate for the H6 is 19.5 mg/s and for the H6MS is 18.23 mg/s. The upper and lower bounds of the transition region between global and local mode are shown for the H6. The transition points between modes 1, 2 and 3 are shown for the H6MS. The magnetic field strength have been aligned by the nominal values of inner magnet coil current of I_{IM} = 3.50 A for the H6 and I_{IM} = 4.00 A for the H6MS as used in Ref. 37.

The discharge currents show remarkable similarity with the largest difference at the highest magnetic field settings. The H6MS mean discharge current is larger at the higher magnetic field setting while the H6 oscillation amplitude is larger. The transition from global to local mode for the H6MS occurs at higher relative magnetic field strength than when the H6 enters the transition region to global mode, however the uncertainty on the H6MS transition point is $\pm 0.05 B_r/B_r^*$ due to larger I_{IM} increments. The mean discharge current values do not differ significantly for $B_r/B_r^* < 1$ regardless of the slight difference in transition point. The H6 shows less change in the discharge current above the transition point (~ 0.5 A) than the H6MS (~ 1.5 A).

C.4 Summary

A mode transition study was conducted in magnetically shielded thrusters similar to Chapter 4 where the magnetic field magnitude was varied to induce mode transitions. The investigations presented here show a global to local mode transition similar to those detailed in Chapter 4 at low magnetic field magnitudes, except that spokes are not observed in the local mode. The equivalent global mode in magnetically shielded thrusters exhibits large amplitude, low frequency (1-10 kHz), breathing mode type oscillations. The equivalent local mode in magnetically shielded thrusters exhibits higher frequency (50-90 kHz), low amplitude, entire channel oscillations that Jorns [60] determined where cathode related oscillations. This shows a strong coupling between the discharge plasma in magnetically shielded thrusters (which is outside the channel compared to unshielded thrusters) and the cathode plasma. Cathode oscillations in unshielded thrusters are discussed in Appendix B and shown in Figure B.7. Unshielded thrusters do show cathode oscillations in the plume region over the inner pole, but their influence does not extend into the discharge channel so they are not detected in the discharge current signal. Therefore, it can be deduced that magnetically shielded thrusters are more susceptible to plasma conditions outside the discharge channel. A second mode transition is observed in magnetically shielded thrusters at higher magnetic field magnitudes where spokes are observed simultaneously with cathode oscillations and breathing mode type oscillations.

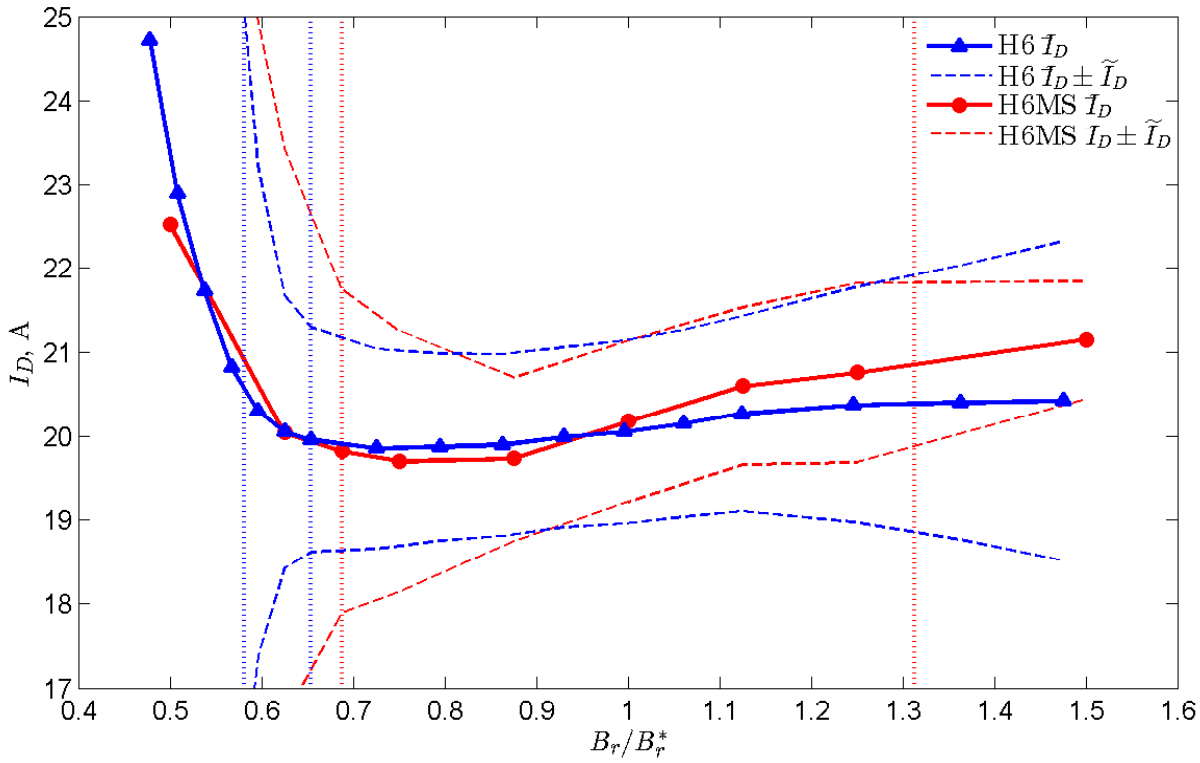

Figure C.12: Comparison of discharge current for the H6 (blue) and H6MS (red) during a B-field sweep for 300 V. The oscillation amplitude (RMS) is shown above and below the mean value. Vertical blue lines are the boundaries for the transition region for the H6 identified in Chapter 4 between local mode and global mode. Vertical red lines are the transition points for the H6MS between mode 1, 2 and 3.

Three different oscillatory modes are identified with the 300MS and H6MS: Mode 1) global mode similar to unshielded thrusters, Mode 2) cathode oscillations and Mode 3) combined spoke, cathode and breathing mode oscillations. The optimal thrust to power and efficiency are achieved in cathode oscillation mode or Mode 2. Thrust decreased by 5-6% with decreasing magnetic field strength. The presence or absence of spokes and strong cathode oscillations did not affect each other or discharge current. The 300MS 400 V condition exhibited a cathode oscillation resonance in Mode 2 close to the spoke transition that did not cause an increase in mean discharge current. Similar to unshielded thrusters, mode transitions and plasma oscillations effect magnetically shielded thruster performance. As magnetically shielded development continues, it will be important to create $I_D - V_D - B$ maps of thruster performance and understand the thruster oscillatory mode using time-resolved diagnostics.

Both magnetically shielded thrusters exhibit two transition points with three different oscillatory modes, and the discharge current responds differently to the transition points. When spokes

appear at the higher transition point, the mean discharge current is unaffected. At the lower transition point, the discharge current increases significantly similar to the local to global mode transition of unshielded thrusters. Previous work by Brown [41] showed that the local to global mode transition corresponded to an increase in electron transport through the channel for unshielded thrusters, and we can assume similar mechanisms are responsible for the increased discharge current in magnetically shielded thrusters at the lower transition point. The discharge current indifference between mode 2 and 3 at the upper transition point leads one to deduce that the appearance of spokes does not measurably affect cross field transport. Furthermore, if the magnetic field is skewed at higher magnetic fields such that the plasma contact with the wall is not minimized as occurs for nominal magnetically shielded operation, this could indicate that plasma contact with the wall is the cause for azimuthal spokes.

BIBLIOGRAPHY

[1] Morozov, A. I., "The conceptual development of stationary plasma thrusters," *Plasma Physics Reports*, Vol. 29, No. 3, March 2003, pp. 235–250.

[2] Morozov, A. I., Esipchuk, Y., Tilinin, G. N., Trofimov, A. V., Sharov, Y. A., and Shchepkin, G. Y., "Plasma accelerator with closed electron drift and extended acceleration zone," *Soviet Physics-Technical Physics*, Vol. 17, No. 1, July 1972, pp. 38–44.

[3] Hofer, R., Katz, I., Mikellides, I., Goebel, D., Jameson, K., Sullivan, R., and Johnson, L., "Efficacy of Electron Mobility Models in Hybrid-PIC Hall Thruster Simulations," AIAA 2008-4924, *44th AIAA/ASME/SAE/ASEE Joint Propulsion Conference & Exhibit*, Hartford, CT, July 2008.

[4] Mikellides, I. G., Katz, I., Hofer, R. R., and Goebel, D. M., "Magnetic shielding of walls from the unmagnetized ion beam in a Hall thruster," *Applied Physics Letters*, Vol. 102, No. 2, 2013, pp. 023509.

[5] Lobbia, R. B., *A Time-resolved Investigation of the Hall Thruster Breathing Mode*, Ph.D. dissertation, University of Michigan, Ann Arbor, MI, Jan. 2010.

[6] McDonald, M., *Electron Transport in Hall Thrusters*, Ph.D. dissertation, University of Michigan, Ann Arbor, MI, 2012.

[7] Tsiolkovskiy, K. E., *Works on Rocket Technology*, Publishing House of the Defense Industry, NASA TT F-243 Translation, Moscow, Russia, 1947.

[8] Sellers, J. J., *Understanding space: an introduction to astronautics*, Space technology series, McGraw-Hill Companies, New York, 3rd ed., 2005.

[9] Choueiri, E. Y., "A Critical History of Electric Propulsion: The First 50 Years (1906-1956)," *Journal of Propulsion and Power*, Vol. 20, No. 2, March 2004, pp. 193–203.

[10] Jahn, R., *Physics of Electric Propulsion*, Dover Publications, Mineola N.Y., 2006.

[11] Goebel, D. and Katz, I., *Fundamentals of Electric Propulsion : Ion and Hall Thrusters*, Wiley, Hoboken N.J., 2008.

[12] Garner, C., Rayman, M., Brophy, J., and Mikes, S., "In-Flight Operation of the Dawn Ion Propulsion System Through Orbit Capture at Vesta," *47th AIAA/ASME/SAE/ASEE Joint Propulsion Conference & Exhibit*, San Diego, CA, Aug. 2011.

[13] Brophy, J. R., Garner, C. E., and Mikes, S., "Dawn Ion Propulsion System: Initial Checkout After Launch," *Journal of Propulsion and Power*, Vol. 25, No. 6, Nov. 2009, pp. 1189–1202.

[14] Frisbee, R. H., "Advanced Space Propulsion for the 21st Century," *Journal of Propulsion and Power*, Vol. 19, No. 6, Nov. 2003, pp. 1129–1154.

[15] Wertz, J., *Space mission analysis and design*, Microcosm, Torrance Calif., 3rd ed., 1999.

[16] Welander, B., Carpenter, C., de Grys, K., Hofer, R., Randolph, T., and Manzella, D., "Life and Operating Range Extension of the BPT-4000 Qualification Model Hall Thruster," AIAA 2006-5263, *42nd AIAA/ASME/SAE/ASEE Joint Propulsion Conference and Exhibit, Sacramento, California*, July 2006.

[17] Zhurin, V. V., Kaufman, H. R., and Robinson, R. S., "Physics of closed drift thrusters," *Plasma Sources Science and Technology*, Vol. 8, No. 1, Feb. 1999, pp. R1–R20.

[18] Gallimore, A. D., "Near- and Far-Field Characterization of Stationary Plasma Thruster Plumes," *Journal of Spacecraft and Rockets*, Vol. 38, No. 3, May 2001, pp. 441–453.

[19] Pidgeon, D., Corey, R., Sauer, B., and Day, M., "Two Years of On-Orbit Performance of SPT-100 Electric Propulsion," AIAA 2006-5353, *24th AIAA International Communications Satellite Systems Conference (ICSSC)*, San Diego, CA, June 2006.

[20] Yendler, B., "Satellite Rescue- Luck of Skillful Application of Technology," AIAA 2012-5287, *AIAA SPACE 2012 Conference & Exposition*, Pasadena, CA, Sept. 2012.

[21] Mikellides, I. G., Katz, I., Hofer, R. R., Goebel, D. M., de Grys, K., and Mathers, A., "Magnetic shielding of the channel walls in a Hall plasma accelerator," *Physics of Plasmas*, Vol. 18, No. 3, 2011, pp. 033501.

[22] Hofer, R. R., Goebel, D. M., Mikellides, I. G., and Katz, I., "Magnetic shielding of a laboratory Hall thruster. II. Experiments," *Journal of Applied Physics*, Vol. 115, No. 4, Jan. 2014, pp. 043304.

[23] Brophy, J. R. and Muirhead, B., "Near-Earth Asteroid Retrieval Mission (ARM) Study," IEPC-2013-82, *33rd International Electric Propulsion Conference*, Washington, D.C., Oct. 2013.

[24] Fisher, J., Wilson, A., Werthman, L., de Grys, K., Meyer, S., and King, D., "The Qualification of a 4.5 kW Hall Thruster Propulsion Subsystem," AIAA 2003-4551, *39th AIAA/ASME/SAE/ASEE Joint Propulsion Conference and Exhibit*, Huntsville, AL, July 2003.

[25] Feuerborn, S. A., Perkins, J., and Neary, D. A., "Finding a Way: Boeing's All Electric Propulsion Satellite," AIAA 2013-4126, *49th AIAA/ASME/SAE/ASEE Joint Propulsion Conference*, San Jose, CA, July 2013.

[26] Liang, R. and Gallimore, A. D., "Constant-Power Performance and Plume Measurements of a Nested-Channel Hall-Effect Thruster," IEPC-2011-049, *32nd International Electric Propulsion Conference*, Wiesbaden, Germany, Sept. 2011.

[27] Florenz, R., Gallimore, A. D., and Peterson, P. Y., "Developmental Status of a 100-kW Class Laboratory Nested channel Hall Thruster," IEPC-2011-246, *32nd International Electric Propulsion Conference*, Wiesbaden, Germany, Sept. 2011.

[28] Kaufman, H. R., "Technology of closed-drift thrusters," *AIAA Journal*, Vol. 23, No. 1, Jan. 1985, pp. 78–87.

[29] Kim, V., "Main Physical Features and Processes Determining the Performance of Stationary Plasma Thrusters," *Journal of Propulsion and Power*, Vol. 14, No. 5, Sept. 1998, pp. 736–743.

[30] Hofer, R. R., *Development and characterization of high-efficiency, high-specific impulse xenon Hall thrusters.*, Ph.D. dissertation, 2004, 1 v.

[31] Liang, R., *The Combination of Two Concentric Discharge Channels into a Nested Hall-Effect Thruster*, Ph.D. dissertation, University of Michigan, Ann Arbor, MI, 2013.

[32] Goebel, D. M., Hofer, R. R., Mikellides, I. G., Katz, I., Polk, J. E., and Dotson, B., "Conducting Wall Hall Thrusters," IEPC-2013-276, *33rd International Electric Propulsion Conference*, Washington, D.C., Oct. 2013.

[33] Barral, S. and Ahedo, E., "Low-frequency model of breathing oscillations in Hall discharges," *Physical Review E*, Vol. 79, No. 4, April 2009.

[34] Hara, K. and Boyd, I. D., "Low Frequency Oscillation Analysis of a Hall Thruster Using a One-Dimensional Hybrid-Direct Kinetic Simulation," IEPC-2013-266, *33rd International Electric Propulsion Conference*, Washington, D.C., Oct. 2013.

[35] Tremolizzo, E., Meier, H., and Estublier, D., "In-Flight Distrubance Torque Evaluation of the SMART-1 Plasma Thruster," ESA SP-548, *18th International Symposium on Space Flight Dynamics*, Munich, Germany, Oct. 2004.

[36] Mikellides, I., Katz, I., Hofer, R., and Goebel, D., "Design of a Laboratory Hall Thruster with Magnetically Shielded Channel Walls, Phase III: Comparison of Theory with Experiment," AIAA 2012-3789, *48th AIAA/ASME/SAE/ASEE Joint Propulsion Conference & Exhibit*, Atlanta, GA, Aug. 2012.

[37] Hofer, R., Goebel, D., Mikellides, I., and Katz, I., "Design of a Laboratory Hall Thruster with Magnetically Shielded Channel Walls, Phase II: Experiments," AIAA 2012-3789, *48th AIAA/ASME/SAE/ASEE Joint Propulsion Conference & Exhibit*, Atlanta, GA, Aug. 2012.

[38] Brown, D. L., Larson, C. W., Beal, B. E., and Gallimore, A. D., "Methodology and Historical Perspective of a Hall Thruster Efficiency Analysis," *Journal of Propulsion and Power*, Vol. 25, No. 6, Nov. 2009, pp. 1163–1177.

[39] Dorf, L., Raitses, Y., Fisch, N. J., and Semenov, V., "Effect of anode dielectric coating on Hall thruster operation," *Applied Physics Letters*, Vol. 84, No. 7, 2004, pp. 1070.

[40] Dorf, L., Raitses, Y., and Fisch, N. J., "Experimental studies of anode sheath phenomena in a Hall thruster discharge," *Journal of Applied Physics*, Vol. 97, No. 10, 2005, pp. 103309.

[41] Brown, D. and Gallimore, A., "Investigation of Low Discharge Current Voltage Hall Thruster Operating Modes and Ionization Processes," IEPC-2009-074, *31st International Electric Propulsion Conference*, Ann Arbor, MI, Sept. 2009.

[42] Hofer, R. R., Jankovsky, R. S., and Gallimore, A. D., "High-Specific Impulse Hall Thrusters, Part 1: Influence of Current Density and Magnetic Field," *Journal of Propulsion and Power*, Vol. 22, No. 4, July 2006, pp. 721–731.

[43] Chen, F. F., *Introduction to plasma physics and controlled fusion.*, Plenum Press., New York, 1990.

[44] Reid, B. M., *The Influence of Neutral Flow Rate in the Operation of Hall Thrusters*, Ph.D. dissertation, University of Michigan, Ann Arbor, MI, 2009.

[45] Cappelli, M., Meezan, N., and Gascon, N., "Transport Physics in Hall Plasma Thrusters," AIAA-2002-0485, *40th AIAA Aerospace Sciences Meeting and Exhibit*, Reno, NV, Jan. 2002.

[46] Yoshikawa, S. and Rose, D. J., "Anomalous Diffusion of a Plasma across a Magnetic Field," *Physics of Fluids*, Vol. 5, No. 3, 1962, pp. 334.

[47] Janes, G. S. and Lowder, R. S., "Anomalous Electron Diffusion and Ion Acceleration in a Low-Density Plasma," *Physics of Fluids*, Vol. 9, No. 6, 1966, pp. 1115.

[48] Ducrocq, A., Adam, J. C., Heron, A., and Laval, G., "High-frequency electron drift instability in the cross-field configuration of Hall thrusters," *Physics of Plasmas*, Vol. 13, No. 10, 2006, pp. 102111.

[49] Cavalier, J., Lemoine, N., Bonhomme, G., Tsikata, S., Honore, C., and Gresillon, D., "Hall thruster plasma fluctuations identified as the EB electron drift instability: Modeling and fitting on experimental data," *Physics of Plasmas*, Vol. 20, No. 8, 2013, pp. 082107.

[50] Adam, J. C., Heron, A., and Laval, G., "Study of stationary plasma thrusters using two-dimensional fully kinetic simulations," *Physics of Plasmas*, Vol. 11, No. 1, 2004, pp. 295.

[51] Szabo, J., Warner, N., Martinez-Sanchez, M., and Batishchev, O., "Full Particle-In-Cell Simulation Methodology for Axisymmetric Hall Effect Thrusters," *Journal of Propulsion and Power*, Vol. 30, No. 1, Jan. 2014, pp. 197–208.

[52] King, L., "A (Re-)examination of Electron Motion in Hall Thruster Fields," IEPC-2005-258, *29th International Electric Propulsion Conference*, Princeton University, 2005.

[53] Beal, B. E., Gallimore, A. D., and Hargus, W. A., "Effects of Cathode Configuration on Hall Thruster Cluster Plume Properties," *Journal of Propulsion and Power*, Vol. 23, No. 4, July 2007, pp. 836–844.

[54] McDonald, M. S. and Gallimore, A. D., "Cathode position and orientation effects on cathode coupling in a 6-kW Hall thruster," SPS-III-33, *JANNAF 3rd Spacecraft Propulsion Joint Subcommittee Meeting*, Orlando, FL, Dec. 2008.

[55] Walker, M. L. and Gallimore, A. D., "Hall Thruster Cluster Operation with a Shared Cathode," *Journal of Propulsion and Power*, Vol. 23, No. 3, May 2007, pp. 528–536.

[56] Sommerville, J. D. and King, L. B., "Hall-Effect Thruster–Cathode Coupling, Part I: Efficiency Improvements from an Extended Outer Pole," *Journal of Propulsion and Power*, Vol. 27, No. 4, July 2011, pp. 744–753.

[57] Sommerville, J. D. and King, L. B., "Hall-Effect Thruster–Cathode Coupling, Part II: Ion Beam and Near-Field Plume," *Journal of Propulsion and Power*, Vol. 27, No. 4, July 2011, pp. 754–767.

[58] Tilley, D., de Grys, K., and Myers, R., "Hall thruster-cathode coupling," AIAA 1999-2865, *35th Joint Propulsion Conference*, Los Angeles, CA, June 1999.

[59] Mikellides, I. G., Katz, I., Hofer, R. R., Goebel, D. M., de Grys, K., and Mathers, A., "Magnetic Shielding of the Acceleration Channel Walls in a Long-Life Hall Thruster," AIAA-2010-6942, *46th AIAA Joint Propulsion Conference & Exhibit*, Nashville, TN, July 2010.

[60] Jorns, B. A. and Hofer, R. R., "Low Frequency Plasma Oscillations in a 6-kW Magnetically Shielded Hall Thruster," *49th AIAA/ASME/SAE/ASEE Joint PropulsionConference*, San Jose, CA, July 2013.

[61] Tilinin, G. N., "High-frequency plasma waves in a Hall accelerator with an extended acceleration zone," *Soviet Physics-Technical Physics*, Aug. 1977.

[62] Bechu, S., Perot, C., Gascon, N., Lasgorceix, P., Hauser, A., and Dudeck, M., "Operating mode investigation of a laboratory stationary plasma thruster," AIAA 1999-2567, *35th Joint Propulsion Conference*, Los Angeles, CA, June 1999.

[63] Bechu, S., Lasgorceix, P., Gascon, N., Roche, S., Prioul, M., Albarede, L., and Dudeck, M., "Comparison between two kinds of Hall thrusters - SPT100 and ATON," AIAA 2000-3524, *36th AIAA/ASME/SAE/ASEE Joint Propulsion*, Huntsville, AL, July 2000.

[64] Zhurin, V., Kahn, J., Kaufman, H., and Day, M., "Dynamic Characteristics of Closed Drift Thrusters," IEPC 1993-095, *23rd International Electric Propulsion Conference*, Seattle, WA, Sept. 1993.

[65] Gascon, N., Dudeck, M., and Barral, S., "Wall material effects in stationary plasma thrusters. I. Parametric studies of an SPT-100," *Physics of Plasmas*, Vol. 10, No. 10, 2003, pp. 4123.

[66] Barral, S., Makowski, K., Peradzynski, Z., Gascon, N., and Dudeck, M., "Wall material effects in stationary plasma thrusters. II. Near-wall and in-wall conductivity," *Physics of Plasmas*, Vol. 10, No. 10, 2003, pp. 4137.

[67] McDonald, M. and Gallimore, A., "Parametric Investigation of the Rotating Spoke Instability in Hall Thrusters," IEPC-2011-242, *32nd International Electric Propulsion Conference*, Wiesbaden, Germany, Sept. 2011.

[68] Yamamoto, N., Nakagawa, T., Komurasaki, K., and Arakawa, Y., "Influence of Discharge Oscillation on Hall Thruster Performance," IEPC-01-055, *27th International Electric Propulsion Conference*, Pasadena, CA, Oct. 2001.

[69] Gascon, N., Meezan, N., and Cappelli, M., "Low Frequency Plasma Wave Dispersion and Propagation in Hall Thrusters," IEPC-01-56, *27th International Electric Propulsion Conference*, Pasadena, CA, Oct. 2001.

[70] Baitin, A., Elizarov, L., Ivanov, A., and Bacal, M., "Maximum value and stability of near-wall current," *24th International Electric Propulsion Conference*, Moscow, Russia, Sept. 1995.

[71] Jolivet, L. and Roussel, J.-F., "Effects of the secondary electron emission on the sheath phenomenon in a Hall thruster," *Third International Conference on Spacecraft Propulsion*, Cannes, France, Oct. 2000.

[72] Mitrofanova, O., Gnizdor, R., Murashko, V., Koryakin, A., and Nesterenko, A., "New Generation of SPT-100," IEPC-2011-041, *32nd International Electric Propulsion Conference*, Wiesbaden, Germany, Sept. 2011.

[73] Choueiri, E. Y., "Plasma oscillations in Hall thrusters," *Physics of Plasmas*, Vol. 8, No. 4, 2001, pp. 1411.

[74] Lobbia, R. B., Sekerak, M. J., Liang, R., and Gallimore, A. D., "High-speed Dual Langmuir Probe Measurements of the Plasma Properties and EEDFs in a HET Plume," IEPC-2011-168, *32nd International Electric Propulsion Conference*, Wiesbaden, Germany, Sept. 2011.

[75] Chesta, E., Lam, C., Meezan, N., Schmidt, D., and Cappelli, M., "A characterization of plasma fluctuations within a Hall discharge," *IEEE Transactions on Plasma Science*, Vol. 29, No. 4, Aug. 2001, pp. 582–591.

[76] Boeuf, J. P. and Garrigues, L., "Low frequency oscillations in a stationary plasma thruster," *Journal of Applied Physics*, Vol. 84, No. 7, 1998, pp. 3541.

[77] Fife, J., Martinez-Sanchez, M., and Szabo, J., "A Numerical Study of Low-Frequency Discharge Oscillations in Hall Thrusters," *33rd AIAA/ASME/SAE/ASEE Joint Propulsion Conference & Exhibit*, Seattle, WA, 1997.

[78] McDonald, M., Bellant, C., St Pierre, B., and Gallimore, A., "Measurement of Cross-Field Electron Current in a Hall Thruster Due to Rotating Spoke Instabilities," AIAA 2011-5810, *47th AIAA/ASME/SAE/ASEE Joint Propulsion Conference & Exhibit*, San Diego, CA, Aug. 2011.

[79] McDonald, M. S. and Gallimore, A. D., "Rotating Spoke Instabilities in Hall Thrusters," *IEEE Transactions on Plasma Science*, Vol. 39, No. 11, Nov. 2011, pp. 2952–2953.

[80] Raitses, Y., Griswold, M., Ellison, L., Parker, J., and Fisch, N., "Studies of Rotating Spoke Oscillations in Cylindrical Hall Thrusters," AIAA 2012-4179, *48th AIAA/ASME/SAE/ASEE Joint Propulsion Conference*, Atlanta, GA, Aug. 2012.

[81] Parker, J. B., Raitses, Y., and Fisch, N. J., "Transition in electron transport in a cylindrical Hall thruster," *Applied Physics Letters*, Vol. 97, No. 9, 2010, pp. 091501.

[82] Ellison, C. L., Raitses, Y., and Fisch, N. J., "Cross-field electron transport induced by a rotating spoke in a cylindrical Hall thruster," *Physics of Plasmas*, Vol. 19, No. 1, 2012.

[83] Mikellides, I., Katz, I., Hofer, R., and Goebel, D., "Hall-Effect Thruster Simulations with 2-D Electron Transport and Hydrodynamics Ions," IEPC-2009-114, *31st International Electric Propulsion Conference*, Ann Arbor, MI, Sept. 2009.

[84] Parra, F. I., Ahedo, E., Fife, J. M., and Martinez-Sanchez, M., "A two-dimensional hybrid model of the Hall thruster discharge," *Journal of Applied Physics*, Vol. 100, No. 2, 2006, pp. 023304.

[85] Barral, S. and Ahedo, E., "Theoretical Study of the Breathing Mode in Hall Thrusters," AIAA 2006-5172, *42nd AIAA/ASME/SAE/ASEE Joint Propulsion Conference & Exhibit*, Sacramento, CA, July 2006.

[86] Hara, K., Boyd, I. D., and Kolobov, V. I., "One-dimensional hybrid-direct kinetic simulation of the discharge plasma in a Hall thruster," *Physics of Plasmas*, Vol. 19, No. 11, 2012, pp. 113508.

[87] Hirakawa, M. and Arakawa, Y., "Particle Simulation of Plasma in Electric Propulsion Thrusters." *Journal of the Japan Society for Aeronautical and Space Sciences*, Vol. 45, No. 523, 1997, pp. 444–452.

[88] Hirakawa, M. and Arakawa, Y., "Numerical simulation of plasma particle behavior in a Hall thruster," AIAA-1996-3195, *32ns Joint Propulsion Conference*, Lake Buena Vista, FL, July 1996.

[89] Lam, C., Knoll, A., Cappelli, M., and Fernandez, E., "Dimensional (z-theta) Simulations of Hall Thruster Anomalous Transport," IEPC-2009-102, *31st International Electric Propulsion Conference*, Sept. 2009.

[90] Esipchuk, Y., Morozov, A. I., Tilinin, G. N., and Trofimov, A. V., "Plasma oscillations in closed-drift accelerators with an extended acceleration zone," *Soviet Physics-Technical Physics*, Vol. 18, No. 7, Jan. 1974, pp. 928–932.

[91] Esipchuk, Y. and Tilinin, G. N., "Drift instability in a Hall-current plasma accelerator," *Soviet Physics-Technical Physics*, Vol. 21, No. 4, April 1976.

[92] Smith, T. B., Huang, W., Reid, B. M., and Gallimore, A. D., "Near-field laser-induced flourescence velocimetry of neutral xenon in a 6-kW Hall thruster plume," IEPC-2007-229, *International Electric Propulsion Conference*, Florence, Italy, Sept. 2007.

[93] Florenz, R. E., *The X3 100-kW Class Nested-Channel Hall Thruster: Motivation, Implementation and Initial Performance*, Ph.D. dissertation, University of Michigan, Ann Arbor, MI, 2014.

[94] Barral, S., Ahedo, E., Hartfuss, H.-J., Dudeck, M., Musielok, J., and Sadowski, M. J., "On the Origin of Low Frequency Oscillations in Hall Thrusters," Vol. 993, 2008, pp. 439–442.

[95] Barral, S. and Peradzynski, Z., "Ionization oscillations in Hall accelerators," *Physics of Plasmas*, Vol. 17, No. 1, 2010.

[96] Lobbia, R. B. and Gallimore, A. D., "High-speed dual Langmuir probe," *Review of Scientific Instruments*, Vol. 81, No. 7, 2010, pp. 073503.

[97] Lobbia, R. B. and Gallimore, A. D., "Fusing Spatially and Temporally Separated Single-point Turbulent Plasma Flow Measurements into Two-dimensional Time-resolved Visualizations," *12th International Conference on Information Fusion*, Seattle, WA, July 2009.

[98] Escobar, D. and Ahedo, E., "Ionization-induced azimuthal oscillation in Hall Effect Thrusters," IEPC-2011-196, *32nd International Electric Propulsion Conference*, Wiesbaden, Germany, Sept. 2011.

[99] Lomas, P. J. and Kilkenny, J. D., "Electrothermal instabilities in a Hall accelerator," *Plasma Physics*, Vol. 19, No. 4, April 1977, pp. 329–341.

[100] McDonald, M. S. and Gallimore, A. D., "Comparison of Breathing and Spoke Mode Strength in the H6 Hall Thruster Using High Speed Imaging," IEPC-2013-353, *33rd International Electric Propulsion Conference*, Washington, D.C., Oct. 2013.

[101] Kapulkin, A. and Guelman, M. M., "Low-Frequency Instability in Near-Anode Region of Hall Thruster," *IEEE Transactions on Plasma Science*, Vol. 36, No. 5, Oct. 2008, pp. 2082–2087.

[102] Frias, W., Smolyakov, A. I., Kaganovich, I. D., and Raitses, Y., "Long wavelength gradient drift instability in Hall plasma devices. I. Fluid theory," *Physics of Plasmas*, Vol. 19, No. 7, 2012, pp. 072112.

[103] Frias, W., Smolyakov, A. I., Kaganovich, I. D., and Raitses, Y., "Long wavelength gradient drift instability in Hall plasma devices. II. Applications," *Physics of Plasmas*, Vol. 20, No. 5, 2013, pp. 052108.

[104] Chesta, E., Meezan, N. B., and Cappelli, M. A., "Stability of a magnetized Hall plasma discharge," *Journal of Applied Physics*, Vol. 89, No. 6, 2001, pp. 3099.

[105] Smolyakov, A. I., Frias, W., Kaganovich, I. D., and Raitses, Y., "Sheath-Induced Instabilities in Plasmas with ExB Drift," *Physical Review Letters*, Vol. 111, No. 11, Sept. 2013.

[106] Reid, B. M., Shastry, R., Gallimore, A. D., and Hofer, R. R., "Angularly-Resolved ExB Probe Spectra in the Plume of a 6-kW Hall Thruster," AIAA 2008-5287, *44th AIAA/ASME/SAE/ASEE Joint Propulsion Conference & Exhibit*, Hartford, CT, July 2008.

[107] Walker, M. L. R., *Effects of Facility Backpressure on the Performance and Plume of a Hall Thruster*, Ph.D. dissertation, University of Michigan, Ann Arbor, MI, 2005.

[108] Vincenti, W. G. and Kruger, C. H., *Introduction to physical gas dynamics*, Krieger, Huntington, N.Y., 1975.

[109] Haag, T. W., "Thrust stand for high-power electric propulsion devices," *Review of Scientific Instruments*, Vol. 62, No. 5, 1991, pp. 1186.

[110] Shastry, R., *Experimental Characterization of the Near-Wall Region in Hall Thrusters and its Implications on Performance and Lifetime*, Ph.D. dissertation, University of Michigan, Ann Arbor, MI, 2011.

[111] Xu, K. G. and Walker, M. L. R., "High-power, null-type, inverted pendulum thrust stand," *Review of Scientific Instruments*, Vol. 80, No. 5, 2009, pp. 055103.

[112] Huang, W., *Study of Hall Thruster Discharge Channel Wall Erosion via Optical Diagnostics*, Ph.D. dissertation, University of Michigan, Ann Arbor, MI, 2011.

[113] Brown, D. L., *Investigation of Low Discharge Voltage Hall Thruster Characteristics and Evaluation of Loss Mechanisms*, Ph.D. dissertation, University of Michigan, Ann Arbor, MI, 2009.

[114] Jameson, K. K., *Investigation of hollow cathode effects on total thruster efficiency in a 6 kW Hall thruster*, Ph.D. dissertation, University of California, Los Angeles, Los Angeles, CA, 2008.

[115] Hofer, R., Mikellides, I., Katz, I., and Goebel, D., "Wall Sheath and Electron Mobility Modeling in Hybrid-PIC Hall Thruster Simulations," AIAA 2007-5267, *43rd AIAA/ASME/SAE/ASEE Joint Propulsion Conference & Exhibit*, Cincinnati, OH, July 2007.

[116] Chen, F. F., "Electric Probes," *Plasma Diagnostic Techniques*, edited by R. H. Huddlestone, Pure and applied physics,v. 21, Academic Press, New York, 1965, pp. 113–200.

[117] Cherrington, B. E., "The use of electrostatic probes for plasma diagnostics - A review," *Plasma Chemistry and Plasma Processing*, Vol. 2, No. 2, June 1982, pp. 113–140.

[118] Hershkowitz, N., "How Langmuir Probes Work," *Plasma diagnostics.*, edited by O. Auciello and D. L. Flamm, Vol. 1. Discharge parameters and chemistry of *Plasma–materials interactions*, Academic Press, Boston, 1989, pp. 113–183.

[119] Huddlestone, R. H., editor, *Plasma diagnostic techniques*, Pure and applied physics,v. 21, Academic Press, New York, 1965, 627 p.

[120] Hutchinson, I. H. and Cambridge University Press, *Principles of Plasma Diagnostics*, Cambridge University Press, Cambridge, 2002.

[121] Schott, L., "Electrical Probes," *Plasma Diagnostics*, edited by W. Lochte-Holtgreven, North-Holland Publishing Company, Amsterdam, 1968, pp. 668–731.

[122] Swift, J. D. and Schwar, M. J. R., *Electrical probes for plasma diagnostics*, Iliffe Books; American Elsevier, London; New York, 1969.

[123] Lieberman, M. A. and Lichtenberg, A. J., *Principles of plasma discharges and materials processing*, Wiley-Interscience, Hoboken, N.J., 2005.

[124] Lobbia, R. B. and Gallimore, A. D., "Temporal limits of a rapidly swept Langmuir probe," *Physics of Plasmas*, Vol. 17, No. 7, 2010, pp. 073502.

[125] Crawford, F. W. and Gard, R., "Low-Frequency Impedance Characteristics of a Langmuir Probe in a Plasma," *Journal of Applied Physics*, Vol. 37, No. 1, 1966, pp. 180.

[126] Bendat, J. S. and Piersol, A. G., *Engineering applications of correlation and spectral analysis*, Wiley, New York, 1980.

[127] Graf, K. A., "Comparison of Langmuir Probe and Microwave Diagnostic Techniques," *Journal of Applied Physics*, Vol. 38, No. 11, 1967, pp. 4466.

[128] Lobbia, R., Liu, T., and Gallimore, A., "Correlating time-resolved optical and Langmuir probe measurements of Hall thruster dynamics," SPS-III-36, *JANNAF 3rd Spacecraft Propulsion Joint Subcommittee Meeting*, Orlando, FL, Dec. 2008.

[129] Griem, H. R. and Cambridge University Press, *Principles of Plasma Spectroscopy*, Cambridge University Press, Cambridge, 1997.

[130] Bevington, P. R. and Robinson, D. K., *Data reduction and error analysis for the physical sciences*, McGraw-Hill, New York, 1992.

[131] "MATLAB R2012a," Feb. 2012.

[132] Strum, R. D., *First principles of discrete systems and digital signal processing*, Addison-Wesley series in electrical engineering, Addison-Wesley, Reading, Mass, 1988.

[133] Roche, S., Bechu, S., Prioul, M., Pagnon, D., Gascon, N., Bouchoule, A., Magne, L., Lasgorceix, P., and Touzeau, M., "Plasma characterisation of an ATON-Hall thruster - Channel and plume investigation," AIAA 2000-3523, *36th Joint Propulsion Conference*, Huntsville, AL, July 2000.

[134] Lide, D. R., *CRC Handbook of Chemistry and Physics.*, CRC Press, Boca Raton, 1992.

[135] Bellan, P. M., *Fundamentals of plasma physics*, Cambridge University Press, Cambridge, 2008.

[136] Grys, K. d., Mathers, A., Welander, B., and Khayms, V., "Demonstration of 10,400 Hours of Operation on 4.5 kW Qualification Model Hall Thruster," *46th AIAA/ASME/SAE/ASEE Joint Propulsion Conference & Exhibit*, AIAA 2010-6698, *46th AIAA/ASME/SAE/ASEE Joint Propulsion Conference & Exhibit*, Nashville, TN, July 2010.

[137] de Grys, K., Welander, B., Dimicco, J., Wenzel, S., Kay, B., Khayms, V., and Paisley, J., "4.5 Kw Hall Thruster System Qualification Status," AIAA 2005-3682, *41st AIAA/ASME/SAE/ASEE Joint Propulsion Conference & Exhibit*, Tucson, AZ, July 2005.

[138] Garrigues, L., Perez-Luna, J., Lo, J., Hagelaar, G. J. M., Boeuf, J. P., and Mazouffre, S., "Empirical electron cross-field mobility in a Hall effect thruster," *Applied Physics Letters*, Vol. 95, No. 14, 2009, pp. 141501.

[139] Acton, F. S., *Analysis of straight-line data.*, Wiley, New York, 1959.

[140] Beall, J. M., "Estimation of wavenumber and frequency spectra using fixed probe pairs," *Journal of Applied Physics*, Vol. 53, No. 6, 1982, pp. 3933.

[141] Stix, T. H., *Waves in plasmas*, American Institute of Physics, New York, 1992.

[142] Barral, S. and Peradzynski, Z., "A new breath for the breathing mode," IEPC-2009-070, *31st International Electric Propulsion Conference*, Ann Arbor, MI, Sept. 2009.

[143] Mazouffre, S. and Bourgeois, G., "Spatio-temporal characteristics of ion velocity in a Hall thruster discharge," *Plasma Sources Science and Technology*, Vol. 19, No. 6, Dec. 2010, pp. 065018.

[144] Durot, C. J., Gallimore, A. D., and Smith, T. B., "Validation and evaluation of a novel time-resolved laser-induced fluorescence technique," *Review of Scientific Instruments*, Vol. 85, No. 1, Jan. 2014, pp. 013508.

[145] Ellis, R. F., Marden-Marshall, E., and Majeski, R., "Collisional drift instability of a weakly ionized argon plasma," *Plasma Physics*, Vol. 22, No. 2, Feb. 1980, pp. 113–131.

[146] Bettinger, R. T. and Chen, A. A., "An End Effect Associated with Cylindrical Langmuir Probes Moving at Satellite Velocities," *Journal of Geophysical Research*, Vol. 73, No. 7, 1968, pp. 2513–2528.

[147] Hester, S. D. and Sonin, A. A., "Ion Temperature Sensitive End Effect in Cylindrical Langmuir Probe Response at Ionosphere Satellite Conditions," *Physics of Fluids*, Vol. 13, No. 5, 1970, pp. 1265.

[148] Chung, P. M., Talbot, L., and Touryan, K. J., "Electric Probes in Stationary and Flowing Plasmas: Part 1. Collisionless and Transitional Probes," *AIAA Journal*, Vol. 12, No. 2, Feb. 1974, pp. 133–144.

[149] Kanal, M., "Theory of Current Collection of Moving Cylindrical Probes," *Journal of Applied Physics*, Vol. 35, No. 6, 1964, pp. 1697.

[150] Hoegy, W. R., "Current to a moving cylindrical electrostatic probe," *Journal of Applied Physics*, Vol. 44, No. 12, 1973, pp. 5365.

[151] Allen, J. E. and Turrin, A., "The collection of positive ions by a probe immersed in a plasma," *Proceedings of the Physical Society*, Vol. 83, No. 1, Jan. 1964, pp. 177–179.

[152] Laframboise, J. G., *Theory of Spherical and Cylindrical Langmuir Probes in a Collisionless Maxwellian Plasma at Rest*, Ph.D. dissertation, April 1966.

[153] Peterson, E. W. and Talbot, L., "Collisionless electrostatic single-probe and double-probe measurements," *AIAA Journal*, Vol. 8, No. 12, Dec. 1970, pp. 2215–2219.

[154] Chen, X., Dickens, J., Hatfield, L. L., Choi, E.-H., and Kristiansen, M., "Approximate analytical solutions for the space-charge-limited current in one-dimensional and two-dimensional cylindrical diodes," *Physics of Plasmas*, Vol. 11, No. 6, 2004, pp. 3278.

[155] Langmuir, I. and Blodgett, K., "Currents Limited by Space Charge between Coaxial Cylinders," *Physical Review*, Vol. 22, No. 4, Oct. 1923, pp. 347–356.

[156] Bettinger, R. T. and Walker, E. H., "Relationship for Plasma Sheaths about Langmuir Probes," *Physics of Fluids*, Vol. 8, No. 4, 1965, pp. 748.

[157] McDonald, M. S., Liang, R., and Gallimore, A. D., "Practical Application ofWide Bandwidth Floating Emissive Probes andWavelet Analysis to the X2 Nested Hall Thruster," IEPC-2013-352, *33rd International Electric Propulsion Conference*, Washington, D.C., Oct. 2013.

[158] Huang, W., Shastry, R., Soulas, G. C., and Kamhawi, H., "Farfield Plume Measurements and Analysis on the NASA-300M and NASA-300MS," IEPC-2013-057, *33rd International Electric Propulsion Conference*, Washington, D.C., Oct. 2013.

[159] Kamhawi, H., Haag, T., Jacobson, D., and Manzella, D., "Performance Evaluation of the NASA-300M 20 kW Hall Thruster," AIAA 2011-5521, *47th AIAA/ASME/SAE/ASEE Joint Propulsion Conference & Exhibit*, San Diego, CA, July 2011.

[160] Mikellides, I., Katz, I., and Hofer, R., "Design of a Laboratory Hall Thruster with Magnetically Shielded Channel Walls, Phase I: Numerical Simulations," AIAA 2011-5809, *47th AIAA/ASME/SAE/ASEE Joint Propulsion Conference & Exhibit*, San Diego, CA, Aug. 2011.